Materialprüfungsanstalt
Universität Stuttgart

Technisch-
Wissenschaftlicher-
Bericht

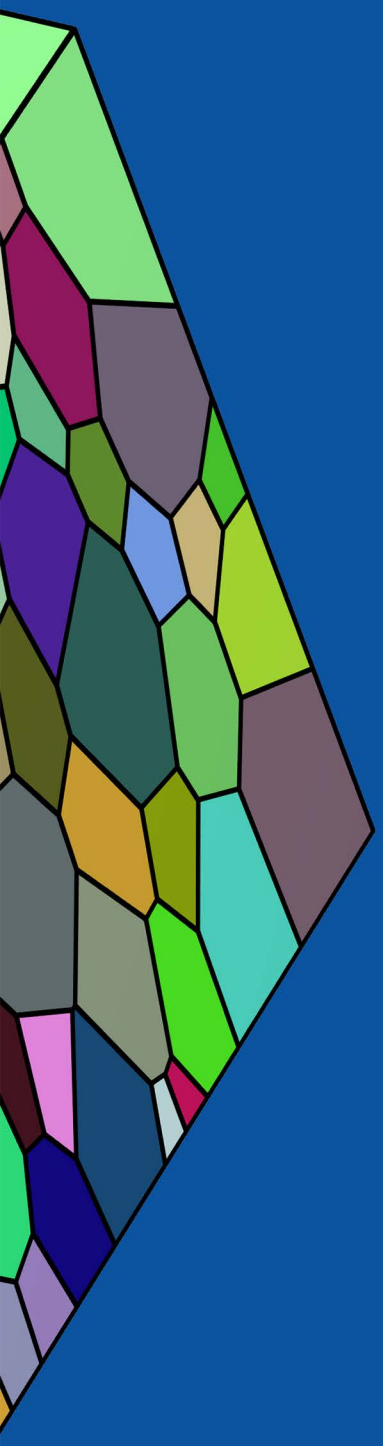

Nikolai Arnaudov

Micromechanical Simulation of Fatigue Crack Initiation under Hydrogen Influence

Micromechanical Simulation of Fatigue Crack Initiation under Hydrogen Influence

vorgelegt von

Nikolai Arnaudov

aus Wertheim

Materialprüfungsanstalt (MPA) der Universität Stuttgart

2021

Technisch-Wissenschaftlicher-Bericht
Band: 2021/01

Arnaudov, Nikolai:
Micromechanical Simulation of Fatigue Crack Initiation under Hydrogen Influence

Herausgeber:

Pfaffenwaldring 32
70569 Stuttgart
Internet: http://www.mpa.uni-stuttgart.de
ISBN 978-3-946789-10-9

Micromechanical Simulation of Fatigue Crack Initiation under Hydrogen Influence

Von der Fakultät Energie-, Verfahrens- und Biotechnik
der Universität Stuttgart zur Erlangung der Würde
eines Doktors der Ingenieurwissenschaften (Dr.-Ing.)
genehmigte Abhandlung

vorgelegt von

Nikolai Arnaudov

aus Wertheim

Hauptberichter :	Prof. Dr.-Ing. Stefan Weihe
Mitberichter :	Prof. Dr.-Ing. Marc-André Keip
Tag der mündlichen Prüfung :	07.12.2020

Materialprüfungsanstalt (MPA) der Universität Stuttgart

2021

Abstract

The development of components in contact with pressurized hydrogen for fuel cell applications demands high safety and reliability requirements. A deteriorating effect of hydrogen on metallic materials must be considered when operating components in gaseous hydrogen atmosphere. The small size of hydrogen atoms enables the gas to diffuse into metals and accumulate on certain locations changing the mechanical properties and material behavior. It is known from experimental investigation that hydrogen can reduce the fatigue lifetime of certain steels. Motivated by the objective to ensure reliable, safe and economical components for fuel cell systems, a modeling framework is developed to predict the fatigue life of steels in hydrogen atmosphere. Incorporating the microstructure of the investigated material, the simulation model is capable to determine local hydrogen concentrations and the distribution of hydrogen due to its interplay with the microstructure.

The formulation is based on a coupled finite element model to describe hydrogen diffusion and large elasto-plastic deformation on a microstructural level. A phenomenological anisotropic crystal plasticity model is used, considering plastic deformation as slip on defined slip systems. The ferritic steel 1.4003 is investigated in this work as an example material which might be used for fuel cell components. Microstructural analysis provides information about the crystal structure and the grain orientations of the steel. The simulations are carried out on representative domains incorporating these information. Experimental fatigue investigations serve to determine material parameter for the model and fatigue data for the subsequent validation. To evaluate the fatigue lifetime of the material based on micromechanical stress and strain quantities from the finite element calculation, a prediction scheme is developed.

This scheme is based on the idea of fatigue indicator parameter, which was shown by several research groups to be a promising method to predict fatigue lifetimes in air atmosphere based on micromechanical simulations. In this work a modification of a fatigue indicator parameter is proposed, considering the local concentration of trapped hydrogen. Therewith, an increased amount of locally accumulated plastic slip results in a premature failure of the material. A comparison to experimental fatigue data shows the capability of the method to predict the fatigue lifetime of the investigated material in both atmospheres, air and hydrogen. Numerical studies are performed to analyze the model's sensitivity towards material parameters and to investigate the influence of microstructural properties concerning hydrogen diffusion and accumulation. The proposed approach enables a better understanding of the microstructure dependent fatigue behavior under hydrogen atmosphere and poses a key element for a reliable component design for industrial applications.

Zusammenfassung

Die Entwicklung von Komponenten für Anwendungen in der Brennstoffzellentechnologie, die in Kontakt mit Druckwasserstoff stehen, stellt hohe Anforderungen an Sicherheit und Zuverlässigkeit. Bei dem Einsatz von Bauteilen in Wasserstoffgasatmosphäre muss der schädigende Effekt von Wasserstoff auf metallische Werkstoffe berücksichtigt werden. Die sehr kleinen Wasserstoffatome ermöglichen eine Diffusion des Gases in das Metall und sammeln sich lokal an, wobei sie mechanische Eigenschaften und das Materialverhalten ändern können. Experimentelle Untersuchungen haben gezeigt, dass Wasserstoff die Ermüdungslebensdauer einiger Stähle reduziert. Mit dem Ziel zuverlässige, sichere und wirtschaftliche Bauteile für das Brennstoffzellensystem zu garantieren, wurde ein Modell entwickelt, um die Lebensdauer von Stählen unter Wasserstoffatmosphäre vorherzusagen. Unter Berücksichtigung der Mikrostruktur des untersuchten Stahles, kann das Simulationsmodell lokale Wasserstoffkonzentrationen sowie die Verteilung des Wasserstoffs bedingt durch die Wechselwirkung mit der Mikrostruktur berechnen.

Die Formulierung basiert auf einem gekoppelten Finite-Elemente Modell, welches den Wasserstofftransport und große elastoplastische Deformationen auf Mikrostrukturebene beschreibt. Dazu wird ein phänomenologisches anisotropes Kristallplastizitätsmodell verwendet, das plastische Deformation als Gleiten auf definierten Gleitsystemen beschreibt. In dieser Arbeit wird beispielhaft der ferritische Stahl 1.4003 untersucht, der für Komponenten der Brennstoffzelle verwendet werden könnte. Mikrostrukturuntersuchungen liefern Informationen wie beispielsweise die Kristallstruktur und die Kornorientierung des Stahls. Diese Informationen werden verwendet um repräsentative Gebiete zu erzeugen, auf denen die Simulationen gerechnet werden. Materialparameter werden mit Hilfe von Ermüdungsexperimenten bestimmt, die anschließend auch zur Validierung des Modells verwendet werden. Es wird eine Vorgehensweise entwickelt, um die Ermüdungslebensdauer des Materials aus mikromechanischen Spannungs- und Dehnungsgrößen abzuleiten, die mittels der Finite-Elemente Simulation bestimmt werden.

Dieser Ansatz basiert auf der Idee von Ermüdungsindikatoren. Einige Forschungsgruppen konnten mit dieser Methode unter Verwendung mikromechanischer Simulationen die Ermüdungslebensdauer an Luft erfolgreich vorhersagen. In dieser Arbeit wird eine Modifikation eines Ermüdungsindikators vorgeschlagen, die die lokale getrappte Wasserstoffkonzentration berücksichtigt. Der daraus resultierende erhöhte Anteil lokaler akkumulierter plastischen Dehnung verursacht ein frühzeitiges Versagen des Materials. Ein Vergleich mit Daten aus Ermüdungsexperimenten validiert das Modell hinsichtlich der Vorhersagegüte der Ermüdungslebensdauer des untersuchten Materials in Luft- wie in Wasserstoffatmosphäre. Mittels numerischer Studien wird die Sensitivität des Modells bezüglich Materialparameter untersucht und der Einfluss der Mikrostruktur auf die Wasserstoffdiffusion und Anhäufung betrachtet. Der hier vorgestellte Ansatz verbessert das physikalische Verständnis für das mikrostrukturabhängige Ermüdungsverhalten unter Wasserstoffatmosphäre und stellt ein zentrales Element für eine zuverlässige Bauteilauslegung für industrielle Anwendungen.

Acknowledgments

This thesis is the result of three exciting years as a doctoral candidate at the Robert Bosch GmbH department of Reliability for Metallic Components and Materials at the Center for Research and Advanced Engineering in Renningen together with the Material Testing Institute of the University of Stuttgart. Many people contributed to this work and I would like to thank all of them.

First, I would like to express my deepest thanks to my supervisor Professor Stefan Weihe for his support, guidance and confidence in this work. I am also very grateful to Professor Marc-André Keip not only for his interest in my research topic, his helpful comments and for his acceptance to become the co-referee for this thesis but also for supporting me during my studies in Simulation Technology.

My utmost gratitude belongs to Professor Christian Miehe, who sadly passed away, during my Master Thesis under his supervision. He was my mentor and raised my interest in computational mechanics with his enthusiasm and knowledge in continuum mechanics, which he eagerly passed over to his students.

My sincerest thanks belong to Dr.-Ing. Manfred Bacher-Höchst, who supported me from the very first day at Bosch with his vast knowledge in metal fatigue and accompanied this work even into his well-earned retirement. This thesis was continuously improved by numerous vivid discussions with my supervisors at Bosch Dr.-Ing. Anton Kolyshkin, Dr.-Ing. Simone Schreijäg, my project leader Dr.-Ing. Petra Sonnweber-Ribic. Moreover, Dr.-Ing. Ulrich Weber and Stefan Zickler from the Material Testing Institute helped this work to ripen with their expertise on hydrogen and finite element analysis.

I would like to thank all colleagues at my department and group for their fruitful interactions and great working atmosphere, from which this work has greatly profited. A special thanks to my fellow Ph.D. candidates Benjamin Schäfer, Marius Graf, Zeynel Benk, Aleksandar Eric, Jannick Kuhn and Ali Durmaz for always being open for discussion on all possible topics, for good conversations and true friendship.

To my friends and family in Stuttgart and in my hometown Wertheim, thanks a lot for enlivening me during my spare time. Thanks as well to my brother-in-law and colleague Frank Meyer for the numerous chats about reliability topics and beyond.

A huge thank you to Moira Peter for her steady encouragement over these three years and the lovely support in so many ways.

I thank my sister Dr. med. Theresa Arnaudov for her precious advice, permanent motivation and always being there for me.

Heartfelt gratitude to my parents Claudia and Dr.-Ing. Konstantin Arnaudov for their limitless support, never losing faith in me and simply their unconditional love.

Thank you all!

Stuttgart, January 2020 Nikolai Arnaudov

Contents

List of Abbreviations and Symbols

Abbreviations

AIDE	Adsorption induced dislocation emission
BCC	Body centered cubic
CPFEM	Crystal plasticity finite element method
CZM	Cohesive zone modeling
DFT	Density functional theory
EBSD	Electron back scattered diffraction
FCC	Face centered cubic
FCV	Fuel cell vehicle
FEM	Finite element method
FIB	Focused ion beam
FIP	Fatigue indicator parameter
HCF	High-cycle fatigue
HCP	Hexagonal close packed
HEDE	Hydrogen enhanced decohesion
HELP	Hydrogen enhanced local plasticity
HESIV	Hydrogen enhanced strain induced vacancy theory
HIPT	Hydrogen induced phase transformation
LCF	Low-cycle fatigue
PBC	Periodic boundary condition
PEM	Proton exchange membrane
PSB	Persistent slip band
RVE	Representative volume element
SDV	Solution dependent variable

SEM	Scanning electron microscopy
SFE	Stacking fault energy
TEM	Transmission electron microscopy
UMAT	User-defined material
UMATHT	User-defined material considering heat transfer

Symbols

$(\bullet)^{\alpha}$	Quantity on a certain slip system α	-
α	Number of hydrogen atom sites per trap	-
$\bar{C}_L$	Scaled hydrogen lattice concentration	mol/mm^3
$\bar{C}_T$	Scaled hydrogen lattice concentration	mol/mm^3
$\bar{C}_{total}$	Scaled total hydrogen concentration	mol/mm^3
$\bar{\varepsilon}^p$	Accumulated plastic slip	-
$\boldsymbol{b}$	Burgers vector	-
$\boldsymbol{E}$	Green-Lagrange strain	-
$\boldsymbol{E}^e$	Elastic Green-Lagrange strain	-
β	Number of interstitial sites per metal atom	-
$\boldsymbol{F}$	Deformation gradient	-
$\boldsymbol{F}^e$	Elastic deformation gradient	-
$\boldsymbol{F}^p$	Plastic deformation gradient	-
$\boldsymbol{L}$	Material velocity gradient	1/s
$\boldsymbol{l}$	Spatial velocity gradient	1/s
$\boldsymbol{M}$	Schmid matrix	-
$\boldsymbol{m}$	Slip direction	-
$\boldsymbol{n}$	Slip plane normal	-
$\boldsymbol{P}$	First Piola-Kirchhoff stress	MPa

$\boldsymbol{S}$	Second Piola-Kirchhoff stress	MPa
$\boldsymbol{\sigma}$	Cauchy stress	MPa
$\boldsymbol{t}$	Cauchy stress vector	MPa
$\boldsymbol{\tau}$	Kirchhoff stress	MPa
$\mathcal{B}_0$	Reference configuration	-
$\mathcal{B}_t$	Current configuration	-
χ_b	Resolved backstress	MPa
$\Delta\sigma$	Stress range	MPa
$\Delta\varepsilon$	Strain range	-
$\bar{\boldsymbol{J}}$	Hydrogen flux vector	$\mathrm{mol}/(\mathrm{mm}^2 s)$
γ	Plastic shear	-
γ_0	Reference shear rate	1/s
$\mathbb{C}^e$	Fourth-order anisotropic elasticity tensor	MPa
μ_L	Chemical potential for lattice hydrogen	$\mathrm{N\,mm}/(\mathrm{mol})$
μ_T	Chemical potential for trapped hydrogen	$\mathrm{N\,mm}/(\mathrm{mol})$
ν	Poisson's ratio	-
σ	Uniaxial stress (engineering stress)	MPa
σ'_f	Coefficient of fatigue strength	MPa
σ_a	Stress amplitude	MPa
σ_f	Fatigue limit	-
σ_m	Mean stress	MPa
σ_Y	Macroscopic yield strenght	MPa
τ	Shear stress	MPa
τ_0	Initial resistance to dislocation motion in a single crystal	MPa
τ_c	Critical resolved shear stress	MPa
τ_s	Saturated shear stress	MPa

τ_{rss}	Resolved shear stress	MPa
θ_L	Lattice site occupancy	-
θ_T	Trap site occupancy	-
$\tilde{\mathcal{B}}$	Intermediate configuration	-
ε	Engineering normal strain	-
ε'_f	Coefficient of fatigue ductility	-
ε_a	Strain amplitude	-
$\varepsilon_{a,el}$	Elastic strain amplitude	-
$\varepsilon_{a,pl}$	Plastic strain amplitude	-
$\varepsilon_{a,t}$	Total strain amplitude	-
A_0	Initial area	mm^2
A_1	Parameter for kinematic hardening	MPa
A_2	Parameter for kinematic hardening	-
b	Exponent of fatigue strength	-
c	Exponent of fatigue ductility	-
C_L	Hydrogen lattice concentration	$1/mm^3$
C_T	Trapped hydrogen concentration	$1/mm^3$
C_{11}	Component of $\mathbb{C}^e$	MPa
C_{12}	Component of $\mathbb{C}^e$	MPa
C_{44}	Component of $\mathbb{C}^e$	MPa
C_{total}	Total hydrogen concentration	$1/mm^3$
D_L	Lattice diffusivity	$mm^2/(s)$
E	Young's modulus	MPa
E_b	Trap binding energy	kJ/mol
F	Uniaxial force	N
f_{load}	Cyclic loading frequency	Hz

FIP_p	Accumulated plastic slip FIP	-
FIP_{FS}	Fatemie-Socie FIP	-
FIP_H	Hydrogen dependent FIP	-
FIP_W	Dissipated energy FIP	-
h_0	Hardening parameter	-
H_T	Sensitivity parameter to hydrogen degradation	-
J^p	Determinant of plastic deformation gradient	-
K	Equilibrium constant	-
m	Power law exponent in shear rate equation	-
M_S	Schmid factor	-
n	Hardening exponent	-
N_A	Avogadro's number	1/mol
N_f	Total lifetime	-
N_L	Number of metal atoms per unit volume	$1/\mathrm{mm}^3$
N_T	Number of traps per unit lattice volume	$1/\mathrm{mm}^3$
N_{cycle}	Number of cycles	-
N_{slip}	Number of slip systems	-
$p_{\mathrm{H_2}}$	Hydrogen pressure	bar
R_Z	Surface roughness	μm
R_σ	Stress ratio	-
R_ε	Strain ratio	-
R_{GS}	Universal gas constant	$\mathrm{N\,mm/(K\,mol)}$
R_m	Ultimate tensile strength	MPa
$R_{p0.2}$	Yield strength	MPa
T	Temperature	K
V_H	Partial molar volume of hydrogen	$\mathrm{mm}^3/(\mathrm{mol})$

1. Introduction

The influence of hydrogen on the fatigue life of industrial applicable steels is governed by the interaction of diffusion with local accumulation of hydrogen in the steel lattice and the elasto-plastic deformation on a microstructural scale. Only cumbersome and costly fatigue experiments allow for an evaluation of the lifetime in hydrogen atmosphere on a macroscopic level, without the possibility to differentiate between the numerous and interacting microstructural effects of hydrogen on the material's mechanical behavior. Computational modeling of such a coupled transport-deformation problem on a microstructural level and the understanding of its effects on the macroscopic behavior are the keys to reliable, constitutive modeling. As motivation for the present contribution a foundation is set for the selection of suitable materials or the design of materials with tailored behavior for the application in contact with hydrogen. This work focuses on the modeling and numerical prediction of the fatigue behavior of ferritic steel. The main objectives are thereby a deeper understanding of the interplay of the polycrystalline microstructure's morphology and the hydrogen diffusion process, the development of a simulation framework capable of predicting the fatigue behavior to crack initiation under hydrogen influence for various steels and the comparison of numerical examples with experimental results.

1.1. Motivation

Searching for emission-free driving concepts for future mobility solutions, two possible solutions are presumably the next technologies replacing internal combustion engines with pure electric motors. These technologies differ in the method which supplies the electric motor with electricity. The pure electric vehicle takes its power from an on-board battery which has to be charged by an external energy source. The fuel cell vehicle generates energy by an internal chemical reaction of hydrogen and oxygen at a proton exchange membrane (PEM). This process only emits heat and pure water, see Jacobson et al. [82]. Electric cars powered by a battery are widely promoted and supported, due to their technological simplicity and their high power efficiency. However, some problems, such as charging times, short ranges, the usage of rare earth metals and recycling concepts, remain unsolved. Fuel cell vehicles (FCV) offer an alternative overcoming some of these issues. Long ranges and the fast filling of the tank with pressurized gaseous hydrogen make the FCV more attractive to customers. Current disadvantages are the relatively high production costs due to a limited number of produced vehicles and the infrastructure concerning hydrogen gas stations, see Wang et al. [191]. Moreover, the safety of a vehicle containing pressurized hydrogen up to 700 bar stored in the tank can be an emotional barrier for potential customers. Therefore, reliable and well-predictable component behaviors are key to an increased acceptance for this promising technology.

The issue of high pressures in the storage tank is technically solved. However, the interplay of hydrogen with metal components and the severity of the deteriorating effect remain critical aspects in the system. On the path from the tank to the PEM the gaseous hydrogen is relaxed and flows through different components such as gas supply lines or valves. Metal parts of these components are in permanent contact to hydrogen molecules. These molecules can be adsorbed and the resulting single hydrogen atoms may be absorbed into the metal material. Absorbed hydrogen in metals can cause premature failure with a rather brittle fracture behavior with low-ductility portions, see Figure 1.1. This phenomenon is often identified in literature as *hydrogen embrittlement*, see Gangloff

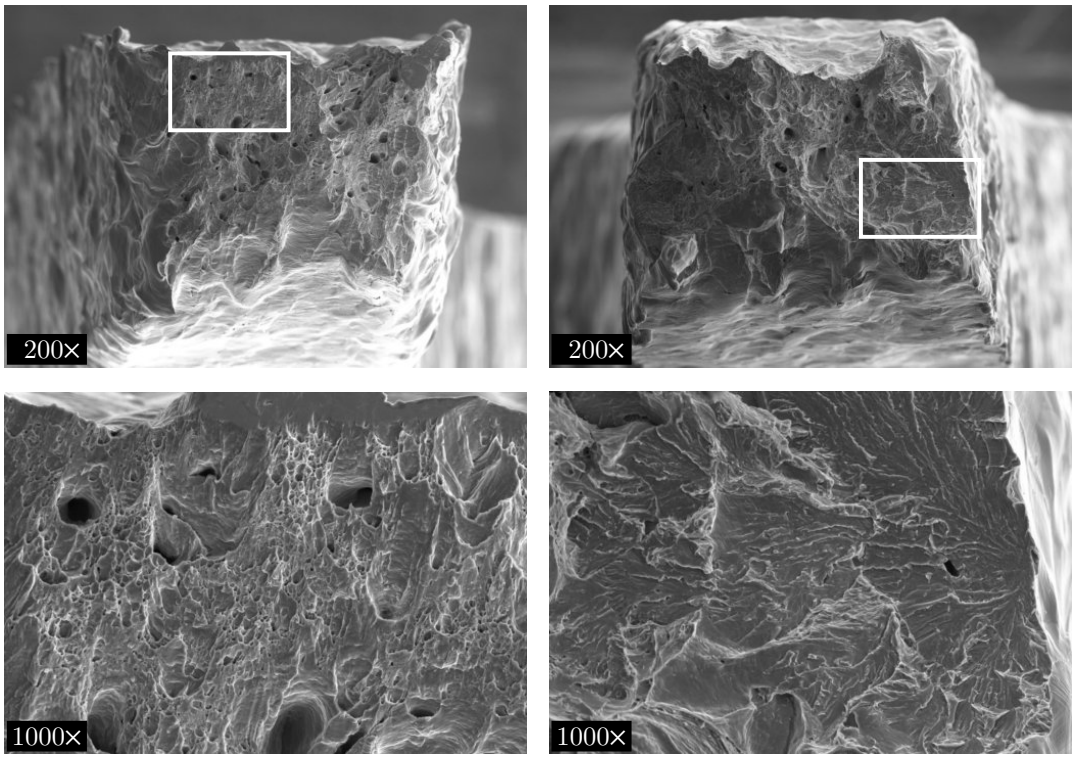

Figure 1.1: Fracture surface of micro fatigue samples of the ferritic steel 1.4003 in air (left) and hydrogen atmosphere (right) from Honecker [78] with entire cross sections (top) and magnifications (bottom).

& Somerday [59]. However, this simplified term or explanation does not suffice to explain experimental observations of processes taking place on the microscale. Various degradation mechanisms as described in Barrera [9], such as the *hydrogen enhanced decohesion* or *hydrogen enhanced local plasticity*, were formulated in the last decades and are controversially discussed by different research groups. A consensus has not been reached to explain the material degradation in hydrogen atmosphere, especially taking into account the very different microstructures of steel.

For industrial applications the longtime exposure to hydrogen and its effect on the fatigue behavior are of special interest. For instance, the components in the fuel cell system are not expected to bear high mechanical loadings but they might be exposed to all kinds of cyclic loadings leading to fatigue failure. For an economical but more important reliable and secure component design this issue must be tackled with experimental or simulative methods or a combination of both. The role of hydrogen in combination with cyclic loading is only addressed sparsely and mostly from an experimental point of view, see [122, 162]. The existing experimental database does not cover all influence factors on the interaction of hydrogen and metals during cyclic loading, which may have a superposed or completely separated effect. Influencing quantities are the material structure, its surface, the amount of hydrogen solved in or diffusing into the material which is connected to the arising pressure and temperature, the gas purity and cyclic loading conditions. As stated recently by Schauer [162], it is difficult to deduce regularities from publications for the fatigue behavior under hydrogen influence.

The present work builds on the results of [162] and aims to propose a model approach for the observed experimental findings of this work. This former work tries to close the gap from existing investigations of mainly austenitic Cr-Ni steels to industrial relevant ferritic and martensitic steels. Based on an extensive experimental program, fatigue data under hydrogen for various steels were systematically produced and fatigue properties for the different material groups were derived.

Motivated by the detection of a tremendous reduction of lifetime of ferritic steels in the low cycle fatigue range, a similar ferritic steel is investigated in the present work, which is actually considered to be used for FCV components. The focus is set on a numerical approach to describe fatigue under hydrogen influence, while experiments are only used to determine essential material parameters and to validate the simulation model.

1.2. Objectives and Overview

The general aim of the present thesis is the development of a comprehensive and verified modeling framework to predict the fatigue life of steels in a hydrogen atmosphere based on a coupled hydrogen diffusion-crystal plasticity finite element model incorporating the microstructure of the metallic material. In summary, the major contributions of this work are:

- Derivation of a coupled finite element model to describe hydrogen diffusion and large elasto-plastic deformation on a microstructural level.
- Experimental investigation on a ferritic steel to determine material parameters for the simulation and fatigue data for the validation of the model.
- Development of a prediction scheme for the fatigue behavior under hydrogen influence based on stress or strain information from the finite element model.
- Verification of this method by applying the model scheme on a ferritic steel relevant for industrial application in the fuel cell mobility.
- Building of a better understanding of microstructural effects on fatigue behavior by variation of the microscopic morphology via numerical examples.

Following this introduction, **Chapter 2** describes the physical phenomenon of hydrogen in metals and more specifically in steels. The hydrogen diffusion in steel begins with the uptake over the steel's surface, continues with the transport into the bulk and results in the microstructure dependent distribution of the hydrogen atoms in the lattice and the traps. Furthermore, different degradation mechanisms and the influence on the fatigue behavior are reviewed. Fundamentals of continuum mechanics are outlined, including an overview of geometrical and physical quantities relevant for the description of the coupled diffusion-deformation problem. In particular, the framework for a large strain formulation together with the physical balance laws is introduced. Based on this existing knowledge, a solution strategy for the objectives of this work is described in **Chapter 3**. An in depth characterization of the ferritic steel 1.4003 is provided in **Chapter 4**. A microstructure analysis in terms of EBSD scanning gives an insight of the material structure on the microscale, while macroscopic fatigue tests in air and hydrogen atmosphere capture the

material response to cyclic loading. Furthermore, hydrogen diffusion coefficients are determined experimentally. A detailed explanation of theoretical and numerical aspect for the development of a coupled simulation framework is given in **Chapter 5**. The phenomenological crystal plasticity formulation is summarized together with the hydrogen transport model. Moreover, the underlying simulation domain is introduced in terms of representative volume elements. In **Chapter 6** a prediction scheme for fatigue crack initiation is described which is extended by an additional hydrogen dependent fatigue describing parameter. Therewith simulations are performed to predict the lifetime of the ferrite in air as well as hydrogen atmosphere and compared with experimental findings. The influence of different microstructural aspects and boundary conditions are investigated in numerical studies and subsequently discussed in **Chapter 7**.

2. Basics of Structure, Fatigue and Modeling of Steels

A short introduction to the fundamentals of metallic materials, their fatigue behavior and their interaction with hydrogen followed by basic continuum mechanical concepts for material modeling is given in this chapter. First, the polycrystal structure of metals is explained on atomic and micro level together with the deformation mechanisms on these scales. Second, the basics of material fatigue, crack initiation and propagation as well as the concepts of lifetime prediction are elucidated, followed by the interaction of hydrogen and steels. The deteriorating influence of hydrogen located in the material on its fatigue behavior is discussed according to the state of knowledge. Last, essential concepts for continuum mechanical material modeling are briefly introduced.

2.1. Metallurgy and Microstructural Behavior

Some fundamentals of the structure of metals and alloys considering microstructural aspects are reviewed, followed by the description of the micromechanical deformation behavior. The deformation is either fully reversible and elastic or elasto-plastic, resulting in irreversible changes in the microstructure.

2.1.1. Structure on Atomic- and Microscale

Metals belong to the group of polycrystalline materials and possess a crystalline structure formed by a regular distribution of atoms. A single crystal can be envisioned as a 3D periodical space lattice with atoms as the corners of the lattice. Such a crystal exhibits a certain *orientation* in space, which makes it anisotropic by inducing a distinctive orientation dependency of some mechanical properties. The orientation is governed by the arrangement of the atom layers. These layers or lines of closest packed atoms form crystallographic planes or directions which are crucial for the description of the material response to mechanical loading. Deformation of a crystalline structure results in shearing on these planes. A real crystal material not only consists of one crystal with a single orientation but of many regions with varying orientations and is therefore called polycrystalline. Regions with the same crystal orientation are denoted as grains and are separated from each other by *grain boundaries*. The grains' shape, size, orientation and boundaries depend on their formation condition. The *texture* of a polycrystal is the distribution of all occurring crystallographic orientations and is influenced by the production steps and heat treatment of the metal or alloy. The lattice structure of all polycrystalline materials is discontinuous containing defects such as dislocations, pores, cracks, inclusions, grain boundaries or stacking faults. Noteworthy for the deformation behavior are the dislocations, which are moved by external loading of a material and yield slip on crystallographic planes. The arrangement and number of above mentioned lattice defects complete the characterization of the microstructure, which determines the final mechanical and physical properties of the material. Here, a focus is set on steel, which is an alloy of iron and carbon accompanied by further elements due to manufacturing or intended improvements of certain requirements. Parts within a steel containing a uniform microstructure are called the structural components and are denoted by austenite, ferrite, cementite, pearlite, ledeburite or martensite, see Gottstein [62]. The fraction of structural components of an alloy is determined by its chemical composition as well as heat treatment and forming history.

Ideal Crystalline Structure. Attraction and repulsion forces act on the atoms of a crystalline structure. The sum of this forces determines the bonding force which is responsible for a distinct arrangement of the atoms in form of a regular space lattice, Figure 2.1 a). The smallest unit of the lattice is a primitive unit cell as illustrated in Figure 2.1 b). They are uniquely determined by the three grid vectors $\boldsymbol{a}$, $\boldsymbol{b}$, $\boldsymbol{c}$ or equivalently the grid constants a, b, c with corresponding angles α, β, γ as parallelepipeds. Distances a, b, c between atoms in most of the metals are in the range of $0.25 - 0.5$ nm. A specific set of the grid constants a, b, c and angles α, β, γ yield seven different types of unit cells by the name of triclinic, monoclinic, orthorhombic, tetragonal, cubic, trigonal and hexagonal cell. The set of grid constants for the three important structures for crystalline materials, tetragonal, cubic and hexagonal, is given in Table 2.1. The primitive or simple unit cells

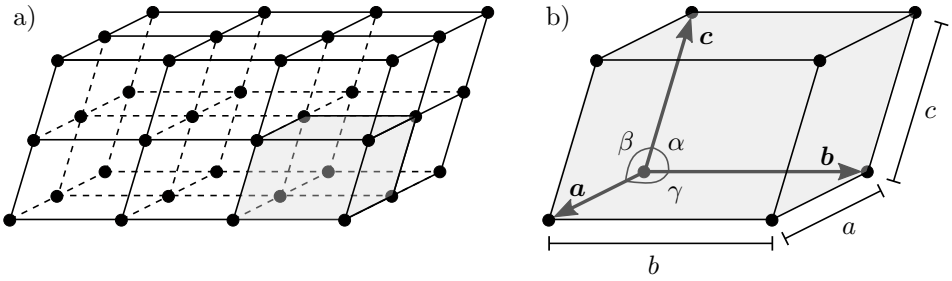

Figure 2.1: Illustration of a regular space lattice in a) together with a gray shaded detailed view of a simple unit cell in b), modified of Gottstein [62]. Shape and size of the unit cell are uniquely defined by the grid vectors $\boldsymbol{a}$, $\boldsymbol{b}$, $\boldsymbol{c}$ or the grid parameters a, b, c in combination with the angles α, β, γ.

consist of eight atoms at the lattice corners. Furthermore, additional atoms may exist in the center of either the faces or the body. First, the base-centered cell with one extra point at the center of each surface of one pair of parallel surfaces of the cell. Second, the body-centered cell with an additional point at the center of the cell and third, the face-centered cell with one extra point at the center of each of the faces of the cell. The seven primitive unit cells are supplemented with seven centered unit cells to 14 so-called *Bravais cells*, [24]. Depending on its temperature, iron and therewith steel can take on two crystalline forms, the *body centered cubic* (BCC) and *face centered cubic* (FCC) illustrated in Figure 2.2. The distance between the atoms of primitive as well as centered unit cells

Unit cell type	Grid constants	Angles
Tetragonal	$a = b \neq c$	$\alpha = \beta = \gamma = 90°$
Cubic	$a = b = c$	$\alpha = \beta = \gamma = 90°$
Hexagonal	$a = b \neq c$	$\alpha = \beta = 90°\,, \gamma = 120°$

Table 2.1: Unit cell types for crystalline materials with specific grid constants and angles.

differ, thus the grid constants a, b, c are not equal. For the BCC cell the face diagonal is the largest whereas the body diagonal is the smallest distance and for FCC cells it behaves the other way round. Varying grid constants result in so-called *crystallographic planes* and *directions*, which are indicated by *Miller indices* in a characteristic coordinate

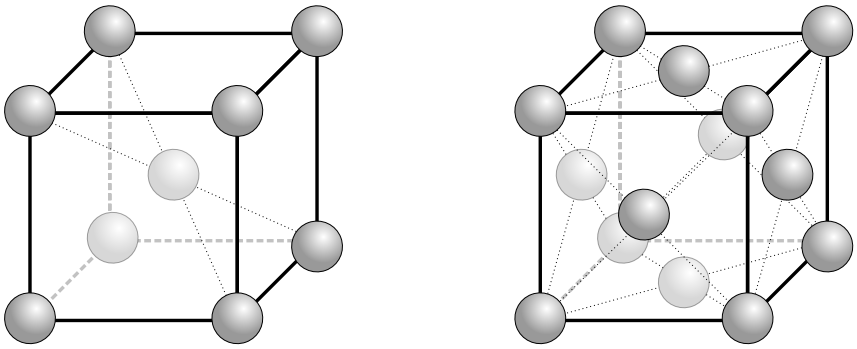

Figure 2.2: Relevant unit cell types for iron and steel, inspired by [62]. The body centered cubic (BCC) cell is shown on the left side and the face centered cubic (FCC) cell on the right side.

system, see Miller [115]. A detailed explanation of the Miller indices can be found for example in Gottstein [62]. A crystallographic plane, which has no intersection with the origin of the coordinate system, can be uniquely defined by three points, namely the three intersections with the coordinate axes. The intersections are determined as multiples of the grid parameters ($m \cdot a$, $n \cdot b$, $p \cdot c$). With the reciprocals ($1/m$, $1/n$, $1/p$) the Miller indices for planes are obtained by multiplication with the least common multiple q_1 of m, n, p

$$(hkl) = q_1 \cdot \left[\frac{1}{m}\frac{1}{n}\frac{1}{p}\right], \tag{2.1}$$

resulting in integers h, k, l. Herein, a bar marks negative coordinates. For the crystallographic planes the Miller indices (hkl) are written in round brackets. The Miller indices for directions are obtained by multiplication of the vector components r, s, t characterizing the crystallographic direction with the smallest common factor q_2

$$[uvw] = q_2 \cdot [r\,s\,t]\,. \tag{2.2}$$

Because of the symmetry of the cubic system, the atomistic arrangement of planes and directions of this system is only unique if a fixed coordinate system is given. For physical properties only the atomistic arrangement independent of the coordinate system is of importance. Hence, crystallographic equivalent planes and directions are summarized in a set of planes written in curly brackets {hkl} and a set of directions in angle brackets $\langle uvw \rangle$. Equivalent planes and directions for the cubic lattice are summarized in Table 2.2 and a selection of planes and directions with their Miller indices are given in Figure 2.3.

Another property of the lattice system is their packing density which can be calculated by the ratio of the volume of atoms in a unit cell with respect to the unit cell's volume. The packing density for BCC lattices is 68% and 74% for FCC cells and it affects the ability to undergo plastic deformation. Plastic gliding occurs predominantly in the direction of highest packing density within the closest packed crystal plane. These are the $\langle 111 \rangle$ direction for the BCC and the $\langle 110 \rangle$ direction for the FCC lattice, see Section 2.1.2.

Real Crystalline Structure. Various types of imperfections, called defects, appear in a real crystal structure contrary to the above described ideal lattice. Defects are categorized

	Set	Elements
Direction	$\langle 100 \rangle$	[100], [010], [001], [$\bar{1}$00], [0$\bar{1}$0], [00$\bar{1}$]
Plane	{100}	(100), (010), (001), ($\bar{1}$00), (0$\bar{1}$0), (00$\bar{1}$)
Direction	$\langle 110 \rangle$	[011], [101], [110], [0$\bar{1}$1], [$\bar{1}$01], [$\bar{1}$10], [0$\bar{1}\bar{1}$], [$\bar{1}$0$\bar{1}$], [$\bar{1}\bar{1}$0], [01$\bar{1}$], [10$\bar{1}$], [1$\bar{1}$0]
Plane	{110}	(011), (101), (110), (0$\bar{1}$1), ($\bar{1}$01), ($\bar{1}$10), (0$\bar{1}\bar{1}$), ($\bar{1}$0$\bar{1}$), ($\bar{1}\bar{1}$0), (01$\bar{1}$), (10$\bar{1}$), (1$\bar{1}$0)
Direction	$\langle 111 \rangle$	[111], [$\bar{1}$11], [1$\bar{1}$1], [11$\bar{1}$], [$\bar{1}\bar{1}\bar{1}$], [1$\bar{1}\bar{1}$], [$\bar{1}$1$\bar{1}$], [$\bar{1}\bar{1}$1]
Plane	{111}	(111), ($\bar{1}$11), (1$\bar{1}$1), (11$\bar{1}$), ($\bar{1}\bar{1}\bar{1}$), (1$\bar{1}\bar{1}$), ($\bar{1}$1$\bar{1}$), ($\bar{1}\bar{1}$1)

Table 2.2: Sets of equivalent crystallographic directions and planes for the cubic cell.

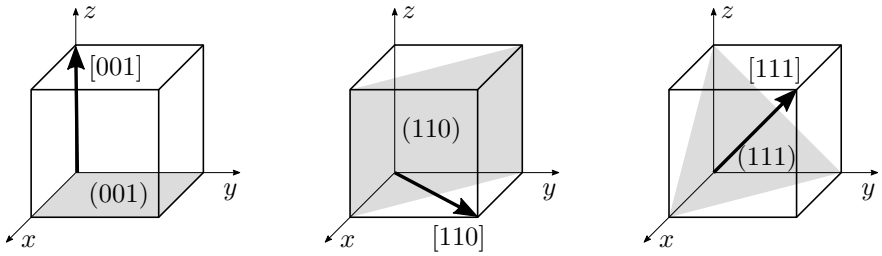

Figure 2.3: Three different crystallographic directions [001], [110], [111] and planes (001), (110), (111) of the cubic lattice, which can be described according to Table 2.2 by the sets $\langle 100 \rangle$, $\langle 110 \rangle$, $\langle 111 \rangle$ and {100}, {110}, {111}, respectively.

by their dimensions. The 0-dimensional *point defects*, illustrated in Figure 2.4 a)-d), contain intrinsic defects such as vacancies or interstitial atoms, which also can occur in combination. Substitutional or interstitial impurity atoms are denoted as extrinsic point defects, which are atoms of a different type or size replacing a regular atom or sitting on a place in-between the lattice, respectively.

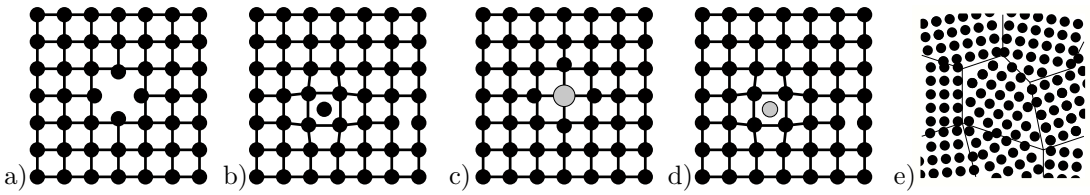

Figure 2.4: Selection of imperfections such as a) vacancy, b) interstitial atom, c) substitutional atom, d) interstitial impurity atom or e) grain boundaries are schematically depicted. Graphic modified of Zimmermann [203].

Dislocations are considered as 1-dimensional *line defects* and govern the micromechanical deformation behavior. The movement of dislocations through the lattice explains the shearing of crystallographic slip planes. Figure 2.5 shows different types of dislocations, the edge dislocations, screw dislocations and a combination of both called mixed dislocations. Edge dislocations can be described as an extra half-plane of atoms midway through the regular crystal, where the symbol $\perp$ at the end of the dislocation axis represents the dislocation line. The dislocation core denotes the end of the half-plane, where the devia-

tion from the ideal structure is the largest. Screw dislocations are spiral-like shifted atom planes in the lattice. The *Burgers vector* $\boldsymbol{b}$ characterizes the direction and size of a lattice distortion due to a dislocation. The energetic state of the lattice is raised by dislocations which reduces the effort to dislocation movement through the crystal. Therefore, dislocations can be seen as the "carrier" of plastic deformation giving metals their good plastic deformability and malleability.

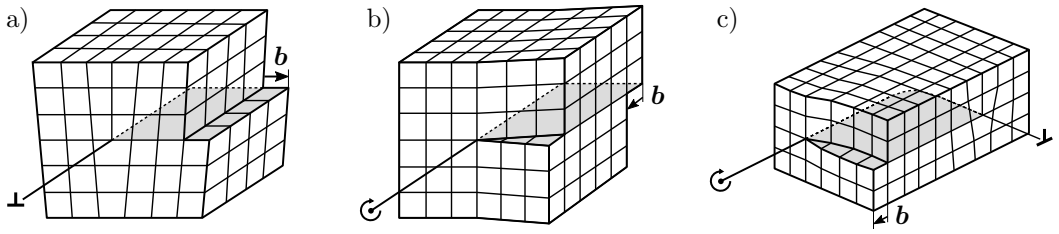

Figure 2.5: Different types of dislocations following KRUPP [90] are shown, including a) the edge dislocation, b) the screw dislocation and c) the mixed dislocation with the corresponding Burgers vector $\boldsymbol{b}$.

2-dimensional *surface defects* include *grain boundaries*, shown in Figure 2.4 e), phase boundaries or twin boundaries. Polycrystalline materials consist of many grains with different orientations separated by grain boundaries. They can be characterized by the difference in crystallographic orientation between each other, called *misorientation*. A distinction is made between low-angle grain boundaries with a misorientation less than about 15° and high-angle grain boundaries, whose misorientation is greater than 15°. Phase boundaries mark the interface region of two separate phases and twin boundaries occur when two grains are mirrored at a grain boundary.

Last, 3-dimensional *volume defects* are voids or precipitates. A void is a small regions where larger number of atoms are missing and which can be thought of as clusters of vacancies. Several foreign atoms of a different phase clustered together form a precipitate. Note, that imperfections play a crucial role in hydrogen diffusion and local distribution, see Section 2.3.2.

2.1.2. Physics of Deformation

To understand elastic and plastic deformations processes in a polycrystalline structure, a closer look on the movement of dislocation should be taken. Shear stresses on a material result in slip deformations on crystallographic planes. A small shear stress induces a change in the angle of the regular lattice, which is known as a reversible elastic deformation.

Elastic Deformation. The ability for elastic deformation is material dependent and is specified by the properties of the active metallic bonding. In a continuum description of deformation the elastic material behavior is often approximated by the Young's modulus E as an isotropic elastic constant together with the Poisson's ratio ν. This assumption should only be made if the material or sample consists of a high number of randomly oriented crystallites exhibiting an isotropic material behavior. In that case, the elastic properties are independent of the grain orientation. From a material mechanics point of view, the anisotropic elastic properties of the crystalline structure should be considered

and requires the introduction of the fourth-order anisotropic elasticity tensor $\mathbb{C}^e = C_{ijkl}$. Major and minor symmetries of the elasticity tensor ($C_{ijkl} = C_{klij}$ and $C_{ijkl} = C_{jikl} = C_{ijlk}$) are induced by the symmetry of the stress tensor and the reversibility of the elastic deformation, see KRUPP [90]. These symmetries allow to contract the 3^4 components of the fourth-order tensor into a simpler 6×6 matrix. This reduction of the dimensions due to symmetry properties is known as Voigt notation. Together with the symmetry of the cubic lattice systems (FCC and BCC) the 81 entries of the elasticity tensor are reduced to three independent elastic constants C_{11}, C_{12} and C_{44}. Therewith, effects, such as mechanical stresses causing local stress concentrations leading to crack initiation, are captured taking into account the anisotropy of elastic properties.

Plastic Deformation. By exceeding a critical shear stress an atom can be forced to change its lattice plane to a neighboring plane causing a glide plane to develop. This process describes an irreversible plastic deformation. Figure 2.6 illustrates the gliding of crystallographic planes, starting with the lattice in its initial state, followed by an elastic distortion induced by a shear stress τ, a plastic deformation and the relaxed state after reversal of elastic strains. This concept and its mechanical theory to describe plasticity was questioned by experimental observations, where the necessary shear stress for plastic deformation was much lower than the theoretical assumed. An improvement and correction was simultaneously given in 1934 by OROWAN [134], POLYANI [145] and TAYLOR [182] through the explanation of plastic deformation in terms of dislocation movement, see Figure 2.7. Shear loading induces a dislocation in an ideal structure. A movement of this dislocation is induced, when atoms from one of the neighboring planes break their bonds and bond again with atoms at the following edge. By breaking and reforming a line of bonds a half plane of atoms is moved trough the lattice. Since the energy for braking a single bond is less than the energy required to break all bonds on a whole plane of atoms at once, much lower stresses cause plastic deformation. With this model concept it was possible to meet the experimental observations by theoretical predictions more accurately.

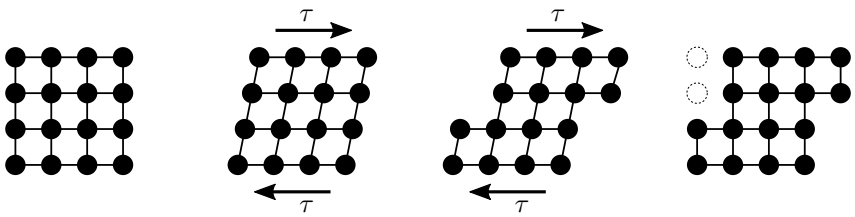

Figure 2.6: Gliding of crystallographic plane under a shear loading τ on an ideal lattice after exceeding the critical shear stress, inspired by [203].

The minimal necessary stress value to induce a plastic deformation in a lattice structure is called *critical resolved shear stress* τ_c and depends on the interatomic spacing with respect to the glide plane distance, the density of dislocations and the temperature. It decreases with a decreasing length of the Burgers vector $\boldsymbol{b}$ compared to the distance between glide planes. A closest packed lattice direction results in a small Burgers vector. The closest packed planes and directions build a set of possible *slip systems* which govern the plastic deformation of a polycrystal. For the FCC lattice exist 12 slip systems with four planes $\{111\}$ and three directions $\langle 110 \rangle$ each. The BCC crystal has 48 slip systems. Six slip

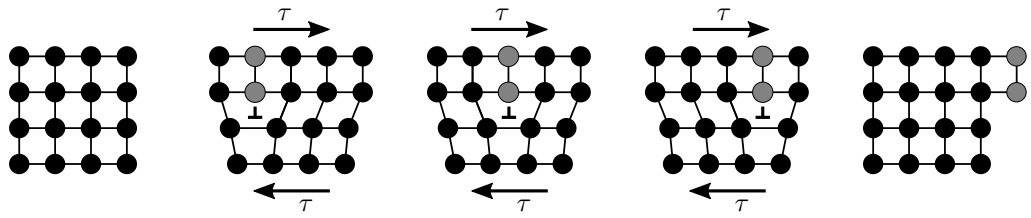

Figure 2.7: Dislocation movement by sliding of a half plane of atoms through a crystal structure under a shearing, inspired by [203].

planes of type {110} exist, each with two ⟨111⟩ directions, often denoted as the primary slip system. Secondary slip systems incorporate 12 {112} and 24 {123} planes, each with one ⟨111⟩ direction. Following Courtney [41] slip in BCC systems on planes other than the {110} occur only under certain conditions and are material and temperature specific. Particularly for modeling purposes the possible slip systems are reduced to the primary system, listed in Table 2.3. A *slip direction* $\mathbf{m}^\alpha$ and a *slip normal* $\mathbf{n}^\alpha$ define the slip system, with $\alpha = 1, ..., N_{slip}$ and N_{slip} is the number of all possible slip systems. With this understanding of deformation in polycrystalline material the foundation is set for the computational modeling by means of crystal plasticity.

α	$\mathbf{m}^\alpha$	$\mathbf{n}^\alpha$	α	$\mathbf{m}^\alpha$	$\mathbf{n}^\alpha$	α	$\mathbf{m}^\alpha$	$\mathbf{n}^\alpha$
1	$[1\bar{1}\bar{1}]$	(110)	5	$[\bar{1}\bar{1}1]$	(101)	9	$[11\bar{1}]$	(011)
2	$[\bar{1}1\bar{1}]$	(110)	6	$[\bar{1}11]$	(101)	10	$[1\bar{1}1]$	(011)
3	[111]	$(1\bar{1}0)$	7	$[\bar{1}\bar{1}\bar{1}]$	$(10\bar{1})$	11	[111]	$(01\bar{1})$
4	$[11\bar{1}]$	$(1\bar{1}0)$	8	$[1\bar{1}1]$	$(10\bar{1})$	12	$[\bar{1}11]$	$(01\bar{1})$

Table 2.3: Relevant slip directions $\mathbf{m}^\alpha$ and planes $\mathbf{n}^\alpha$ for the BCC crystal.

Which slip system is the first to be activated in a single crystal specimen under consideration of the geometrical arrangement of possible slip planes depends on the *resolved shear stress* τ_{rss} acting on the different slip systems. The resolved shear stress is determined with *Schmid's law* relating τ_{rss} to the angle ϕ between the slip plane normal and the axis of the applied uniaxial tensile stress $\sigma = F/A_0$ as well as the angle λ between the slip direction and the stress axis. Visualized in Figure 2.8 a), the Schmid's law in uniaxial tension reads

$$\tau_{rss} = \sigma(\cos\phi \cdot \cos\lambda) = \sigma M_S \,, \tag{2.3}$$

where M_S denotes the Schmid factor. Maximal shear stress arises for angles $\phi = \lambda = 45°$ with a Schmid factor $M_S = 0.5$. The slip system with the highest Schmid factor will be activated first. As can be seen in Figure 2.8 b), slip along the first active slip systems would lead to a shift of the crystal with respect to the loading axis. Since this shift is blocked by a fixation of the sample (single crystal) or by the surrounding grains (polycrystal), a rotation and bending is imposed on the slip systems, see Figure 2.8 c). Due to the resulting change of the Schmid factor, further conjugate slip systems can be activated.

Transferring this concept to a polycrystal, plastic deformation initiates in the grain with the highest Schmid factor. Elastic stresses are induced in neighboring grains to balance the

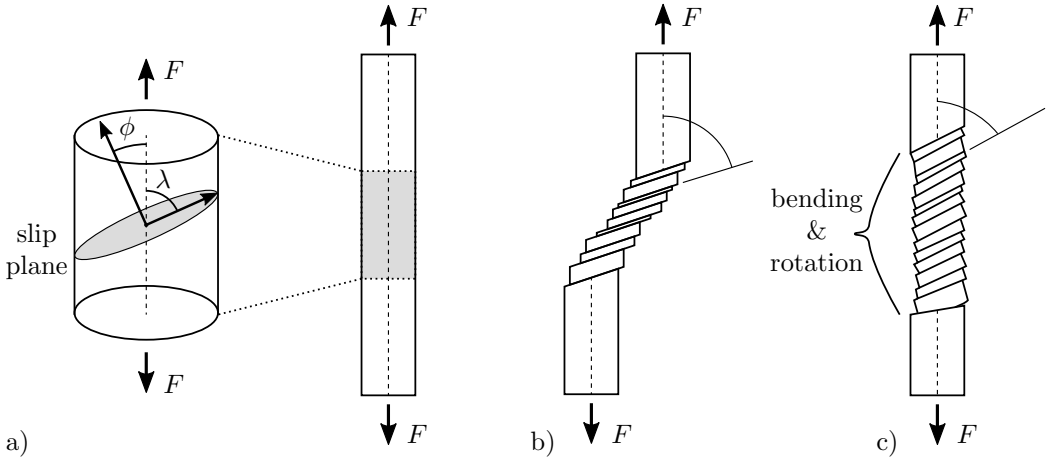

Figure 2.8: Slip in a single crystal tensile specimen, after KRUPP [90]. A cut out of the specimen in a) shows the resolution of applied stress into a shear stress acting in slip direction on a slip plane. Without geometrical restraints the shape would change as shown in b), but a fixation provides axial alignment enforcing a bending and rotation of the slip system.

resulting change in the shape of the plastically deformed grain, causing stress concentrations especially along the corresponding grain boundaries. With continuing deformation grains with lower Schmid factors start to deform plastically. A complete plastification of all grains is marked by reaching the macroscopic yield strength σ_Y. Dislocation propagation along slip planes are hindered by grain boundaries due to discontinuities in the lattice. The dislocations pile up in front of the grain boundary until the shear stress is sufficiently large to provoke a dislocation movement in the grain ahead. Smaller grains decrease the amount of possible pile ups at the grain boundary, which increases the amount of energy necessary to transport a dislocation through a boundary. This effect can be macroscopically observed by an increasing yield strength of the material and is mathematically described by the *Hall-Petch* relationship [67, 139]

$$\tau_Y = \tau_0 + \frac{k}{\sqrt{d}}\,, \tag{2.4}$$

where k is a material dependent parameter, τ_Y is yield strength for shear, τ_0 the initial resistance of the lattice to dislocation motion in a single crystal and d the grain size. With increasing grain size ($d \to \infty$) at least the initial critical shear strength τ_0 must be overcome to allow for plastic shearing. Note, that the Hall-Petch relationship is only an empirical fit to experimental data. The work of KRUPP [90] shows that dislocation transfer is a more complex process depending on several factors, such as the dislocation structure or the 3D grain boundary orientation.

Cyclic Deformation. During cyclic deformation of crystalline material multiple dislocations move along the same slip planes and lead to a slip line on the surface which is visible under the microscope. Dislocation pile ups or the formation of an oxide layer hinder the gliding of activated slip planes, see SURESH [176], and cause an impediment of the activated slip planes resulting in the activation of new slip planes in the vicinity. Accumulation of side by side developing and hardening slip lines leads to the formation of slip bands or persistent slip bands (PSBs), illustrated in Figure 2.9. These slip bands

consist of extrusions and intrusions, which is material emerging our of the surface and small indentations on the surface, respectively. Instead of a smooth interface, the intrusions and extrusions will cause extremely fine surface structures on the material. Stress concentrations between extrusions and the surrounding material might act as an initiation spot for micro cracks.

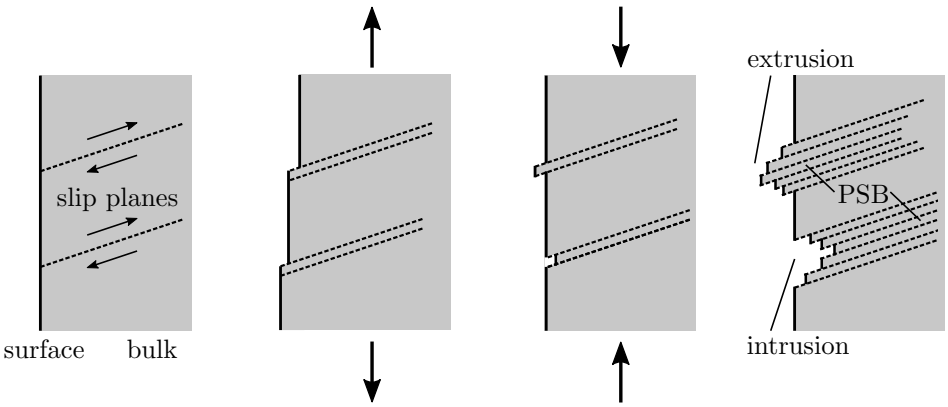

Figure 2.9: Dislocation motion through the bulk along slip planes to the free surface due to cyclic loading, inspired by Suresh [176]. Formation of persistent slip bands (PSBs) building extrusions and intrusions on the surface.

2.2. Fatigue and Fracture

Motivated by the catastrophic crash of a steam locomotive in 1842 caused by a broken axis, the investigation of the reason for failure marks the origin of research in the field of material fatigue. The term *fatigue* was first mentioned by Braithwaite [23] in 1854 and in the following decade Wöhler [193] set the basis for operating load dependent *design against fatigue* with his systematical experimental investigations on locomotive axes. A further milestone marks the first discussion of cyclic deformation mechanisms by Bauschinger [15], whose theoretical considerations were supported for the first time by observation of slip bands at the beginning of the 20th century. With modern experimental and optical magnification techniques, the significance of microstructural processes for the understanding of fatigue was recognized. Furthermore, the influence of microcracks and inhomogeneities on fatigue behavior was payed attention to in a new discipline *fracture mechanics*, which merged to a large extend with the fatigue analysis. A short introduction of important terms and concepts of fatigue, fracture and lifetime prediction approaches is given in the following. The books of Christ [37], Radaj & Vormwald [152], Haibach [66] and Schijve [164] are suggested for in-depth information on this topics or the work of Krupp [90] for a helpful overview.

2.2.1. Material Behavior under Cyclic Loading

While comparing the failure behavior of a ductile metal during monotonous tensile loading and cyclic loading, one observes, that the latter shows macroscopically a spontaneous fracture behavior, whereas the tensile specimen exhibit *necking*[1] before fracture. The

[1]Necking denotes a disproportional strain localization in a small region of a material resulting in a decrease in local cross-sectional area.

stress-strain curve of the uniaxial tensile test shows the transition from elastic reversible behavior, described by the linear Hooke's law

$$\sigma = E\varepsilon\,, \tag{2.5}$$

to plastic irreversible deformation by exceeding the yield stress σ_y. Hereby, $\boldsymbol{\varepsilon} = \Delta l/l_0$ denotes the engineering normal strain and σ the component of the Cauchy stress tensor, defined in Section 2.5.2, in loading direction. E is the Young's modulus for isotropic material. However, WÖHLER [193] observed that failure due to cyclic loading occurs even under loadings much below the static yield stress and from a macroscopic point of view, in the range where reversible elastic material behavior occurs. As a consequence of this phenomenon, the development and design of reliable components cannot only rely on tensile test data but must take into account reliable fatigue experiments and data.

Fatigue of materials is induced by a time dependent stress or strain controlled cyclic loading process. As shown in Figure 2.10 a) the wave shape cyclic loading follows in its simplest form a sinusoidal curve or a saw tooth profile. The stress-strain relation can be visualized in the *stress-strain hysteresis*, Figure 2.10 b). The stress cycle can be characterized by different quantities. One pair is the stress amplitude σ_a together with the mean stress σ_m, which can be replaced by the maximum and minimum stress σ_{max} and σ_{min}. A third possibility for a description of the load cycle is given by the stress range $\Delta\sigma$ combined with the stress ratio R, defined as

$$R_\sigma = \frac{\sigma_{min}}{\sigma_{max}}\,. \tag{2.6}$$

Commonly used stress ratios to reproduce real loadings are the fully reversed load-

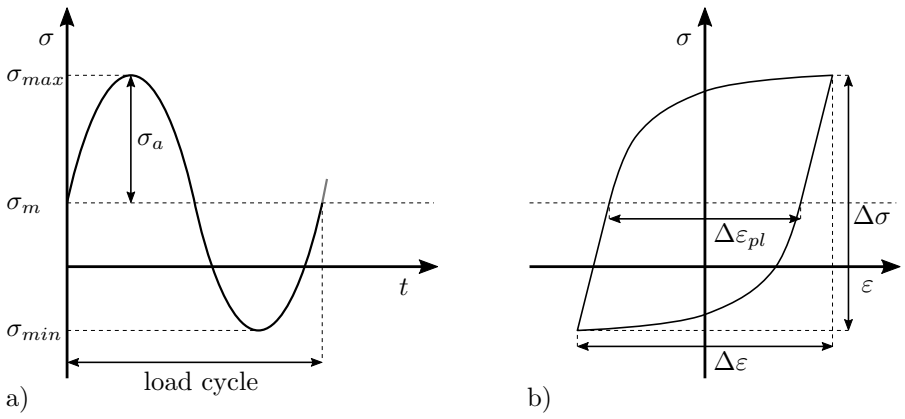

Figure 2.10: Schematic drawing with characteristic quantities of time dependent cyclic stress loading with sinusoidal profile shown in a) and stress-strain hysteresis in b).

ing ($R_\sigma = -1$, $\sigma_m = 0$) and pulsating tension ($R_\sigma = 0$, $\sigma_{min} = 0$). By subtracting the elastic strain from the total strain, the plastic strain amplitude is obtained as $\Delta\varepsilon_{pl}/2 = \Delta\varepsilon/2 - (\Delta\sigma/2)/E$. Note, that the stress controlled loading can be replaced analogously by a strain driven cyclic loading. The cyclic loading frequency f_{load} is necessary to fully describe the stress-strain cycle as time depending sequence. It determines the number of cycles per second and therewith the length of a load cycle. The frequency can affect the fatigue mechanism if time dependent phenomena occur, such as corrosion,

creep or diffusion mechanisms induced by temperature changes due to frequency. The latter is particularly interesting in this work.

Stress-strain hystereses normally change their shape at increasing numbers of cycles, even at constant stress amplitude or strain amplitude tests. Therefore, they are unwieldy to be assessed especially for higher numbers of cycles. To overcome this issue and get information about the material behavior over the whole lifetime, a common representation is the *cyclic deformation curve*, see Figure 2.11 a). For example at constant strain amplitude testing the stress amplitude σ_a is plotted over the number of cycles until fatigue damage results in rupture of the sample. The loading is controlled by a constant strain amplitude ε_a or the other way round by a constant stress amplitude together with the strain amplitude as observed quantity in the cyclic deformation curve. The diagram can be divided in three sections, where the first (I) indicates cyclic softening or hardening behavior, evidenced respectively by a decrease or increase of the stress amplitude and is dependent on the material and its deformation history. The second sector (II) is governed by a quasi-stationary development of the cyclic deformation with a constant material response without hardening or softening behavior. The material reaches a stage of cyclic saturation which ranges over large parts of the material's lifetime and where the stress-strain hystereses remain nearly unchanged. In a final step, all materials suffer at a distinct load amplitude from fatigue damage (III). The failure of the sample is signalized by a pronounced drop of the stress amplitude where crack propagation results in fracture after the total lifetime N_f, see Section 2.2.2.

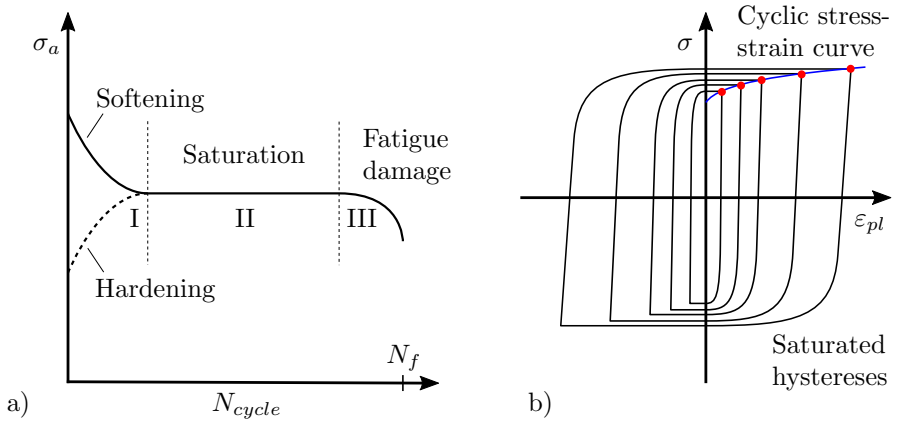

Figure 2.11: Schematic illustration of cyclic deformation curve a), showing the stress amplitude σ_a as a function of the number of cycles N_{cycle} until fatigue fracture at constant strain amplitude ε_a. The material undergoes cyclic softening (solid) or hardening (dashed), followed by a saturation phase which results in fatigue failure at the end of the lifetime N_f. The relation between hystereses taken in the state of cyclic saturation and the cyclic stress-strain curve (blue) is depicted in b).

In a similar manner to the stress-strain curve of the tensile test, the material behavior during cyclic loading is described by a *cyclic stress-strain curve*, blue curve in Figure 2.11 b). It relates the stress amplitude to the plastic strain amplitude $\varepsilon_{a,pl}$ in the range of cyclic saturation. During the saturation phase the shape and size of the so called saturated hystereses are constant and the cyclic stress-strain curve is obtained by connecting the upper tips (red dots) of the stable hystereses. In case of indistinct saturation behavior, when phase II is not perfectly constant, the hystereses are taken at half lifetime

$N_f/2$. A comparison of the quasi-static and cyclic stress-strain curve allows for an evaluation of the material's cyclic hardening behavior. If the cyclic stress-strain curve lies above the standard stress-strain curve cyclic hardening occurs at the beginning of the life test. The opposing case indicates cyclic softening. The analysis of cyclic deformation behavior with stress-strain hystereses and stress-cycle curves does not include processes on the microstructure such as crack formation and propagation, which is considered in the following.

2.2.2. Fatigue Stages to Failure

Material failure caused by cyclic loading is accompanied by different stages of fatigue. These stages are schematically described in Figure 2.12 and explained in detail afterwards.

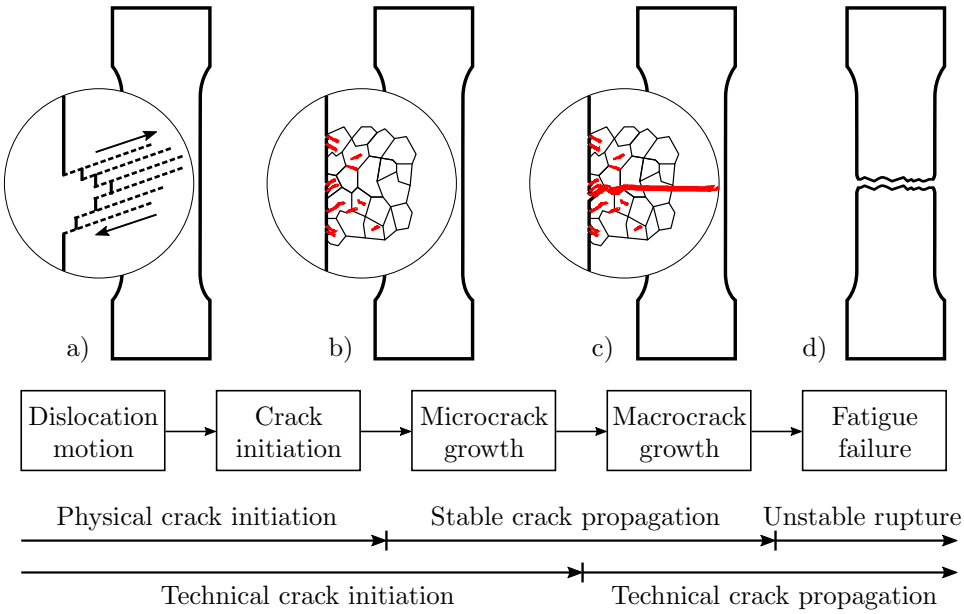

Figure 2.12: Schematic drawing of different stages of fatigue cracking together with corresponding physical and technical classification following Radaj & Vormwald [152].

The *crack free phase* before crack initiation takes place is described in Section 2.1.2. Plastic strain is propagated by dislocation generation and movement under cyclic loading in certain slip plains, which can localize in the material building PSBs due to the irreversibility of shear displacements along the slip bands. As shown in Figure 2.12 a), these PSBs emerge at the free surface developing extrusions and intrusions, see Wood [194]. Under cyclic loading the width and height of the slip band increases leading to a raise in surface roughness, see Man et al. [105]. The growing slip band also causes an intensified stress concentration at the transition of the slip band and the surrounding surface which may lead to micro crack initiation. An overview of all existing models to describe the mechanism of accumulated plastic strain in slip bands together with microstructural prerequisites to initiate a crack is given in Man et al. [106]. The model proposed by Essmann et al. [50] explains the shape of a PSB by the active generation and movement of edge dislocations and their annihilation. Not all cyclically induced dislocations contribute to plastic slip. Some of them annihilate each other and form vacancies. This may lead to a change in the growing direction of the PSB with respect to the crystal-

lographic slip direction and results in uneven extrusions at the surface. Not annihilated dislocations reach either the surface of the PSB or the interface between the PSB and the material matrix at the surface. At this interface they cause compressive stresses in the PSB and tension stresses in the matrix. The stress concentration and the geometric step at the interface of the PSB and the surface may lead to crack initiation. Even if the model has been the subject of criticism by Polak [144] it could be experimentally supported by Man et al. [105]. Also intercrystalline crack initiation can be explained by this model. In this case, dislocations pile up at grain boundaries provoking additional elastic stresses resulting in crack nucleation. Furthermore, stress concentration can occur on lattice defects such as inclusions leading to crack initiation within the material matrix, see Suresh [176].

After *crack initiation* one or multiple microcracks propagate in the *crack formation* phase along slip planes or at interfaces such as grain or phase boundaries. Preferably under an angle of 45° to the loading axis in the direction of the primary slip system, micro cracks propagate through multiple grains, see Figure 2.12 b). These micro cracks are shear driven and grow depending on the grain morphology, the applied loading and temperature. Subsequent macro cracks grow independent of the crystallographic orientation perpendicular to the applied loading, see Figure 2.12 c). The reason for this change in the crack growth direction lies in the increasing stress concentration at the crack tip which activates secondary slip systems. This phase of crack propagation can be observed after failure of the sample at the fracture surface by so-called fatigue striations. These striations, first observed by Zapffe & Worden [199], are ripples on the fracture surface.

Illustrated in Figure 2.12 d), the macro crack propagation results in *fatigue failure* due to an ongoing reduction in the sample's cross section. At a certain point, plastic flow takes places in the whole cross section called general yielding and not only at the crack tip. By exceeding the tensile strength the sample breaks completely, marking the fatigue lifetime of the sample.

In the following methods for the prediction of the lifetime are summarized.

2.2.3. Methods for Fatigue Lifetime Prediction

Phenomenological Stress- and Strain-Based Approach. Either the σ-N curve or the ε-N curve (strain-cycle curve or strain-based Wöhler curve) visualizes the number of cycles until a material or component reaches a defined damage criterion at distinct loadings. Such a criterion can be final fracture, cracks reaching a critical length or the exceeding of a maximal strain.

Figure 2.13 a) shows the σ-N curve, which relates the cyclic stress amplitude to the number of cycles to failure and is obtained as a result of a number of fatigue tests at different stress levels. Each specimen is tested at a constant stress amplitude until failure. In cases of large number of cycles (e.g. $N_{cycle} > 10^6$) the experiment might be stopped and the result might be interpreted as quasi-infinite life. As known, fatigue failure may occur also at very high numbers of cycles, e.g. 10^8 cycles, see Christ [38]. On the horizontal axis the number of cycles to fracture is given on the logarithmic scale. The vertical axis contains the stress amplitude of the cycle (linear or more common logarithmic). A stress-based approach for the description of the lifetime was proposed by Basquin [13] at the beginning of the 20th century. It relates the number of cycles to fracture N_f (corresponding to $2N_f$

load reversals) and the respective stress amplitude σ_a of load, reading

$$\sigma_a = \sigma'_f (2N_f)^b \,, \tag{2.7}$$

where σ'_f and b are the coefficient and the exponent of fatigue strength, respectively. For some materials there is a stress amplitude level below which the material will not fail. This lower amplitude in the σ-N curve marks the so-called fatigue limit σ_f. Many factors have an influence on the level of the fatigue limit. These include, among others, geometry, stress ratio, surface conditions, temperature and residual stresses. On a double logarithmic (log-log) scale the curve can be considered to be linear with slope k. Furthermore, the curve can be divided in two regions, the high-cycle fatigue (HCF) and low-cycle fatigue (LCF). In the HCF regime induced deformations are primarily elastic. Whereas the maximum stress level in the LCF regime is higher than the yield strength, resulting in macroscopic plastic material response, see Suresh [176]. Hence, the number of cycles to failure is considerably smaller as in the HCF region. The transition between LCF and HCF is defined by the amount of plasticity in the net section and not by a certain number of cycles[2].

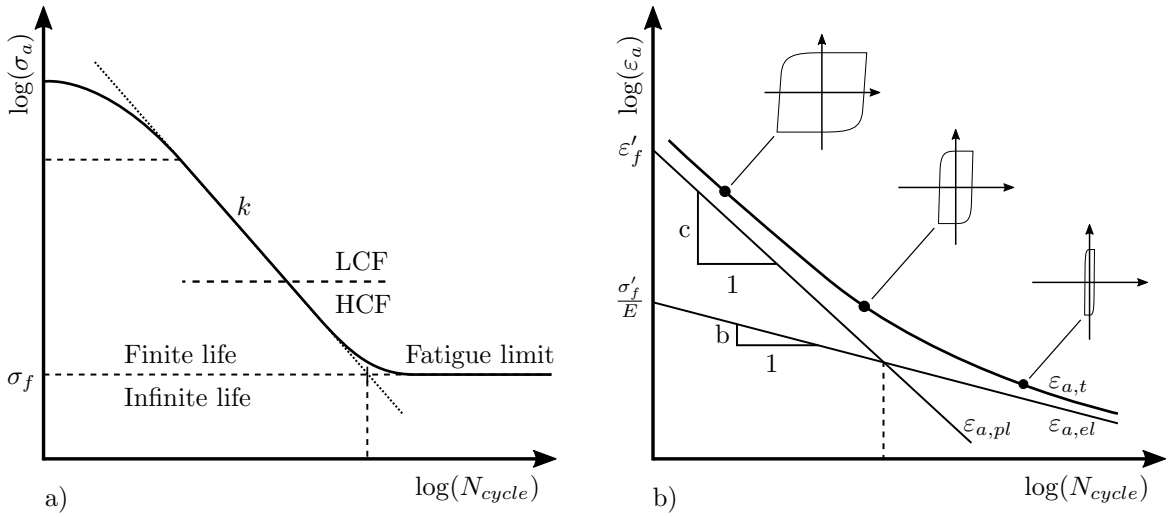

Figure 2.13: Schematic representation of a σ-N curve in a) with important quantities and regimes. The total ε-N curve together with its elastic and plastic proportions is illustrated in b).

Manson [108] and Coffin [39] independently proposed a relation between the plastic strain amplitude ε_a and the number of load reversals $2N_f$ to fracture. It is still used to describe the LCF regime with an empirical potential law as

$$\varepsilon_{a,pl} = \varepsilon'_f (2N_f)^c \,, \tag{2.8}$$

where ε'_f and c are coefficient and the exponent of fatigue ductility, respectively. These quantities are defined in analogy to the Basquin relationship, which is commonly used

[2]Note, that some authors still define numbers of cycle as a reference to distinguish the LCF and HCF region. For instance [37] proposes $N_f(LCF) < 5 \cdot 10^4 < N_f(HCF)$.

to describe the HCF regime. Reformulating the stress-based Basquin law (2.7) by using Hooke's law (2.5) yields an expression for the elastic strain

$$\varepsilon_{a,el} = \frac{\sigma'_f}{E}(2N_f)^b \,. \tag{2.9}$$

The total strain-cycle curve is an superposition of the modified Basquin equation (2.9) for the HCF regime and the Manson-Coffin law (2.8) for the LCF regime, as shown in Figure 2.13 b). Following Morrow [120] the total strain amplitude as a function of the number of cycles reads

$$\varepsilon_{a,t} = \varepsilon_{a,el} + \varepsilon_{a,pl} = \frac{\sigma'_f}{E}(2N_f)^b + \varepsilon'_f(2N_f)^c \,. \tag{2.10}$$

In the log-log scale representation of Figure 2.13 b) the asymptotes of the total strain curve are the limit cases for the LCF regime ($\varepsilon_{a,pl} >> \varepsilon_{a,el}$) and the HCF regime ($\varepsilon_{a,el} >> \varepsilon_{a,pl}$). Exponents b and c can be identified as the slopes of the lines and the coefficients σ'_f and ε'_f can be determined by the intersections of the lines with the ordinate. The intersection of both lines (indicated by the dotted line) marks the number of cycles with equally sized elastic and plastic strain amplitude. The number depends on the material condition and is smaller with increasing material strength and decreasing ductility.

For the investigation of material fatigue properties a coarse classification is made, associating the reason for fatigue failure to surface condition or non-metallic inclusions and voids, see Haibach [66]. Furthermore, Wöhler curves for components are also affected by a multitude of parameters, as stated by Radaj & Vormwald [152]. Important factors are the heat treatment and forming history, the consequential shape, size and surface properties such as residual stresses, surface roughness and topology. Moreover, the environmental condition play a significant role such as the kind of loadings, temperature conditions or a corrosive atmosphere.

Fracture Mechanics. Static and fatigue strength of crack-containing structures can be estimated by concepts of fracture mechanics, which can be divided into linear-elastic and elasto-plastic fracture mechanics. An overview of different mechanisms and models is given in Dönges [47]. In terms of the linear-elastic approach, the crack growth can be described using the stress intensity factor K. This factor represents a measure for the intensity of the stress field avoiding the infinite number of calculated stress at the crack tip. Unstable crack propagation takes place for static loadings when the material dependent critical stress intensity factor, also called fracture toughness, is reached. Under cyclic loading below the fracture toughness a stable crack propagation may occur, described by the empirical relation proposed by Paris & Erdogan [136]. Known as the Paris' law, this relation determines the rate of growth per cycle for a fatigue crack. The rate of crack growth is experimentally shown to be a function of the range of stress intensity of a corresponding loading cycle. The linear-elastic approach is only valid if the plastic zone at the crack tip is small compared to the crack length, see Gross & Seelig [64].

Otherwise, elasto-plastic fracture mechanics can describe the crack propagation with two alternative parameters defined at the crack tip. First, the J-integral, going back to Cherepanov [35] and Rice [154], which is equivalent to the stress intensity factor but considers inelastic deformations ahead of the crack tip. Second, the crack opening displacement, which is a measurement for the plastic deformation at the crack tip. For further details the reader is referred to [64, 176].

Crystal Plasticity Simulation. The above introduced approaches to predict the fatigue behavior of materials are widely used but suffer a disadvantage. They do not take into account the material's microstructure which is undoubtedly determining and important for the understanding and prediction of fatigue failure mechanisms. A numerical approach to describe elasto-plastic material behavior considering the microstructure of crystalline materials is given by the crystal plasticity simulation method. Depending on the crystal structure, slip systems are defined and rotated with regard to the individual grain orientations. Plastic slip induced by shear stresses is calculated on each slip system to describe the deformation of the material.

Repetto & Ortiz [153] modeled the formation of extrusions and intrusions at the intersection of a PSB and the material surface. Cyclic loading leads to void formation due to annihilation of dislocations and result in a volume expansion in a PSB. This volume expansion induces extrusion. The movement of voids from the PSB to the matrix causes shrinkages resulting in intrusions. The model captures the volume expansion and shrinkage numerically. Resulting notch geometries intensify with increasing number of simulated loading cycles and describe the mechanism for crack initiation. However, the location of the PSB must be known or set in advance of the simulation such that a prediction of the crack initiation location is not possible.

With a crystal plasticity finite element based approach of Manonukul & Dunne [107] the calculation of the crack initiation spot is possible. They propose the accumulated plastic slip on each slip system as a criterion for crack initiation for a nickel alloy C263. Such a damage metric for crack nucleation is often referred to as fatigue indicator parameter (FIP). Bennett & McDowell [16] propose a FIP based on the work of Fatemie & Socie [52], where the irreversibility of the plastic strain and the normal stress applied on the critical slip plane cause crack initiation. Their results are exemplified at a 4340 steel. Different FIP formulations are discussed in Hochhalter et al. [76]. Recently, these micromechanical measures for fatigue are also used to model short crack growth. Yeratapally [198] investigated the effect of different microstructural features and the associated micromechanical quantities on crack initiation and short crack propagation in nickel-base superalloys. It is concluded that FIPs are able to describe the nucleation and propagation of a crack by capturing the interplay of micromechanical quantities and microstructural features. Castelluccio & McDowell [31] simulate short crack growth based on the Fatemie-Socie FIP in RR1000 nickel-base superalloys. A sensitivity to adjacent grains is considered in terms of a non-local model. A growing research community suggests the application of micromechanical simulation methods to model material fatigue and confirm the validity of this approach.

The possibility to include and investigate microstructural features within the crystal plasticity model is a crucial advantage compared to isotropic elasto-plastic material simulations, but is associated with increasing computational costs. The interaction between hydrogen, the material, cyclic loading and resulting fatigue mechanisms is highly dependent on the microstructure. Therefore, the FIP approach to model crack initiation is adapted in this work and expanded to capture the influence of hydrogen on the fatigue behavior. A drawback of microstructure based simulation approaches is the limitation to small regions. If the interest of the investigation is not only on the pure material behavior but also on the influence of geometries of specimens or entire components, the gap in the length scale must be overcome. Multiscale methods transferring information between

scales are commonly used to calculate large scale components without neglecting relevant microstructural features, see Sorić et al. [174].

2.3. Interaction with Hydrogen

The deteriorating effect of hydrogen on mechanical properties of metals is a sequence of several time-dependent physical processes. It provokes a loss of ductility, reduces the load bearing capacity and changes the fracture behavior under static loading, see Herring [71]. During cyclic loading a reduction of lifetime is observed by Schauer [162] especially in the LCF regime. Note, that all these effects vary in their severity between different groups of steels. The first crucial step to hydrogen induced degradation is the supply of molecular or atomic hydrogen. A distinction is made between hydrogen induced during the manufacturing chain and during the operation of steel components in hydrogen environment. After the adsorption and absorption of hydrogen, its atoms diffuse into the lattice and accumulate depending on the internal stress state and the material's microstructure. Exceeding a critical local hydrogen concentration in the bulk can cause the onset and interplay of different damage mechanisms. These phenomena are explained in detail in this section.

2.3.1. Surface Mechanisms

Hydrogen can be found in steels due to two different processes. The first possible option is an introduction of hydrogen in the metal structure during manufacturing processes such as shaping, coating, tempering and surface treatments, see Pohl [143]. In this case hydrogen is already in the material or component at the beginning of its practical life cycle, leading to premature failure, which is often referred to as *internal hydrogen embrittlement*. In the following, a focus is put on the second possibility for hydrogen to enter steels, where an uptake over the surface through environmental exposure takes place. Hydrogen is provided in form of atomic or molecular hydrogen or as constituents of larger molecules such as methane or hydrogen sulfide, Wendler-Kalsch [192]. Corrosion processes on the metal surface or cathodic charging are wells for hydrogen, which may occur unexpectedly. Whereas components directly exposed to gaseous hydrogen, such as pipelines, tanks or valves, are expected to be entered by hydrogen dependent on surrounding conditions like temperature or pressure and are of main interest in this work.

The uptake of gaseous hydrogen through the surface is described in detail by Protopopoff & Marcus [146] and Turnbull [187]. The process comprises the molecular and dissociative *adsorption* as well as the *absorption*. The adsorption is divided into the *physisorption* of molecules on the surface and the *chemisorption* of molecular to atomic hydrogen. The absorption of atoms into the metal bulk is followed by lattice diffusion of the interstitial solute. These are reversible processes reading

$$\mathrm{H_2}(G) \overset{\text{physisorption}}{\longleftrightarrow} \mathrm{H_2}(M) \overset{\text{chemisorption}}{\longleftrightarrow} 2\,\mathrm{H}(D) \overset{\text{absorption}}{\longleftrightarrow} 2\,\mathrm{H}(S)\,. \tag{2.11}$$

As illustrated in Figure 2.14, the gaseous hydrogen G in the vicinity of the metal is adsorbed to the metal surface. The adsorption can be classified in physisorption M, where the molecules are bond to the solid surface through rather weak physical forces (van der Waals forces) and its chemical properties, such as the molecular structure of the H_2 molecule, remain unchanged. Another part of the adsorption is the chemisorption D, where the molecule is dissociated into two H atoms by overcoming an energy barrier. Only

the atomic hydrogen can be absorbed in a following step resulting in an interstitial solute S in a crystal surface layer, from where hydrogen continues its path into the metal bulk by diffusion. Physics and kinetics of these sorption processes are discussed in Morris et al. [119] and Pisarev & Ogorodnikova [142].

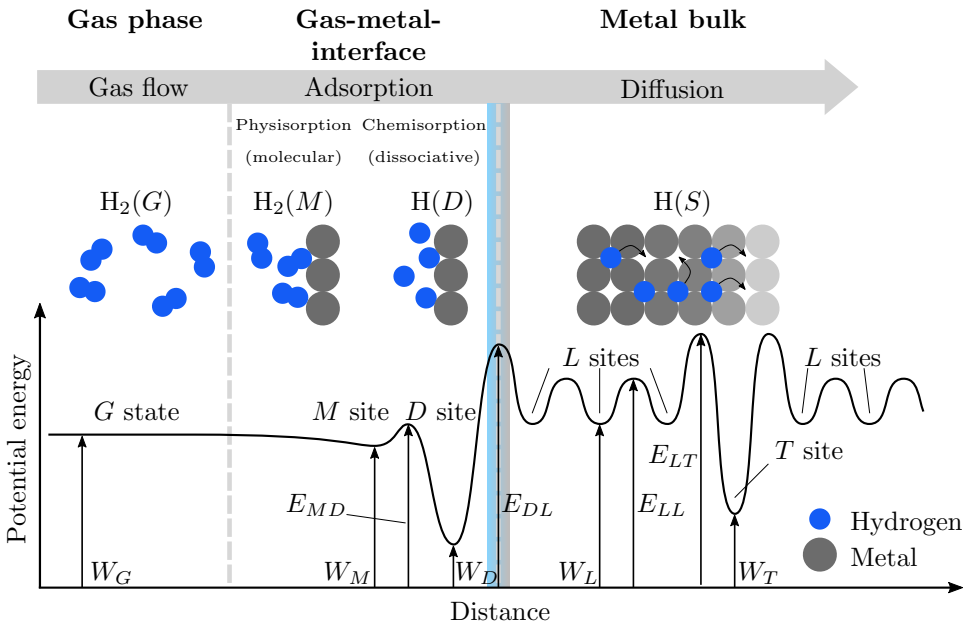

Figure 2.14: Hydrogen uptake process from the gas phase over the adsorption to the absorption and bulk diffusion, inspired by Toribio & Kharin [184]. The upper part illustrates the sequential steps in form of molecule and atom interaction. The blue-grey band indicates the metal surface. Different sites as well as their potential energy characteristics are drawn in the lower part. W_X denote the free energy of a X-site well and E_{XY} the free energy of a saddle point between X and Y.

The hydrogen adsorption depends strongly on the metal itself as well as the surface condition of the metal, Pisarev [141]. It might be accelerated by active or bright surfaces and might be retarded by defects, roughness or passivation layers. An oxide film for instance can reduce the solubility of hydrogen especially in the more corrosion-resistant alloys such as stainless steel and hence, slows down the hydrogen uptake. Turnbull [187] states, how difficult but crucial it is to consider reduced hydrogen uptake due to the protective oxide layer in testing and modeling approaches. Especially the consequences of film rupture due to dynamic plastic deformation might have a severe impact on a component's lifetime.

2.3.2. Hydrogen Diffusion

After reaching the subsurface layers in form of single atoms, hydrogen starts to diffuse through the solid driven by a concentration gradient in order to reach a chemical equilibrium. Hydrogen in solids is either located in interstitial lattice sites or in trap sites. Atoms in interstitial sites can in general move freely and hop according to the potential energy between those sites. Whereas hydrogen is tied to trap sites, depending on their nature. Previous to a detailed discussion of interstitial and trap sites, a general remark about hydrogen diffusivity in different steels is given. A large scattering is observed investigating the diffusivity of various ferritic, bainitic, martensitic or austenitic

steels, see Figure 2.15. However, the following physically motivated explanation help to classify the individual groups. The mobility of hydrogen atoms between interstitial sites is influenced positively by a lattice dilatation, Li et al. [97]. With increasing space for an interstitial site the energetic configuration becomes favorable for hydrogen to change the position towards this larger space. The reason therefore is, that the atoms are slightly too big for a standard interstitial site and expand the lattice by occupying an undilated interstitial site. A lattice dilatation can be induced mechanically or thermally. In BCC lattices the diffusivity is orders of magnitudes higher than in FCC lattices. Lattices with a BCC configuration exhibit more interstitial sites and therefore the sites have smaller distances among one another, which facilitates jumps for the atoms. Hence, austenitic steels (FCC) exhibit a much slower hydrogen diffusion behavior than ferritic (BCC) steels. Murakami [121, 85] denotes the increased diffusivity in martensitic parts of austenites as *hydrogen diffusion highways*. Hydrogen traps reduce the diffusivity by attracting and binding mobile hydrogen, as described by McNabb & Foster [111] and Oriani [133]. The influence of grain boundaries is controversially discussed in literature. Yao & Cahoon [197] describe a retarding effect of grain boundaries on hydrogen diffusion based on experimental investigations. Whereas Di Stefano et al. [46] investigate hydrogen diffusion behavior at grain boundaries with first-principle analysis and calculate an enhanced hydrogen diffusivity along certain grain boundaries which act as migration pathways. Further atomistic studies by Suzuki & Mishin [177] and Pedersen & Jonsson [137] investigate differences of diffusion rate between the diffusion across and parallel to the grain boundary plane. While twist boundaries block diffusion across the boundary, diffusion parallel to the boundary is enhanced.

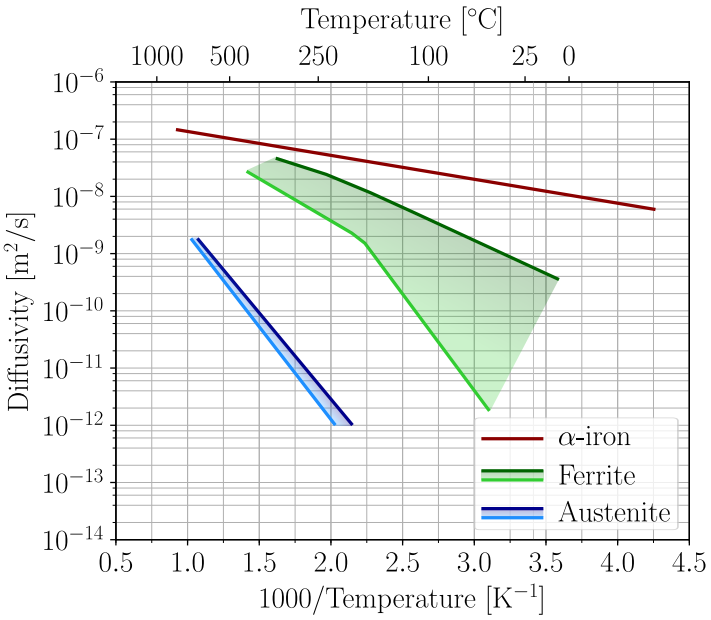

Figure 2.15: Scatter bands for hydrogen diffusion coefficients in α-iron, ferritic and austenitic steels at temperatures from -50 to 1000°C, data extracted of Böllinghaus et al. [21].

As stated above the total hydrogen concentration can be additively split in a part of interstitial lattice hydrogen C_L and the trapped hydrogen concentration C_T, which consists

of a reversible $C_{T,r}$ and an irreversible $C_{T,ir}$ proportion. The classification of traps follows the binding energy E_b (mostly defined as a negative quantity), see Oriani [133] and Hirth [74]. It assigns shallow reversible traps to a binding energy $-E_b < 30$ kJ/mol and deep irreversible traps to $-E_b > 50$ kJ/mol. As shown in Figure 2.16, the binding energy is the difference of potential energy between the interstitial and trapped sites. In terms of Figure 2.14 the binding energy can be calculated as the absolute energy difference $E_b = W_T - W_L$ of the saddle point E_{LT} between a lattice and trap site and the energy well W_T of the trap. The required activation energy to enable an atom to escape a trap site is denoted by E_t and to change its position between two interstitial sites L is E_a.

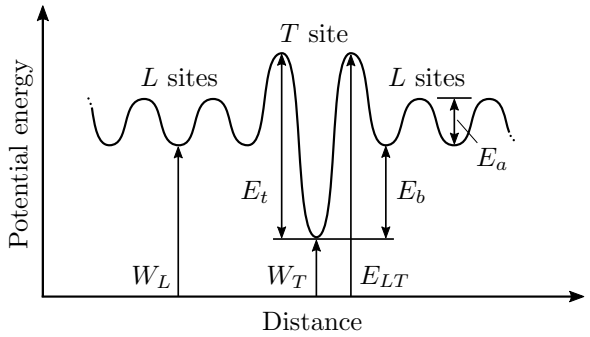

Figure 2.16: Cutout of Figure 2.14 to visualize the energy landscape of interstitial lattice and trap sites. The arrows indicate the activation energies for lattice sites E_a and trap sites E_t as well as the binding energy for traps E_b.

Interstitial Sites. Interstitial sites vary in their type, size and number depending on the corresponding lattice configuration. Figure 2.17 depicts the tetrahedral and octahedral interstitial sites for a BCC lattice, with 12 and 6 sites per unit cell, respectively. Whereas FCC metals possess 8 tetrahedral and 4 octahedral sites per unit cell. As stated above, the BCC configuration has a higher density of interstitial sites, which reduces the distance between the sites and hence, increases the diffusivity compared to FCC structures. The solubility is generally much higher in FCC than in BCC metals, because of large octahedral interstitial sites in FCC metals. In BCC lattices the tetrahedral sites provide more space and are therefore preferable occupied by hydrogen atoms compared to the octahedral sites.

Energy Barriers and Traps. Beside the hydrogen as an interstitial solute a significant amount of hydrogen is located in reversible or irreversible traps. Trapping sites are various kinds of lattice imperfections which different binding energies E_b. Traps in the lattice are shown in Figure 2.18 and can be dislocations, vacancies, grain boundaries, hydrostatic stress fields, segregations or carbide interfaces. Furthermore, substitutional atoms have an attracting effect on hydrogen atoms. These trapping sites act as potential wells, binding hydrogen atoms and thus increasing their effective concentration in the metal while reducing the amount of free diffusible hydrogen. Trapping sites can increase the total concentration significantly, especially in defect-rich metals, such as high-carbon or martensitic steels. A quantification of the binding energies for traps are summarized in Table 2.4 and result from both first principles calculations and experimental data of Hirth [74], Kumnick & Johnson [91], Wendler-Kalsch [192] and Frappart et al. [56]. The binding energies scatter in certain ranges determined by different

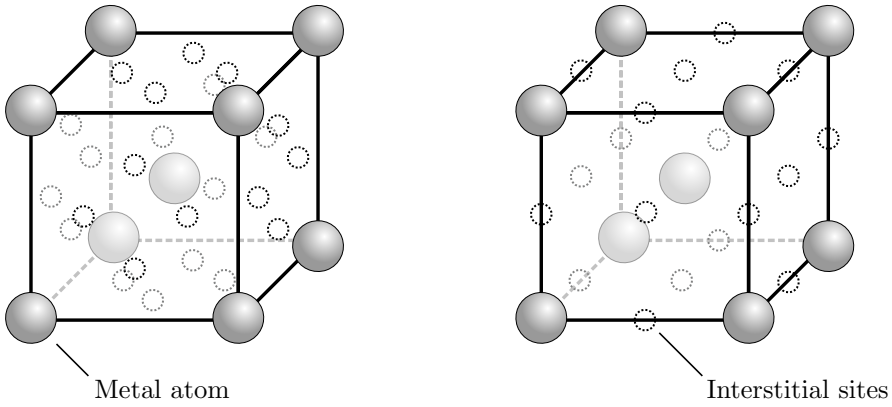

Figure 2.17: Interstitial sites in BCC lattice. The tetrahedral sites are shown on the left side and the octahedral sites on the right side. The larger grey spheres mark the metal atoms and the dotted small circles the interstitial sites. 12 tetrahedral and 6 octahedral sites exist per unit cell.

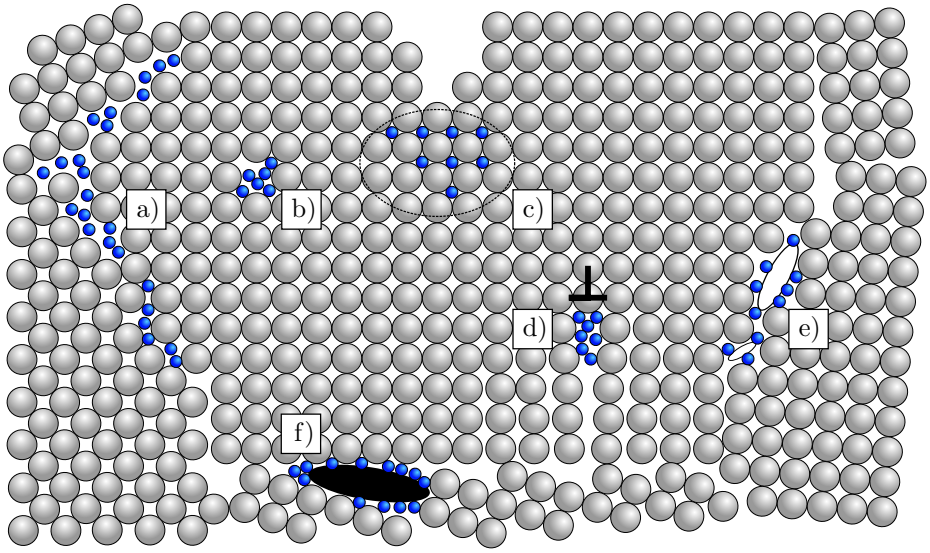

Figure 2.18: Schematic representation of different trap types in a polycrystal structure inspired by Pundt [148] and Lynch [102]. Hydrogen accumulates and is bonded at a) grain boundaries, b) vacancies, c) regions of high hydrostatic stresses, for instance in front of cracks, d) dislocations, e) micropores or voids at grain boundaries or f) interfaces of segregation or carbides.

authors. Nevertheless, general conclusions can be drawn. The binding energies of some substitutional atoms such as Mn, Mo and Cr are negligible small and these atoms do not exhibit a trapping effect, while elements like Ti, Zr, N and Si may act as weak trapping sites. Substitutional atoms may also affect hydrogen solubility significantly if their concentration is high enough. An increase of solubility is observed for substitutional atoms larger than iron, while smaller atoms tend to decrease it. Effective diffusivities show the opposite trend. Other weak sites include screw dislocations and dislocation stress fields while edge dislocations, vacancies and grain boundaries are moderate traps. The strongest binding energies are found at carbide interfaces. All weak traps are reversible

at room temperature together with some of the moderate traps. Most of the moderate traps ($-E_b > 50$ kJ/mol) and the strong traps are irreversible and require an enormous lift of the hydrogen atom's energy level to escape such a deep trap.

Trap site type	$-E_b$ [kJ/mol]
Dislocation stress field	0-20
Substitutional atoms	0-26
Dislocation core (screw)	20-30
Dislocation core (edge)	50
Dislocation core (mixed)	50-60
Voids	30-65
Grain boundary	60
Free surface (adsorption)	70-99
Fe_3C - interface	84
TiC - interface	98

Table 2.4: Trap binding energies for various microstructural defects and imperfections determined by experiments and calculations, see [74, 91, 192, 56].

2.3.3. Degradation Mechanisms at Mechanical Loading

Various hydrogen degradation mechanisms have been controversially discussed by many authors over the last decades. The mechanism behind hydrogen induced failure is often referred to as *hydrogen embrittlement* but the term is misleading, since the degradation process is by far more complex and takes place on different length- and timescales. A summary of established failure mechanisms is given in this section including *hydrogen enhanced local plasticity* (HELP), *hydrogen enhanced decohesion* (HEDE), *adsorption induced dislocation emission* (AIDE), *hydrogen enhanced strain induced vacancy theory* (HESIV) and *hydrogen induced phase transformation* (HIPT). Experimental investigations to clearly verify one of these theories as cause for premature failure in steels are very difficult due to local effects, strong dependency on the material and the surface structure as well as operating conditions. A general consensus has emerged stating that multiple mechanisms interplay successively or at the same time. Lately, more sophisticated experimental methods, such as in-situ testing and observation, in combination with ab-initio or molecular dynamic simulations provide new insights. For detailed reviews of the degradation mechanisms see Lynch [101, 102], Robertson et al. [157] or Barrera et al. [9].

Hydrogen Enhanced Local Plasticity (HELP). In this theory hydrogen induced degradation of a plastically deforming material is a result of an increasing mobility of dislocations, see Birnbaum & Sofronis [17]. Hydrogen is attracted to regions with high dislocation densities and diffuses preferably into the local stress field of the dislocation, to the dislocation core and the slip plane in front of the dislocation, as described in Robertson et al. [156]. It is suggested that dislocation mobility and slip localization are enhanced by a decrease of dislocation motion barriers. Experimental work of Ferreira et al. [53] shows that the stacking fault energy (SFE) decreases in the present

of hydrogen, thus increases dislocation mobility local to the regions of high stress concentrations, such as crack tips. Stress intensification facilitates microcrack formation in the localized deformation area and accelerates crack growth. The constriction work of partial dislocations increases with a smaller SFE, restricting cross-slip. Methods to detect HELP in different steels include macroscopic flow stress measurements, fractographic analysis, in-situ transmission electron microscopy (TEM) studies or measurements of dislocation motion. Contrary to the common usage of embrittlement, localized plastic failure due to enhanced plasticity can be associated with a local softening effect Shan et al. [170]. But Lynch [102] and Barrera et al. [9] claim that this effect alone cannot explain macroscopic brittle material response. Depending on the accumulation spot of hydrogen and the underlying microstructure, fracture can be either transgranular or intergranular.

Hydrogen Enhanced Decohesion (HEDE). This mechanism hypothesizes that a weakening of metal-metal bonds due to the presence of hydrogen increases the risk of decohesion. The HEDE mechanism is preferentially used to describe hydrogen induced embrittlement effects in metals, which were first observed by Pfeil [140] who describes brittle fracture surfaces of both single- and polycrystalline hydrogen charged iron. Gerberich et al. [60] formulated the mechanism to explain an increase of the crack-tip-opening angle caused by a reduction of the cleavage toughness dependent on the amount of hydrogen. A lattice dilatation at the crack tip induced by high hydrostatic stresses enable the hydrogen to exceed the solubility limit in the lattice. The accumulated atoms reduce the cohesive energy of the metal matrix or at specific interfaces such as certain crystallographic planes, grain boundaries, or phase boundaries which act as hydrogen traps. A brittle transgranular fracture surface observed in high-strength steels as well as brittle intergranular fracture can be explained with this degradation mechanism as stated in Lynch [102]. Until now, the HEDE mechanism could not be directly proven by experiments but atomistic simulation methods allow for the calculations of relevant energies to gain evidence supporting the theory. For instance a lower tensile strength of the grain boundary due to an increasing hydrogen concentrations was estimated by the atomistic simulation, see Du et al. [48].

Adsorption Induced Dislocation Emission (AIDE). Inspired by the similarities between stress corrosion cracking and hydrogen-assisted cracking for many materials, Lynch [99, 100] postulated that the hydrogen induced degradation is also caused by the adsorption of hydrogen at the crack tip. Embrittlement could be observed in metals exposed to hydrogen where the crack growth velocity is so high, that it is impossible for the hydrogen to diffuse ahead of the crack. This observation supports a mechanism induced by hydrogen adsorption at the crack tip, which facilitates emission of dislocations. Furthermore, coalescence of voids ahead of crack tips is accelerated and leads to an embrittlement. Dislocation emission includes both nucleation and the movement of dislocation away from the crack tip enhancing crack growth. Especially for ductile materials this mechanism helps to understand the effect of dislocation emission on crack growth leading to brittle fracture. AIDE might occur in combination with the HELP mechanism, which enhances the dislocation mobility away from the crack tip, or with the HEDE mechanism, which might be fortified by an increases of backstresses from dislocation emission, see Barrera et al. [9].

Hydrogen Enhanced Strain Induced Vacancy Theory (HESIV). Following the proposal of Nagumo [124], hydrogen enhances the density and agglomeration of vacancies

in the metal lattice. In regions of high deformation vacancy cluster arise leading to coalescence of microvoids with subsequent microcrack growth. Larger voids result from this process decreasing the ductile crack growth resistance and finally, leading to premature failure. Experimentally this mechanism can be observed on hydrogen-charged samples undergoing tensile or fracture toughness tests. The density of microvoids is notable higher in hydrogen-charged specimens compared to uncharged samples after the same fatigue samples. Since HESIV alone does not suffice to interpret the complete embrittlement mechanism, Neeraj et al. [127] combined this idea with the HELP mechanism to explain fracture path observations for various steels.

Hydrogen Induced Phase Transformation (HIPT). Another type of degradation mechanism encompasses structural changes in the surface layer of hydrogen charged alloys and steels. This phase transforming process results in either hydride formation or martensitic transformation. First, cracking in hydride forming metals, such as Ti, Nb, Zr and Ta, can be caused by hydrogen exceeding the solubility limit. Low energy fracture paths develop due to newly formed brittle hydride precipitates, see Wendler-Kalsch [192]. This process can be observed and confirmed by microscope and thermodynamic analysis, Flanagan [55]. Second, Bugaev et al. [26] describe a hydrogen induced martensitic transformation of the FCC γ phase into hexagonal close packed (HCP) ϵ-martensite or BCC α-martensite phases.

Assessment of Degradation Mechanisms. Following the reviews [101, 157, 9] a discrete classification of hydrogen induced degradation observed by experiments into the above introduced failure mechanisms is not possible and in many cases ambiguous. To explain macroscopic brittle failure a combination of two or more mechanisms often helps to describe observed phenomena. The deteriorating influence of hydrogen on mechanical properties cannot be limited to a certain group of steels or alloys. Simple iron lattices might be just as susceptible to hydrogen degradation as high-strength steels. Modern techniques combining experiments and simulations at different length scales provide the key to fully understand the effect of hydrogen in steels. However, most authors agree that the following factors affect the degradation and promote certain mechanisms. The most important factors are the diffusion behavior and the resulting local hydrogen concentration, the material's microstructure, the dislocation distribution and the strain rate of testing.

2.4. Hydrogen Influence on Fatigue

The effect of hydrogen on the fatigue behavior of steels is widely discussed in literature, but no general validity is yet to be found. Most observations are based on experiments which are conducted by researchers under a variety of testing conditions, which makes a comparison of the provided data difficult. Under such circumstances only relative comparisons are possible. The available experimental data shows that the influence of hydrogen on the fatigue behavior of a single metallic material is governed by its chemical composition and microstructure particularities, its shape and surface conditions as well as by applied loading and hydrogen exposure conditions such as amplitude, frequency, temperature or hydrogen gas pressure. Furthermore, the way how hydrogen is provided to the sample takes a crucial role.

The exact determination or measurement of the local hydrogen concentration is to the

authors best knowledge not possible and is a subject to modern research. This fact impedes the correlation of hydrogen local concentration to local material degradation and only integral content measurements allow for an approximation of the hydrogen content and the resulting deteriorating effect on the material's fatigue behavior.

Internal hydrogen embrittlement describes a condition with an initial hydrogen concentration in the material with no external hydrogen supply, where effusion processes during testing could reduce the hydrogen degradation. A continuous provision of hydrogen during testing or operation is called *external* or *environmental hydrogen embrittlement* and might intensify the effect by accumulating hydrogen at local stress peaks due to microcracks or imperfections in the vicinity of the surface. A short overview of the hydrogen impact on LCF and HCF fatigue is given in the subsequent sections with a reference on Nanninga [126] for a detailed description.

2.4.1. Hydrogen on Low Cycle Fatigue

Especially noticeable is the significant reduction of the lifetime for most steels in the LCF regime, which is a key motivation for this work. With the fundamentals of hydrogen behavior in steel described in Section 2.3 explanations for the susceptibility of LCF tests to hydrogen can be found. High loading amplitudes cause areas of large hydrostatic tensile stresses leading to an increase of the local hydrogen concentration. A passivation layer or oxide film on the material's surface can be destroyed due to large plastic strains, which facilitates the hydrogen ingress and uptake. A premature fatigue crack formation in the LCF regime underlines both of the above stated effects. Moreover, following the theories of degradation mechanisms hydrogen might change the cyclic hardening behavior due to its influence on the dislocation motion. LCF tests can be conducted at low frequencies in an acceptable time period which provides the hydrogen with enough time for kinetic processes such as diffusion and redistribution. Extensive experimental investigation and a detailed literature review for various steels can be found in Schauer [162].

2.4.2. Hydrogen on High Cycle Fatigue

Only a reduced or negligible influence of hydrogen on fatigue is observed in the HCF regime for the majority of steels, see Schauer [162]. The need of low frequencies for time-dependent kinematic processes overshoots economical aspects and available time frames in ranges of over 10^6 cycles. This often forces researchers to an extrapolation from the LCF regime supported by only a few experimental results of the HCF regime, which delivers statistical insufficient or questionable data. However, if the testing frequency is increased, one cannot be sure whether the total degradation effect of hydrogen is captured by these tests. Schauer [162] lists numerous steels tested in hydrogen atmosphere by different research groups and sums up that ferritic-perlitic steels, martensitic and austenitic steels do not suffer from hydrogen degradation in the HCF region. Some Cr-Ni steels even show a slight increase in their fatigue lifetime. A decrease of fatigue strength in hydrogen atmosphere is observed for cathodically charged high-strength martensitic steels. Austenitic steels predominantly suffer from hydrogen under high pressure atmosphere.

2.4.3. Effect on Cracking Behavior at Fatigue Loading

Hydrogen accumulation in areas of large tensile stresses coincides with locations for fatigue damaging, which hence can be initiated or supported. Crack formation and its interplay with hydrogen are strongly dependent on microstructural aspects, whereas the influence

on crack propagation is highly localized in a small area around the crack tip.

Crack formation is accelerated by an increase in accumulated plastic strain due to the presence of hydrogen. Nanninga [126] describes this effect in detail and states, that intrusions, extrusions and imperfections are preferred locations. Hydrogen facilitates the dislocation movement and therefore, it may influence the formation of PSB. However, experimental observations are rare. Uyama et al. [189] investigated the strain hardening under cyclic loading of an annealed plain carbon steel. They observed surface glide band formation in the hydrogen charged specimens to be more localized. This resulted in a greater number of fatigue cracks initiating from slip bands within grains in hydrogen charged specimens. Marsh & Gerberich [109] identify inner interfaces as critical spots for hydrogen induced fatigue crack initiation and show that crack initiation is intensified at grain boundaries. The enhanced absorption of hydrogen at phase boundaries between inclusion and matrix in combination with the increased stress can result in premature crack formation, see Takai et al. [181].

Crack propagation is mainly influenced by the local accumulation of hydrogen at the crack tip due to high hydrostatic tensile stresses, foremost mentioned by Sofronis & McMeeking [173]. The interplay with a higher adsorption ability due to the degradation of the passivation layer elevates the local hydrogen concentration exceeding a critical amount, Murakami [123]. Crack growth rate, test frequency and hydrogen supply in and around the sample are regulatory elements for this process. Mechanisms responsible for increased crack growth rates in the presence of hydrogen are traced back to enhanced dislocation movement, a changed crack-closure behavior as well as hydrogen induced decohesion at grain boundaries. The reader is referred to [123, 126, 162] for an in-depth discussion of literature towards hydrogen influence on crack initiation and propagation.

2.4.4. Existing Modeling Approaches

In the last decades numerous numerical models for the simulation of hydrogen interaction with steels have been developed. First, they aimed to describe macroscopic observations by capturing effects on a macroscopic continuous scale. Modern computing power in combination with atomistic simulations allow for an investigation of distinct phenomena and interactions on smallest scales. An overview of different existing modeling approaches is given in the following.

The first step of modeling hydrogen induced degradation in steels lies in the calculation of the local concentration determined by a diffusion process. McNabb & Foster [111] were the first to introduce a theory to describe diffusion with trapping sites in a ferrite. Oriani [133] assumed a local chemical equilibrium between interstitial and trap sites. This theory was adapted by Sofronis & McMeeking [173]. They were the first who coupled diffusion with elasto-plastic deformation in the large-strain regime. Later, Krom et al. [88] corrected and enhanced this formulation by an additional strain-rate dependency for the evolution of trap sites. Di Leo & Anand [44] elevated this theory in a thermodynamically-consistent framework. Coupling and implementation schemes of standard plasticity with hydrogen diffusion are described by Oh et al. [130], Barrera et al. [12] and Díaz et al. [43].

Therewith, phenomenological models for the damage mechanisms of Section 2.3.3 have been developed. As done in Moody et al. [117], continuum models of the HEDE mechanism often correlates the material failure to the exceeding of a critical hydrogen

concentration. A combination of HEDE and HELP mechanisms is considered by Barrera et al. [10, 11, 12] where the HEDE mechanism is captured by a cohesive zone modeling (CZM) approach and the HELP mechanism is taken into account by a hydrogen dependent yield stress. Hydrogen induced failure at matrix-carbide interfaces or at grain boundaries are modeled by several groups using the CZM approach ([3], [25], [83], [118], [169]). Hereby, the damage process is described by interface elements and a constitutive law for the cohesive energy, which captures the accelerating effect of hydrogen on the material damage. A model for hydrogen enhanced slip localization and mobility (HELP) is extensively discussed in publications of Sofronis and coworkers ([96, 98, 173, 180]). Based on experimental observations they proposed an empirical model to estimate the yield stress under hydrogen influence. This yield stress decreases with increasing hydrogen concentration. An approach to strain-induced vacancies (HESIV) is given by Nagumo [125] modifying a formulation for porous ductile fracture.

The above reviewed modeling approaches focus mainly on quasi-static loadings. Hydrogen modeling under cyclic loading is addressed by Turnbull [186] who reviews available phenomenological models for environmental fatigue crack propagation under hydrogen influence. Thereby, a focus is set on evolution equations for crack growth which is split in two parts: the growth rate in the absence of hydrogen and a rate associated with plastic fatigue deformation. The latter is dependent on the hydrogen concentration and local diffusivity. A model for crack propagation under cyclic loading based on a decohesion mechanism is proposed by Xing et al. [196]. These models usually do not consider features of the microstructure, such as the grain morphology and orientation, which are crucial for crack initiation and propagation. The gap of knowledge on certain microstructural interaction mechanism was certainly a reason for the simplified and practical approaches.

Today's atomistic simulation methods can support mesoscopic and continuum models. Using the density functional theory (DFT) an investigation of the electronic structure of single or multiple atoms is possible without any simplifications or assumptions. Single interaction effects for specific atomic configurations with a constrictive number of atoms can be investigated and evaluated with these methods, which declare them as an important tool towards a better understanding of hydrogen degradation mechanisms. In the context of hydrogen interaction with steels research groups calculated preferred hydrogen diffusion paths on tetrahedral sites over octahedral sites for BCC structures ([40, 72, 84]). Furthermore, grain boundary interactions with hydrogen for distinct types of boundaries are evaluated by [46, 48, 72]. Many evidences for different damage mechanism are collected in terms of atomistic methods, summarized in Barrera et al. [9]. However, time and length scales are a limiting factor of quantum mechanical approaches. They calculate processes for a few hundred atoms over a time period in the order of pico- to nanoseconds. For practical applications and the evaluation of material behavior in hydrogen atmosphere a compromise must be found between a length and time scale suitable for practical problems but still being able to resolve as many relevant features as possible.

The framework of crystal plasticity simulation offers the possibility to calculate micromechanical stresses and strains on a micro- to macroscopic scale including features of the microstructure and their interactions. Realizing this advantage, in the last years various research groups consider the grain morphology in their simulations by coupling the diffusion model with crystal plasticity finite element models. Miresmaeili et al. [116] were

the first to propose a coupled crystal plasticity-transient hydrogen diffusion model investigating the influence of the microstructure on hydrogen transport. Following their simulation results, segregation of hydrogen takes place mainly at grain boundaries. LEGRAND ET AL. [94] evaluated diffusion properties by numerical permeation tests for polycrystal structures. The effect of the stress-strain heterogeneity in stainless steel microstructures on diffusion were investigated by ILIN ET AL. [81]. A comparison between the hydrogen transport in polycrystals and equivalent homogeneous materials was drawn by CHARLES ET AL. [34]. They emphasize the importance of suitable trap models for physically realistic simulations. Recently, UL HASSAN ET AL. [188] propose a coupled model for the study of permeation simulation with trapping effects using ABAQUS. Therewith, they provide a tool to investigate microstructural effects on hydrogen transport.

Up to now a concept for the assessment of fatigue behavior of steels in hydrogen atmosphere under consideration of the microstructure is missing. A framework based on experimentally gained data in combination with simulative approaches on microstructural scale for the fast evaluation of fatigue life in hydrogen atmosphere is proposed in this work for the first time. It considers the evolution of the material's fatigue degradation dependent on the local hydrogen concentration and the interaction with the grain structure. The crystal plasticity model describes the evolution of a fatigue measure which is dependent on the local hydrogen concentration in lattice and trap sites. A theoretical foundation for material modeling is given in the following section.

2.5. Fundamentals of Continuum Mechanics

Basic concepts of continuum mechanics are summarized in this section, which provide a framework for the mathematical description of a continuous medium. Therewith, various physical phenomena in mechanical systems, which undergo deformation, can be described. The basic notation of continuum mechanics, kinematics, and geometric settings are introduced. The concepts of stresses in different configurations are discussed, which are necessary for the formulation of the essential governing balance laws. For a more detailed insight in continuum mechanics the reader is referred to textbooks of HOLZAPFEL [77], TRUESDELL & NOLL [185], ALTENBACH & ALTENBACH [2], BONET & WOOD [22] and HAUPT [69]. DE SOUZA NETO ET AL. [42] focus especially on the modeling of plasticity and crystal plasticity. Notations are mainly adopted from lecture notes of MIEHE [113, 114]. Note, that the focus of this section is on the introduction of the specific quantities used for the crystal plasticity and diffusion model in Chapter 5.

2.5.1. Kinematics of Finite Deformation

First, the basic kinematic quantities for solids at finite strains are discussed. The kinematics focuses only on the geometric description of the deformation of continuous media neglecting the physics. It requires a definition of material bodies, their configurations and the associated deformation map.

Description of Motion. A *material body* B is a physical object which consists of a set of material points $P \in B$ that occupy a certain domain $\mathcal{B} \subset \mathcal{R}^3$ in the Euclidean three-dimensional space $\mathcal{R}^3$. The mapping of the matter into the Euclidean space at a certain time t is described by

$$\chi_t : \begin{cases} B \to \mathcal{B}_t \subset \mathcal{R}^3 \\ P \mapsto \boldsymbol{x} = \chi_t(P) \,. \end{cases} \tag{2.12}$$

Hereby, each particle P is mapped onto a coordinate triple $\boldsymbol{x}$ by χ_t in the *current configuration* (also called *spatial* or *Eulerian configuration*), see Figure 2.19. The set of subsequent placements χ_t in a given time interval defines a set of subsequent configurations of B and thereby completely describes the *motion* of the body B.

To identify material points over time and during deformation processes, it is common to label them by an arbitrary *reference configuration* (also called *material* or *Lagrangian configuration*) $\mathcal{B}_0$ in the Euclidean space at an initial time $t = t_0$. This reference placement χ_0 defines a *reference* or *material position* $\boldsymbol{X} = \chi_0(P)$ for each particle P and places the body B in its *reference configuration* $\mathcal{B}_0$ which is normally in a stress-free state.

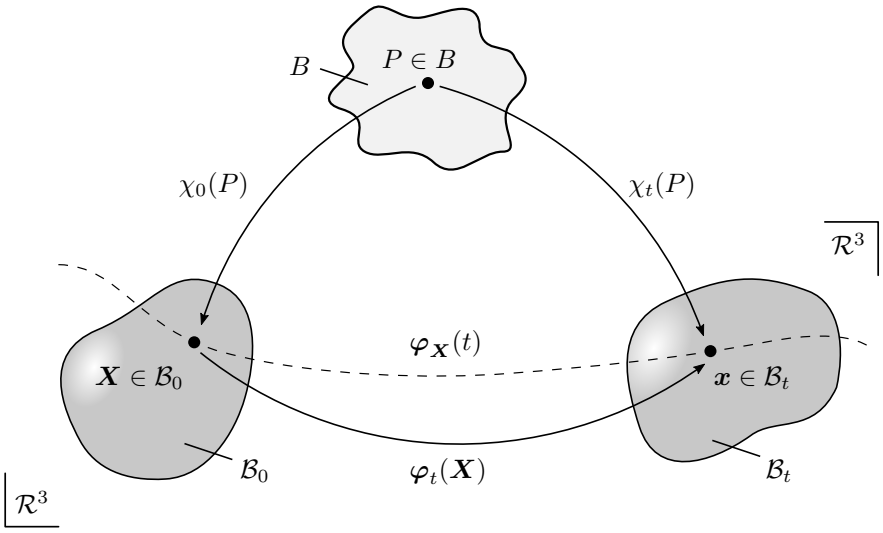

Figure 2.19: Motion of a material body B in the Euclidean space $\mathcal{R}^3$. Reference configuration $\mathcal{B}_0$ with position $\boldsymbol{X}$ at time t_0 and current configuration $\mathcal{B}_t$ with position $\boldsymbol{x}$ at time t. The reference description of the *motion* $\boldsymbol{\varphi}(\boldsymbol{X}, t)$ is identified as well as its *configuration* $\boldsymbol{\varphi}_t(\boldsymbol{X})$ of the body and the *path* $\boldsymbol{\varphi}_{\boldsymbol{X}}(t)$ of a particle P.

The mapping

$$\boldsymbol{\varphi} : \begin{cases} \mathcal{B}_0 \times \mathcal{T} \to \mathcal{B}_t \subset \mathcal{R}^3 \\ (\boldsymbol{X}, t) \;\; \mapsto \boldsymbol{x} = \boldsymbol{\varphi}(\boldsymbol{X}, t) \end{cases} \tag{2.13}$$

is called the *reference description of the motion*. It maps the referential position $\boldsymbol{X} \in \mathcal{B}_0$ of a particle $P \in B$ to its current position $\boldsymbol{x} \in \mathcal{B}_t$ at the time $t \in \mathcal{T} \subset \mathcal{R}_+$ ($\mathcal{T}$ denotes a time interval), as shown in Figure 2.19. The entire motion of a deforming body is fully described with (2.13), whereas the *configuration* at a frozen time t is described by the *deformation map* or *point map* as

$$\boldsymbol{\varphi}_t : \begin{cases} \mathcal{B}_0 \to \mathcal{B}_t \subset \mathcal{R}^3 \\ \boldsymbol{X} \mapsto \boldsymbol{x} = \boldsymbol{\varphi}_t(\boldsymbol{X}) \end{cases} \tag{2.14}$$

Kinematic Mappings. Additional mappings are considered, which are all related to the *point map* (2.14), namely the *tangent map*, *normal map* and *volume map*. Mathematical derivations for kinematic mappings are omitted and can be found in the above mentioned textbooks, for instance in [77].

The *deformation gradient* or *tangent map* is the gradient with respect to the reference position $\boldsymbol{X} \in \mathcal{B}_0$ and is defined as

$$\boldsymbol{F}(\boldsymbol{X}) := \nabla_{\boldsymbol{X}} \boldsymbol{\varphi}_t(\boldsymbol{X}) = \mathrm{Grad}(\boldsymbol{\varphi}_t)\,, \tag{2.15}$$

where $\nabla_{\boldsymbol{X}}(\cdot)$ or $\mathrm{Grad}(\cdot)$ are the referential or material gradient of $(\cdot)$ with respect to $\boldsymbol{X}$. As a direct consequence of the one-to-one map $\boldsymbol{\varphi}_t$, the deformation gradient is invertible. Hence, its determinant fulfills the condition $\det(\boldsymbol{F}) \neq 0$ and must satisfy the non-penetration constraint which forbids negative values. Combining both consequences one obtains

$$J_t = \det[\boldsymbol{F}] > 0\,. \tag{2.16}$$

The deformation gradient $\boldsymbol{F}$ is a linear map, which transfers material tangent vectors $\boldsymbol{T}$ to spatial tangent vectors $\boldsymbol{t}$, see Figure 2.20. The tangent vectors $\boldsymbol{T}$ and $\boldsymbol{t}$ are tangents to undeformed and deformed material curves, respectively. These tangent vectors are defined in tangent spaces, where $\boldsymbol{T} \in T_{\boldsymbol{X}}\mathcal{B}_0$ is found in the tangent space of the manifold $\mathcal{B}_0$ at base point $\boldsymbol{X}$ and $\boldsymbol{t} \in T_{\boldsymbol{x}}\mathcal{B}_t$ is found in the tangent space of the manifold $\mathcal{B}_t$ at base point $\boldsymbol{x}$. Thus, the deformation gradient is the *tangent map* (map of vectors)

$$\boldsymbol{F} = \nabla_{\boldsymbol{X}} \boldsymbol{\varphi}_t : \begin{cases} T_{\boldsymbol{X}}\mathcal{B}_0 \to T_{\boldsymbol{x}}\mathcal{B}_t \\ \boldsymbol{T} \qquad \mapsto \boldsymbol{t} = \boldsymbol{F}\boldsymbol{T}\,. \end{cases} \tag{2.17}$$

The *cofactor transformation* or *normal map* is defined as follows. Consider two curves, respectively in the reference and current deformation. At the intersection of both curves, the cross product of the two material tangent vectors in the reference configuration defines a material area or normal vector $\boldsymbol{A} := \boldsymbol{T} \times \hat{\boldsymbol{T}}$, while the cross product of the two spatial tangent vectors defines the corresponding deformed area or normal vector $\boldsymbol{a} := \boldsymbol{t} \times \hat{\boldsymbol{t}}$. To find a mapping to transfer $\boldsymbol{A}$ to $\boldsymbol{a}$, the tangent map (2.17) and some tensor calculus is used, yielding

$$\boldsymbol{a} = t \times \hat{t} = (\boldsymbol{F}\boldsymbol{T}) \times (\hat{\boldsymbol{F}}\hat{\boldsymbol{T}}) = \det[\boldsymbol{F}]\, \boldsymbol{F}^{-T}\boldsymbol{T} \times \hat{\boldsymbol{T}} = \mathrm{cof}[\boldsymbol{F}]\boldsymbol{A}\,. \tag{2.18}$$

The *normal map* is identified as the cofactor of $\boldsymbol{F}$ and (2.18) is a mapping between cotangent spaces, as depicted in Figure 2.20. Normal $\boldsymbol{A} \in T^*_{\boldsymbol{X}}\mathcal{B}_0$ is found in the cotangent space of the reference configuration at $\boldsymbol{X} \in \mathcal{B}_0$ and $\boldsymbol{a} \in T^*_{\boldsymbol{x}}\mathcal{B}_t$ is found in the cotangent space of the current configuration at $\boldsymbol{x} \in \mathcal{B}_t$. The normal map (map of areas) reads

$$\mathrm{cof}[\boldsymbol{F}] = \det[\nabla_{\boldsymbol{X}} \boldsymbol{\varphi}_t](\nabla_{\boldsymbol{X}} \boldsymbol{\varphi}_t)^{-T} : \begin{cases} T^*_{\boldsymbol{X}}\mathcal{B}_0 \to T^*_{\boldsymbol{x}}\mathcal{B}_t \\ \boldsymbol{A} \qquad \mapsto \boldsymbol{a} = \mathrm{cof}[\boldsymbol{F}]\boldsymbol{A}\,. \end{cases} \tag{2.19}$$

To identify the *Jacobian* or *volume map* consider an intersection of three curves. There, the triple scalar product between three tangent vectors defines a material volume in the reference configuration as $V = \boldsymbol{T} \cdot (\hat{\boldsymbol{T}} \times \bar{\boldsymbol{T}})$ and analogously a deformed spatial volume in the current configuration as $v = \boldsymbol{t} \cdot (\hat{\boldsymbol{t}} \times \bar{\boldsymbol{t}})$. By the definition of the determinant we derive the mapping to transfer V to v as

$$v = \boldsymbol{t} \cdot (\hat{\boldsymbol{t}} \times \bar{\boldsymbol{t}}) = (\boldsymbol{F}\boldsymbol{T}) \cdot \big((\boldsymbol{F}\hat{\boldsymbol{T}}) \times (\boldsymbol{F}\bar{\boldsymbol{T}})\big) = \det[\boldsymbol{F}]\, \boldsymbol{T} \cdot (\hat{\boldsymbol{T}} \times \bar{\boldsymbol{T}}) = \det[\boldsymbol{F}]\, V\,, \tag{2.20}$$

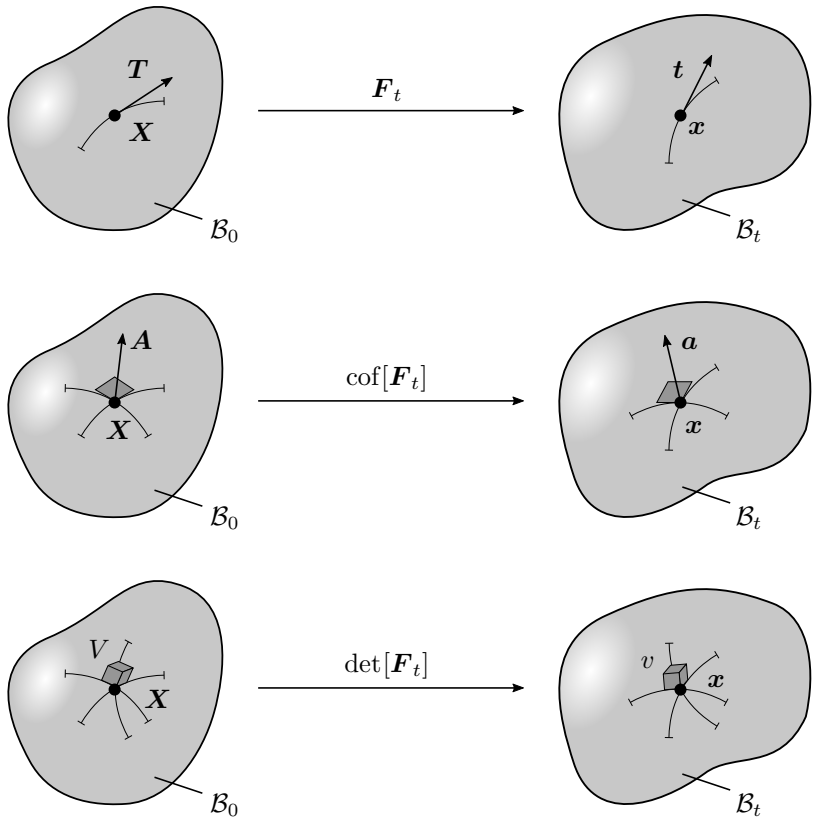

Figure 2.20: Basic kinematic mappings to transfer elements from the reference configuration $\mathcal{B}_0$ to the current configuration $\mathcal{B}_t$. Tangents are mapped by the deformation gradient, the cofactor of the deformation gradient maps areas and the volume mapping is governed by the determinant of the deformation gradient.

where the determinant of the deformation gradient linearly maps material volumes to corresponding deformed spatial volumes, see Figure 2.20. This clarifies constraint (2.17), which simply states that negative volumes are impossible. The Jacobian J_t is the volume map

$$J_t = \det[\nabla_{\boldsymbol{X}} \boldsymbol{\varphi}_t] : \begin{cases} \mathcal{R}_+ \to \mathcal{R}_+ \\ V \quad \mapsto v = \det[\boldsymbol{F}]\, V\,. \end{cases} \tag{2.21}$$

Polar decomposition. The deformation gradient (2.15) can be decomposed uniquely into positive definite, symmetric material stretch tensors $\boldsymbol{U}$ and $\boldsymbol{V}$ and a proper orthogonal rotation tensor $\boldsymbol{R} \in \mathcal{SO}(3)$

$$\boldsymbol{F} = \boldsymbol{R}\boldsymbol{U} = \boldsymbol{V}\boldsymbol{R}\,. \tag{2.22}$$

The mappings $\boldsymbol{U}$ and $\boldsymbol{V}$ stretch line elements, while $\boldsymbol{R}$ rotates them.

Metric Tensors and Strains. In order to measure length of line elements and angles between line elements the definition of metric tensors is required. In case of an orthonormal coordinate system, such as the Cartesian coordinate system, the standard material

and spatial metric tensors[3] are defined by the Kronecker symbol as

$$\boldsymbol{G} = \delta_{AB}\boldsymbol{E}^A \otimes \boldsymbol{E}^B \quad \text{and} \quad \boldsymbol{g} = \delta_{ab}\boldsymbol{e}^a \otimes \boldsymbol{e}^b\,, \tag{2.23}$$

where $\{\boldsymbol{E}_i\}_{i=1,3}$ and $\{\boldsymbol{e}_i\}_{i=1,3}$ are the global Cartesian frames in reference and current configuration, respectively. These metric tensors link the tangent and the cotangent spaces as follows

$$\boldsymbol{G} : \begin{cases} T_{\boldsymbol{X}}\mathcal{B}_0 \to T^*_{\boldsymbol{X}}\mathcal{B}_0 \\ \boldsymbol{T} \quad\;\; \mapsto \boldsymbol{A} = \boldsymbol{G}\boldsymbol{T} \end{cases} \quad \text{and} \quad \boldsymbol{g} : \begin{cases} T_{\boldsymbol{x}}\mathcal{B}_t \to T^*_{\boldsymbol{x}}\mathcal{B}_t \\ \boldsymbol{t} \quad\;\; \mapsto \boldsymbol{a} = \boldsymbol{g}\boldsymbol{t}\,. \end{cases} \tag{2.24}$$

By comparison of metric tensors in the reference or current configuration *strain tensors* are defined such that they are zero in the reference state. Common strain measures can be summarized in a reference setting by a set of tensors given by

$$\boldsymbol{E}^{(m)} := \begin{cases} \frac{1}{2}\ln \boldsymbol{C} & \text{for } m = 0 \\ \frac{1}{m}\left[\boldsymbol{C}^{\frac{m}{2}} - \boldsymbol{G}\right] & \text{otherwise} \end{cases} \tag{2.25}$$

with the Cauchy-Green tensor $\boldsymbol{C} = \boldsymbol{F}^T\boldsymbol{F}$ and in a current setting by

$$\boldsymbol{e}^{(m)} := \begin{cases} \frac{1}{2}\ln \boldsymbol{c} & \text{for } m = 0 \\ \frac{1}{m}\left[\boldsymbol{g} - \boldsymbol{c}^{\frac{m}{2}}\right] & \text{otherwise}\,. \end{cases} \tag{2.26}$$

with $\boldsymbol{c} = \boldsymbol{F}^{-T}\boldsymbol{F}^{-1}$. These strain measures are nonlinear functions of the stretch. Often used strain tensors are obtained by setting $m = 2$. Therewith, the *Green strain tensor* and the *Almansi strain tensor* are identified in the reference and current configuration, respectively, as

$$\boldsymbol{E} = \tfrac{1}{2}[\boldsymbol{C} - \boldsymbol{G}] \quad \text{and} \quad \boldsymbol{e} = \tfrac{1}{2}[\boldsymbol{g} - \boldsymbol{c}]\,. \tag{2.27}$$

Evolution of Kinematic Objects. To describe the evolution of kinematic objects in time, the *material velocity gradient* and the *spatial velocity gradient*[4] are defined as

$$\boldsymbol{L} = \dot{\boldsymbol{F}} \quad \text{and} \quad \boldsymbol{l} = \dot{\boldsymbol{F}}\boldsymbol{F}^{-1}\,. \tag{2.28}$$

A split of $\boldsymbol{gl}$ in its symmetric and skew parts yields the spatial *rate-of-deformation tensor* $\boldsymbol{d}$ and *spin tensor* $\boldsymbol{w}$

$$\boldsymbol{d} := \operatorname{sym}[\boldsymbol{gl}] = \frac{1}{2}[\boldsymbol{gl} + \boldsymbol{l}^T\boldsymbol{g}] \quad \text{and} \quad \boldsymbol{w} := \operatorname{skew}[\boldsymbol{gl}] = \frac{1}{2}[\boldsymbol{gl} - \boldsymbol{l}^T\boldsymbol{g}] \tag{2.29}$$

such that $\boldsymbol{l} = \boldsymbol{d} + \boldsymbol{w}$.

2.5.2. Fundamental Stress Measures

Before introducing the classical balance laws of continuum mechanics a definition of a stress term is required. In order to make stresses inside of a body visible, Euler's cut principle is used, which is illustrated in Figure 2.21. Therefore, an arbitrary part $\mathcal{P}_0 \subseteq \mathcal{B}_0$ is "cut out" of a referential domain $\mathcal{B}_0$ as well as the corresponding deformed spatial part $\mathcal{P}_t \subseteq \mathcal{B}_t$. Mechanical influences of the rest of the body $\mathcal{B}_t \setminus \mathcal{P}_t$ on the cutout part $\mathcal{P}_t$ are replaced by the mechanical surface traction $\boldsymbol{t}(\boldsymbol{x}, t; \boldsymbol{n})$. It acts in the current configuration and is a function of the position $\boldsymbol{x}$ and the local orientation of the cut represented by the spatial outward normal vector $\boldsymbol{n}$ on an area element $da \subset \partial\mathcal{P}_t$ of the spatial surface.

[3] Since the developed modeling framework of coupled diffusion and crystal plasticity is completely set up in the Cartesian system, metric tensors $\boldsymbol{G}$ and $\boldsymbol{g}$ are collapsed to unity tensor in the following chapters.

[4] Note, that the spatial velocity gradient $\boldsymbol{l}$ is often denoted in literature with an upper case letter $\boldsymbol{L}$, even if it is in the current configuration.

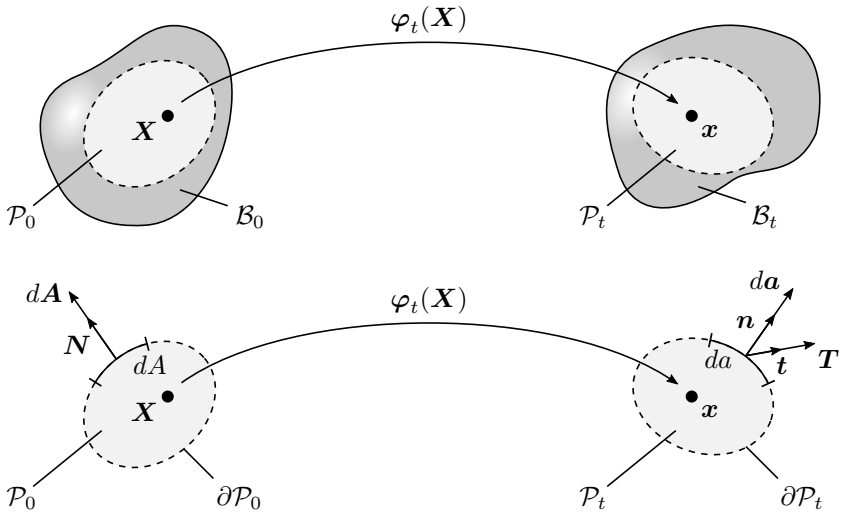

Figure 2.21: Euler's cut principle to visualize stresses inside of a body. Material and spatial parts $\mathcal{P}_0$ and $\mathcal{P}_t$ are cut out the body in the reference configuration $\mathcal{B}_0$ and current configuration $\mathcal{B}_t$. The mechanical action of the rest of the body is substituted by the traction vector $\boldsymbol{t}(\boldsymbol{x}, t; \boldsymbol{n})$ attached to the surface $\partial\mathcal{P}_t$ of the cutout.

Cauchy Stress. A linear relation between the mechanical surface traction $\boldsymbol{t}$ and the normal vector $\boldsymbol{n}$ is postulated by *Cauchy's theorem*

$$\boldsymbol{t}(\boldsymbol{x}, t; \boldsymbol{n}) := \boldsymbol{\sigma}(\boldsymbol{x}, t)\boldsymbol{n}\,, \tag{2.30}$$

where $\boldsymbol{\sigma}$ is the *Cauchy stress tensor* or *true stress*. It relates the current contact force to the deformed unit spatial area da, thus, holding the basic physical meaning of stress. There are other formulations of stress tensors which have proofed to be more convenient for modeling purposes.

Kirchhoff Stress. The *Kirchhoff stress* is obtained by weighting $\boldsymbol{\sigma}$ with the volume map $J = \det[\boldsymbol{F}]$ as

$$\boldsymbol{\tau}(\boldsymbol{x}, t) := J\boldsymbol{\sigma}(\boldsymbol{x}, t)\,. \tag{2.31}$$

Both stress tensors are purely objects of the current configuration mapping spatial normals onto spatial tangents

$$\boldsymbol{\sigma} : \begin{cases} T^*_{\boldsymbol{x}}\mathcal{B}_t \to T_{\boldsymbol{x}}\mathcal{B}_t \\ \boldsymbol{n} \quad \mapsto \boldsymbol{t} = \boldsymbol{\sigma}\boldsymbol{n} \end{cases} \quad \text{and} \quad \boldsymbol{\tau} : \begin{cases} T^*_{\boldsymbol{x}}\mathcal{B}_t \to T_{\boldsymbol{x}}\mathcal{B}_t \\ \boldsymbol{n} \quad \mapsto J\boldsymbol{t} = \boldsymbol{\tau}\boldsymbol{n}\,. \end{cases} \tag{2.32}$$

First and Second Piola-Kirchhoff Stress. A nominal traction vector $\boldsymbol{T}$ parallel to $\boldsymbol{t}$ is introduced, that measures the current force per undeformed unit reference area dA, where $\boldsymbol{T}dA = \boldsymbol{t}da$. Similar to Cauchy's theorem the *first Piola-Kirchoff stress* $\tilde{\boldsymbol{P}}(\boldsymbol{X}, t)$ relates this nominal traction vector to the outward reference unit normal $\boldsymbol{N}$ on $\partial\mathcal{P}_0$ by

$$\boldsymbol{T}(\boldsymbol{X}, t; \boldsymbol{N}) := \tilde{\boldsymbol{P}}(\boldsymbol{X}, t)\boldsymbol{N}\,. \tag{2.33}$$

$\tilde{\boldsymbol{P}}$ is also called *nominal stress* and is often used for experimental analysis, for instance in tensile tests of metals, since the undeformed are of the tensile sample is a priori known

and the current force is easy to determine. While the Cauchy and Kirchhoff stress tensors are symmetric one-point tensors, the first Piola-Kirchhoff stress is unsymmetric and a two-point tensor field which can be written as mapping

$$\tilde{\boldsymbol{P}} : \begin{cases} T^*_{\boldsymbol{X}}\mathcal{B}_0 \to T_{\boldsymbol{x}}\mathcal{B}_t \\ \boldsymbol{N} \quad \mapsto \boldsymbol{T} = \tilde{\boldsymbol{P}}\boldsymbol{N} \,. \end{cases} \tag{2.34}$$

The first Piola-Kirchhoff stress can be transformed into the other stress tensors by

$$\tilde{\boldsymbol{P}} = \boldsymbol{\tau}\boldsymbol{F}^{-T} = J\boldsymbol{\sigma}\boldsymbol{F}^{-T} \,. \tag{2.35}$$

Often, a modified representation of $\tilde{\boldsymbol{P}}$ is used reading $\boldsymbol{P} = \boldsymbol{g}\tilde{\boldsymbol{P}}$. For a Cartesian system the metric $\boldsymbol{g}$ is reduced to the identity tensor $\boldsymbol{I}$ such that no distinction is made between the two representations and in the following chapters the first Piola-Kirchhoff tensor is denoted with $\boldsymbol{P}$. By multiplying $\tilde{\boldsymbol{P}}$ by $\boldsymbol{F}^{-1}$ the *second Piola-Kirchhoff* stress tensor is obtained

$$\boldsymbol{S} = \boldsymbol{F}^{-1}\tilde{\boldsymbol{P}} = \boldsymbol{F}^{-1}\boldsymbol{\tau}\boldsymbol{F}^{-T} = J\boldsymbol{F}^{-1}\boldsymbol{\sigma}\boldsymbol{F}^{-T} \,, \tag{2.36}$$

which is the pull back of the Kirchhoff stress, purely in a reference setting, with the mapping property

$$\boldsymbol{S} : \begin{cases} T^*_{\boldsymbol{X}}\mathcal{B}_0 \to T_{\boldsymbol{X}}\mathcal{B}_0 \\ \boldsymbol{N} \quad \mapsto \boldsymbol{F}^{-1}\boldsymbol{T} = \boldsymbol{S}\boldsymbol{N} \,. \end{cases} \tag{2.37}$$

An overview of the mapping properties of all defined stress tensors is given on the left hand side of Figure 2.22.

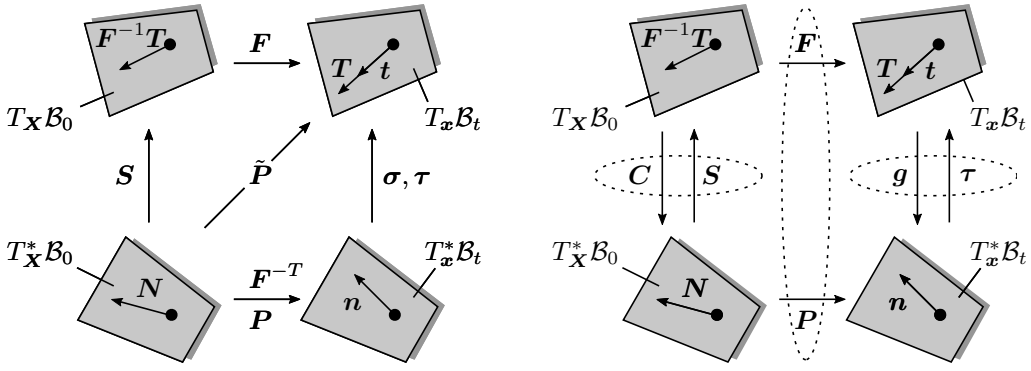

Figure 2.22: Mapping properties of stress tensors are depicted on the left. $\boldsymbol{\sigma}$, $\boldsymbol{\tau}$, $\tilde{\boldsymbol{P}}$, $\boldsymbol{P}$ and $\boldsymbol{S}$ are related by the tangent and normal mapping. The stress power $\mathcal{P}$ can be defined in terms of dual objects $(\boldsymbol{P}, \boldsymbol{F})$, $(\boldsymbol{S}, \boldsymbol{C})$ or $(\boldsymbol{\tau}, \boldsymbol{g})$, which are indicated by dotted lines on the right.

Stress Power of Dual Objects. The *stress power* $\mathcal{P}$ per unit volume in the reference configuration provides an interpretation of the stress tensors and their dual strain tensors,

$$\mathcal{P} = \boldsymbol{P} : \dot{\boldsymbol{F}} = \boldsymbol{S} : \tfrac{1}{2}\dot{\boldsymbol{C}} = \boldsymbol{\tau} : \tfrac{1}{2}\,\pounds_{\boldsymbol{v}}\boldsymbol{g} \,, \tag{2.38}$$

where $\boldsymbol{\pounds}_{\boldsymbol{v}}$ is the Lie-derivative

$$\boldsymbol{\pounds}_{\boldsymbol{v}}(\cdot) := \boldsymbol{\varphi}_* \left[\frac{d}{dt} \boldsymbol{\varphi}^*(\cdot) \right] . \tag{2.39}$$

The dual objects, illustrated on the right side of Figure 2.22, are $(\boldsymbol{P}, \boldsymbol{F})$ in the two-point setting fundamental in non-linear continuum mechanics, $(\boldsymbol{S}, \boldsymbol{C})$ in the Lagrangian setting often used for complex anisotropic models and $(\boldsymbol{\tau}, \boldsymbol{g})$ in the Eulerian setting suitable for sparse matrix implementation in context of finite element analysis.

2.5.3. Physical Balance Principles

The following physical balance principles must hold for every material and do not depend on any material parameters. Evaluating these statements in a cut out part $\mathcal{P}_t$ of the deformed body yields global statements of the balance laws. Since they must be valid for the whole body as well as every arbitrary part of it, the global forms can be localized to local balance principles holding at arbitrary positions of the spatial configuration $\boldsymbol{x} \in \mathcal{B}_t$. Alternatively the local expression can be formulated with respect to an arbitrary reference positions $\boldsymbol{X} \in \mathcal{B}_0$.

Balance of Mass. The conservation of mass demands that the total mass of the body $\mathcal{P}_t$ remains constant over time, provided, that no flux of mass over the surface $\partial\mathcal{P}_t$ takes place and no mass production occurs. The density in the current configuration reads $\rho(\boldsymbol{x}, t)$ and in the reference configuration $\rho_0(\boldsymbol{X})$. Since the total mass $\mathcal{M}_{\mathcal{P}_t}$ must be constant over time and hence, must be identical to the mass in the reference configuration $\mathcal{M}_{\mathcal{P}_0}$

$$\mathcal{M}_{\mathcal{P}_t} = \mathcal{M}_{\mathcal{P}_0} , \tag{2.40}$$

the global mass balance reads

$$\frac{d}{dt} \mathcal{M}_{\mathcal{P}_t} = \frac{d}{dt} \int_{\mathcal{P}_t} \rho \, dv = 0 . \tag{2.41}$$

Therewith, the material and spatial local statements of the balance of mass are obtained as

$$J\rho = \rho_0 \quad \text{and} \quad \dot{\rho} + \rho \, \mathrm{div}[\boldsymbol{v}] = 0 , \tag{2.42}$$

where $\boldsymbol{v}(\boldsymbol{x}, t)$ is the spatial velocity and $\mathrm{div}[\cdot]$ the spatial divergence of a quantity $(\cdot)$.

Balance of Linear Momentum. The balance of linear momentum requires the change of the linear momentum $\mathcal{I}_{\mathcal{P}_t}$ over time of an arbitrary subregion to be equal to the resulting force $\mathcal{F}_{ext}$ acting on that region. A mass specific body force $\boldsymbol{b}(\boldsymbol{x}, t)$ is introduced together with a surface traction $\boldsymbol{t}(\boldsymbol{x}, t)$. The global form reads

$$\frac{d}{dt} \mathcal{I}_{\mathcal{P}_t} = \frac{d}{dt} \int_{\mathcal{P}_t} \rho \boldsymbol{v} \, dv = \int_{\mathcal{P}_t} \rho \boldsymbol{b} \, dv + \int_{\partial\mathcal{P}_t} \boldsymbol{t} \, da = \mathcal{F}_{ext} . \tag{2.43}$$

Applying Gauss' theorem and using the localization theorem yields the material and spatial local forms of the balance of linear momentum

$$\rho_0 \dot{\boldsymbol{V}} = \rho_0 \boldsymbol{b} + \mathrm{Div}[\boldsymbol{P}] \quad \text{and} \quad \rho \dot{\boldsymbol{v}} = \rho \boldsymbol{b} + \mathrm{div}[\boldsymbol{\sigma}] , \tag{2.44}$$

where $\boldsymbol{V}(\boldsymbol{X}, t)$ is the material velocity and $\mathrm{Div}[\cdot]$ the material divergence of a quantity $(\cdot)$.

Balance of Angular Momentum. The balance of angular momentum postulates the temporal change of the angular momentum $\mathcal{D}^{\mathcal{O}}_{\mathcal{P}_t}$ with respect to the origin $\mathcal{O}$ of a fixed coordinate system to be equal to the resultant torque $\mathcal{M}^{\mathcal{O}}_{ext}$ acting on the body. The global form is defined by

$$\frac{d}{dt}\mathcal{D}^{\mathcal{O}}_{\mathcal{P}_t} = \frac{d}{dt}\int_{\mathcal{P}_t} \boldsymbol{x} \times \rho \boldsymbol{v}\, dv = \int_{\mathcal{P}_t} \boldsymbol{x} \times \rho \boldsymbol{b}\, dv + \int_{\partial \mathcal{P}_t} \boldsymbol{x} \times \boldsymbol{t}\, da = \mathcal{M}^{\mathcal{O}}_{ext}\,. \tag{2.45}$$

The local forms of the angular momentum balance result in

$$\boldsymbol{\sigma}^T = \boldsymbol{\sigma} \quad , \quad \boldsymbol{\tau}^T = \boldsymbol{\tau} \quad , \quad \boldsymbol{P}\boldsymbol{F}^T = \boldsymbol{F}\boldsymbol{P}^T \quad \text{and} \quad \boldsymbol{S}^T = \boldsymbol{S}\,, \tag{2.46}$$

inducing symmetry conditions for the Cauchy stress, Kirchhoff stress and second Piola-Kirchhoff stress. The first Piola-Kirchhoff stress is not symmetric but follows the above stated property.

Laws of Thermodynamics. For the sake of completeness, material modeling must satisfy at all time the first law of thermodynamics, also called the *energy balance*, as well as the second law of thermodynamics, called the *entropy inequality principle*.

3. Solution Strategy and Modeling Approach

Key elements of the simulative procedure for a crack initiation lifetime prediction of a ferritic steel under hydrogen atmosphere are highlighted in this chapter. A simulative method for fatigue damage assessment in metallic materials subjected to hydrogen impact is proposed. The method includes the necessary experimental investigations, the numerical model framework, the fatigue prediction scheme and the evaluation of the results. The ambition of this thesis lies in the development of a cross-scale model to describe large strain mechanical deformation on a microstructural informed domain with coupled hydrogen transport. Furthermore, numerically determined micromechanical stresses and strains are used to estimate the material's lifetime to crack initiation under the influence of hydrogen. The developed model should provide a tool which allows a reliable assessment of the fatigue behavior for metallic materials. Numerical studies and the possibility of microstructural variations in combination with the application of different boundary conditions should give an insight on their effect towards diffusion and fatigue phenomena. Validity and plausibility of the proposed model are checked by comparison with experimental results. An overview of the entire framework is illustrated in Figure 3.1. The single modules are closer described in the following.

Material Characterization. Cutouts of the bar material are used to investigate the microstructure and the underlying grain morphology in terms of electron backscatter diffraction (EBSD) measurements. A description of features and possibilities of this method can be found in Schwartz [167]. Using EBSD data grain size, shape and orientation information are obtained which serve as input quantities for the generation of a representative simulation domain. The model framework derived in this work should be applicable to all metallic materials. To assess the capability of the model, an exemplary steel is chosen. As a potential material for components in the fuel cell system for mobility solutions, such as the hydrogen gas injector, the ferritic steel 1.4003 is considered. It is a stainless steel with good corrosion resistance and a rather ductile material behavior. This exemplary material is used to parametrize and validate the material model.

Simulation Model. A robust and fast model is required which enables the prediction of fatigue crack initiation lifetime respectively cycles under hydrogen atmosphere. The model must be practical and should reduce the experimental effort compared to standard testing methods. The methodology used in this work is based on two existing modeling approaches which had to be coupled. The first one describes material elasto-plastic deformation behavior in the large strain regime under consideration of polycrystal orientations in a phenomenological rate dependent crystal plasticity model. The second module consists of a hydrogen diffusion model calculating the local hydrogen concentration in lattice and trap sites. To allow for an interaction between both model, mechanical quantities are incorporated in the hydrogen transport model which influence the diffusion behavior. The entire model is implemented in a user material framework of ABAQUS and solved numerically by means of finite element analysis. A suitable domain representing the microstructure is required on which the model equations are solved.

Representative Volume Element. Information of the microstructure are used to create a representative volume element (RVE) for the simulation. This volume element should capture all relevant features of the material's structure. To generate such a representative domain, measured grain morphology and the corresponding orientation data can

be directly processed into a RVE. Another possibility starts with a statistical evaluation of the grain morphology which is employed in a synthetic generation of RVEs.

Fatigue Experiments. The simulation model requires a set of material parameters which are taken from literature or obtained from experiments. Therefore, cyclic loading tests are performed on the unnotched samples in air atmosphere. It turned out that testing at three different total strain amplitudes is sufficient to determine all required material parameter for the crystal plasticity model. For a validation of the model additional fatigue experiments at more different strain amplitudes are carried out in both air and hydrogen atmosphere. Therewith a general study of the differences in the material response in both environments is possible.

Fatigue Prediction Scheme. A micromechanical fatigue prediction concept for crack initiation based on fatigue indicator parameter (FIP) is introduced and adapted for the investigated material. A new formulation for a hydrogen dependent FIP is proposed, modeling the effect of local hydrogen on the evolution of fatigue in the material.

Validation Procedure. A comparison of experimental LCF data and simulative predicted lifetimes to crack initiation enables a validation of the proposed modeling framework. Numerical studies varying microstructural features and boundary conditions serve not only to investigate the model's sensitivity to certain parameters or application cases but also for further comparison with known experiences, if available.

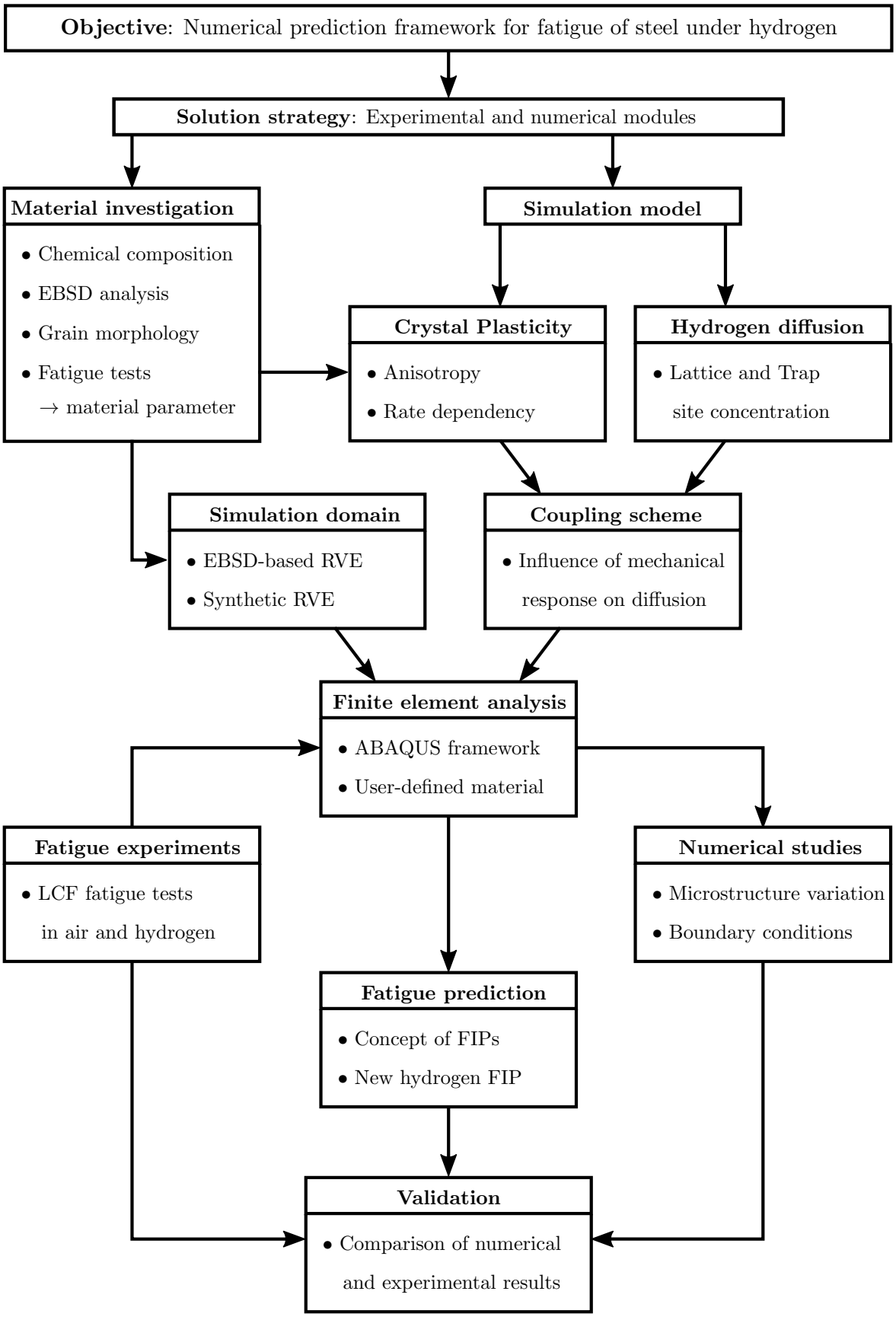

Figure 3.1: Solution strategy for this thesis with experimental and simulative key modules.

4. Material Characterization of 1.4003

To define characteristics and properties of the investigated ferritic steel, microstructure analysis and mechanical tests under cyclic loadings are performed. Beside the manufacturing process of specimen, the microstructure and grain morphology is investigated by means of electron backscatter diffraction (EBSD). The mechanical testing procedure includes strain controlled fatigue tests performed on unnotched samples. The experiments are conducted in air as well as 10 bar hydrogen atmosphere. Furthermore, concentration and permeation measurements contribute to a better understanding of the hydrogen behavior in the present material.

4.1. Production and Microstructure Analysis

The investigated material is a ferritic stainless steel 1.4003 (EN 1.4003; AISI 3Cr12; UNS S40977; DIN X2CrNi12). It is provided in form of bars (21 mm diameter) produced in a manufacturing process, which includes hot rolling, grinding, cold drawing and annealing for specific magnetic properties. The steel can be applied in electromagnetic components which require distinct ferromagnetic properties. Table 4.1 lists the mean values of the containing alloying elements determined by spark emission spectroscopy by the steel manufacturer. The steel is corrosion-resistant due to the elevated proportion of chromium. Specific values from mechanical tensile tests after ISO 6892-1 characterize the rather ductile material with a yield strength of $R_{p0.2} = 293$ MPa, an ultimate tensile strength of $R_m = 452$ MPa and an elongation at fracture of $A_5 = 43\%$.

	C	Si	Mn	P	S	N	Cr	Ni	Mo
1.4003	0.013	0.67	1.08	0.018	0.021	0.013	11.9	0.43	0.33

Table 4.1: Chemical composition of ferritic stainless steel 1.4003 in %.

Grain Morphology. Going back to Nishikawa & Kikuchi [129], the EBSD analysis is a commonly used method to investigate the microstructure of crystalline or polycrystalline materials such as metals and steels. An EBSD measurement requires a scanning electron microscope (SEM) equipped with an EBSD detector. Here, the analysis was performed with a SEM *Supra 55VP* from *Zeiss*, equipped with the EBSD system *AZtec / Channel 5* from *Oxford-Instruments* at an accelerating voltage of 20 kV. The technique provides an insight in the structure, crystal orientation or phase distribution of the material, see Schwartz et al. [167]. The raw data of such an EBSD measurement is provided for the ferritic steel and is analyzed and visualized with the open source Matlab toolbox MTEX. Further information about MTEX can be found in Bachmann et al. [8]. The EBSD data was taken at the surface of metallographic specimens, cut out of the material bar in longitudinal direction and of the cross section, see Figure 4.1. The position and direction of the specimens becomes important in Section 5.4 for the construction of the representative volume element and the application of boundary condition in the finite element model.

To obtain EBSD data a sample with planar and artifact free surface is placed in the SEM and usually tilted to 70°. An EBSD detector is placed close to the sample, which is pointwise scanned by the electron beam of the SEM. The detector captures a pattern consisting of straight bright bands, so called Kikuchi bands, which are directly related to

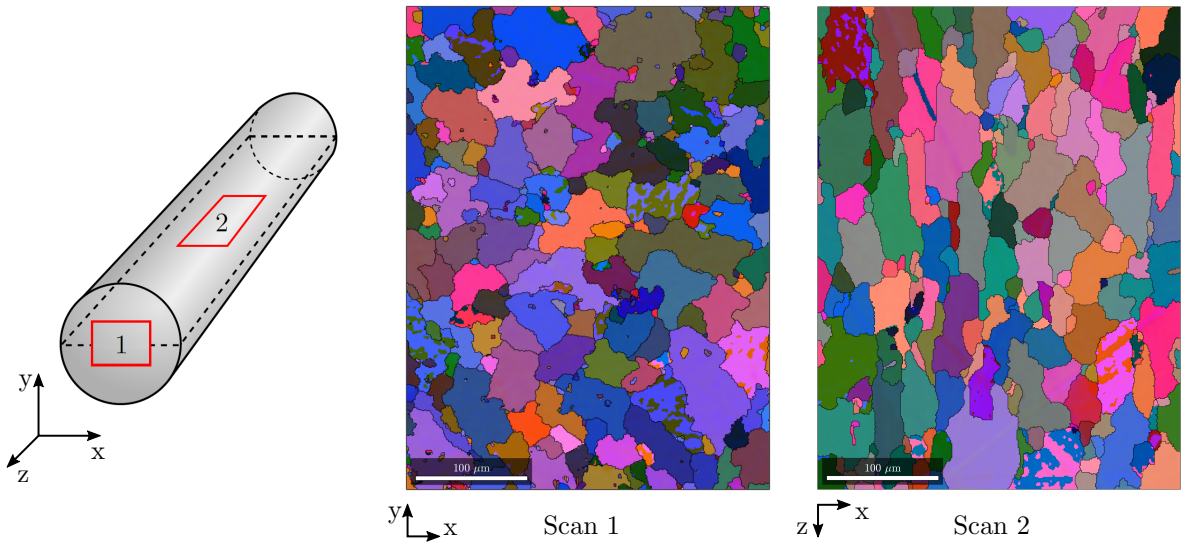

Figure 4.1: EBSD images from ferritic steel 1.4003 taken on a cutout of the bar of the cross section indicated as scan 1 and of the longitudinal direction as scan 2. The color scheme maps the Euler angle to a specific RGB color value, see (4.2).

the lattice planes of the diffracting crystal. Crystallographic phase and orientation can be determined from the geometry of the Kikuchi bands. Here, the crystal orientations are saved in a representation following Bunge [27]. The three Euler angles represent the rotation of the crystal coordinate systems. First rotation of angle ϕ_1 rotates around the z-axis, second rotation of angle Φ around the x-axis and third rotation of angle ϕ_2 rotates again around the z-axis. Restricting the angles to the following intervals

$$0° \leq \phi_1 \leq 360° \quad , \quad 0° \leq \Phi \leq 90° \quad \text{and} \quad 0° \leq \phi_2 \leq 90° \,, \tag{4.1}$$

is sufficient to describe all possible crystal orientations with cubical symmetry. For the visualization of the grain orientation a RGB color scheme is used, relating the angles to a red, green and blue color value $(\phi_1, \Phi, \phi_2)_{\text{Euler}} \rightarrow (R, G, B)$. The three color values are calculated respecting the intervals of (4.1) as

$$R = \frac{\phi_1}{360°} \cdot 255 \quad , \quad G = \frac{\Phi}{90°} \cdot 255 \quad \text{and} \quad B = \frac{\phi_2}{90°} \cdot 255 \,. \tag{4.2}$$

Hence, grains with the same color in Figure 4.1 obtain the same orientation. The step size of both EBSD scans is 1 μm and covers an area of 324×432 μm. EBSD scan 1, taken from the cross section of the bar, shows grains up to a diameter size of 80 μm with a bulged grain shape. Nonmetallic inclusions are only found as manganese sulfides. Scan 2 shows the EBSD data from the metallographic specimen taken out of longitudinal direction. The size of the grains is roughly the same as in scan 1, but they are slightly stretched in the longitudinal direction of the material bar, which might be induced by the hot rolling and cold drawing process.

Texture Analysis. Another property of a polycrystal, which can be investigated with the data of the EBSD analysis, is governed by the distribution of the crystallographic orientations. If all orientations of a sample are entirely random, it has no distinct texture. The presence of preferred orientations results in a texture, which degree depends on the

percentage of crystals having the preferred orientation. The texture has an influence on the mechanical properties. A material with perfectly random distributed orientations has isotropic properties at length scales sufficiently larger than the size of the crystallites. A perfect single crystal exhibits anisotropic properties du to its single orientation.

To visualize the degree of texture of a material, pole figures are often used, in which a distinct crystallographic pole from a representative number of orientations is plotted in a stereographic projection. A detailed description of the projection procedure can be found for example in Gottstein [62]. Figure 4.2 shows the pole figures for the ferritic steel calculated with MTEX from the EBSD data visualized in Figure 4.1. Under consideration of the relevant directions for cubical symmetries, the cross section cutout and the longitudinal cutout are listed in the upper and lower row, respectively. Pole figures of both scans exhibit a slight texture, which may lead to differences in the cyclic deformation properties when the material is loaded in cross or longitudinal direction. Hence, the modeling approach should take the texture into account. Therewith, the relevant features of the microstructure are characterized which are incorporated in the modeling framework. In the following, the material response to mechanical loading is investigated and compared in air and hydrogen pressure atmosphere.

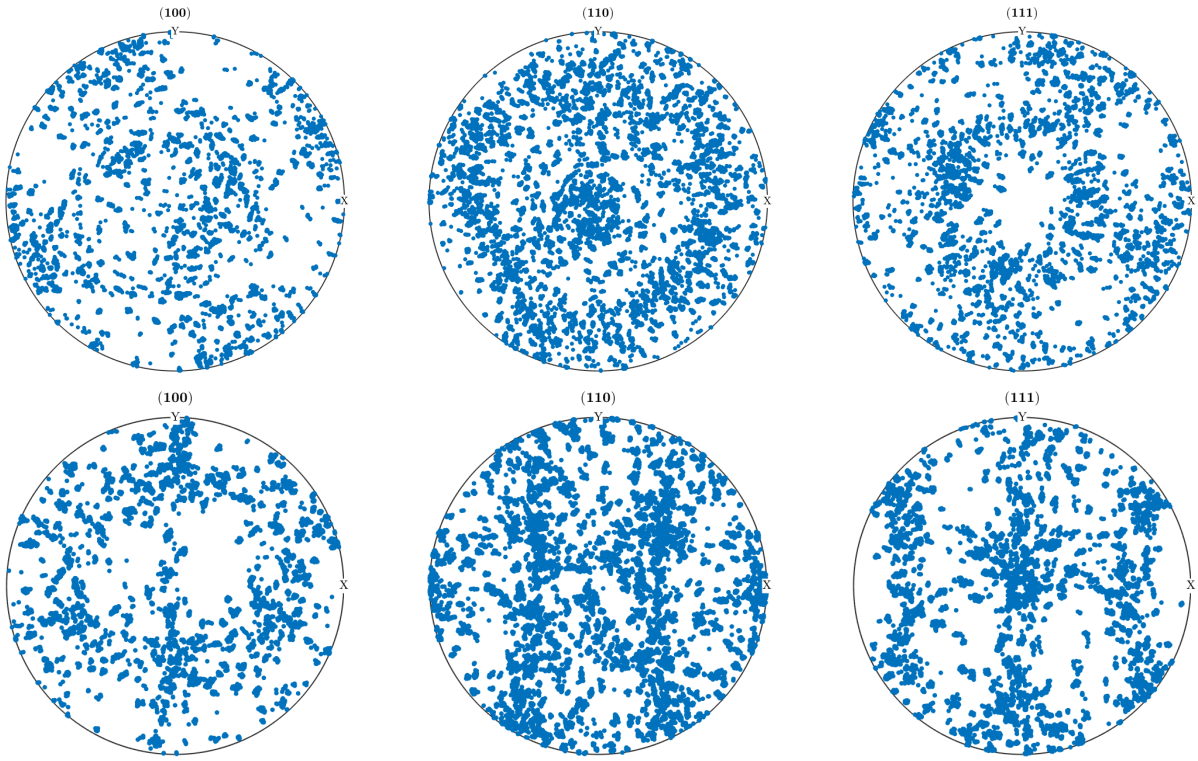

Figure 4.2: Pole figures of metallographic specimens of the cross section on the upper side and of the longitudinal section on the lower side. Each direction contains 5000 representative orientations marked with a dot, drawn from the set of 140 000 total scanning points.

4.2. Macro Fatigue Testing

To compare the material behavior under cyclic loading in air and hydrogen atmosphere, strain controlled fatigue experiments are carried out with unnotched samples.

4.2.1. Experimental Setup

For the fatigue testing, the smooth cylindrical specimens without notches are turned out of the bar material in longitudinal direction for air and hydrogen environment conditions. The specimen geometry with corresponding dimensions in mm as well as an image of one of the ferritic steel samples is shown in Figure 4.3. The conic sample bridge which is the most stressed part of the sample during testing has a surface roughness of maximal $R_Z = 2.5$ μm after the precision turning process step.

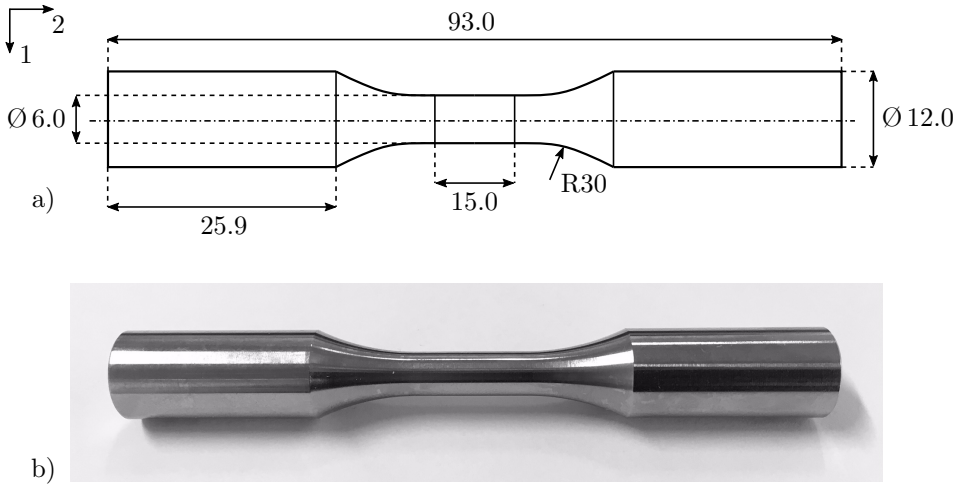

Figure 4.3: Geometry and dimensions in mm of the unnotched fatigue test specimens in a) and an image of the specimen made of the ferritic steel 1.4003 in b).

Cyclic loading tests are conducted at a servo-hydraulic test rig of the Robert Bosch GmbH, see Figure 4.4. The test setup consists of an autoclave system of Moehwald, a load frame PC63N of Instron with a control unit of Zwick in combination with the testing software testXpert II version 1.813.170.118769. To keep exactly track of the strain during strain-controlled experiments, the usage of an extensometer is required, which is build by Sandner Messtechnik GmbH and named as EXA 10-2 O.

The first part of fatigue tests are conducted in normal laboratory air atmosphere, with no further manipulation of the testing environment. This testing condition is referred to as "testing in air" in the following. Further tests referred to as "testing in hydrogen" are carried out in almost pure hydrogen atmosphere. To guarantee the highest gas purity a flushing procedure of the autoclave is applied before each fatigue experiment. After installation of the sample in the tensioning tool, the autoclave is closed airtight and the flushing procedure starts. The process is cycled three times and starts with a nitrogen (N_2) flushing, followed by a hydrogen (H_2) flushing and a subsequent hydrogen pressure build up to $p_{H_2} = 10$ bar. After the third iteration the sample testing is initiated at a constant pressure of 10 bar. To ensure worst-case condition the purity of the hydrogen atmosphere should be higher than at operating condition. Therefore measurements were performed by Linde AG and yield a purity of hydrogen gas of over 99.99%. A detailed description of the measurement is given by Schauer [162], who also used this test rig in his experiments. Within the scope of Schauer [162], the testing procedure was optimized by several experiments and analyses.

The test procedure in both air and hydrogen atmosphere is as follows. Before testing,

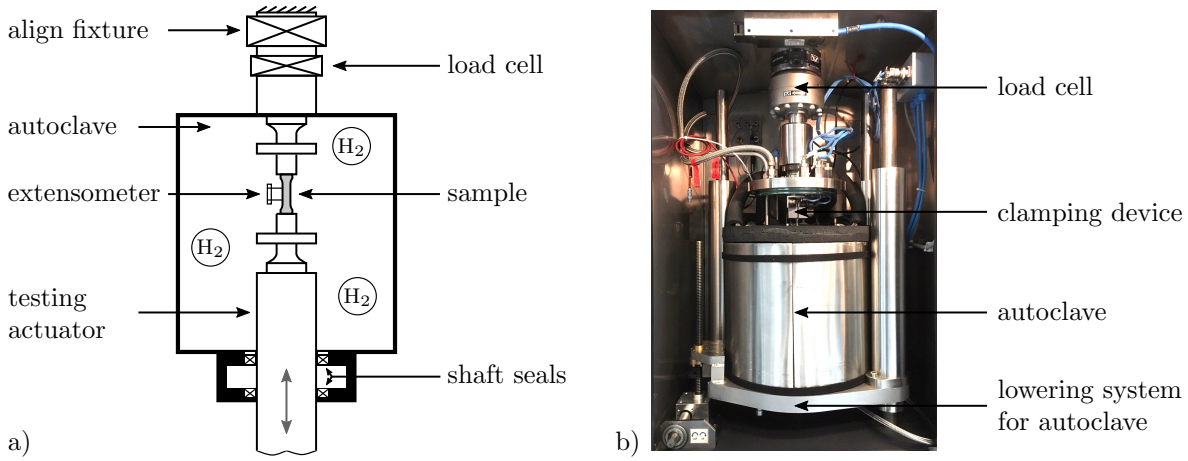

Figure 4.4: Schematic illustration of the hydrogen fatigue test system build up at the Robert Bosch GmbH in a) together with a picture of the closed entire system in b).

the fatigue samples shown in Figure 4.3 b) are cleaned in ultrasonic baths filled with cold cleaning solvent, Cyclohexane and Isopropanol for 6 min, respectively. Thereafter, the sample is installed in the test bench and the test starts either in air or the autoclave is closed and the flushing procedure starts. All fatigue experiments are carried out at room temperature of about 20°C. The loading signal is sinusoidal and the strain ratio is $R_\varepsilon = -1$. As described in Section 2.4.1 a low test frequency is used to ensure enough time for hydrogen related kinetic processes as diffusion and redistribution. Within the range of proposed test frequencies, listed in the norm ANSI/CSA CHMC [36], the frequency is set to $f_{load} = 1$ Hz. To realize an efficient test duration for the high cycle range, the frequency is set to $f_{load} = 5$ Hz after 200 000 cycles. The cycling of the sample ends at the detection of a technical crack initiation indicated by a load drop of 10% of the stabilized condition. If no critical load drop is observed after $N_{cycle} > 1 \cdot 10^6$ the test is stopped and interpreted as *runout* sample with infinity lifetime. After the introduction of all relevant test parameter the reproducibility of the experiments is ensured and the results are presented.

4.2.2. Results of Fatigue Testing

The first experiments in air atmosphere show an unusual material behavior. During the cyclic testing the loading control exhibits an erratic behavior as a response of the strain measurement by the extensometer, instead of a smooth loading. In a certain range of the strain amplitude no differences in the lifetime of the samples can be observed for difference amplitudes $\varepsilon_{a,t} = 0.3\%$ to 1.0%.

Lüders Bands. The reason for this behavior lies in the development of so called *Lüders bands* and can be seen in the static tensile test, Figure 4.5[5]. Plastic deformation during a tensile test starts after the shear stress on possible slip systems exceeds the critical stress required for moving dislocations on these planes. Described in Section 2.1.2 highest shear stresses occur under an angle of 45° to the direction of tension. Since slip systems in some grains of the polycrystal are closer to the 45°-condition, yielding and dislocation move-

[5]Note, that the samples shown in b) are only schematic drawings. For the tensile test the samples shown in Figure 4.3 are used as well.

ment starts earlier in these grains. The question is if this is visible from the macroscopic point of view during the loading. Usually it is not noticeable from the outside, since the sample deforms in general homogeneously. With the first isolated dislocation movements, they start to interact, clash and hinder each other and local work hardening occurs locally. The force applied by the machine will no longer be high enough to move the early dislocations, and with increasing stresses dislocation movement starts elsewhere. Dislocation moving increases from single grains to many grains, to fully plastic deformation everywhere. However, if the dislocation motion is inhibited by interstitial atoms, such as carbon, the above mentioned effect becomes visible. The area in which dislocations are pinned by interstitial atoms is called *Cotrell atmospheres* or *Cotrell clouds*. With increasing loading some dislocations will rip free of these Cotrell atmospheres and move easily as the upper yield strength is reached, see Figure 4.5 stage ①. A localized plastic straining takes place in a band shaped area on the sample, called Lüders band, see Hall et al. [4, 179]. Deformation occurs easily in this region and the machine quickly reduces the applied loading to the lower yield strength to obtain the demanded constant strain rate. The stress raises again after initially freed dislocation get stuck again and hence neighboring dislocations are freed. This leads to the development of a second Lüders band close to the first one, shown in stage ② in Figure 4.5. Now the stress goes down again and so on. As can be seen in Figure 4.5 stage ③, the stress will jump up and down around the lower yield strength until the whole sample is deforming plastically.

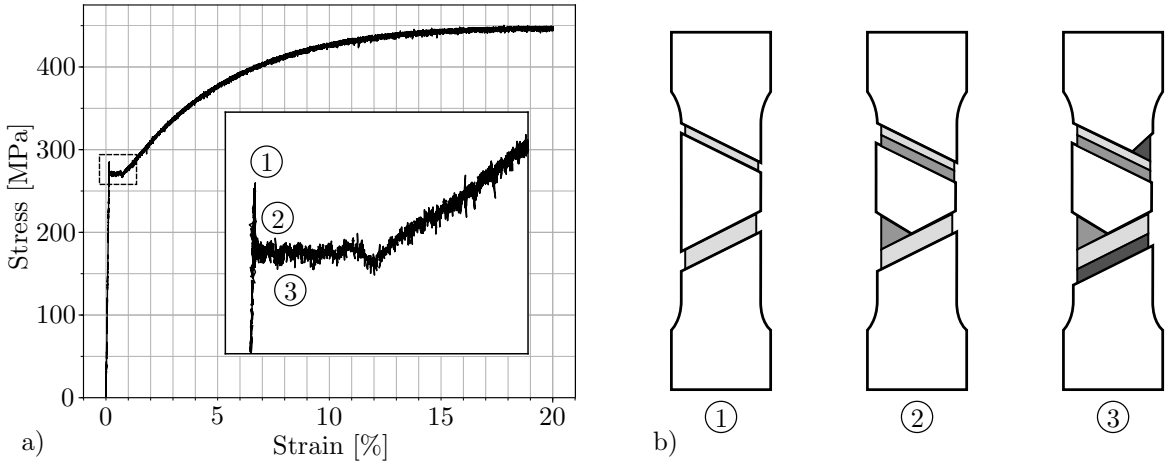

Figure 4.5: Static tensile test of a ferritic 1.4003 specimen up to 20% strain in a) with a zoom to the pronounced yield point (dashed area) where Lüders bands develop. Different stages of Lüders band development is shown in b), which correspond to the numbered stages in a).

Depending on the position of the extensometer on the sample and the initiation location of the Lüders bands, a consistent and reproducible strain tracking is not possible. Laue [92] investigated this phenomenon and proposed solution strategies to overcome this issue. Following his advice, all samples used for the following fatigue tests either in air or hydrogen atmosphere are cyclically preformed at a low strain amplitude of $\varepsilon_{a,t} = 0.2\%$ over 10 000 cycles. An exception are the tests performed at the two lowest strain amplitudes of 0.15% and 0.2%, where no pre-cycling is performed, since the samples never exceed a critical stress level where Lüders bands could initiate.

Cyclic Deformation Curve. To understand the cyclic deformation behavior of the investigated material the cyclic deformation curve introduced in Section 2.2.1 is depicted in Figure 4.6 for the data gathered during the fatigue testing at room temperature in air a) and under $p_{H_2} = 10$ bar hydrogen atmosphere in b). The maximum and minimum stress in loading direction are plotted against the normalized lifetime for the LCF tests at $R_\varepsilon = -1$ with constant total strain amplitudes $\varepsilon_{a,t}$. In general it is obvious that the curves in air and hydrogen atmosphere exhibit a very similar deformation behavior with only slight deviations. These deviations may be traced back to variations in the specimens due to the manufacturing or microstructural differences. During the first stage of their lifetime, either a hardening for the lower strain amplitudes or a softening behavior for the higher amplitudes is observed for both testing environments. An explanation for this given in the precycling procedure which was only applied to amplitudes greater than 0.2%. After the initial phase, all samples enter a stage of constant maximum and minimum stresses which dominate the subsequent lifetime. The proportion between the first stage and the stable condition is sufficiently small, to neglect the initial phase in the following fatigue modeling approach. Following Christ [38], cyclic stable material conditions indicated by almost horizontal maximum and minimum stress curves in Figure 4.6 represent the dominating part of the material's lifetime and set the basis for fatigue calculations. The end of the fatigue test is indicated by a drop in the stress curve towards zero stress which marks the stage of fatigue damage. As the maximum stress curve and its minimum counterpart in air a) are almost perfectly symmetric around the zero stress axis, vertical displacements of both curves are visible in b). The reason for this is the difficult handling of the samples and the fixation of the extensometer during testing under hydrogen within the framework of the autoclave. Resetting the extensometer after the precycling process might have lacked in precision.

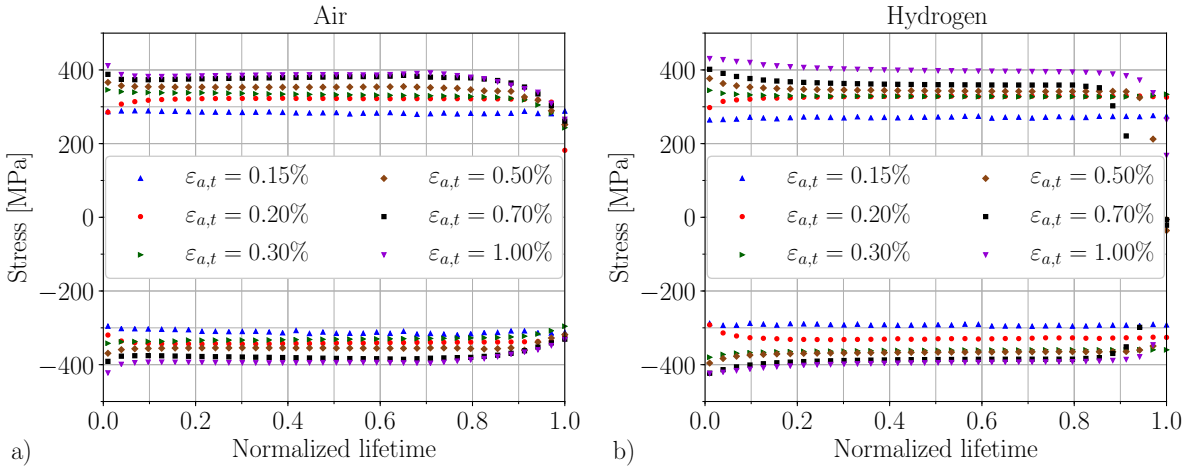

Figure 4.6: Cyclic deformation curve describing the maximal and minimal stresses over the normalized lifetime at different strain amplitudes for cyclic testing at room temperature under air a) and hydrogen b) atmosphere at $p_{H_2} = 10$ bar.

Stress-Strain Hysteresis. Selected stress-strain hystereses for each strain amplitude are plotted in Figure 4.7 for air in a) and hydrogen in b). The material response to cyclic loading is taken at the half of the total lifetime of the sample (normalized lifetime = 0.5). In the subsequent modeling approach the hystereses are the basis for the determination

of cyclic hardening material parameter. Thus, a comparison of the material behavior in air and hydrogen atmosphere is necessary to find out if the macroscopic hardening behavior is influenced by the hydrogen. Figure 4.8 compares both the hystereses in air

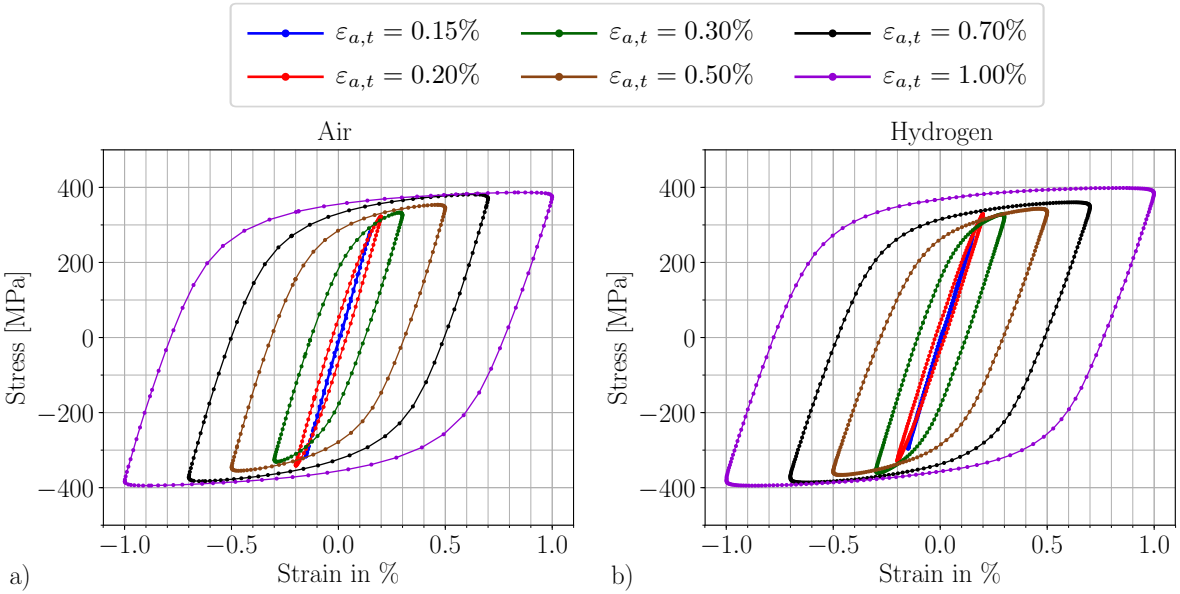

Figure 4.7: Cyclic stress-strain hystereses for air a) and hydrogen b) atmosphere taken at the half of the fatigue lifetime, which is within the saturated stage of Figure 4.6.

and under hydrogen atmosphere and reveals a predominant concordance of the two data sets. Hence, one single parameter set should be sufficient for the modeling by means of crystal plasticity to capture the material response to cyclic loading in both environments.

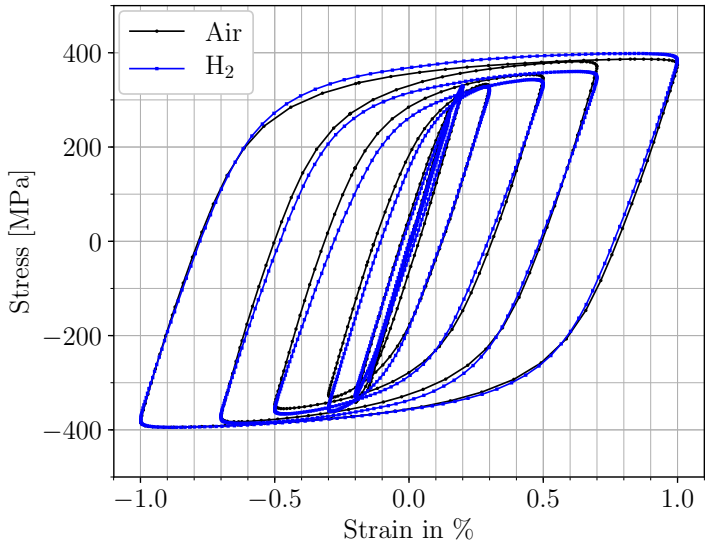

Figure 4.8: Direct comparison of stress-strain hystereses in air atmosphere (black lines with round markers) and hydrogen atmosphere (blue line with quadratic markers).

Strain-based Wöhler curve. The impact of the hydrogen on the lifetime can be seen in the strain-cycle curve. Following Manson, Coffin and Morrow as introduced in Section 2.2.3 the partition in an elastic and a plastic strain contribution yields the total strain-cycle curve by adding both terms. The curves resulting from the strain-controlled fatigue experiments are shown in Figure 4.9 for air a) and hydrogen b). The ferritic steel 1.4003 exhibits a comparable elastic strain portion (red line) for both environments, while the plastic strain proportion (orange line) is significantly lowered under hydrogen influence. This difference becomes smaller at lower strain amplitudes, hence higher cycle numbers. Compared to results of SCHAUER [162], who investigated different ferritic steels under the same testing conditions, the experimental findings agree very well to a similar ferrite 1.4005. Therefore the testing method and procedure proves itself to be reproducible and accurate. For the sake of time effectiveness all samples over a cycle number of $N_{cycle} > 1 \cdot 10^6$ are denoted as runouts and stopped eventually without indicating signs of failure.

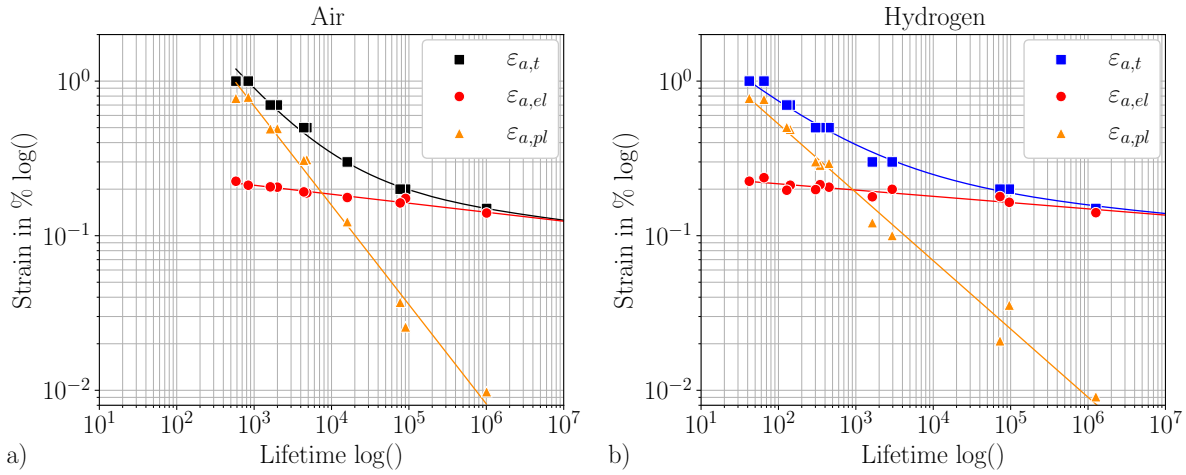

Figure 4.9: Strain-based Wöhler curve after Manson, Coffin and Morrow for air a) and hydrogen b) plotting the total, elastic and plastic strain portion over the total lifetime in a double logarithmic plot.

Focusing on the effect of hydrogen on the fatigue lifetime, a direct comparison is drawn in Figure 4.10. No influence of hydrogen on the fatigue behavior is observable for total strain amplitudes $\varepsilon_{a,t} \leq 0.2\%$. The experimental data points overlap each other. With increasing total strain amplitude for the cyclic loading, a considerable reduction of the fatigue lifetime is visible. From a strain amplitude $\varepsilon_{a,t} \geq 0.3\%$ a reduction up to one decade of the total lifetime takes place under hydrogen. Taking into account Figures 4.6 and 4.8 no influence on the cyclic softening or hardening behavior is visible. The failure of the sample take place without notable decrease or increase in the maximum or minimum stress response per cycle.

With only two tested samples per load level a sparse statistic basis is given for an experimental strain-cycle curve. The complex, time-consuming and expensive testing procedure is the reason for this limited testing program. However, only small variation in all measured data points speak in favor of the validity of these experimental findings. These results not only provide the necessary data to fit the computational material model but also they allow a direct comparison of the simulation results in the subsequent chapters

with measured experimental behavior.

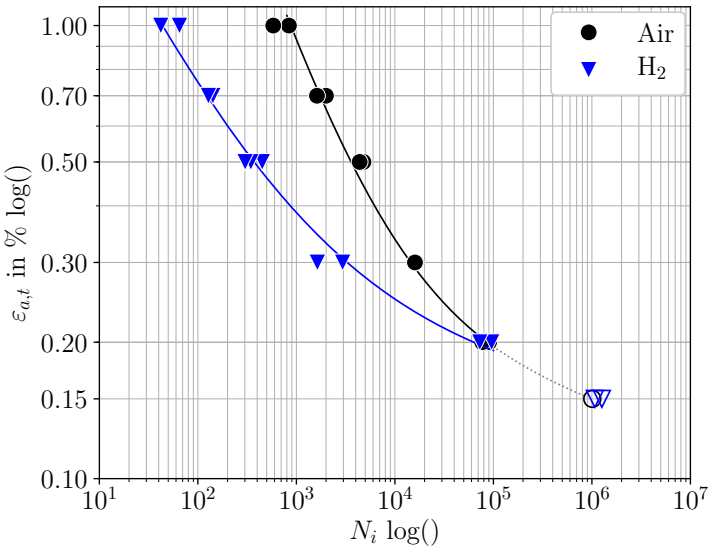

Figure 4.10: Direct comparison of strain-based Wöhler curve in air (black) and hydrogen (blue) showing the impact of hydrogen on the fatigue lifetime at higher total strain amplitudes with decreasing influence at lower total strain amplitudes.

4.3. Permeation Measurements

The determination of local hydrogen concentration in a metal bulk is still an unsolved issue in the hydrogen research community. Therefore an experimental validation of simulation models for hydrogen transport in a material is currently not possible. However, the subsequent modeling approach includes diffusion parameter which can be determined by experiments.

The parameter with a major effect on the diffusion behavior is the diffusion coefficient. As shown in Figure 2.15, a wide scatter band contains the diffusivities of ferritic BCC steels, in which alloying elements leads to a reduction of the diffusivity compared to pure α-iron. For the ferritic steel 1.4003 permeation measurements using the Devanathan-Stachurski method following the norm DIN EN ISO 17081 [45] were performed at the Institute for Materials of the Ruhr-University Bochum. Therefore, a sample is cut out the bar material in form of a small disc and clamped in a permeation cell, more precisely in between two individual electrolytic cells filled with electrolyte solution. Hydrogen is produced electrochemically in one cell by cathodic polarization and is adsorbed on the material sample's surface. Hydrogen atoms are then atomically absorbed into the bulk of the investigated material. After the hydrogen diffused through the sample and reached the other cell, which is the anodic counterpart, it is oxidized at a constant potential while tracking the anodic current. This oxidation current is directly proportional to the amount of hydrogen, which is transported through the material over time by diffusion. Here, both cells were filled with a 0.1 mol NaOH solution and the measurements were performed at room temperature. The cathodic hydrogen charging is conducted by applying a charging current of -5 mA/cm^2. The anodic hydrogen oxidation was carried out at a constant potential of 0,336 mV with respect to the reference electrode which is made

of Ag/AgCl. The reference electrodes were positioned with respect to the surface of the material disc by Luggin-Haber capillaries and the counter electrodes on both sides consist of platinum. The results for a cut out in longitudinal direction in terms of the effective diffusion coefficient reads $D_{eff}^{long} = 4.516 \times 10^{-12}\,\mathrm{m^2/s}$ and for a cut out of the cross section $D_{eff}^{cross} = 3.085 \times 10^{-12}\,\mathrm{m^2/s}$. Both values are determined by a time-lag method and their mean value is illustrated in Figure 4.11 together with the diffusivity scatter bands of Figure 2.15. The experimentally determined diffusivity of the investigated steel is located at the lower bound of the scatter band for ferrites.

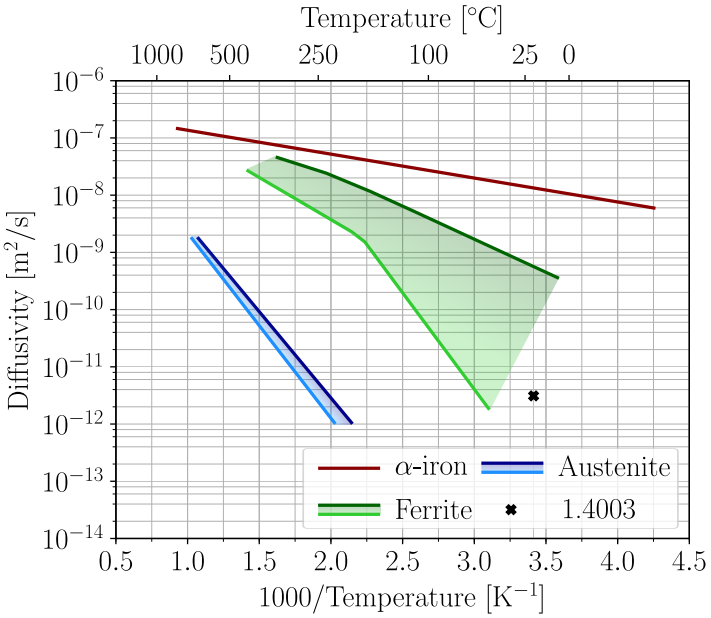

Figure 4.11: Experimentally determined diffusivity of steel 1.4003 together with scatter bands for different steels, see also Figure 2.15.

5. Development of a Coupled Modeling Framework

The numerical model to analyze mechanical quantities used in the subsequent fatigue prediction scheme consists of three main parts. First, a phenomenological crystal plasticity model is introduced which describes the mechanical deformation behavior of polycrystalline materials. In a second part, the hydrogen diffusion in crystalline structures is captured by a hydrogen transport model. Both the crystal plasticity and the hydrogen diffusion model must be coupled to each other and are numerically solved by means of the finite element analysis. This mathematical procedure requires a discretized domain. In a third module, this domain is further specified and identified as a representative volume element of the underlying microstructure.

5.1. Crystal Plasticity Model

Compared to standard plasticity formulations the theory of crystal plasticity explicitly considers slip systems within the crystal lattice to account for plastic slip, dislocation motion and their interactions. It provides a robust framework leading to the development of better phenomenological plasticity models for polycrystalline materials. First crystal plasticity finite element models (CPFEM) go back to Asaro & Rice [7], Asaro & Needleman [6] and Pierce et al. [138] and were continuously enhanced in the subsequent decades through extensions to a polycrystalline arrangement, advanced numeric and homogenization schemes, size effects using phenomenological strain gradient theories and more, see Roters [158] for a detailed revision.

To describe the elasto-plastic material response for polycrystalline steels under cyclic loading, a phenomenological rate-dependent CPFEM model in the large strain regime is used under the assumption of constant temperatures. Hereby, theoretical and numerical aspects are adopted from Meissonnier et al. [112] and Boeff et al. [18, 19]. The model framework and important constitutive equations are introduced in the following.

5.1.1. Continuum Mechanical Framework

A fundamental and physically-based theory of finite plasticity is based on the concept of multiplicative decomposition first proposed by Kröner [89] and Lee [93]. The decomposition assumes that the total deformation gradient $\boldsymbol{F}$ introduced in Section 2.5.1 can be decomposed into an elastic map and plastic map yielding

$$\boldsymbol{F} = \boldsymbol{F}^e \boldsymbol{F}^p \,. \tag{5.1}$$

Herein, $\boldsymbol{F}^e$ describes the reversible distortion of the lattice together with the rigid body rotation of the lattice and $\boldsymbol{F}^p$ describes the plastic part of the total deformation only caused by slip on crystallographic planes. Note, that $\boldsymbol{F}^p$ does not change the crystal lattice orientation even though it can include a rotational part. Furthermore, $\det \boldsymbol{F}^p = J^p = 1$ holds to satisfy inelastic incompressibility. Illustrated in Figure 5.1, the decomposition of the deformation gradient introduces a local intermediate stress-free configuration in between the reference and current configuration. The plastic deformation gradient $\boldsymbol{F}^p$ maps material points from the reference configuration to the intermediate configuration, while the elastic deformation gradient $\boldsymbol{F}^e$ maps points from the intermediate configuration to the current configuration. Note, that this is an abstract concept for the theoretical model, which in general does not correspond to the actual physical deformation sequence.

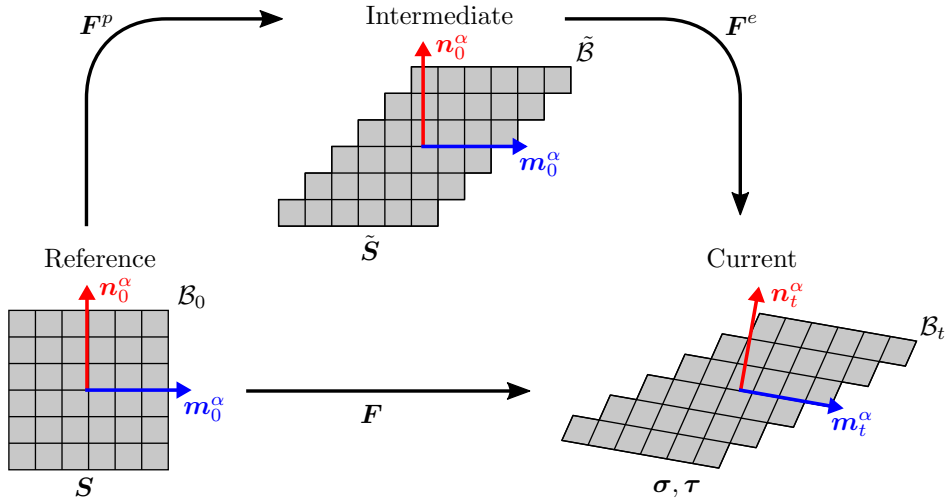

Figure 5.1: Kinematic setting for crystal plasticity with decomposition of the total deformation gradient $\boldsymbol{F}$ into a plastic part $\boldsymbol{F}^p$ and an elastic part $\boldsymbol{F}^e$. Between the reference $\mathcal{B}_0$ and current $\mathcal{B}_t$ configuration a local intermediate configuration $\tilde{\mathcal{B}}$ is introduced.

5.1.2. Schmid's Law

Plastic gliding may occur on a slip system only if the resolved shear stress on that system reaches a critical level. Therefore it is necessary to calculate the resolved shear stress τ^α on each slip system α. By a generalization of the uniaxial formulation of Schmid's law in Section 2.1.2, the stress state described by the Cauchy stress tensor $\boldsymbol{\sigma}$ at a material point is considered. To determine the Cauchy stress vector $\boldsymbol{t}^\alpha$, the applied stress is projected on the glide plane with the glide plane normal $\boldsymbol{n}^\alpha$. The resolved shear stress is determined by projecting the Cauchy stress vector in glide direction $\boldsymbol{m}^\alpha$

$$\boldsymbol{t}^\alpha = \boldsymbol{\sigma}\boldsymbol{n}^\alpha \quad \text{and} \quad \tau^\alpha = \boldsymbol{t}^\alpha \cdot \boldsymbol{m}^\alpha \,. \tag{5.2}$$

Inserting the Cauchy stress vector leads to

$$\tau^\alpha = (\boldsymbol{\sigma}\boldsymbol{n}^\alpha) \cdot \boldsymbol{m}^\alpha = \boldsymbol{\sigma} : (\boldsymbol{m}^\alpha \otimes \boldsymbol{n}^\alpha) = \boldsymbol{\sigma} : \boldsymbol{M}^\alpha \,, \tag{5.3}$$

where $\boldsymbol{M}^\alpha = \boldsymbol{m}^\alpha \otimes \boldsymbol{n}^\alpha$ is the Schmid matrix combining the projection on plane and into slip direction. The resolved shear stress in the finite strain formulation can be defined by the second Piola-Kirchhoff stress in intermediate configuration $\tilde{\boldsymbol{S}}$, see Figure 5.1. The Cauchy stress and the Schmid matrix are pulled back from the current configuration to the intermediate configuration by

$$\boldsymbol{\sigma} = \frac{1}{J^e}\boldsymbol{F}^e \tilde{\boldsymbol{S}} \boldsymbol{F}^{e^T} \tag{5.4}$$

and

$$\boldsymbol{M}^\alpha = \boldsymbol{F}^e \tilde{\boldsymbol{M}}^\alpha \boldsymbol{F}^{e^{-1}} \quad \text{with} \quad \boldsymbol{n}_0^\alpha = \boldsymbol{n}^\alpha \boldsymbol{F}^e \quad \text{and} \quad \boldsymbol{m}_0^\alpha = \boldsymbol{F}^{e^{-1}} \boldsymbol{m}^\alpha \,. \tag{5.5}$$

Since the lattice orientation remains unchanged by $\boldsymbol{F}^p$ the Schmid matrix in the reference and intermediate configuration are identical $\boldsymbol{M}_0^\alpha = \tilde{\boldsymbol{M}}^\alpha$. Here, the notation $\tilde{\boldsymbol{M}}^\alpha$ is only

used to emphasize the intermediate configuration. Inserting relations (5.4) and (5.5) into (5.3) yields

$$\tau^{\alpha} = \frac{1}{J^e} \boldsymbol{F}^{e^T} \boldsymbol{F}^e \tilde{\boldsymbol{S}} : \tilde{\boldsymbol{M}}^{\alpha} \approx \tilde{\boldsymbol{S}} : \tilde{\boldsymbol{M}}^{\alpha} , \tag{5.6}$$

where elastic strain contributions are neglected by making the reasonable assumption that elastic strains are relatively small compared to plastic strains in metallic materials.

5.1.3. Stress Formulation

Following Meissonnier et al. [112] the hyperelastic response of the material in the intermediate configuration is governed by

$$\tilde{\boldsymbol{S}} = \frac{\partial \Phi\{\boldsymbol{E}^e\}}{\partial \boldsymbol{E}^e} , \tag{5.7}$$

where $\Phi\{\boldsymbol{E}^e\}$ is the Helmholtz potential energy of the lattice per unit reference volume and $\boldsymbol{E}^e$ the elastic Green-Lagrange strain in the intermediate configuration defined by

$$\boldsymbol{E}^e = \tfrac{1}{2} \left(\boldsymbol{F}^{e^T} \boldsymbol{F}^e - \boldsymbol{1} \right) . \tag{5.8}$$

Differentiation of (5.7) yields

$$\dot{\tilde{\boldsymbol{S}}} = \mathbb{K} : \dot{\boldsymbol{E}}^e \quad \text{with} \quad \mathbb{K} := \frac{\partial^2 \Phi\{\boldsymbol{E}^e\}}{\partial \boldsymbol{E}^{e2}} . \tag{5.9}$$

Using again the argumentation of small elastic strains for metal materials, the fourth-order tensor $\mathbb{K}$ can be approximated by the anisotropic elastic moduli $\mathbb{C}^e$, introduced in Section 2.1.2. The elastic stress-strain relation then reads

$$\tilde{\boldsymbol{S}} \approx \mathbb{C}^e : \boldsymbol{E}^e . \tag{5.10}$$

5.1.4. Constitutive Formulation and Flow Rule

The time rate of change of the plastic deformation gradient derived from the kinematics of dislocation motion is given by Asaro & Rice [7] under assumption that dislocation gliding is only responsible for plastic deformations

$$\dot{\boldsymbol{F}}^p = \Big(\sum_{\alpha=1}^{N_{Slip}} \dot{\gamma}^{\alpha} \tilde{\boldsymbol{M}}^{\alpha} \Big) \boldsymbol{F}^p . \tag{5.11}$$

Here, the plastic velocity gradient $\tilde{\boldsymbol{L}}_p$ in the intermediate configuration is identified as the sum of all slip rates $\dot{\gamma}^{\alpha}$ on the existing slip systems α

$$\tilde{\boldsymbol{L}}_p = \sum_{\alpha=1}^{N_{Slip}} \dot{\gamma}^{\alpha} \tilde{\boldsymbol{M}}^{\alpha} . \tag{5.12}$$

Since the slip rate is the constitutive variable which drives the crystal plasticity formulation, various physically motivated evolution laws have been defined over the decades. Rice [155], Hutchinson [80] or de Souza Neto et al. [42] describe the evolution of the slip rate with a phenomenological rate-dependent viscoplastic flow rule. With their

method, an iterative procedure to identify active slip systems can be avoided and it helps to stabilize material behavior. They proposed a power law-type constitutive equation for the rate of plastic slip on each slip system

$$\dot{\gamma}^{\alpha} = \dot{\gamma}_0^{\alpha} \left| \frac{\tau^{\alpha}}{\tau_c^{\alpha}} \right|^m \operatorname{sign}(\tau^{\alpha}) \,, \tag{5.13}$$

where τ^{α} is the resolved shear stress on the slip system and τ_c^{α} the critical resolved shear stress. $\dot{\gamma}_0^{\alpha}$ is the reference slip rate and m the power law exponent which are both material properties. The critical resolved shear stress describes the resistance of a slip system against shear deformation. If τ^{α} approaches τ_c^{α}, the slip rate $\dot{\gamma}^{\alpha}$ becomes greater than zero.

5.1.5. Hardening Laws

If a solid is plastically deformed, then unloaded, and then it is tried to be re-load to induce further plastic flow, its resistance to plastic deformation will have increased. This is known as 'strain hardening'. The physical phenomena behind hardening of crystals are based on dislocation movement and their representation within the continuum setting is complex and remains an open challenge. Therefore purely phenomenological models are used to describe strain hardening. Isotropic hardening for monotonic loading and kinematic hardening for cyclic loading are embedded in the model formulation and explained in the following.

Isotropic Hardening. Isotropic hardening increases the critical resolved shear stress during loading. With every new loading τ_c^{α} increases until a stage is reached that the solid deforms elastically throughout. In terms of dislocation motion this can be described as hardening due to the general presence of dislocations on their own slip systems (self hardening) and their interaction with dislocations on other slip systems (latent hardening). A law for the evolution of critical resolved shear stress for isotropic hardening goes back to Asaro & Needleman [6] and is defined as

$$\dot{\tau}_c^{\alpha} = \sum_{\beta=1}^{N_{Slip}} h_{\alpha\beta} \left| \dot{\gamma}^{\beta} \right| = \sum_{\beta=1}^{N_{Slip}} h_0 \Big(1 - \frac{\tau_c^{\beta}}{\tau_s} \Big)^n M_{\alpha\beta} \left| \dot{\gamma}^{\beta} \right| \tag{5.14}$$

where h_0 is the hardening parameter, n is the hardening exponent and τ_s is the saturated shear stress. This evolution law accounts for interactions among different glide systems via the hardening matrix $M_{\alpha\beta}$. The hardening matrix is defined such that the value for the interaction of coplanar glide systems is $M_{\alpha\beta} = 1.0$ and for the interaction of all other glide systems $M_{\alpha\beta} = 1.4$. Two glide systems α and β are coplanar if their normal vectors $\boldsymbol{n}^{\alpha}$ and $\boldsymbol{n}^{\beta}$ point in the same or opposing direction, thus they must be linear dependent. Both evolution equations (5.13) and (5.14) are widely used for application to monotonic loading conditions. Isotropic hardening predicts that after a few cycles, the solid just hardens until it responds elastically. Hence, it is not able to capture the Bauschinger effect [15], which is observed under cyclic loading conditions, necessary for the investigation of fatigue behavior.

Kinematic Hardening. To overcome this issue kinematic hardening laws have been introduced. To account for the Bauschinger effect correctly, a hardening contribution modifies the resolved shear stress in terms of a resolved backstress χ_b. This backstress

is caused by dislocation pileups on individual glide systems and modifies the constitutive evolution law for the slip rate (5.13) following Cailletaud [28] to

$$\dot{\gamma}^\alpha = \dot{\gamma}_0^\alpha \left| \frac{\tau^\alpha - \chi_b^\alpha}{\tau_c^\alpha} \right|^m \operatorname{sign}(\tau^\alpha - \chi_b^\alpha) \,. \tag{5.15}$$

The evolution of backstress for kinematic hardening is described by the nonlinear hardening model of Frederick & Armstrong [57, 58]

$$\dot{\chi}_b^\alpha = A_1 \dot{\gamma}^\alpha - A_2 |\dot{\gamma}^\alpha| \chi_b^\alpha \,, \tag{5.16}$$

where A_1 and A_2 are material parameter. Note, that these material parameter used in the hardening laws have to be fitted to results of cyclic fatigue experiments, see Section 6.1. In Schäfer et al. [160] a detailed comparison between this formulation and enhanced approaches to capture cyclic hardening effects proposed by Chaboche [32, 33] and Ohno & Wang [131] is drawn. They focus on the ability to account for certain material effects such as mean stress relaxation.

5.1.6. Implementation Scheme

Therewith, the kinematic setting and constitutive equations for the phenomenological rate-dependent CPFEM model are defined. A nontrivial task is the integration of the elasto-plastic equations, which is required for the numerical implementation. The applied integration scheme in this work follows the approach of Meissonnier et al. [112] and Boeff et al. [18]. For more details the reader is referred to Appendix A.

The constitutive material model is embedded in an established numerical solution procedure in terms of the finite element analysis. Theoretical basics of the finite element method (FEM) such as the strong and weak formulation of the mechanical equilibrium condition are omitted here and can be found in literature such as Zienkiewicz [202], Bathe [14] or Schwarz [168]. The appearing global system of nonlinear equations is solved by the implicit solver of ABAQUS, while the constitutive material response on integration point level is defined in a user-defined material (UMAT), which interface is provided by ABAQUS. The UMAT routine has well defined kinematic variables, see Huang [79], and for a given increment of the deformation gradient, an update of the stresses and solution dependent variables[6] (SDVs) is required, explained in detail by Boeff et al. [18]. In order to achieve quadratic convergence of the global Newton-Raphson algorithm to solve the nonlinear system of equations, the consistent material tangent has to be defined in every increment. The crystal plasticity model uses an additional local Newton-Raphson iteration to update the stresses and SDVs simultaneously for every integration point, see Appendix A.2, which is associate with high computational costs.

With this purely mechanical model for crystal plasticity on hand the hydrogen diffusion model is considered in the subsequent section.

5.2. Hydrogen Diffusion Model

The local hydrogen concentration in the metal lattice and trap sites are crucial to model the influence of hydrogen on the fatigue lifetime. Hence, a reliable simulation model should

[6] This terminology is used by ABAQUS. In literature those quantities can also be found as history or internal variables.

capture the physical aspects of hydrogen diffusion into a metal described in Section 2.3.2. A first approach was given by McNabb & Foster [111], who modeled the mobility of hydrogen dissolved in an iron lattice containing traps. Their diffusion equation was solved with terms for sources and sinks. Another today widely used model approach is based on the assumption of Oriani [133] of a local equilibrium between the free diffusible and the trapped atoms for a restricted domain and a specific range of trap binding energy. This idea was later used by Sofronis & McMeeking [173] to formulate a hydrogen transport model coupled with large deformation elastic-plastic behavior. This approach is adapted and used for the coupling with the crystal plasticity model. Theoretical aspect are discussed in the following together with the numerical implementation scheme for a user defined framework of ABAQUS.

5.2.1. Theory of the Transport Model

In the diffusion model the total hydrogen concentration C_{total} in the metal bulk is composed of free diffusible atoms residing on normal interstitial sites and atoms trapped in internal microstructural defects. The hydrogen concentration in the lattice is denoted as C_L and the trapped hydrogen concentration as C_T leading to

$$C_{total} = C_L + C_T \,, \tag{5.17}$$

which holds for every material point. The hydrogen concentration in the lattice sites reads

$$C_L = \beta \theta_L N_L \,, \tag{5.18}$$

where β is the number of interstitial sites per metal atom and θ_L is the fraction of total lattice sites occupied ($0 \leq \theta_L \leq 1$). The number of metal atoms per unit volume for iron can be calculated as

$$N_L = \frac{\rho_{Fe} N_A}{A_{Fe}} = \text{const.} \,, \tag{5.19}$$

with density $\rho_{Fe} = 7.87 \cdot 10^{-3}\,\mathrm{g/mm^3}$, relative atomic mass $A_{Fe} = 55.845\,\mathrm{g/mol}$ and Avogadro's number $N_A = 6.02214 \cdot 10^{-23}\,1/\mathrm{mol}$. Note, that the values of pure α-iron are used to approximate the ferritic steel treated in this work, which both share the BCC crystal structure.

Trap sites are located at microstructural defects such as dislocation cores, grain boundaries and interfaces of particles with the matrix material. However, in this model all trap sites are condensed to one kind of trap site with one binding energy. Approaches to include multiple trap sites are proposed by Toribio & Kharin [183]. Here, the concentration of trapped hydrogen reads

$$C_T = \alpha \theta_T N_T \,, \tag{5.20}$$

where the number of hydrogen atom sites per trap α is set to 1, θ_T is the fraction of total trap sites occupied ($0 \leq \theta_T \leq 1$) and N_T denotes the number of traps per unit lattice volume. Kumnick & Johnson [91] performed permeation tests on pure iron with hydrogen under gaseous loading. They observed a variation in the density of trap sites with plastic deformation of the material, shown in Figure 5.2. A steep increase in the number of trap sites can be observed at lower deformation while a more gradually

increase takes place at higher deformation levels. The experimental data was fitted by Sofronis & McMeeking [173] and is adopted here by the subsequent relation

$$\log N_T(\varepsilon^p) = 23.26 - 2.33\, e^{-5.5\,\varepsilon^p}\,. \tag{5.21}$$

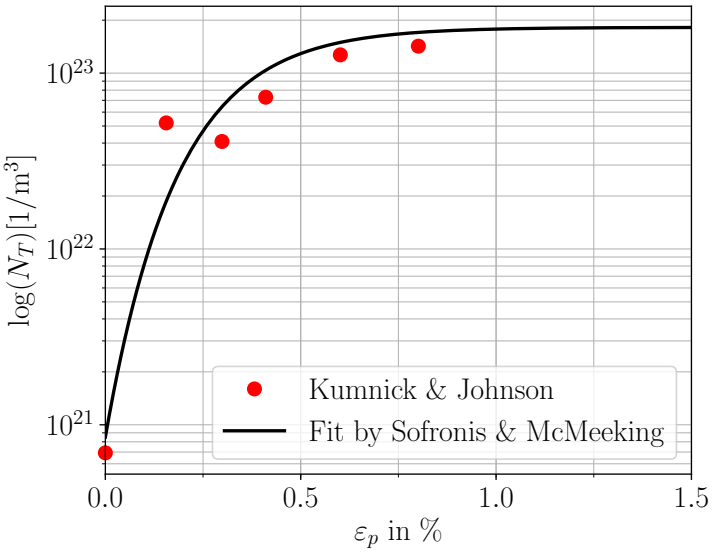

Figure 5.2: Experimental data of Kumnick & Johnson [91] for the evolution of the number of trap sites in pure iron with respect to the equivalent plastic strain marked by dots. The solid line indicates a fitting curve proposed by Sofronis & McMeeking [173] in form of (5.21).

In the following concentration quantities are scaled by the Avogadro constant as proposed by Barrera et al. [12] and expressed in units of mol/mm^3 indicated by a bar over the symbol such as

$$\bar{C}_L = \frac{C_L}{N_A} \quad \text{and} \quad \bar{C}_T = \frac{C_T}{N_A} \tag{5.22}$$

$$\bar{N}_L = \frac{N_L}{N_A} \quad \text{and} \quad \bar{N}_T = \frac{N_T}{N_A}\,. \tag{5.23}$$

Mass conservation relates variation in the hydrogen concentration to fluxes in the material. Assuming no internal sources, the rate of change of the total hydrogen concentration in a volume V must be equal to the flux $\bar{\boldsymbol{J}}$ through the surrounding surface S yielding

$$\frac{d}{dt}\int_V (\bar{C}_L + \bar{C}_T)\,\mathrm{d}V + \int_S \bar{\boldsymbol{J}}\cdot\boldsymbol{n}\,\mathrm{d}S = 0\,, \tag{5.24}$$

where $\boldsymbol{n}$ is the outward normal vector to S. Positive fluxes correspond to hydrogen leaving the volume. The hydrogen flux $\bar{\boldsymbol{J}}$ is presumed to obey Fick's law [54]. It depends on the gradient of the chemical potential μ_L and reads

$$\bar{\boldsymbol{J}} = -\frac{D_L \bar{C}_L}{R_{GS} T}\nabla\mu_L\,, \tag{5.25}$$

where D_L is the lattice diffusion coefficient, $R_{GS} = 8314.46$ (N mm)/(K mol) the universal gas constant and T the temperature. Mobility between trap sites is assumed to be near zero considering only traps with deep energy potential wells, which hinder diffusion from trap to trap. Di Leo & Anand [44] and Díaz et al. [43] propose a formulation including trap mobility. Hence, only lattice diffusivity is taken into account as a contributor to the flux and the chemical potential of hydrogen in lattice sites is defined as

$$\mu_L = \mu_L^0 + R_{GS}T \ln \frac{\theta_L}{1-\theta_L} - \sigma_H V_H \tag{5.26}$$

where μ_L^0 is the chemical potential at standard state. Additionally, the influence of the stress state is taken into account by means of the hydrostatic stress $\sigma_H = \frac{1}{3}\mathrm{tr}[\boldsymbol{\sigma}]$ and a partial molar volume of hydrogen $V_H = 2000$ mm^3/mol for α-iron at around 300 K, see Hirth [74]. Both interstitial sites, tetrahedral and octahedral, are too narrow for the size of a single hydrogen atom. As a consequence, the solute hydrogen atoms cause a volume increase and are in an energetic favorable state at regions with higher hydrostatic stresses, where the lattice is expanded by pure dilatation. The chemical potential of hydrogen in regions of an increased hydrostatic stress is consequently lower. In order to lower the chemical potential hydrogen will diffuse in direction of regions subjected to high hydrostatic stresses. The flux is governed by the hydrostatic stress state of the material as well as the concentration gradient of diffusible hydrogen. By inserting (5.26) into (5.25) the flux is obtained as

$$\bar{\boldsymbol{J}} = \frac{D_L V_H \bar{C}_L}{R_{GS}T} \nabla \sigma_H - D_L \frac{\bar{C}_L}{1-\theta_L} \left(\frac{\nabla \bar{C}_L}{\bar{C}_L} - \frac{\nabla \bar{N}_L}{\bar{N}_L} \right). \tag{5.27}$$

Following Díaz et al. [43] the number of interstitial sites (5.19) is assumed to be constant on the whole domain $\nabla \bar{N}_L = 0$. This simplification is adopted in the model, but it is emphasized, that the number of interstitial sites could vary in reality with the creation of new trap sites. Especially in BCC crystal structures a low occupancy of lattice sites $\theta_L \ll 1$ is expected because the number of interstitial sites by far exceeds the amount of available hydrogen $N_L \gg C_L$. Considering these simplifications and substituting (5.27) into (5.24) the mass balance reads

$$\frac{d}{dt} \int_V (\bar{C}_L + \bar{C}_T)\, \mathrm{d}V + \int_S \left(\frac{D_L V_H \bar{C}_L}{R_{GS}T} \nabla \sigma_H - D_L \nabla \bar{C}_L \right) \cdot \boldsymbol{n}\, \mathrm{d}S = 0\,. \tag{5.28}$$

Using Gauss's theorem and the standard localization argument, the resulting parabolic partial differential equation reads

$$\frac{\partial \bar{C}_L}{\partial t} + \frac{\partial \bar{C}_T}{\partial t} + \nabla \cdot \left(\frac{D_L V_H \bar{C}_L}{R_{GS}T} \nabla \sigma_H \right) - \nabla \cdot (D_L \nabla \bar{C}_L) = 0\,. \tag{5.29}$$

Assuming that the stress state of the material is known, $\bar{C}_L$ and $\bar{C}_T$ remain unknown in equation (5.29). Following the theory of Oriani [133] a chemical equilibrium exists between lattice and trapped hydrogen for a limited domain and a certain range of trap binding energy. The chemical potential for the trapped hydrogen μ_T is analogously defined

to (5.26) and equating both potentials results in

$$\begin{aligned} \mu_T &= \mu_L \\ \mu_T^0 + R_{GS}T \ln \frac{\theta_T}{1-\theta_T} - \sigma_H V_H &= \mu_L^0 + R_{GS}T \ln \frac{\theta_L}{1-\theta_L} - \sigma_H V_H \\ \ln\Big(\frac{\theta_T}{1-\theta_T} - \frac{\theta_L}{1-\theta_L}\Big) &= \frac{\mu_L^0 - \mu_T^0}{R_{GS}T} \\ \frac{\theta_T}{1-\theta_T}\frac{1-\theta_L}{\theta_L} &= \exp\Big(\frac{\mu_L^0 - \mu_T^0}{R_{GS}T}\Big)\,. \end{aligned} \tag{5.30}$$

This equilibrium provides another equation with both concentration variables and hence, allows for the calculation of $\bar{C}_T$ once $\bar{C}_L$ is determined. Recalling the assumption of low lattice occupation ($\theta_L \ll 1$) together with Oriani's equilibrium leads to

$$\frac{\theta_T}{1-\theta_T}\frac{1}{\theta_L} = K = \exp\Big(-\frac{E_b}{R_{GS}T}\Big)\,. \tag{5.31}$$

where K is the equilibrium constant, which is a function of the trap binding energy $E_b = \mu_L^0 - \mu_T^0$, introduced in Section 2.3.2. The concentration in trap sites can now be determined from (5.20) and (5.31) by

$$\bar{C}_T(\bar{C}_L, \bar{N}_T) = \frac{N_T\theta_T}{N_A} = \frac{\bar{N}_T}{1 + \dfrac{1-\theta_T}{\theta_T}} = \frac{\bar{N}_T}{1 + \dfrac{1}{K\theta_L}} = \frac{\bar{N}_T}{1 + \dfrac{\beta\bar{N}_L}{K\bar{C}_L}}\,. \tag{5.32}$$

The evolution in time of the trapped hydrogen concentration required in (5.29) depends on the lattice concentration and the evolution of the trap density (5.21). The density itself depends on the plastic strain determining the rate at which traps are generated. Applying the chain rule to get the time derivative of $\bar{C}_T$ yields

$$\frac{\partial\bar{C}_T}{\partial t} = \frac{\partial\bar{C}_T}{\partial\bar{C}_L}\frac{\partial\bar{C}_L}{\partial t} + \frac{\partial\bar{C}_T}{\partial\bar{N}_T}\frac{\partial\bar{N}_T}{\partial\varepsilon_p}\frac{\partial\varepsilon_p}{\partial t}\,, \tag{5.33}$$

with the following partial derivatives

$$\frac{\partial\bar{C}_T}{\partial\bar{C}_L} = \frac{\bar{C}_T(1-\theta_T)}{\bar{C}_L} \tag{5.34}$$

$$\frac{\partial\bar{C}_T}{\partial\bar{N}_T} = \frac{1}{1 + \dfrac{\beta\bar{N}_L}{K\bar{C}_L}} = \theta_T\,. \tag{5.35}$$

The final formulation for the hydrogen transport model considering the effects of mechanical deformation on diffusion as proposed by Sofronis & McMeeking [173] with the plastic strain rate term introduced by Krom et al. [88] is obtained by substituting (5.33, 5.34, 5.35) in (5.29)

$$\frac{\bar{C}_L + \bar{C}_T(1-\theta_T)}{\bar{C}_L}\frac{\partial\bar{C}_L}{\partial t} - \nabla\cdot(D_L\nabla\bar{C}_L) + \nabla\cdot\Big(\frac{D_L\bar{C}_L V_H}{R_{GS}T}\nabla\sigma_H\Big) + \theta_T\frac{\partial\bar{N}_T}{\partial\varepsilon_p}\frac{\partial\varepsilon_p}{\partial t} = 0\,. \tag{5.36}$$

In this form, the diffusion equation can be discretized for computational implementation.

5.2.2. Numerical Implementation

The numerical treatment of the diffusion model is widely discussed in literature and an efficient framework is given in ABAQUS as described by several research groups [130, 86, 11, 12, 43, 188, 1].

Heat Transfer Analogy. For the implementation of the hydrogen transport model the mathematical analogy between the diffusion and heat transfer equation is exploited. ABAQUS provides an interface for a user-defined material considering heat transfer (UMATHT). Here, the thermal constitutive behavior of the material and internal heat generation during heat transfer can be defined by the variation of internal energy with respect to temperature ($\frac{\partial U_q}{\partial T}$) and with respect to the spatial temperature gradient ($\frac{\partial U_q}{\partial \nabla T}$). Table 5.1 shows the analogy with the variables for the diffusion problem, see Barrera et al. [12]. The internal solution procedure of ABAQUS requires for the hydrogen problem the variation of total hydrogen concentration $\bar{C}_{total}$ with respect to $\bar{C}_L$ and with respect to the trap density $\bar{N}_T(\varepsilon_p)$. Furthermore, the variation of heat flux with temperature and spatial temperature gradient corresponds to the variation of hydrogen flux $\bar{\boldsymbol{J}}$ with hydrogen concentration $\bar{C}_L$ and with the hydrogen concentration gradient. Terms to be defined are listed in the following and can be determined from and with equations (5.34, 5.35, 5.27)

$$\frac{\partial \bar{C}_{total}}{\partial \bar{C}_L} = 1 + \frac{\bar{C}_T(1-\theta_T)}{\bar{C}_L} \tag{5.37}$$

$$\frac{\partial \bar{C}_{total}}{\partial \bar{N}_T} = \theta_T \tag{5.38}$$

$$\frac{\partial \bar{\boldsymbol{J}}}{\partial \bar{C}_L} = \frac{D_L V_H}{R_{GS} T} \nabla \sigma_H \tag{5.39}$$

$$\frac{\partial \bar{\boldsymbol{J}}}{\partial (\nabla \bar{C}_L)} = -D_L \boldsymbol{1} \,, \tag{5.40}$$

where $\boldsymbol{1}$ is the second order identity tensor. Quantities of the right hand side of the equation are either defined by literature values or updated in every increment in the UMATHT routine. The only exception is the hydrostatic stress gradient in (5.39), which must be calculated in a tedious manner, explained in the following.

Heat transfer	**Mass diffusion**
$\rho c_P \frac{\partial T}{\partial t} + \nabla \cdot \boldsymbol{J}_q = 0$	$\frac{\partial \bar{C}_{total}}{\partial t} + \nabla \cdot \bar{\boldsymbol{J}} = 0$
Derivative of thermal energy per unit mass: $\dot{U}_q = c_P \frac{\partial T}{\partial t}$	Derivative of total H concentration: $\frac{\partial \bar{C}_{total}}{\partial t} = \frac{\partial (\bar{C}_L + \bar{C}_T)}{\partial t}$
Degree of freedom: T (temperature)	Degree of freedom: $\bar{C}_L$
Heat flux: $\boldsymbol{J}_q$	Hydrogen flux: $\bar{\boldsymbol{J}}$
Density: ρ	1

Table 5.1: Analogy between variables in heat transfer and diffusion analysis in ABAQUS.

Determination of Hydrostatic Stress Gradient. The determination of $\nabla \sigma_H$ is not straight forward since only the stress tensor or the hydrostatic pressure $p = -\sigma_H$ are calculated by the UMAT routine and available at the integration or gauss points. To

solve this issue Barrera et al. [12] and Díaz et al. [43] use an 8-node 2D coupled temperature-displacement plane strain element CPE8HT or CPE8RT with biquadratic shape functions for the displacement and bilinear shape functions for the hydrogen concentration. Thereby, inequality of hydrostatic stress exists between the 9 integration points in the element and a gradient calculation within one element is possible by using the corresponding shape functions. However, quadratic shape functions extend the computation time, which should be avoided considering the already computational expensive calculation for the complex crystal plasticity material model. On the contrary, Oh et al. [130] and ul Hassan et al. [188] overcome the problem by using 4-node linear coupled temperature-displacement plane strain element CPE4T with 4 integration points. The gradient is calculated by reading and processing stress data from the result ODB file with external PYTHON scripts. This workaround is indispensable, because ABAQUS imposes a constant hydrostatic pressure in first order elements. External reading and writing processes are very time consuming and lack efficiency.

Here, a sophisticated calculation scheme for the determination of the hydrostatic stress gradient, proposed by Farukh et al. [51] for oxygen diffusion in single crystal superalloys, is adapted. The subroutine URDFIL enables an access on result values during the analysis from the preceding increment in the internal user routine framework of ABAQUS. Such internally accessible quantities are saved in the output FIL file. URDFIL is called at the end of each increment to read the average nodal values of hydrostatic stress from this file and their gradients are determined using the Jacobian matrix that connects global to local coordinates and the corresponding shape functions. For a detailed description the reader is referred to Farukh et al. [51] and Hao [68]. This writing and reading process is done by internal ABAQUS FORTRAN routines, which results in a tremendous speedup. The method is validated by a common numerical example in which hydrogen diffusion near a crack tip is analyzed. This boundary value problem mentioned first by Sofronis & McMeeking [173] and adopted in [88], [130], [43] is calculated with both methods (using PYTHON scripts or the URDFIL subroutine) for linear elements. Quantitative results of the comparison are reported by Hao [68]. Both methods deliver the same results and agree well with the literature. Remarkable is, however, that the improved calculation method for the hydrostatic stress gradient, without external reading and writing procedures, reduces the computation time in this 2D example with 1332 elements from 35 minutes to 3 minutes, which accounts for a time saving of 91%.

5.3. Numerical Coupling Scheme

While Oh et al. [130], Barrera et al. [12] and Díaz et al. [43] couple the hydrogen transport to standard plasticity, Hassan et al. [188] and Abdolvand [1] consider the microstructure by using a crystal plasticity formulation for the description of polycrystals.

Both models, the crystal plasticity and the hydrogen diffusion model, are solved in the coupled temperature-displacement analysis frame of ABAQUS. Following experimental observations, Section 4.2.2, the hydrogen has no significant influence on the material's hardening behavior. Therefore, a one way coupling scheme is applied where only mechanical quantities, including hydrostatic stresses and accumulated plastic strains, influence the diffusion behavior directly. However, in order to nevertheless take the hydrogen into account for its deteriorating effect on fatigue life, the local trapped hydrogen concentration is considered in the calculation of the fatigue indicator parameter as described in

Section 6.2.3.

Both models are sequentially linked through the hydrostatic stress gradient and the accumulated plastic strain. The main steps in the global Newton-Raphson scheme, to solve the nonlinear system of equations, are explained in the following and illustrated in Figure 5.3. The mechanical field variables are calculated in the i th increment loop within the crystal plasticity model and the stresses are saved in the data output FIL file. Also the accumulated plastic strain is calculated in the UMAT. The hydrostatic stress gradient is required at each gauss point for the solution of the diffusion in the UMATHT. Hence, at the beginning of the $i+1$ th loop the gradient is calculated by internal FORTRAN routines using the interpolation functions. These quantities can now be used in the $i+1$ th loop to calculate the hydrogen concentration by the mechanically influenced diffusion model.

The coupled model can be implemented by the above described procedure. What is missing, is a choice of initial conditions including geometries, microstructural aspects and boundary conditions. All of these are defined in the ABAQUS input file and specified in the subsequent section.

5.4. Representative Volume Element

The proposed coupled model is solved on a suitable domain considering the material's microstructure. Therefore, the idea of a representative volume element (RVE) is introduced. The generation of such a RVE is either based on microstructure analysis data, such as the EBSD data discussed in Section 4.1, or is entirely artificial, informed by statistical features of the microstructure and created by mathematical tessellation strategies. Both methods are explained in the following together with the imposition of periodic boundary conditions for the finite element analysis.

5.4.1. Generation of a Representative Structure

For a multiscale approach towards material modeling, it is important to consider that assumptions and simplifications made on the macroscale might lose their validity on the microscale. A schematic drawing of the multiscale approach is given in Figure 5.4. The size of a material testing sample is considered on the macroscale in the order of 10^{-2} m. As commonly done in literature, the assumption of a homogeneous material is made on this scale. But taking into account the polycrystalline microstructure in an order of 10^{-5} m a distinct heterogeneity is observable. This issue can be overcome by consideration of representative volume elements, see Nemat-Nasser & Hori [128]. The principle of the RVE is based on the idea, that material might be heterogeneous in their microstructure but effective properties of the material can be homogeneous for a certain volume. As a link between the component on the macro-scale and the material behavior on the micro-scale, this technique is commonly used in two-scale simulations. A summary of properties and applications of RVEs can be found in Zeman [200] or Schröder & Hackl [166]. The question, concerning the size of the RVE to capture an area or volume which is structurally completely typical for the whole structure, cannot be answered clearly and has to be evaluated individually for every material. The RVE should be larger than the size of individual constituents of the microstructure but much smaller than the component or macro sample to guarantee computational efficiency. Stroeven et al. [175] state, that the convergence behavior of an effective quantity calculated within the RVE depends

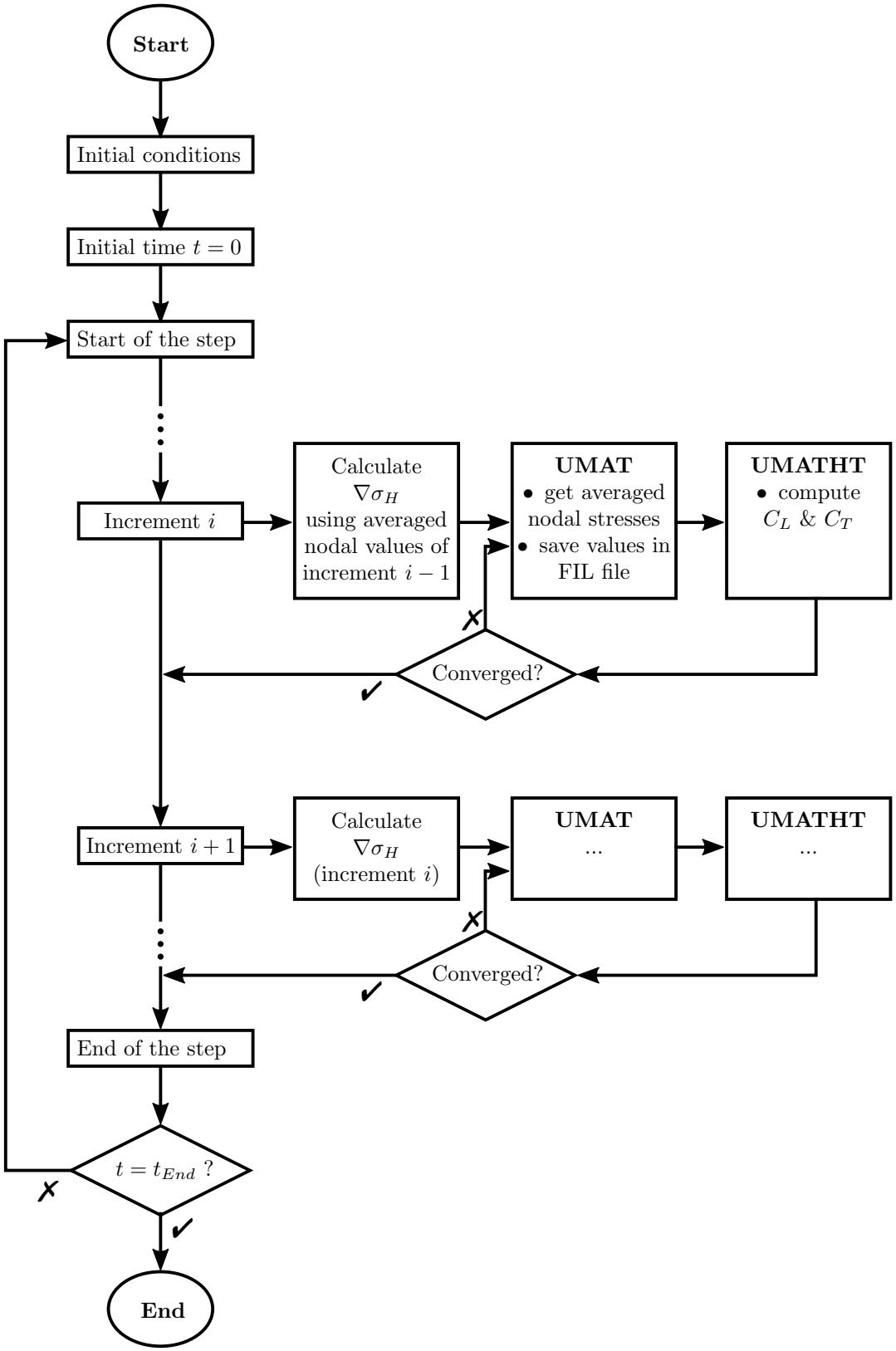

Figure 5.3: Numerical solution scheme for sequential coupling of crystal plasticity (UMAT) and hydrogen diffusion (UMATHT) model in ABAQUS.

not only on the material structure considered but also on the physical quantity of interest. For instance, energy dissipation only converges for rather large volume elements, while effective elastic behavior is also captured by smaller RVEs.

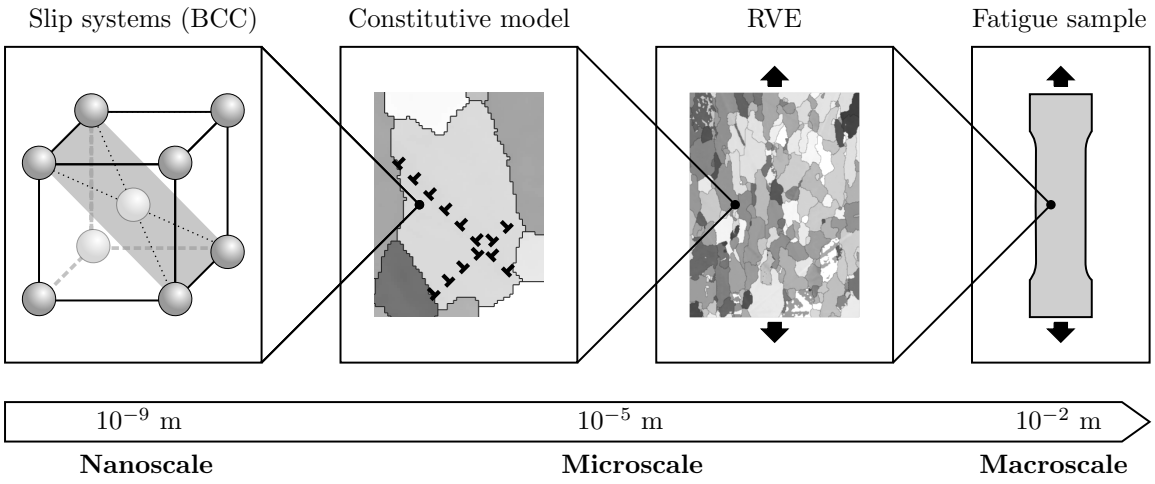

Figure 5.4: Multiscale approach in context of crystal plasticity finite element modeling.

EBSD-based Generation. The first option to generate a RVE is a direct reproduction of an image of the real microstructure. For metals these images are based on EBSD data, which can be processed and discretized straight forward to ABAQUS input files and consider all grain orientations. A limitation of this approach is the restriction to the image size of the EBSD data and that microstructural features cannot be varied for statistical investigations or the study of microstructural influence factors. The data contains the coordinates of each scanned point in a certain grid with corresponding Euler angles for the crystal orientation at this specific location. Furthermore, confidence indicators provide information about the quality of the measurements. To visualize or analyze crystallographic textures by means of EBSD or pole figure data, the open source Matlab toolbox MTEX is used, which is further specified in Bachmann et al. [8]. Another drawback is the limitation to 2D data. 3D data could be obtained by serial sectioning by means of a focused ion beam (FIB) and the sequential characterization of each section with EBSD analysis. This sequential 3D EBSD data generation is extremely elaborate and costly, such that only 2D images are available in the present work. 2D or quasi 3D simulations can be carried out with input data based on 2D EBSD information. Following Manonukul & Dunne [107], quasi 3D models denote the extrusion of the 2D microstructure into the third dimension, which enables the use of volume elements for the discretization and finite element analysis. As shown in Figure 5.5 the EBSD data is covered by a regular mesh. The orientations of the EBSD data corresponding to the coordinates of each element center of the mesh are assigned to this element. Thereby the measuring point closest to the element center is considered. The orientation information for each grain is saved in a corresponding set of elements and declared as an own material within the ABAQUS input file. Note, that the EBSD data depicted on the left hand side of Figure 5.5 is already filtered and free of errors of the EBSD measurement, see Section 4.1. Impurities and roughness on the sample after preparation for the microstructure

analysis might lead to wrong orientations at these locations. Without a filter procedure these incorrect orientation could be assigned to single elements in the RVE, resulting in unphysical stress or strain localizations due to elastic incompatibilities. A drawback of using a regular or structured mesh is the pixelated representation of the EBSD image with a loss of the smooth grain boundaries. These boundaries are approximated by straight lines or steps and match the real boundary better with decreasing element size. The mesh dependency on effective quantities was investigated by Zhang et al. [201]. They state, that the stepwise approximation of grain boundaries have a negligible influence on effective properties when using a sufficient fine mesh. Furthermore, Böhlke et al. [20] compared the stress and strain fields of a micro sample under tension calculated with a structured and unstructured mesh with approximately the same number of degrees of freedom. The distributions agree well in both cases, such that they conclude that the usage of a structured mesh is admissible.

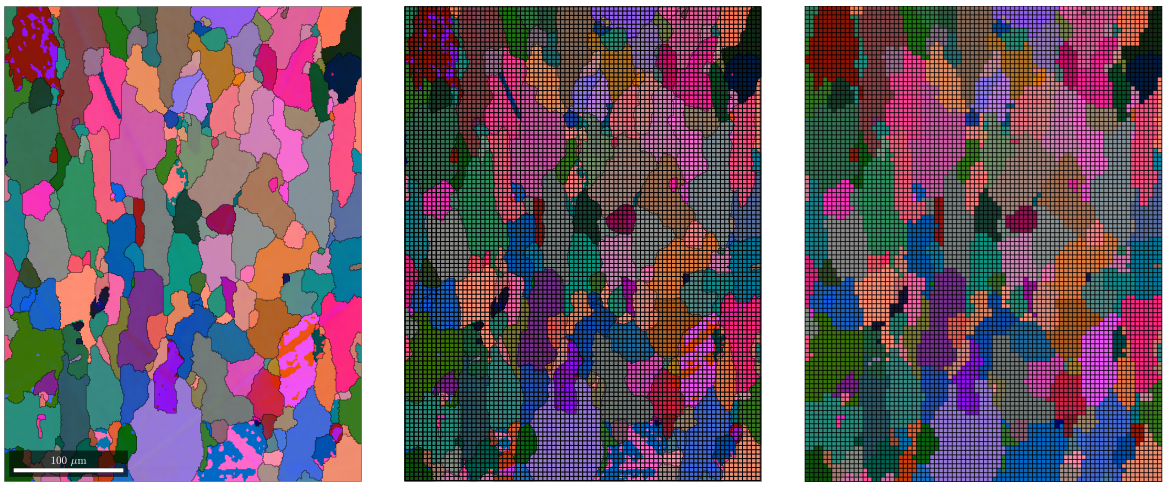

Figure 5.5: Generation of representative volume element of ferritic steel 1.4003 based on EBSD data on the left. Discretized by a regular mesh of 80×107 elements in the center and the assignment of orientations to the specific elements on the right.

Artificial Generation. A second possibility to create a RVE is based on statistical information of the microstructure, such as the grain size or the texture of the material. The synthetic structure is generated by a mathematical tessellation procedure and is fitted to the statistical features. An advantage over the EBSD-based generation lies in the possibility of a systematical variation of these features which allows for the assessment of critical microstructural properties. However, exact grain shapes as given by EBSD data cannot be replicated and are approximated as explained in the following.

To approximate the microstructure of a polycrystal, a common approach is the Voronoi tessellation, see Gosh et al. [61]. This approach partitions a given plane into convex polygons, the Voronoi cells, such that each polygon contains only one generating point, called seed, and every point in a given polygon is closer to its seed than to any other generating point. However, the geometry of cells defined by distances between seeds only, making all nuclei equal. This may be too restrictive for many applications, thinking only of the variety of grain morphologies for steels. The Voronoi Laguerre tessellation, also called radical Voronoi algorithm or power diagram in computational geometry, allows for

the assignment of a weight to each seed, such that mighty nuclei grow to larger cells. Additional to the generating points of the original Voronoi tessellation, each nuclei holds the information of a radius, which can be interpreted as weighting factor determining the size or volume of the Voronoi cell. The synthetic microstructure is now influenced by the seed point location and the corresponding radii. A collection of these algorithms with specific modifications is implemented in the software package Neper. Herewith, polycrystal generation and meshing for a variety of microstructures is possible by the methods described in Quey et al. [149, 150, 151]. 2D as well as 3D polycrystals with large numbers of grains can efficiently be generated in iterative procedures with the regulation of grain size, grain shape and other properties via statistical distributions as input parameters, see Figure 5.6.

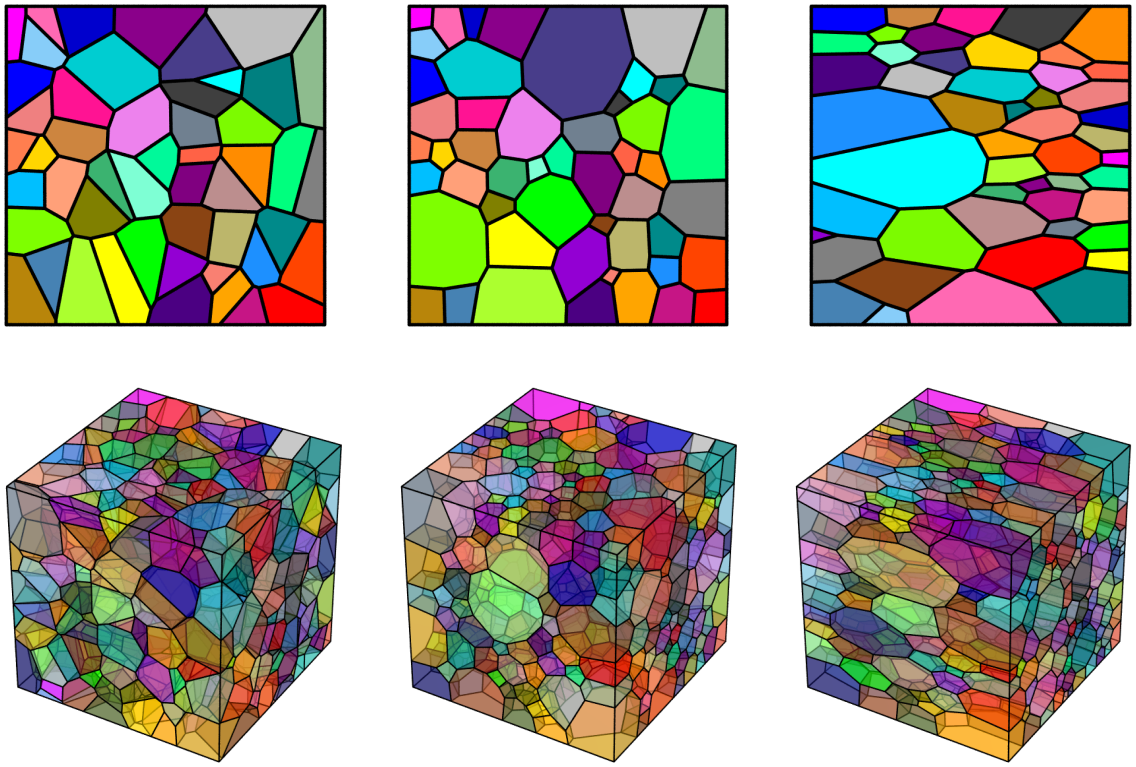

Figure 5.6: Microstructure generation with Neper for 2D and 3D RVEs. Different tessellation techniques are shown, including Voronoi tessellation on the left, grain growth in the middle and grain growth with variable aspect ratios on the right.

A description of generating a microstructure synthetically with the objective to obtain a statistical equivalent representation of the real grain morphology is given in the following. First the grain size and shape is investigated and an approximation of the structure on the left hand side of Figure 5.7 a) is tried to be achieved. As can be seen in both pictures and the plot in b) a good statistical accordance of the grain size distribution is reached by the artificial structure. Taking into account only grains with an equivalent diameter over 5 μm both structures count 186 grains with an average diameter of 26.6 μm and 26.3 μm for the EBSD based and synthetic RVE, respectively. Obviously only convex grains can be generated with Neper. Therewith, an adequate imitation of the real grain shapes is not possible. However, the slight stretching of the grains caused by the drawing process

during the steel production can be mimicked nicely by the aspect ratio option of Neper.

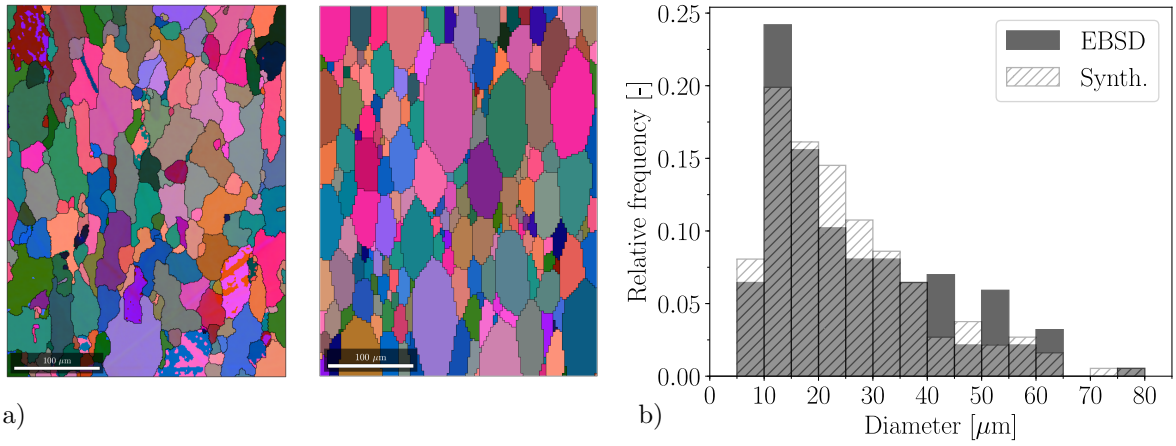

Figure 5.7: Illustration of the grain structure in the real microstructure on the left side and the artificially created one on the right side of a). The relative frequency of all grains with a diameter over 5 μm is compared for those two structures in b).

Another criteria for the quality of the synthetic RVE is the misorientation distribution. The misorientation is the minimal rotation necessary to rotate one set of crystal axes to be congruent with the other crystal. Hence, the misorientation angle is a measurement of how two adjacent grains are positioned to each other in terms of rotation with respect to a reference frame. The role of misorientations and grain boundaries for the crack initiation is discussed by Sangid et al. [159]. Two neighboring domains with a misorientation angle greater than 5° are considered as two different grains. Figure 5.8 a) shows the misorientation angles plotted on the particular grain boundaries for both RVEs. In b) the distribution of all calculated angles is plotted, showing a good agreement for the artificial with the real structure.

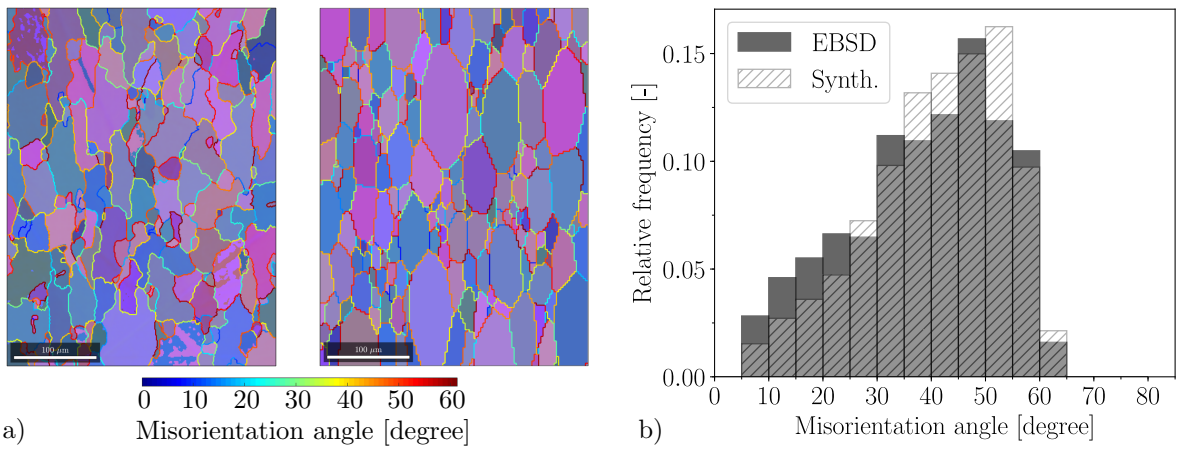

Figure 5.8: The misorientation angles are plotted on the corresponding grain boundaries of the EBSD based and synthetic RVE on the left and right side of a), respectively. The misorientation angle distribution is compared in b).

The pole figures of the investigated material reveal a texture with preferred grain orientations visible on the top of Figure 5.9. Out of 140 000 measured orientations 5000 are plotted as a reference. To mimic this specific texture with the synthetic microstructure, grains are assigned to randomly drawn orientations out of a pool of all available orientations of the EBSD data. With all grains of the artificial structure and their orientations, a good agreement of the texture is achieved, compare the lower row showing the synthetic texture with the upper row of Figure 5.9.

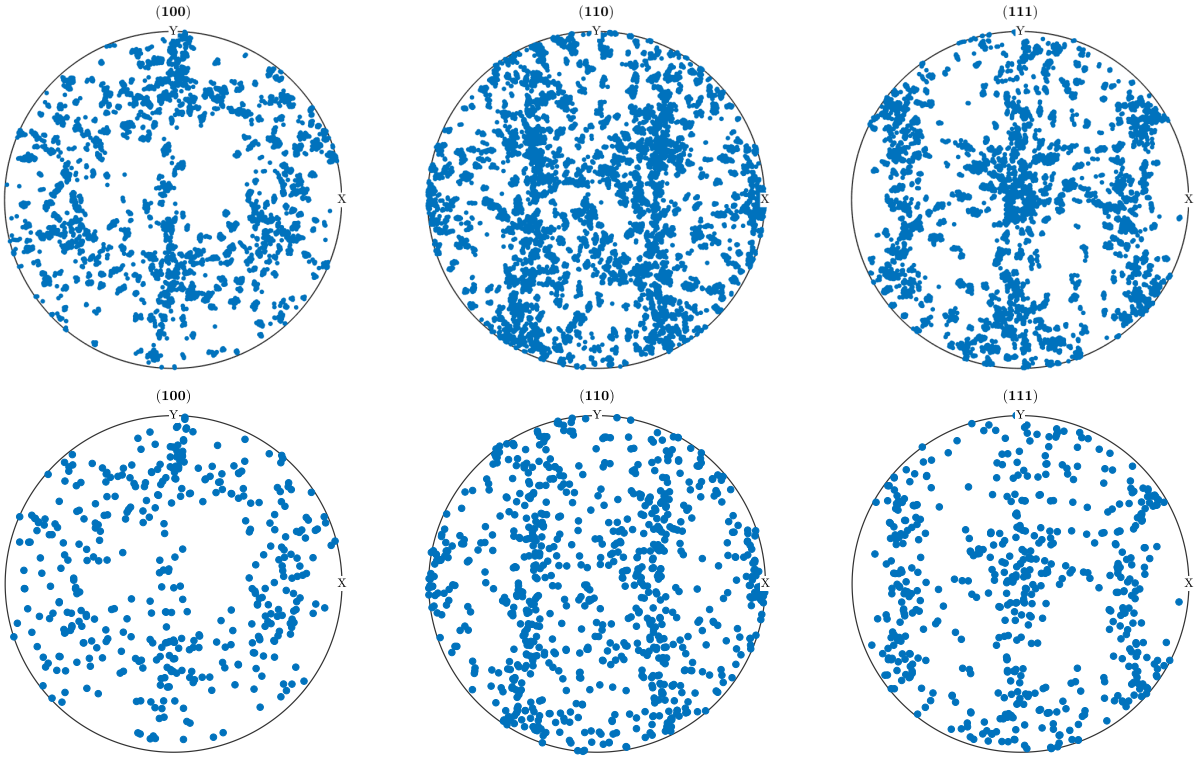

Figure 5.9: Texture comparison with pole figures corresponding to the EBSD data on the top and the artificial microstructure on the bottom side.

5.4.2. Boundary Conditions

Different choices for boundary condition possible to impose on RVEs are introduced. The detailed description of Schröder & Hackl [166] and Boeff [18] are adapted in the following. First, a link between macro variables and their microscopic counterparts is defined by a volume average, which reads for an arbitrary tensor quantity $\boldsymbol{A}$

$$\langle \boldsymbol{A} \rangle = \frac{1}{V} \int_{\mathcal{B}_0} \boldsymbol{A} \, \mathrm{d}V \,, \tag{5.41}$$

where V is the volume of the RVE in its reference configuration $\mathcal{B}_0$. A criterion for the representativeness of a RVE was proposed by Hill [73] and Mandel [104] and is called the *macro-homogeneity condition*. Accordingly, the volume average of the virtual work of the RVE at the microscale must be equal to the virtual work of the homogenized properties of the macroscale. This statement is often called Hill or Hill-Mandel condition

and reads in the finite strain setting

$$\frac{1}{V}\int_{\mathcal{B}_0} \boldsymbol{P} : \dot{\boldsymbol{F}}\,\mathrm{d}V = \langle \boldsymbol{P}\rangle : \langle \dot{\boldsymbol{F}}\rangle\,. \tag{5.42}$$

in terms of the first Piola-Kirchhoff stress $\boldsymbol{P}$ and the time derivative of the deformation gradient $\dot{\boldsymbol{F}} = \mathrm{Grad}_X\,\dot{\boldsymbol{x}}$. The small strain counterpart of the formulation can be found in [18] and the extension to further stress-strain formulations is listed in [166]. Equation 5.42 is fulfilled if the right hand side of the following identity vanishes

$$\frac{1}{V}\int_{\mathcal{B}_0} \boldsymbol{P} : \dot{\boldsymbol{F}}\,\mathrm{d}V - \langle \boldsymbol{P}\rangle : \langle \dot{\boldsymbol{F}}\rangle = \frac{1}{V}\int_{\mathcal{B}_0} \Big[\big(\boldsymbol{P} - \langle \boldsymbol{P}\rangle\big) : \big(\dot{\boldsymbol{F}} - \langle \dot{\boldsymbol{F}}\rangle\big)\Big]\,\mathrm{d}V\,. \tag{5.43}$$

Here, the differences in the center term can be understood as the virtual work of fluctuations in the stress and deformation state. For a detailed derivation of the above used terms, the reader is referred to Lehmann [95]. The macro-homogeneity condition is fulfilled, if these fluctuations cancel out averaged over the domain. Boundary conditions have to be introduced to solve equation (5.43). Straight forward approaches set either the stress or deformation rate term to zero. Assuming constant stress within the RVE is called *Reuss condition* and constant deformation rates are known as *Voigt condition*, reading

$$\boldsymbol{P} = \langle \boldsymbol{P}\rangle \quad \forall \boldsymbol{X} \in \mathcal{B}_0 \quad \text{and} \quad \dot{\boldsymbol{F}} = \langle \dot{\boldsymbol{F}}\rangle \quad \forall \boldsymbol{X} \in \mathcal{B}_0\,. \tag{5.44}$$

These two conditions are called constraint condition in the following. Equation (5.43) can be reformulated by using the equilibrium condition $\mathrm{Div}_X(\boldsymbol{P} - \langle \boldsymbol{P}\rangle)$ from the balance of linear momentum, see Section 2.5.3, and the Cauchy theorem $\boldsymbol{t}_0 = \boldsymbol{P}\boldsymbol{N}$, yielding

$$\int_{\partial\mathcal{B}_0} \big(\boldsymbol{t}_0 - \langle \boldsymbol{P}\rangle \boldsymbol{N}\big) \cdot \big(\dot{\boldsymbol{x}} - \langle \dot{\boldsymbol{F}}\rangle \boldsymbol{X}\big)\,\mathrm{d}A = 0\,, \tag{5.45}$$

which also holds for $\boldsymbol{F}$, see [166]. Using this information and enforcing the second term in (5.45) to be zero, results in the *Dirichlet boundary conditions*

$$\boldsymbol{x} = \langle \boldsymbol{F}\rangle \boldsymbol{X} \quad \forall \boldsymbol{X} \in \partial\mathcal{B}_0\,, \tag{5.46}$$

which require a displacement to be defined at the boundary. Setting the first term in (5.45) to zero defines *Neumann boundary conditions*

$$\boldsymbol{t}_0 = \langle \boldsymbol{P}\rangle \boldsymbol{N} \quad \forall \boldsymbol{X} \in \partial\mathcal{B}_0\,. \tag{5.47}$$

A stress vector is prescribed at the surface to apply a Neumann boundary condition. Following the above derived argumentation, both type of boundary conditions are applicable and have a strong influence on the global macroscopic response as well as on the local deformation.

Imagine a virtual duplication of the RVE in all spatial directions resulting in a patchwork carpet like structure. A compatibility of all parts is not guaranteed for Neumann boundary conditions, because holes and overlaps can be observed at the surface of the carpet, see Figure 5.10 a). This issue is overcome with Dirichlet type boundary conditions as opposite surfaces undergo the same prescribed displacements, resulting in zero relative displacement, shown in Figure 5.10 b). A consequence thereof is, that the piece of the

patchwork carpet is compatible with the rest in terms of deformation on the interfaces. However, high forces will occur at the domains surface to hold compatibility and inhibit inherently natural contraction due to lateral strain. Schröder & Hackl [166] underline the drawbacks of both boundary conditions and point out that they might not lead to realistic deformation behavior of the RVE. The system response is too soft in case of Neumann boundary conditions due to incompatible and under constraint deformation at the interface. Whereas unrealistic high forces and a too stiff material behavior in case of the Dirichlet boundary conditions are a result of the enforced compatibility at the interfaces. To overcome these limitations periodic boundary conditions (PBCs), illustrated in Figure 5.10 c), are introduced and applied for the boundary value problems in this work.

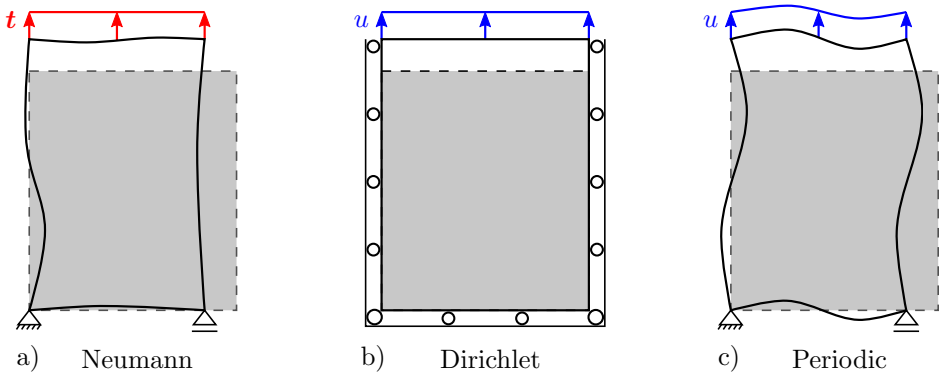

Figure 5.10: Three possible types of boundary conditions for the modeling with RVEs with applied forces $\boldsymbol{t}$ or displacements u, inspired by Boeff [18].

RVE modeling with imposed PBCs lead to an intermediate response between Neumann and Dirichlet conditions and a more realistic deformation behavior. Following Smit et al. [172] and Schröder & Hackl [166] an implementation scheme is introduced to apply PBCs to a boundary value problem of a finite element calculation. The boundary of the microstructure $\partial\mathcal{B}_0$ is subdivided into two parts

$$\partial\mathcal{B}_0 = \partial\mathcal{B}_0^+ \cup \partial\mathcal{B}_0^- \,. \tag{5.48}$$

Each point $\boldsymbol{X}^+ \in \partial\mathcal{B}_0^+$ has an associated point $\boldsymbol{X}^- \in \partial\mathcal{B}_0^-$ with outward unit normals $\boldsymbol{N}^+$ and $\boldsymbol{N}^-$. Assuming $\langle\boldsymbol{F}\rangle$ and $\boldsymbol{X}$ to be given quantities, a fluctuation field is defined

$$\tilde{\boldsymbol{w}} := \boldsymbol{x} - \langle\boldsymbol{F}\rangle\boldsymbol{X} \,. \tag{5.49}$$

Inserting (5.49) in (5.45) yields

$$\begin{aligned}\int_{\partial\mathcal{B}_0} \left(\boldsymbol{t}_0 - \langle\boldsymbol{P}\rangle\boldsymbol{N}\right)\cdot\tilde{\boldsymbol{w}}\,\mathrm{d}A = &\int_{\partial\mathcal{B}_0^+} \left(\boldsymbol{t}_0^+ - \langle\boldsymbol{P}\rangle\boldsymbol{N}^+\right)\cdot\tilde{\boldsymbol{w}}^+\,\mathrm{d}A + \\ &\int_{\partial\mathcal{B}_0^-} \left(\boldsymbol{t}_0^- - \langle\boldsymbol{P}\rangle\boldsymbol{N}^-\right)\cdot\tilde{\boldsymbol{w}}^-\,\mathrm{d}A \,.\end{aligned} \tag{5.50}$$

Considering the characterization of a periodic fluctuation field $\tilde{\boldsymbol{w}}^+ = \tilde{\boldsymbol{w}}^-$ and $\boldsymbol{N}^+ = -\boldsymbol{N}^-$ results in

$$\int_{\partial\mathcal{B}_0^+} \left[\left(\boldsymbol{t}_0^+ - \langle\boldsymbol{P}\rangle\boldsymbol{N}^+\right)\cdot\tilde{\boldsymbol{w}}^+ + \left(\boldsymbol{t}_0^- + \langle\boldsymbol{P}\rangle\boldsymbol{N}^+\right)\cdot\tilde{\boldsymbol{w}}^+\right]\mathrm{d}A = \int_{\partial\mathcal{B}_0^+} \left(\boldsymbol{t}_0^+ + \boldsymbol{t}_0^-\right)\cdot\tilde{\boldsymbol{w}}^+\,\mathrm{d}A \,. \tag{5.51}$$

Here, the latter term becomes zero if the stress vectors on opposite surfaces with surface normal $\boldsymbol{N}$ are the same but pointing in opposite directions $\boldsymbol{t}_0^+ = -\boldsymbol{t}_0^-$. The realization of PBCs is based on the idea of the same relative displacement of opposite nodes. A global strain in a certain direction is still allowed, while nodal displacements of two opposing nodes in this direction are coupled to each other. Within the input framework of ABAQUS the PBCs can be imposed by using the '*Equation' keyword. The implementation scheme for the 2D case is explained in the following and the 3D extension can be found in Boeff [18].

2D Implementation of PBCs. First a convention for the names of nodes and edges of a periodic RVE is set, as depicted in Figure 5.11. Corner nodes are denoted as vertex V_1 to V_4 and the edges are defined as node sets with the names *Bottom*, *Right*, *Top* and *Left*. The origin of a coordinate frame is located at vertex V_1. The relative displacement of nodes located on opposing edges are equal to the displacement, which is introduced by an average strain on the distance between the two nodes. For instance picking two nodes from *Top* and *Bottom*, the relative displacement reads

$$u_y^T - u_y^B = \varepsilon_{yy} \cdot l_y \,, \tag{5.52}$$

such that an average strain between opposing nodes is possible. For the domain in Figure 5.11 the global strain is directly coupled to the corner nodes V_1, V_2 and V_4. Thus, all boundary conditions has to be applied on these nodes only. An implicit transfer to the nodes at the corresponding edges is induced by the periodic boundary conditions. To avoid an over constraint by coupling all displacements of nodes on opposite edges, only vertex V_1 is coupled to V_2, V_1 to V_4 and V_4 to V_3, which results in a periodic response. As visualized in Figure 5.11 boundary conditions, such as tension, compression or shear, can be applied on the connected vertices which are free (green), while orange colored vertices are coupled with periodic constraints and the black vertices are connected implicitly by the PBCs. To avoid over-constraining the edge node sets are treated differently to the corner nodes. Pure edge nodes and the vertices are coupled separately as explained in Figure 5.11. With these equations V_1, V_2 and V_4 are independent, while V_3 is coupled to the other nodes.

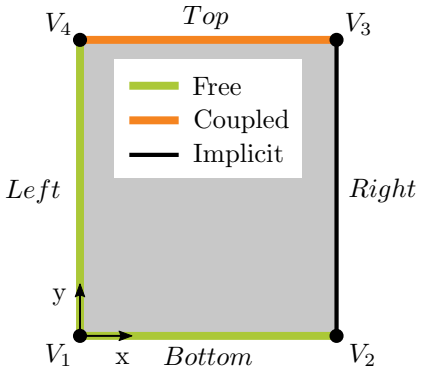

Bottom to *Top* node set: $\boldsymbol{u}_i^T - \boldsymbol{u}_i^B = \boldsymbol{u}^{V_4} - \boldsymbol{u}^{V_1}$

Left to *Right* node set: $\boldsymbol{u}_i^R - \boldsymbol{u}_i^L = \boldsymbol{u}^{V_2} - \boldsymbol{u}^{V_1}$

Vertex coupling: $\boldsymbol{u}^{V_3} - \boldsymbol{u}^{V_2} = \boldsymbol{u}^{V_4} - \boldsymbol{u}^{V_1}$

Figure 5.11: Implementation scheme for periodic boundary conditions for a 2D RVE with coupling equations. Here, $\boldsymbol{u}_i$ is the displacement vector to the i th node in the corresponding node set.

6. Micromechanical Fatigue Simulation

The introduced simulation model requires material parameter for the crystal plasticity as well as the diffusion model. A calibration strategy is applied to obtain a suitable set of parameter reproducing the micromechanical material response measured by experiments. Thereafter, a prediction scheme is introduced using fatigue indicator parameters to determine the number of loading cycles until crack initiation. Besides established FIPs a novel hydrogen dependent FIP is considered to predict the fatigue lifetime under hydrogen atmosphere. Simulation results are presented and the variation of boundary conditions and microstructural morphologies are investigated and discussed.

6.1. Parameter Identification

Material parameters are required for the numerical model and must be chosen and determined as suitable as possible for the investigated material-medium system. Two sets of parameters are defined, including the quantities for the crystal plasticity and the diffusion model, respectively. The first set contains elastic constants, parameter related to the flow rule, isotropic and kinematic hardening parameter, which are all listed in Table 6.1. Elastic constants for the elastic stiffness tensor $\mathbb{C}^e$, introduced in Section 2.1.2, for ferritic steels are provided in Osipov et al. [135]. Following the explanation in Section 2.1.2 a restriction to the primary 12 slip systems is made. The reference shear rate is adapted from Hennessey et al. [70], who also underlines that high exponents for the strain rate sensitivity m make numerical convergence difficult. Hence, the value for m is chosen relatively low, according to Boeff [18]. The investigated ferritic steel exhibit cycle stable material behavior, see Figure 4.6. Therefore, isotropic hardening is neglected in this work and the related parameters are not determined. Remaining constitutive material parameters are the critical resolved shear stress τ_c and the parameters A_1 and A_2 for the kinematic hardening after Armstrong and Frederick, see equation 5.16. A multi-objective optimization procedure proposed in Schäfer et al. [160] is applied to find the best set of those three parameters regarding the experimental cyclic stress-strain response of the material, shown in Figure 4.8. Therefore all parameters mentioned above are kept constant while the best fit of the three remaining parameters is found during the optimization procedure. The reference hystereses used for the calibration are taken from experimental LCF tests at $\varepsilon_{a,t} = [0.3\%, 0.7\%, 1.0\%]$. An evolutionary algorithm provided by the commercial optimization software OPTISLANG [132] is used in combination with ABAQUS. Therewith, the best set of the three parameters for a least-square minimization problem is found. 200 crystal plasticity simulations are performed over 5 loading cycles on a 2D microstructure based on EBSD data of the ferritic steel 1.4003 in ABAQUS. After each simulation the three material parameters of interest are varied after the optimization algorithm of OPTISLANG. The best fit of parameters, obtained by comparison of the experimental cyclic stabilized hystereses and the effective cyclic material response from simulation, is used for all further simulations and can be found in Table 6.1. For a detailed description of the calibration procedure the reader is referred to Schäfer et al. [160]. A comparison of the experimental and numerical stress-strain response is drawn in Figure 6.1. Dots represent the experimental and solid lines the calculated hystereses. The green lines are the hystereses of the total strain amplitudes used for the calibration process and they show excellent agreement with experimental findings. Especially interesting are the red lines. These lines show the numerically obtained material response at

Parameter	Name	Value	Unit
$\mathbb{C}^e_{11}$	Elastic constant	219.5	GPa
$\mathbb{C}^e_{12}$	Elastic constant	78.1	GPa
$\mathbb{C}^e_{44}$	Elastic constant	70.7	GPa
N_{Slip}	Number of slip systems	12	-
$\dot{\gamma}_0$	Reference shear rate	0.001	1/s
m	Strain rate sensitivity exponent	30.0	-
τ_c	Critical resolved shear stress	90.0	MPa
h_0	Hardening parameter	-	-
τ_s	Saturated shear stress	-	-
n	Hardening exponent	-	-
A_1	Kinematic hardening 1	27100.0	MPa
A_2	Kinematic hardening 2	727.5	-

Table 6.1: Parameter set for the crystal plasticity model.

amplitudes, which are not used for the optimization procedure. A qualitative comparison with experimental curves shows again a good agreement. It proves, that the parameter set is also suitable for other strain amplitudes ($\varepsilon_{a,t} = [0.15\%, 0.2\%, 0.5\%]$). Slight deviations are visible for the lowest strain amplitudes ($\varepsilon_{a,t} < 0.2\%$) where the energy of plastic deformation, the area included by the hysteresis curve, gets close to zero.

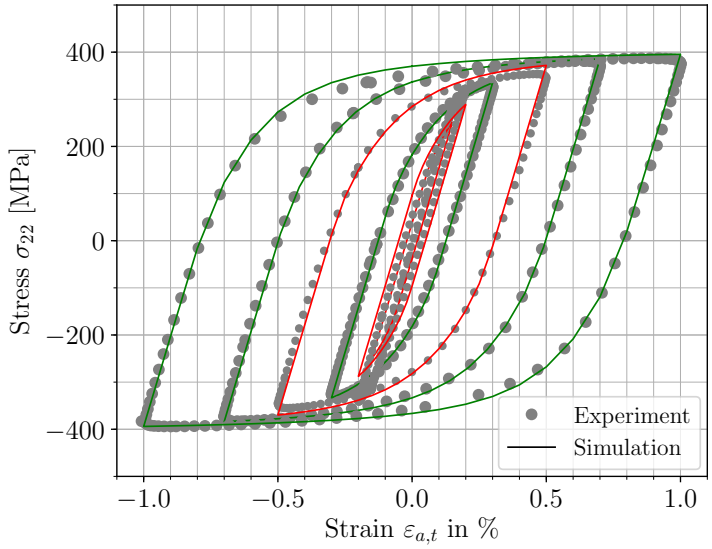

Figure 6.1: Comparison of simulative stress-strain hystereses with experimental data. The parameter set used in the simulation was fitted to three total strain amplitudes (green) while the simulation results of amplitudes not used for the calibration are indicated by red lines.

Constants and parameters necessary for the hydrogen diffusion model are taken from [173] and [88] and are listed in Table 6.2. While some parameters, such as β and N_L are

fixed for a given lattice, here BCC, others have to be determined or approximated with regard to the investigated material. Permeation measurements are suited to determine the effective diffusion coefficient, which is influenced by alloying elements and impurities. These imperfections of the lattice are not explicitly modeled. Therefore we approximate the lattice diffusivity with experimental measurements for a pure BCC lattice, whereas the effective diffusivity is expected to be lower, see Section 4.3. Different trap binding energies are listed in Table 2.4 and a trap binding energy proposed in [173] is adapted, which models medium to strong trapping behavior. Therewith, all parameters required for the coupled model are introduced.

Parameter	Name	Value	Unit
T	Temperature	300.0	K
α	Number of trapping sites per solvent atom	1.0	-
β	Number of interstitial sites per solvent atom	6.0	-
V_H	Partial molar volume of hydrogen	$2.0 \cdot 10^3$	mm^3/mol
N_L	Number of lattice sites	$1.41 \cdot 10^{-4}$	mol/mm^3
D_L	Diffusion coefficient	$1.27 \cdot 10^{-2}$	mm^2/s
E_b	Trap binding energy	$-6.0 \cdot 10^7$	mJ/mol

Table 6.2: Parameters for the hydrogen transport model.

6.2. Fatigue Prediction Scheme

Experimental methods to investigate fatigue behavior are continuously enhanced and even very high cycle numbers can be reached in a reasonable time. However, numerical models to predict these fatigue properties based on the material's microstructure are sparsely developed. To capture and understand phenomenas leading to fatigue on a microstructural scale, it is not sufficient to only track global loading amplitudes and relate them to the fatigue behavior. Micromechanical simulations could provide new information on fatigue, where experimental setups fail due to the high complexity on these small scales. Stress and strain measurement and image acquisition must be sufficiently precise, which poses a challenging task at small scales. The initiation of fatigue damage is triggered by irreversible plastic slip on the microscale, see Przybyla & McDowell [147]. A modeling framework for the prediction of fatigue crack initiation in nickel-based alloys was proposed by McDowell et al. [171, 147, 30] and applied in Boeff [18]. They introduce micromechanical sensitive fatigue indicator parameters (FIPs) as measurements for the local degradation state and a driving force for fatigue crack initiation. Different approaches are introduced in the subsequent sections.

6.2.1. Fatigue Indicator Parameters

FIPs provide information about the evolution of stress and strain fields during a loading cycle dependent on the material's microstructure. Multiple fatigue criteria have been proposed for the prediction of crack formation in fatigue modeling and their suitability depends on the material and specific cyclic loading conditions. In literature discussed approaches contain a purely strain based FIP used by Manonukul & Dunne [107]

and McDowell & Dunne [110] in form of the accumulated plastic strain. Fatemi & Socie [52] proposed a stress-strain dependent approach, while Korsunsky et al. [87] apply an energy dissipation criterion. An overview of different fatigue metrics is given in Hochhalter et al. [76].

Accumulated Plastic Slip. The slip rate $\dot{\gamma^\alpha}$, introduced in 5.15, is determined in the crystal plasticity framework for each slip system α, where the applied stress projected on each glide system defines the slip rate. It quantifies the activity of plastic gliding on each slip system. Therewith, the plastic velocity gradient can be determined with 5.12, in which the Schmid matrix limits the deformations within the grain in dependency of the lattice structure. The accumulated plastic slip is calculated from the plastic velocity gradient and describes the amount of effective plastic deformation a material has experienced over time at a local material point, see Boeff [18]. It is the first introduced FIP and reads

$$FIP_p = \bar{\varepsilon}^p = \int_0^t \sqrt{\tfrac{2}{3}\, \boldsymbol{L}^p : \boldsymbol{L}^p}\, \mathrm{d}t\,. \tag{6.1}$$

The accumulated plastic slip keeps track of the plastic deformation history at an integration point and increases monotonically during cyclic loading and the corresponding gliding. In the framework of crystal plasticity the velocity gradient is calculated allowing a direct evaluation of FIP_p after each increment within the UMAT.

Fatemie Socie Criterion. Fatemie & Socie [52] found that the normal stress on the plane of maximum shear strain amplitude influences the fatigue crack formation. They introduced a crack initiation criterion combining the maximum shear strain amplitude and the maximum normal stress on the plane of maximum shear strain amplitude. This critical plane approach is calculated as

$$FIP_{FS} = \frac{\Delta\gamma_p^{max}}{2}\left(1 + k\frac{\sigma_{max}^n}{\tau_c}\right), \tag{6.2}$$

with

$$\Delta\gamma_p^{max} = \max\left(\int_0^t \dot{\gamma}_p \mathrm{d}t\right) - \min\left(\int_0^t \dot{\gamma}_p \mathrm{d}t\right), \tag{6.3}$$

where γ_p^{max} is the local maximum cyclic plastic shear range, σ_{max}^n is the maximum normal stress to the plane of γ_p^{max}, τ_c is the (initial) critical resolved shear stress and k is a constant set to 1.0 controlling the influence of the normal stress. In comparison with FIP_p, the determination of FIP_{FS} is more complex and requires the maximal cyclic slip range and the normal stress on each slip system to be determined incrementally within the UMAT.

Energy Dissipation Criterion. An energy dissipation criterion in the context of a crystal plasticity model was proposed by Korsunsky et al. [87]. In this context the criterion considered the amount of energy dissipated over all slip systems under cyclic loading in a nickel-based superalloy. They found good agreements between the number of cycles to failure and the energy dissipation per cycle. The approach is defined as

$$FIP_W = \int_0^t \sum_{\alpha=1}^{N_{Slip}} \tau^\alpha \cdot \dot{\gamma^\alpha}\, \mathrm{d}t\,, \tag{6.4}$$

where τ^α is the resolved shear stress and $\dot{\gamma}^\alpha$ the slip rate. The implementation in the UMAT framework is similar to the determination of the accumulated plastic slip.

A comparison of the different FIPs and their suitability for fatigue crack initiation prediction are discussed in Boeff et al. [19] and Schäfer et al. [161].

6.2.2. Crack Initiation Lifetime

The fatigue crack initiation time of a component or material constitutes a large fraction of the total lifetime, see Krupp [90]. With decreasing strain amplitude for the cyclic loading, the fraction increases. Additionally, as stated by Suresh [176], the crack initiation cycles respectively time is strongly influenced by the microstructure. Motivated by those facts, a method for the prediction of number of cycles to crack initiation is introduced, following Boeff et al. [19] and Arnaudov et al. [5]. To explain the method the sketch of the estimation procedure in Figure 6.2 is used.

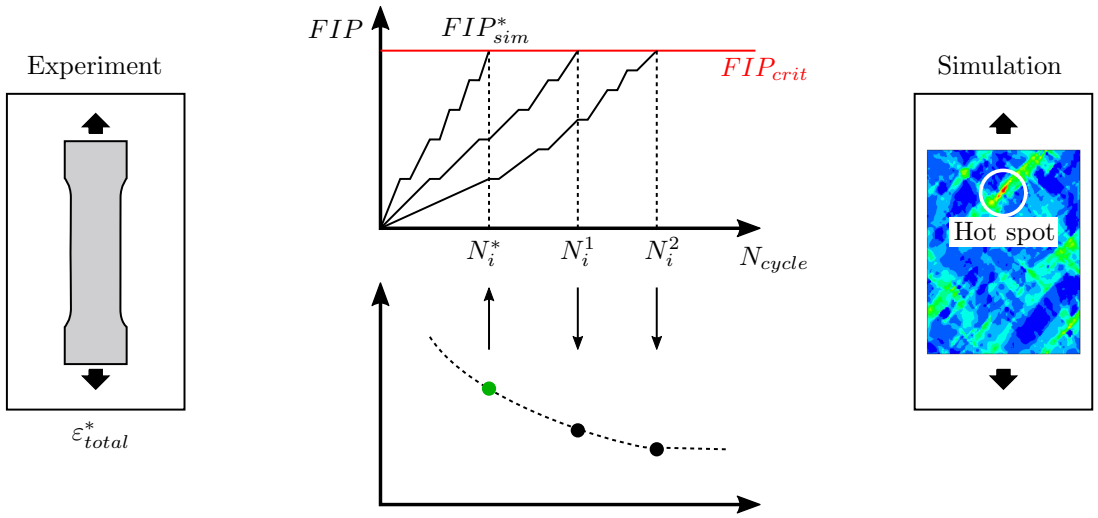

Figure 6.2: Prediction scheme based on a single experiment and subsequent micromechanical simulations leading to a strain-based crack initiation curve, inspired by [19].

As described by Manonukul & Dunne [107] a critical value for the fatigue indicator parameter FIP_{crit} has to be determined, red line in Figure 6.2. It is assumed with reaching this material specific damage value FIP_{crit} of the scalar FIP, fracture-inducing irreversible damage or crack initiation takes place. In order to find out the critical FIP, a strain-controlled experiment at $R_\varepsilon = -1$ is required at an arbitrary total strain amplitude $\varepsilon^*_{a,t}$. In this work $\varepsilon^*_{a,t} = 0.7\%$ is used. The number of loading cycles to crack initiation N^*_i in the experiment can now be used to determine FIP_{crit}. A micromechanical simulation is performed at the same strain amplitude as the experiment on a RVE which represents the microstructure of the tested specimen. The development of the scalar FIP is tracked at the location of its maximum, called the hot spot. Not the entire monotonically increasing FIP is of interest, but the development of the FIP in each cycle. To mimic cyclically stable material behavior, the simulation is carried out until the FIP reaches a saturation state, meaning that the amount of FIP gathered in one cycle does not change from the previous to the current cycle. This simulated saturated FIP ΔFIP^*_{sim} can now be used to calculate the critical FIP by a multiplication with the number to crack initiation from

the experiment.

$$FIP_{crit} = \Delta FIP^{*}_{sim} \cdot N^{*}_{i} \,. \tag{6.5}$$

The number of cycles to crack initiation of different strain amplitudes ε^{j}_{total} can be simulated without further experiments, under the assumption that FIP_{crit} is independent of the external loading. Therefore, simulations are performed at the strain amplitudes of interests and their saturated FIP ΔFIP^{j}_{sim} is extrapolated to the critical FIP yielding the crack initiation lifetime, see the bottom diagram of Figure 6.2,

$$N^{j}_{i} = \frac{FIP_{crit}}{\Delta FIP^{j}_{sim}} \,. \tag{6.6}$$

Note, that the hot spot of the maximum FIP might vary at different amplitudes, such that the critical location must be determined newly for every amplitude. Manonukul & Dunne [107] assume, that the critical FIP remains constant across the LCF and the HCF regime such that it can be used for strain amplitudes in the beginning of the HCF regime, while it is only calibrated against LCF data. Furthermore, the assumption is made, that the fatigue crack initiation stage represents the lifetime governing regime. Thus, the evolution of short cracks on the microscale is neglected.

The evolution of the FIP over the cyclic loading procedure underlies a hardening or softening behavior until it reaches a saturated state and the FIP is constant for each further cycle. The number of necessary simulated cycles varies with the material and loading conditions. Castelluccio [29] proposes 3 to 10 cycles, while Manonukul & Dunne [107] state that 2 to 3 cycles should be sufficient. To ensure reaching a fully saturated state, 4 to 5 loading cycles are simulated in this work for pure air atmosphere. Kinematic processes of diffusion and redistribution must be taken into account when the hydrogen transport model should be considered. Hence, more cycles must be simulated to yield a sufficient time period for the diffusion. It is important to keep in mind, that the crystal plasticity model is length scale and time-independent. Whereas the hydrogen diffusion is a length scale and time-dependent process. Loading frequencies and dimensions must be accurately taken from the performed experiments to obtain comparable simulation results. With the above introduced FIPs, the hydrogen content is not considered yet. A modification of FIP_p is proposed to account for the local hydrogen concentration in trap sites as an additional driving force for fatigue.

6.2.3. Hydrogen Dependent FIP

Nanninga [126] states that the presence of hydrogen accelerates crack initiation by an increase in accumulated plastic strain. Therefore, FIP_p is scaled with a hydrogen dependent term in each cycle, which rises the local accumulated plastic strain with increasing local hydrogen content in trap sites. The modification of the FIP reads

$$FIP_H(\bar{C}_T) = \bar{\varepsilon}^{p}(\bar{C}_T) = \int_0^t \left(1 + \frac{\bar{C}_T H_T}{\bar{C}_0}\right) \sqrt{\tfrac{2}{3}\, \boldsymbol{L}^{p} : \boldsymbol{L}^{p}}\, dt \,, \tag{6.7}$$

where $\bar{C}_0$ is the hydrogen lattice concentration applied on the boundaries which will be reached when the diffusion process is in equilibrium. H_T is a parameter, which is determined with one fatigue experiment in hydrogen at a single total strain amplitude. The cycle number of this experiment is taken to fit the parameter H_T such that simulation result at this strain amplitude captures the deteriorating effect of the hydrogen quantitatively.

6.3. Numerical Fatigue Estimation

For the simulative prediction of the fatigue lifetime to crack initiation the material is cyclically loaded. As introduced in Section 5.4.2 the macro-homogeneity condition has to be fulfilled. Periodic boundary conditions are most suitable for RVEs, since they guarantee equivalent shape topography as well as opposing tractions on opposite surfaces and thereby yield the most realistic deformation behavior. Following Boeff [18], displacement or force boundary conditions can be applied to the free nodes shown in Figure 5.11. Displacement boundaries can be thought of as a prescribed macroscopic strain state under consideration of the RVE's edge length, while force boundary conditions can be transformed to a prescribed macroscopic stress state considering the RVE's cross-sections.

Since all experiments are performed strain-controlled, only displacement boundaries are applied in this work. As shown in Figure 6.3 vertex V1 is fixed for the 2D case in the two spatial directions, V2 and V4 are fixed in 1 and 2 direction, respectively and a displacement load $\boldsymbol{u}$ is only applied in 2 direction on vertex 4. Due to periodic boundary condition all nodes on the upper edge are loaded likewise. The loading frequency is adopted from the experimental procedure and is $f_{load} = 1$ Hz. In the following subsections the focus is first set on a pure fatigue simulation without accounting for hydrogen and later different loading scenarios for coupled crystal plasticity with hydrogen diffusion are applied and investigated.

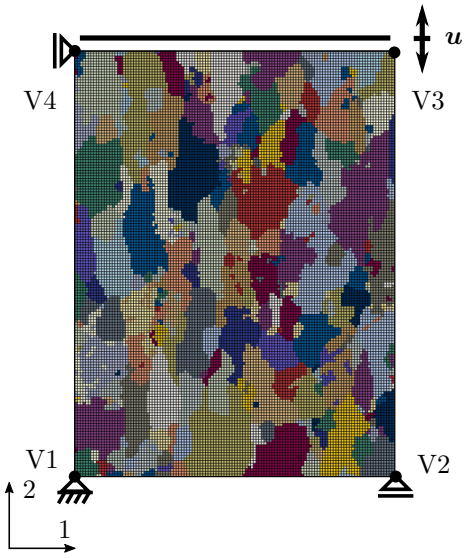

Figure 6.3: RVE with applied mechanical boundary conditions on underlying microstructure. A cyclic loading $\boldsymbol{u}$ is applied together with periodic boundary conditions.

6.3.1. Comparison of Proposed FIPs

A comparison of the suitability of the proposed FIPs to predict the fatigue behavior in air atmosphere is drawn in Figure 6.4. The experimental results are plotted as black dots with the corresponding experimental Manson-Coffin relation as solid black line. The simulated number of cycles to crack initiation for FIP_p, FIP_{FS} and FIP_W are indicated by the orange plus markers, the blue crosses and the red diamonds, respectively. According

to the plot, the accumulated plastic slip shows a good qualitative agreement with experimental results. At the largest applied total strain amplitude $\varepsilon_{a,t} = 1.0\%$ the numerical prediction becomes slightly non-conservative but is still close to the experiments. For strain amplitudes $\varepsilon_{a,t} \leq 0.2\%$ increased deviations are observed, between the simulation and experimental data. The prediction based on the Fatemie-Socie parameter as well as the dissipated energy criteria show a similar trend with a good qualitative agreement to the experimental data. They are predominantly conservative and exhibit an increasing deviation at lower total strain amplitudes. The slightly higher number of cycles to crack initiation in micromechanical simulations using FIP_W instead of FIP_p confirm observations by Sweeney et al. [178]. The deviation in the simulation results for smaller strain amplitudes can be explained by the overestimated amount of plasticity for small strain amplitudes by the proposed material model and the corresponding parameter set, see Figure 6.1. Another possible reason for the increasing deviations at small strain amplitudes could be the neglect of the first stages of fatigue crack growth. High applied strains in the LCF regime provoke a propagation of most nucleated cracks to fracture. Lower strain amplitudes of the HCF regime might nucleate cracks, but the subsequent deformation may rest and crack retardation must be considered. Przybyla et al. [147] stated, that the HCF regime is dominated by crack initiation together with microstructural small crack propagation.

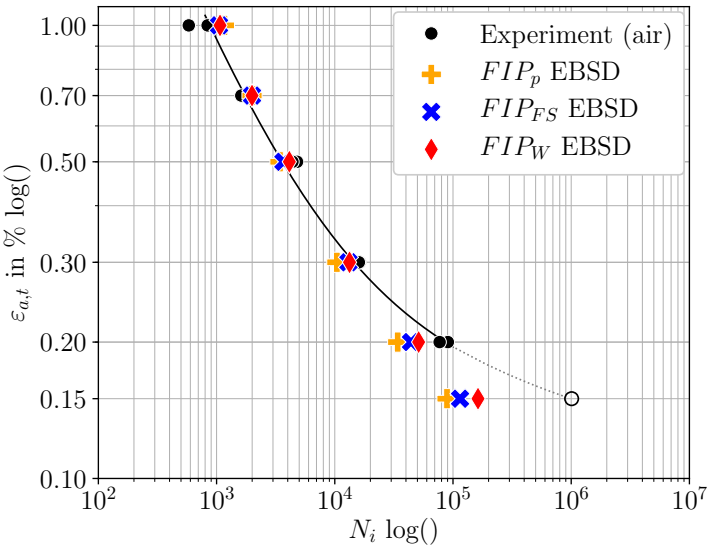

Figure 6.4: Comparisons of the fatigue crack initiation predictions based on the three proposed fatigue indicator parameters FIP_p, FIP_{FS} and FIP_W compared to results of experiments conducted in air atmosphere, see Section 4.2.2.

6.3.2. Influence of Critical Resolved Shear Stress

A sensitivity study is carried out to evaluate the influence of the mechanical material parameters listed in Table 6.1. Here, the focus is set on the critical resolved shear stress τ_c which is obtained by the multi objective calibration procedure described in Section 6.1. This parameter determines the onset of irreversible plastic deformation and hence, it is critical for the accurate simulative prediction of fatigue damage. The experimental determination of τ_c is very complex and mostly done only for a pure single crystal. Gottstein

[62] states, that the critical resolved shear stress should be equal for all slip systems. In this work as strong assumption is made, that the τ_c is also constant for all grains in the polycrystal. The Hall-Petch effect is neglected, which states that the grain size has an influence on dislocation movement due to the barrier effect of grain boundaries for to dislocation motion. A more realistic approach would include a grain size dependency to the critical resolved shear stress, such as proposed in Wu et al. [195]. However, further experiments such as nanoindentations are required to obtain this dependency. The approach of a constant value for τ_c used in this work is investigated by varying this value and evaluating the effect on the stress-strain response and the fatigue crack initiation prediction.

Besides the value determined in the calibration procedure, $\tau_c = 90$ MPa, a lower value of 70 MPa and a higher value of 110 MPa are used for the simulations. The effect of the stress-strain hystereses are plotted in Figure 6.5 a). In contrast to the best fit in green, the lower critical resolved shear stress (blue) leads to an overestimation of plastic deformation, indicated by the width of the hystereses. Premature plastic gliding leads to a reduced stress response for each total strain amplitude. Accordingly, the red line for $\tau_c = 110$ MPa shows the opposite behavior with a reduced plastic deformation proportion. The significance of these differences in the plastic deformation behavior on the prediction of lifetime to crack initiation is shown in Figure 6.5 b), where the accumulated plastic strain is used as the FIP. For low total strain amplitudes a decrease of the cycle number to crack initiation is observed with decreasing critical resolved shear stress. This is an expected behavior, since a faster onset of plastic deformation results in more accumulated plastic strain and the critical FIP value is reached earlier. Zooming into the hystereses for the lowest two total strain amplitudes shows that the width of the hysteresis at $\tau_c = 70$ MPa and $\varepsilon_{a,t} = 0.15\%$ match the width of the hysteresis at $\tau_c = 110$ MPa and $\varepsilon_{a,t} = 0.2\%$. This leads to the same number of cycles to crack initiation which can be seen in the vertical alignment of the lowest blue cross and the red cross above. For higher total strain amplitudes no change in the cycle number are predicted. Occurring shear stresses exceed the values for all critical resolved shear stresses already in the first cycle leading to a similar amount of accumulated plastic strain. With lower total strain amplitudes for cyclic loading the effect of the critical resolved shear stress and the related onset of plastic gliding becomes more relevant for the prediction of the fatigue crack initiation.

6.3.3. Microstructure Variation in Air

To evaluate the influence of the microstructure on the prediction of fatigue crack formation various different polycrystalline structures are generated with Neper [149]. The statistical input quantities governing the grain morphology are kept constant. Merely, the initial locations for the seeds, around which the grains grow, are varied randomly. The resulting microstructures M1 to M5 are illustrated in the upper row of Figure 6.6. Note, that the microstructures are not geometrically periodic. Hence, the other part of a grain cut by an edge of the domain cannot be found on the opposing side of the domain. Schneider et al. [165] show that a fully periodic topology and mesh discretization with periodic boundary conditions is not necessary in order to determine effective quantities if the domain contains a sufficiently large number of grains. With the comparison of different microstructures the sensitivity of the fatigue prediction scheme towards grain morphology is investigated. Therefore, each microstructure is discretized with 120×160 elements and four times cyclically loaded at different total strain amplitudes $\varepsilon_{a,t}$. The

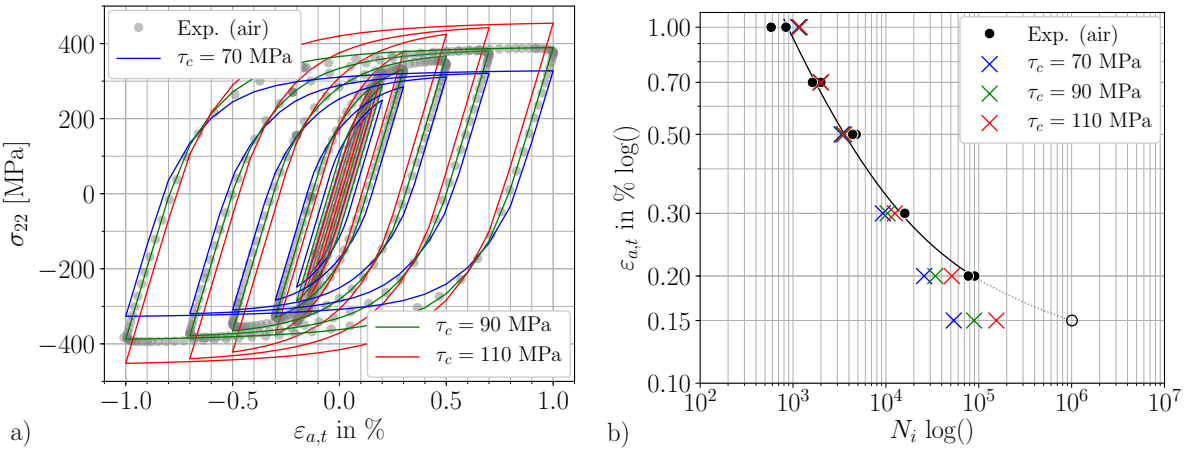

Figure 6.5: Effect of different critical resolved shear stresses τ_c on the simulative stress-strain response in air a) and on the predicted cycles to crack initiation b).

resulting accumulated plastic strain distribution is shown in the lower row in Figure 6.6 at a total strain amplitude of 0.2%. The hot spot with the maximum FIP is indicated by a black dashed circle for each structure. Note, that this location does not only vary with a different microstructure, but also with changing total strain amplitudes for a single microstructure. With the prediction method, introduced in Section 6.2.2, lifetimes are calculated for each microstructure with the accumulated plastic strain FIP_p and shown in Figure 6.7. The lifetimes for higher strain amplitudes show almost no difference between the different microstructures. With decreasing strain amplitudes $\varepsilon_{a,t} \leq 0.3\%$ microstructural differences have a greater influence on the total lifetime until fatigue crack initiation. But still the developing scatter band is rather small. At large total strain amplitudes shear stresses are sufficiently high to induce plastic slip in most grains. This results in a development of the maximum FIP per cycle independent of the underlying microstructure, whereas at small amplitudes gliding is only induced in certain grains with favorable orientation towards shearing. Therefore, the individual local microstructure and grain morphology is crucial. In summary, the influence of microstructural morphology on the fatigue lifetime to crack initiation is not as strong as the dependency of the material response on the material parameter set determined in Section 6.1. However, the predicted location of crack initiation clearly depends on the local grain orientation.

6.3.4. Model Extension to 3D Microstructures

So far only 2D RVEs are used as a simplification in form of cutting planes for actual 3D microstructures. With this approach the 3D nature of the polycrystal is not fully considered, neglecting more complex interactions of grains and inducing a different constraint behavior. However, this idealization to a 2D domain reduces the computational effort significantly and enables larger studies for parameter variation and sensitivity. Depending on the finite element mesh the 3D calculations may result in computational times severals orders of magnitude higher compared to 2D simulations. From a physical point of view a realization in 3D seems preferable. But an accurate and qualitative data set describing the 3D structure is often not possible to obtain for a material of interest, due to the enormous experimental effort, see Section 5.4.1. Usually, only 2D information are available, such as in this work for the ferritic steel. Nonetheless, the differences between

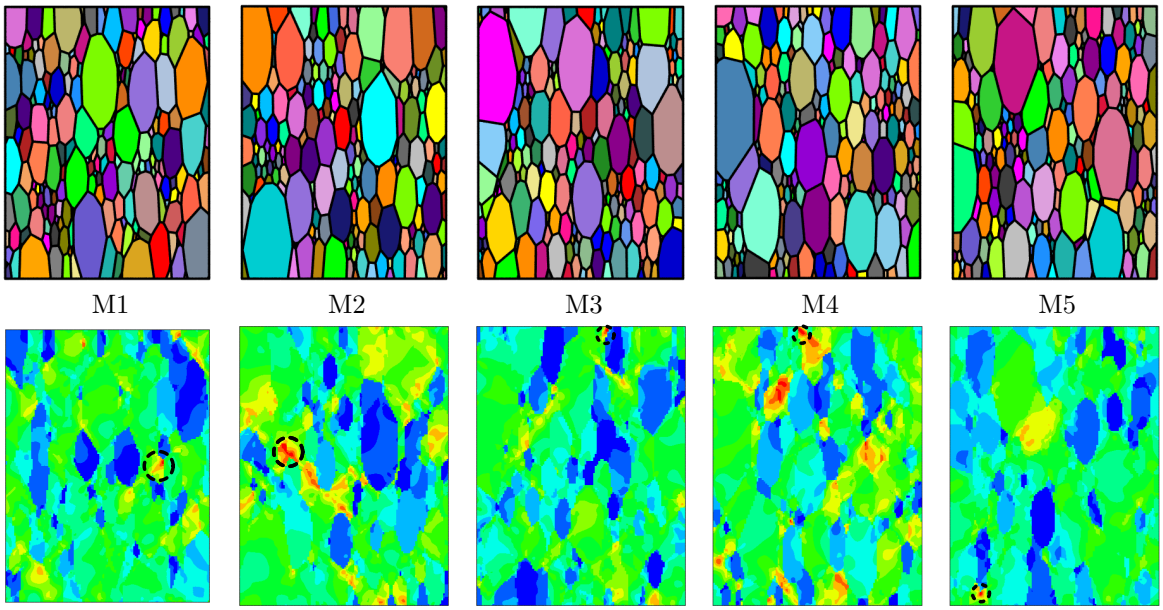

Figure 6.6: Variation of synthetic microstructures M1-5 with different seed locations. The upper row shows the different polycrystals and the lower row gives an impression of the FIP_p distribution at the end of 4 simulated cycles at $\varepsilon_{a,t} = 0.2\%$ with critical FIP location marked by a dashed black circle.

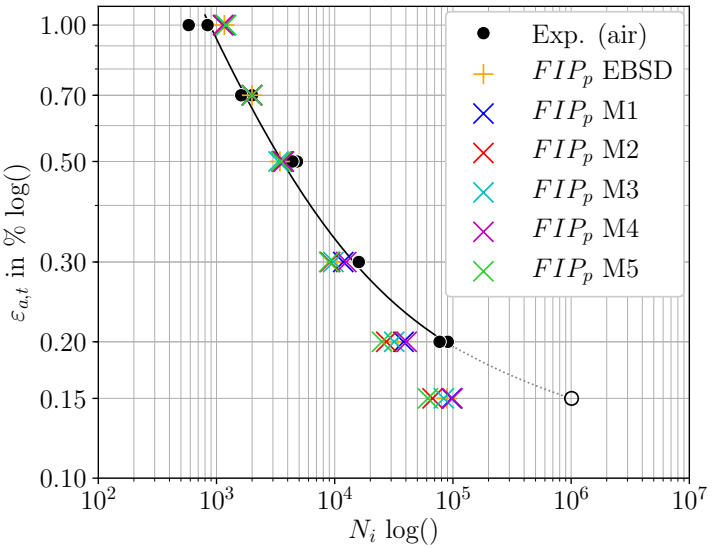

Figure 6.7: Numerical prediction of fatigue crack initiation under variation of synthetic microstructures M1-5 indicated by x-shaped markers using the accumulated plastic strain FIP_p. The experimental data (dots) of Section 4.2.2 and the results of simulation performed on the EBSD-based microstructure (crosses) of Figure 6.4 are plotted for comparison.

a 2D and a 3D simulation on the prediction for fatigue crack initiation are investigated by means of a synthetic 3D microstructure generated with statistical information of 2D EBSD data about the grain morphology.

The artificial microstructure, shown in Figure 6.8 a), is generated with Neper and con-

tains 1325 grains. As in the 2D structure a stretching of the grains is apparent. Again, the admissible orientations for the grains are taken from the EBSD data, yielding the texture shown in Figure 5.9. The RVE is discretized with $50 \times 50 \times 50$ C3D8R elements as illustrated in 6.8 b). Before running the fatigue simulations, the parameter identification

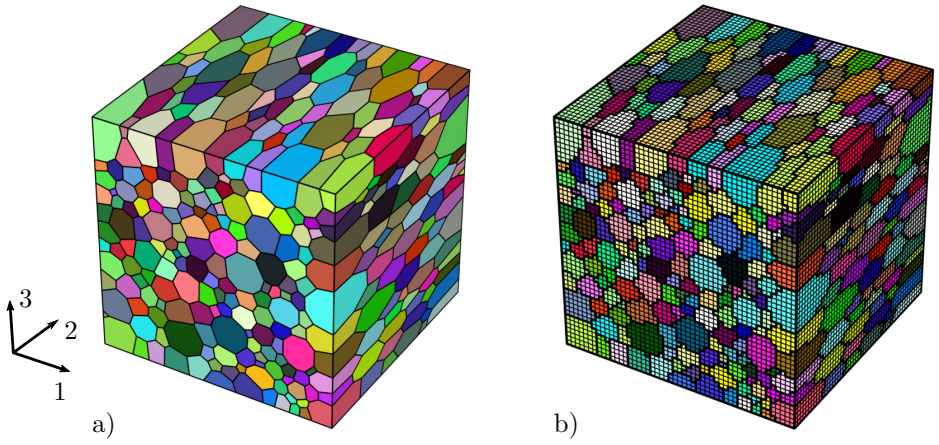

Figure 6.8: 3D microstructure based on statistical grain data from EBSD analysis created with Neper in a) and discretized RVE with 125 000 elements in b).

process introduced in Section 6.1 must be repeated for a 3D structure as described in Schäfer et al. [160]. The application of 3D periodic boundary conditions is implemented analogously to the 2D problem and is in detail described by Boeff [18]. Due to the differences between the plain strain 2D formulation and the 3D elements the effective stress response to strain-controlled cyclic loading is differing. To match the experimental hystereses as in Figure 6.1 a new set of material parameter is determined in the calibration procedure. In comparison to Table 6.1 a new critical resolved shear stress as well as new constants for the kinematic hardening model are obtained and listed in Table 6.3. With these parameter on hand the structure depicted in Figure 6.8 is cyclically loaded in direction of the second axis of the marked coordinate system at different total strain amplitudes. The loading conditions are the same as for the 2D problem, including a strain ratio of $R_\varepsilon = -1$ and a loading frequency of 1 Hz.

Parameter	Name	Value	Unit
τ_c	Critical resolved shear stress	104.5	MPa
A_1	Kinematic hardening 1	27107.9	MPa
A_2	Kinematic hardening 2	900.5	-

Table 6.3: New parameters for the 3D crystal plasticity calculation.

The FIP evolution during the 3D crystal plasticity simulation leads to the results plotted in Figure 6.9. Besides the experimental fatigue data, the already known simulation results for a 2D structure directly based on the EBSD data marked by red crosses are used for comparison. The predicted cycle numbers to fatigue crack initiation are indicated by the blue x-shaped markers. Two fatigue measurements are considered, namely the

accumulated plastic strain FIP_p and the Fatemie Socie measure FIP_{FS} in Figure 6.9 a) and b), respectively. For both FIPs the predicted crack initiation cycles for $\varepsilon_{a,t} \geq 0.3\%$ are almost the same for the 2D and 3D simulations. Only for the lower total strain amplitudes variations occur, whereas the 3D simulation results in lower cycle numbers to crack initiation for FIP_p and higher values for N_i for FIP_{FS}. Main difference between the two FIPs is the inclusion of a stress dependent term, the maximum normal stress to the plane with the maximal local plastic shear range, see (6.2). Due to the third dimension slight changes in the stress distributions occur which are negligible in the FIP evolution for the LCF and HCF regime with high strain amplitudes but with more influence at lower strain amplitudes. Comparing the 2D and 3D simulation results with each other justifies the simplification of pure 2D RVEs for numerical studies of the micromechanical model.

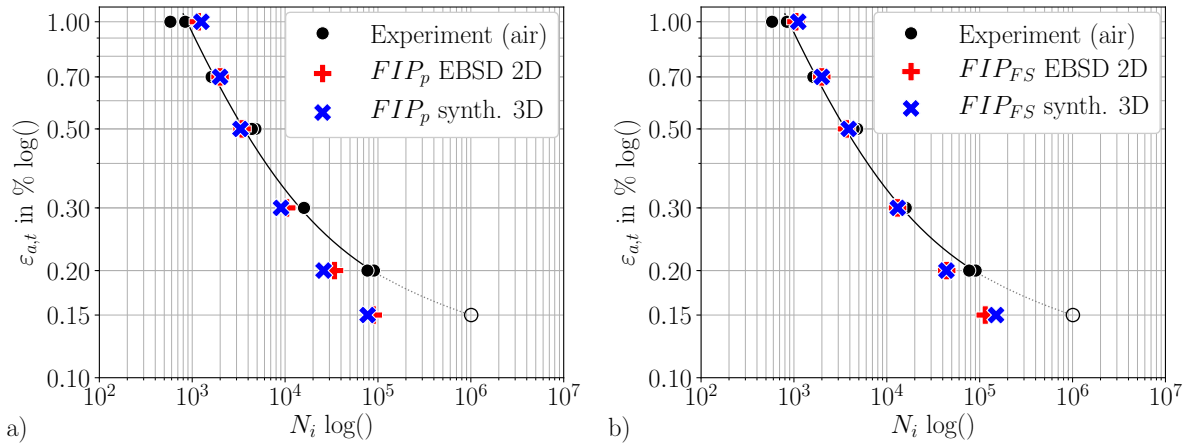

Figure 6.9: Fatigue crack initiation prediction for a 2D EBSD based RVE and a 3D synthetic RVE. The FIPs used for the evaluation are the accumulated plastic strain FIP in a) and the Fatemie Socie FIP b). Both are compared to experimental data 4.2.2.

6.3.5. Prediction under Hydrogen Atmosphere based on EBSD Data

To investigate the adequacy of the modified hydrogen dependent fatigue indicator parameter FIP_H defined in (6.7) the 2D EBSD based microstructure is taken as simulation domain with boundary conditions as shown in Figure 6.3. Additionally the following hydrogen related boundary conditions are applied. The RVE is preloaded with the initial lattice hydrogen concentration $\bar{C}_0$. Furthermore the concentration $\bar{C}_0$ is applied as constant concentration boundaries on all four edges over the whole simulation period. To allow kinematic processes related to hydrogen, such as diffusion and lattice-trap site interaction, 15 loading cycles are carried out.

A sensitivity study is performed to evaluate the effect of the dimensionless parameter H_T in the modified FIP. Therefore, the parameter is varied in a range of $H_T = [0.0, 0.1]$. The hydrogen dependent term in the FIP formulation (6.7) vanishes by setting H_T to zero. Hence, no hydrogen influence is considered and the hydrogen FIP is reduced to the accumulated plastic slip FIP

$$FIP_H(H_T = 0) = FIP_p\,. \tag{6.8}$$

With increasing H_T the effect of trapped hydrogen on the accumulated plastic strain grows, causing a larger amount of accumulated plastic strain per cycle. Moreover, the relation for the evolution of number of trap sites $N_T(\bar{\varepsilon}^p)$ is now dependent on the hydrogen content in traps $N_T(\bar{\varepsilon}^p(\bar{C}_T)))$. Equation (6.7) states, that a higher hydrogen concentration in traps leads to more accumulated plastic strain which results in an increase in number of traps sites, following the relation in (5.21). This concatenation of dependencies yields a mutually supported accelerated damaging effect, since new available empty trap sites bind more hydrogen atoms from the lattice sites to traps resulting again in a higher concentration $\bar{C}_T$. Results of the fatigue simulations are plotted in Figure 6.10. The critical FIP was determined at $\varepsilon_{a,t} = 0.7\%$ and $H_T = 0.0$ together with the corresponding experiment in air atmosphere. The predicted cycle number without hydrogen influence is indicated by green crosses. A reduction of the lifetime is obvious with increasing values for H_T. For strain amplitudes $\varepsilon_{a,t} > 0.3\%$ the predicted lifetimes differ significantly from each other, while for the two lower amplitudes similar lifetimes are obtained numerically. This observation is a consequence of the accelerated damaging effect mentioned above, resulting from the mutually supported plastic stain and hydrogen impact at higher total strain amplitudes. The identification of an optimal value for H_T within the proposed

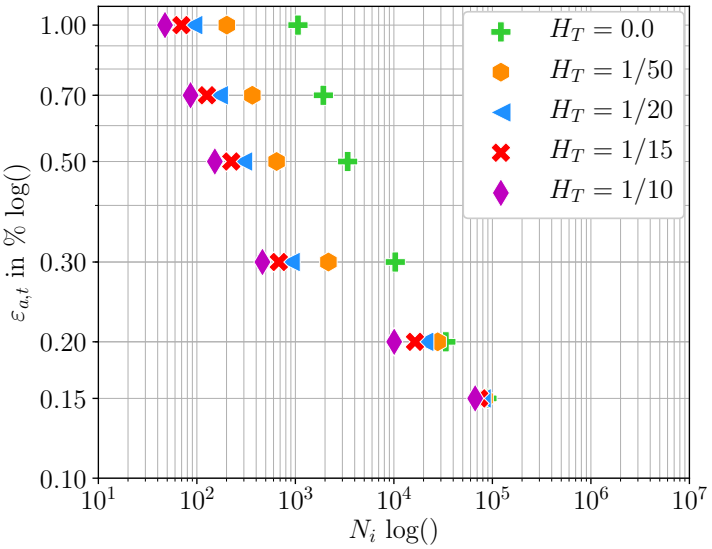

Figure 6.10: Parameter study evaluating the sensitivity of H_T on the influence of the local trapped hydrogen concentration $\bar{C}_T$ on the FIP.

phenomenological approach to hydrogen influenced fatigue prediction requires one fatigue experiment in hydrogen atmosphere at a single total strain amplitude. Here, $\varepsilon_{a,t} = 0.7\%$ is used and the optimal value is found as $H_T = 1/15$. A juxtaposition between the simulative predicted and experimentally measured cycles until fatigue crack initiation in both, air and hydrogen atmosphere, is shown in Figure 6.11. Measured fatigue data are represented by black dots for air and blue triangles for hydrogen atmosphere. Solid lines indicate the corresponding Manson-Coffin and Morrow fits. The green cross stands for the numerical calculation using the standard FIP_p, while the red x-shaped markers symbolize results using the modified FIP_H. As seen before, accumulated plastic slip agrees qualitatively well with experimental results. While predicted results for higher strain amplitudes are rather non-conservative, an increasing deviation between simulation and experimental

results can be seen for lower strain amplitudes. Simulating cyclic loading in hydrogen atmosphere and using the modified hydrogen dependent FIP the qualitative comparison agree again well with the experiments. The characteristic reduction of cycles to fatigue crack initiation under hydrogen was observed by SCHAUER [162, 163]. The bending of the strain-cycle curve is captured adequately by the numerical model and the modified FIP. However, similar trends are revealed, where the cycle number is underestimated increasingly for strain amplitudes lower than 0.3%. These deviations can be caused by a discrepancy of the simulated stress-strain hystereses at small strain amplitudes, see Figure 6.1. As described in ELLYIN [49], an increased level of plastic deformation energy results in a reduced fatigue lifetime. Another possibility for increased deviations at small total strain amplitudes could be caused by neglecting the crack growth in its early stages. Lower strain amplitudes in the HCF regime are sufficiently large to nucleate cracks, but in reality these cracks may stop and also crack retardation may become relevant which increases the experimentally observed lifetime until initiation. As described in Section 4.2 a load drop of 10% indicates a technical crack initiation, which might be insufficient for an exact tracking of different crack growth stages.

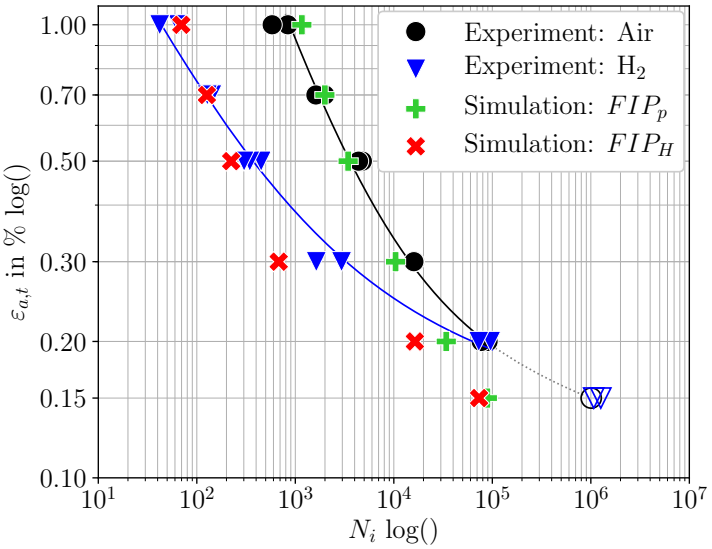

Figure 6.11: Numerical predicted strain-cycle curves in air and hydrogen atmosphere in comparison with experimental findings, see Section 4.2.2. The hydrogen degradation parameter is set to $H_T = 1/15$.

6.3.6. Variation of Hydrogen Boundary Conditions

The conducted experiments have been performed on samples which were not in contact with hydrogen before testing. The charging takes place during fatigue testing only. Nevertheless, the possibility of preloading exists and is analyzed by SCHAUER [162]. The developed simulation tool provides the flexibility to test various boundary conditions modeling different realistic scenarios. Therefore, the hydrogen boundary conditions illustrated in Figure 6.12 are covered in several simulation runs. The first scenario S1 represents the fully saturated sample which is loaded with the initial lattice concentration $\bar{C}_0$. A constant hydrogen atmosphere in the experiment is simplified modeled in the simulation with a constant concentration boundary also set to $\bar{C}_0$. In scenario S2 the sample is initially

hydrogen free with a constant hydrogen concentration on the boundaries during cyclic loading. A precharged sample is given in scenario S3 with a subsequent testing in air atmosphere. S4 serves to investigate the influence of a passivation layer with a barrier or accelerating effect on the hydrogen uptake and the consequences on fatigue. During all scenarios, the diffusion coefficient for bulk diffusion is as given in Table 6.2. However, the diffusion coefficient for the surface layer in scenario S4 is varied. Hereby, the values range as follows

$$\begin{aligned} \mathrm{S4}_1: &\quad D_L^{surface} = 1.27 \cdot 10^{-3} \\ \mathrm{S4}_2: &\quad D_L^{surface} = 1.27 \cdot 10^{-4} \\ \mathrm{S4}_3: &\quad D_L^{surface} = 1.27 \cdot 10^{-5} \\ \mathrm{S4}_4: &\quad D_L^{surface} = 1.27 \cdot 10^{-6} \end{aligned}$$

and serve to model reduced diffusion velocities through a surface layer around the microstructure without claim on physical correctness. The expected hydrogen diffusion flow is indicated by the arrows. While in S1 a slight diffusion or effusion process is possible, in S2 a pure hydrogen uptake is expected. In S3 only effusion of hydrogen is possible and scenarios of S4 are expected to be similar to S2 but with a decelerated hydrogen uptake over the passivation layers with lower diffusivities.

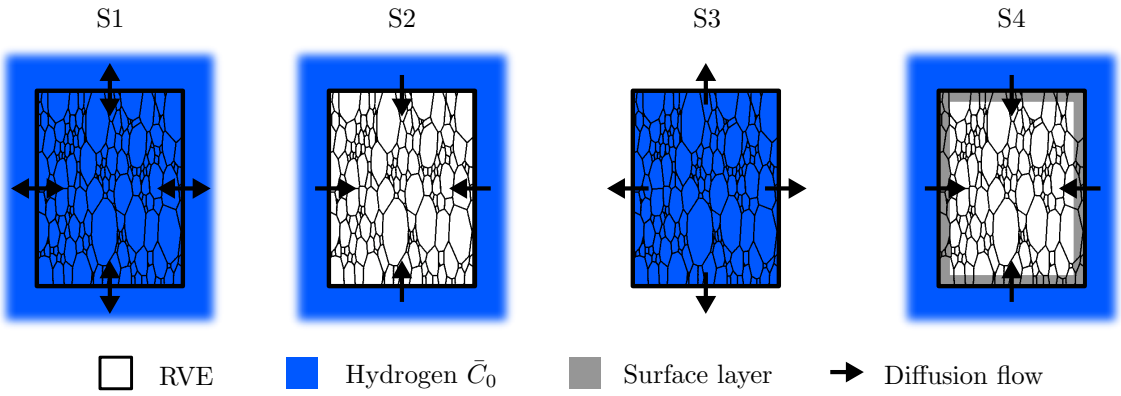

Figure 6.12: Schematic illustration of different hydrogen loading scenarios S1-S4 being applied by means of concentration boundary conditions. The initial hydrogen concentration $\bar{C}_0$ at boundaries and in the RVE are illustrated together with the main diffusion directions.

Contour plots of lattice and trap concentrations as well as the hydrogen dependent FIP are depicted for the scenarios in Figures 6.13-6.15. The Figures are organized such that each scenarios has its own column and different moments of the 2D simulation are captured in each row. The snapshots are taken at the beginning of the simulation, after 7 and after 15 loading cycles, indicated by the red dots at the bottom sketch for cyclic loading of Figure 6.13. All plots are taken from simulation with a total strain amplitude of $\varepsilon_{a,t} = 0.5\%$. Note, that the scales can vary between the different scenarios and are all logarithmically scaled to ensure a clear representation of the simulation data.

The lattice concentration $\bar{C}_L$ distributed over the microstructure shown in Figure 6.13 represents the loading condition at the beginning of the simulation in the upper row. S1 and S3 are initially preloaded by $\bar{C}_0 = 1.1 \cdot 10^{-11}$ mol/mm^3 and S2 and $\mathrm{S4}_2$ are set to

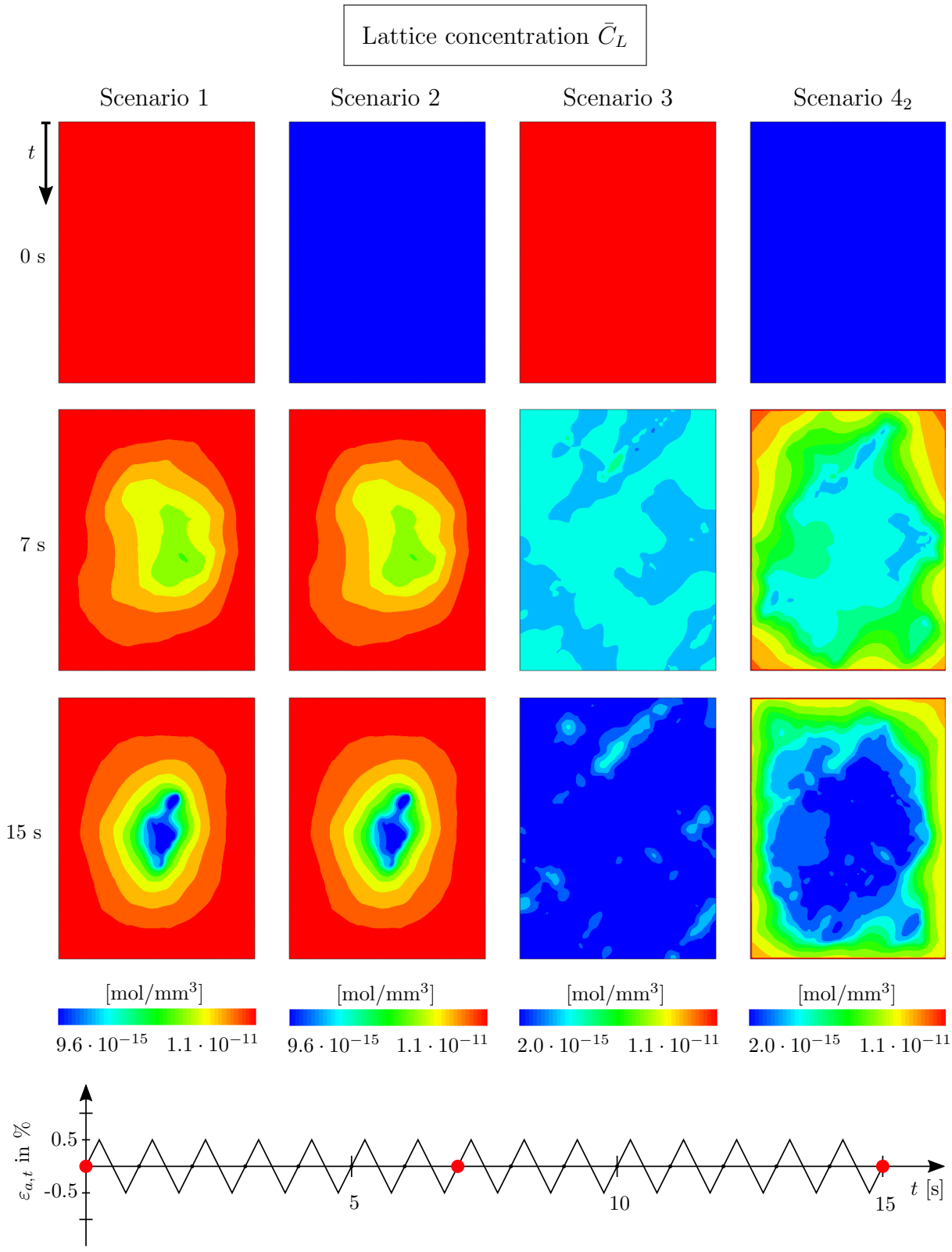

Figure 6.13: Contour plots of hydrogen lattice concentration $\bar{C}_L$ at initial time, after 7 and after 15 simulated cycles at a total strain amplitude of $\varepsilon_{a,t} = 0.5\%$ taken of different scenarios. The time spots are indicated by red dots at the schematic drawing of the cyclic loading over time.

10^{-20} mol/mm^3 to model almost no hydrogen content. The concentration must be greater than zero to avoid a division through zero in (5.36). At the chosen diffusion coefficient almost the entire microstructure is already saturated after 3 cycles in S2. After 7 loading cycles a reduction of lattice hydrogen can be seen in both S1 and S2 which is correlated to the increase of number of trap sites and the trapping of hydrogen visible in an increase of $\bar{C}_T$ in Figure 6.14. Since a constant hydrogen concentration is provided at the surface in both cases, a steady hydrogen inflow keeps the hydrogen lattice concentration at the edges of the domain high. However, in S3 where no hydrogen is provided from the outside, an effusion process is visible, causing a constant reduction of the lattice concentration. In $S4_2$ hydrogen diffusion into the microstructure is slowed down by the lower diffusion coefficient of the surface layer. Hence, hydrogen is faster trapped in the newly generated trap sites than it can enter the domain from the outside. After 15 simulated cycles even more hydrogen is trapped in the evolving trap sites, reducing $\bar{C}_L$ in S1 and S2 in the center region tremendously similar to $S4_2$. In S3 almost all hydrogen is bound in trap sites or effused over the domain boundaries. The inhomogeneous distribution is caused by two factors both triggered by the underlying microstructure. The first one and dominating part is the evolution of trap sites linked to the accumulated plastic strain, which is dependent of the grain orientation. The hydrostatic stress distribution is a second mechanical influence on diffusion and causes local changes in the concentration with an increase at high hydrostatic stress regions.

In Figure 6.14 all traps are initially empty but are filled immediately in S1 and S3 and for the both other scenarios as soon as lattice hydrogen diffuses inside of the domain. The initial trap sites density is given by inserting zero accumulated plastic strain into (5.21). With ongoing cyclic loading the accumulation of plastic strain and hence dislocations, causes new trap sites. Depending on the trap binding energy E_b these new trap sites are filled by binding the lattice hydrogen to the traps. Here, a rather high binding energy is chosen, see Table 6.2. Again S1 and S2 show the same behavior. With increasing number of trap sites after 7 or 15 cycles, more and more hydrogen is bound and the trap site concentration exceeds the lattice concentration. In comparison, the effusing lattice hydrogen results also in a lower trap site concentration, since less hydrogen is provided in the microstructure to be trapped. The process of hydrogen being reduced from the lattice site and subsequently trapped is visible in S3 after 7 cycles. Light blue areas of the $\bar{C}_L$ distribution indicate a reduced amount of lattice hydrogen compared to cyan regions. Exactly these light blue areas match the red zones in the $\bar{C}_T$ distribution where large amount of trapped hydrogen exist. The inhibited hydrogen uptake through the passivation layer in $S4_2$ allows only for an increase of trap site concentration at the edge regions of the microstructure.

A tracking of the hydrogen dependent FIP in Figure 6.15 shows similar distribution pattern for all scenarios at first sight. All cases start with zero FIP_H and the combination of accumulated plastic strain and growing trap site concentration increases the FIP valued with each cycle. Since scenarios are based on the same microstructure, the pure measurement of the accumulated plastic slip without hydrogen influence would result in the same contour plots for each case. However, differences in the FIP are here revealed after 15 cycles and under consideration of the scale bar of each scenario. S1 and S2 exhibit the highest values for FIP_H while $S4_2$ shows lower values and S3 the lowest. This observation coincides with the trap concentration profile discussed above. An increased trap concentration results in a higher value for the hydrogen dependent FIP which causes the

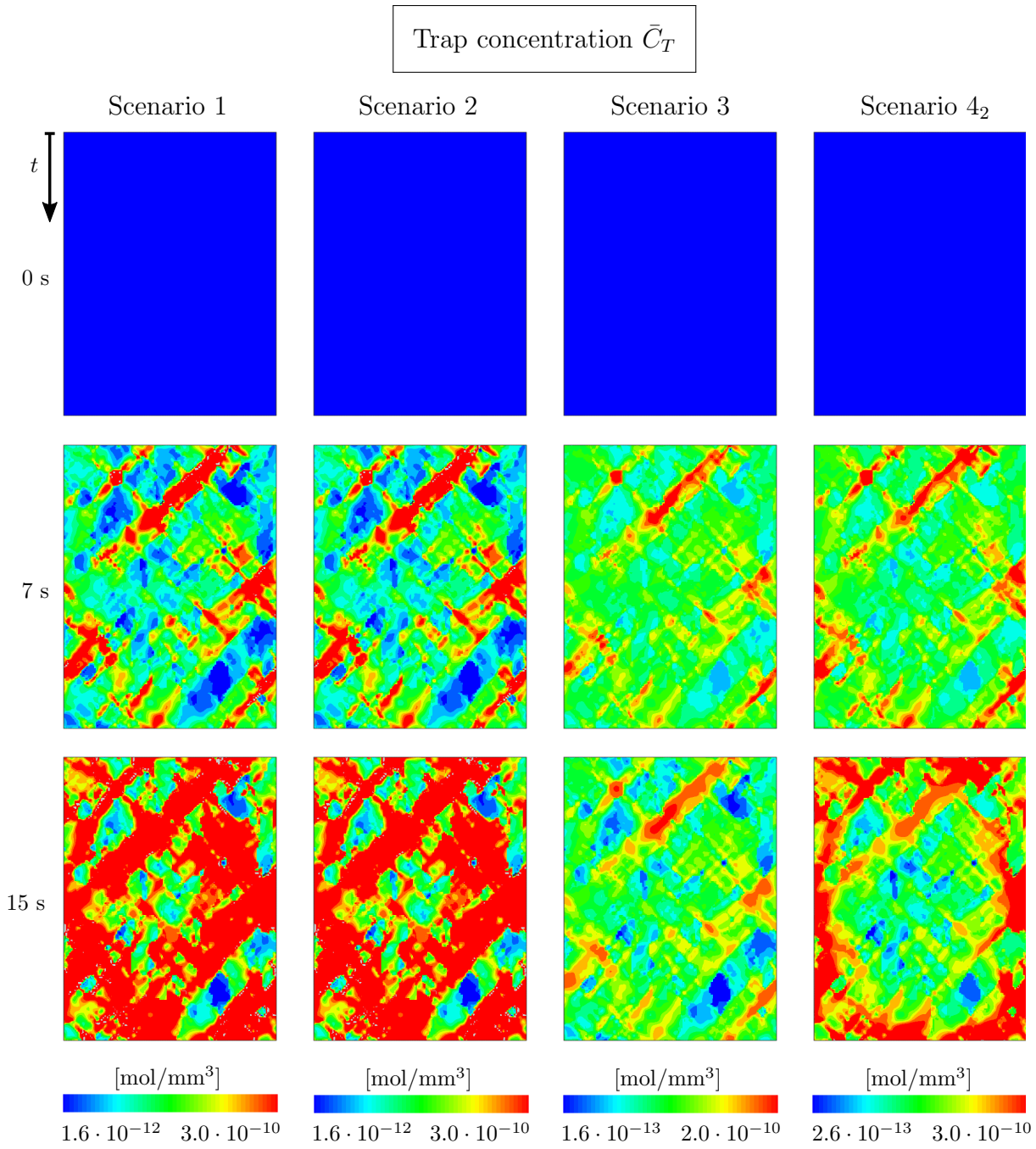

Figure 6.14: Contour plots of hydrogen trap site concentration $\bar{C}_T$ at initial time, after 7 and after 15 simulated cycles at a total strain amplitude of $\varepsilon_{a,t} = 0.5\%$ taken of different scenarios.

number of trap sites to increase further. Hence, the model reflects the mutually supported impact of plastic strain and hydrogen resulting in the accelerated damaging effect that was observed experimentally in Figure 4.10. The effect of the varying FIP distributions of different scenarios on the corresponding lifetimes are investigated in the following.

Predicted strain-life curves for the different hydrogen charging conditions are shown in Figure 6.16. Experimental data of the tests in hydrogen atmosphere are additionally plot-

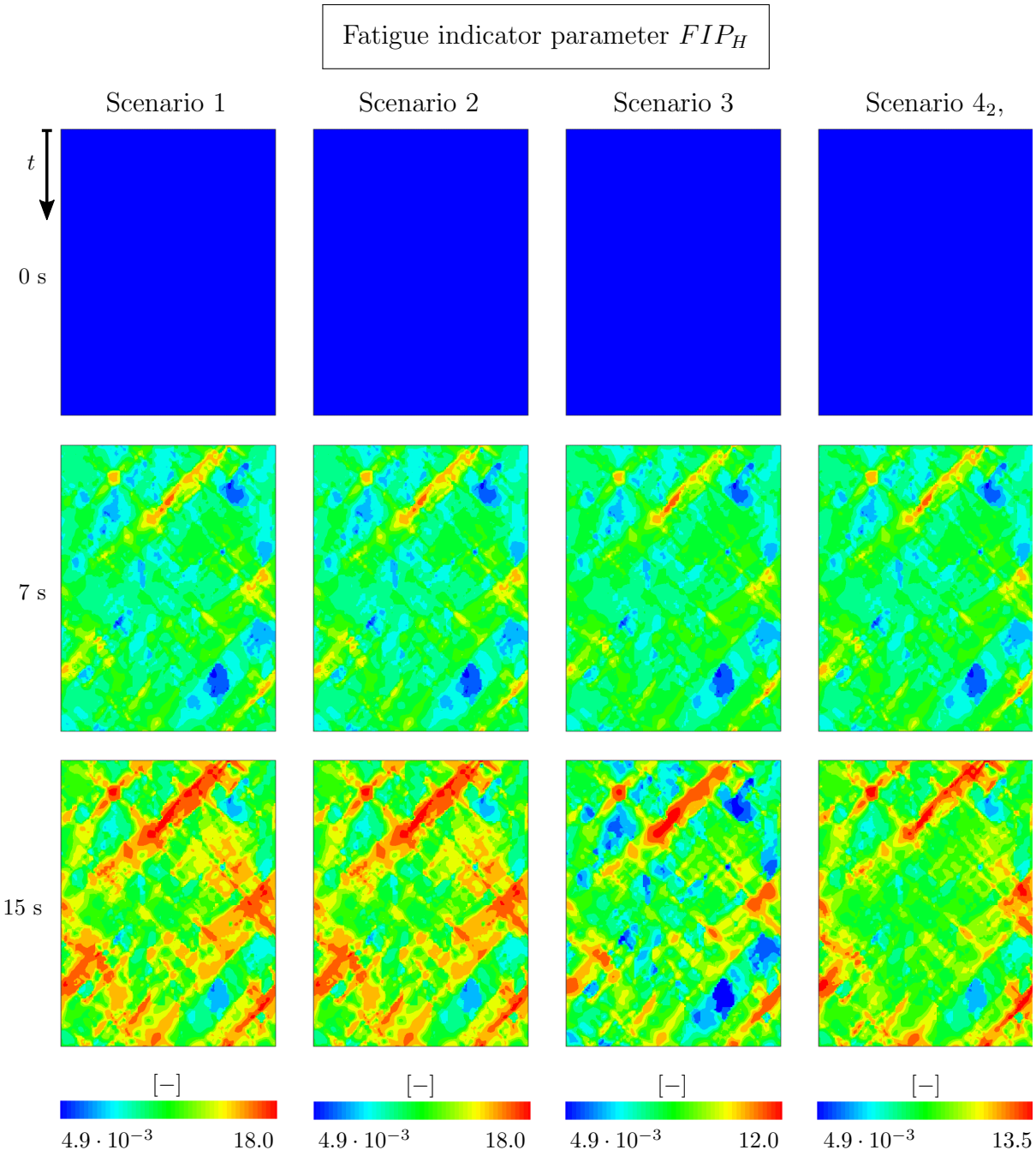

Figure 6.15: Contour plots of hydrogen dependent FIP FIP_H at initial time, after 7 and after 15 simulated cycles at a total strain amplitude of $\varepsilon_{a,t} = 0.5\%$ taken of different scenarios.

ted for orientation as blue triangles and the fitted strain-life curve. Results for scenarios S1-S3 are given in a) and for scenario S4 with varying diffusivities for the boundary layer are given in b). As expected considering the contour plots shown above, the simulation of the precharged samples in S2 exhibits the same fatigue properties as the samples of S1. The time for diffusion from the boundaries into the center of the sample during the 15 simulation cycles is sufficiently large to reach similar concentration values as in the precharged case. Therefore the trap site concentration is equal and FIP_H increases to the

same values. In contrast, S3 can bear more loading cycles at higher strain amplitudes. As can be seen in the contour plots the effusing hydrogen reduces the available lattice hydrogen concentration. The consequence is a reduction of trap site hydrogen and subsequently a lower fatigue indicator parameter as compared to S1 and S2. The effect intensifies at high strain amplitudes leading to larger amounts of accumulated plastic strain. Hence, more trap sites are generated which remain unfilled in S3. The same argument is used to describe the increased lifetime with decreasing diffusivity for the surface layer $D_L^{surface}$ Figure 6.16 b). However, the reduced amount of hydrogen in the center region of the microstructure is not caused by effusion but by a retarded hydrogen uptake over the surface layer. The extent of this retardation is determined by $D_L^{surface}$. Diffusion velocities one or two magnitudes smaller as the bulk diffusivity as in $S4_1$ or $S4_2$ have no influence on the fatigue lifetime. A further reduction of the diffusivity of the surface as in $S4_3$ or $S4_4$ hinders a fast hydrogen uptake and the amount of available lattice hydrogen for trapping is shorten. Consequently, a smaller trap site concentration reduces the hydrogen dependent FIP and leads to an increased predicted lifetime.

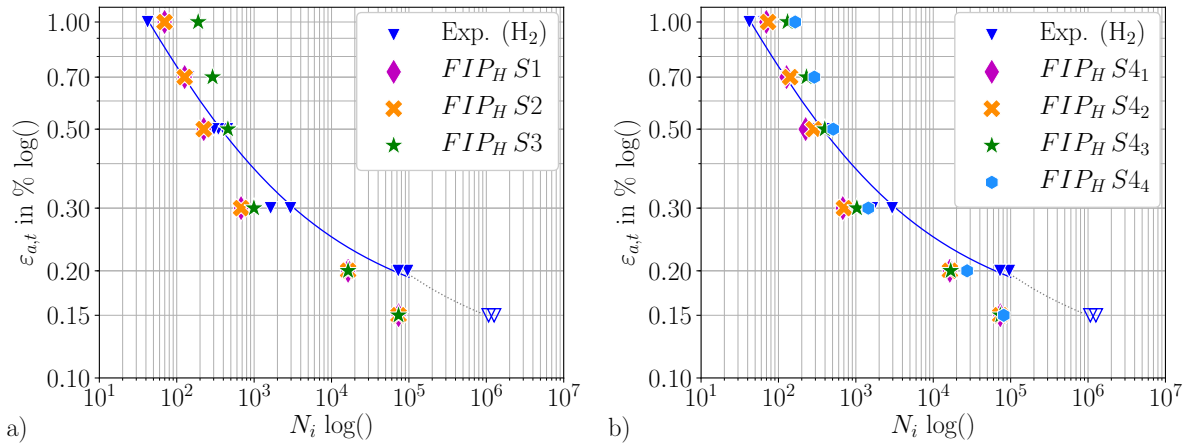

Figure 6.16: Predicted strain-life curves for varying boundary conditions of hydrogen supply to the microstructure in a) and an additional passivation layer with different diffusion properties in b) as defined in Figure 6.12 compared to experimental data of Section 4.2.2.

6.3.7. Modeling Approach of Grain Boundaries

The effect of grain boundaries on diffusion is not fully understood yet and controversially discussed, as stated in Section 2.3.2. Some groups foretell a decelerating effect by experimental observations while others describe an accelerated hydrogen diffusion along grain boundaries. Hoch [75] investigated the effects of grain boundary networks on the effective diffusivity in polycrystalline materials, using the finite element method. Therefore, an explicit modeling of grain boundaries is proposed. In this work, grain boundaries are modeled indirectly following the subsequent method. The creation of a RVE containing grain boundaries is illustrated in Figure 6.17. In the initial RVE all elements of a grain, depicted with the same color, have the same mechanical material properties $\mathcal{M}$ and the same diffusivity D_L. The diffusivity could be chosen separately for each grain. However, the same hydrogen diffusion velocity D_L is assumed for all grains and hence elements in the entire RVE. In a second step all elements on the boundary of a grain are identified. An algorithm checks all neighbors of each element in a loop over all elements, whether

they are from the same grain or from a different grain. If they are from a different grain, the initial element has at least one neighbor from a different grain and hence is marked as a grain boundary element, indicated in the figure by a white frame around the element. All elements marked as a grain boundary element from the same grain are saved in a new element set. This boundary element set shares the same material parameter set of the inner grain but might take a different diffusivity D_{GB} for the modeling of an enhanced or retarded diffusion through these boundary elements. The grain boundary elements are indicated on the right side of Figure 6.17 by a translucent coloring of their initial grain's color. This simplified scheme can be applied to synthetic microstructures in the 2D and 3D cases. Surface elements are not treated differently and can also be marked as boundary elements when having an adjacent edge or area with a neighbor grain.

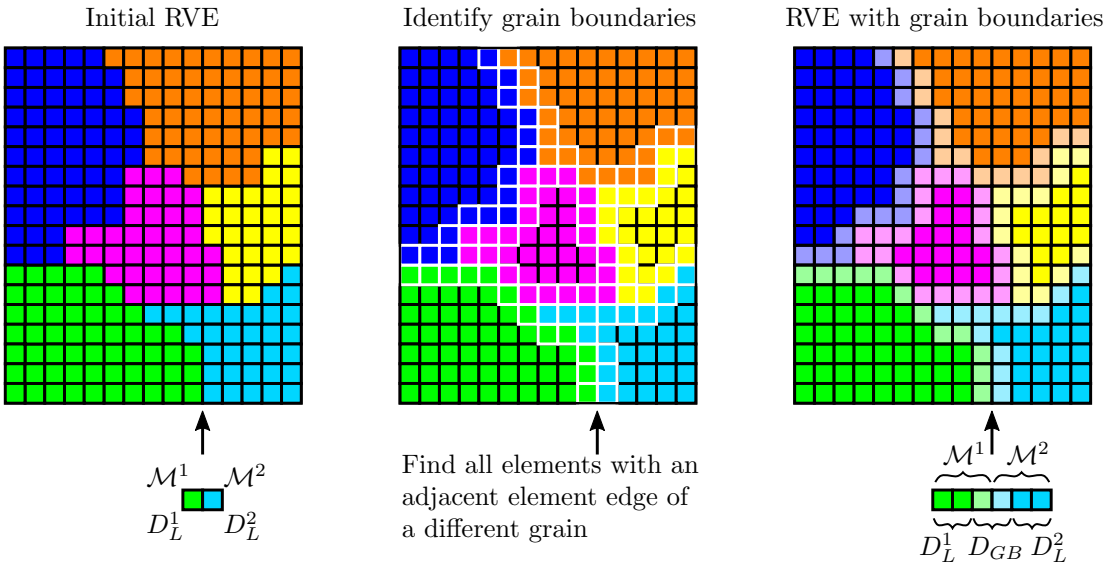

Figure 6.17: Steps to model grain boundaries with material properties $\mathcal{M}$ and diffusivities D_L for lattice diffusion in the bulk or D_{GB} in grain boundaries.

To investigate the influence of different diffusion velocities in the bulk and the grain boundaries, six scenarios GB1-6 are constructed for the 2D case. In the first three scenarios the bulk diffusivity is kept constant while the grain boundary diffusivity is varied and for the last three scenarios it is the other way round. The values of the diffusion velocities in each scenario is as follows

$$
\begin{aligned}
&\text{GB1}: && D_L = 1.27 \cdot 10^{-2} && \text{and} && D_{GB} = 1.27 \cdot 10^{-3} \\
&\text{GB2}: && D_L = 1.27 \cdot 10^{-2} && \text{and} && D_{GB} = 1.27 \cdot 10^{-4} \\
&\text{GB3}: && D_L = 1.27 \cdot 10^{-2} && \text{and} && D_{GB} = 1.27 \cdot 10^{-5} \\
&\text{GB4}: && D_L = 1.27 \cdot 10^{-3} && \text{and} && D_{GB} = 1.27 \cdot 10^{-2} \\
&\text{GB5}: && D_L = 1.27 \cdot 10^{-4} && \text{and} && D_{GB} = 1.27 \cdot 10^{-2} \\
&\text{GB6}: && D_L = 1.27 \cdot 10^{-5} && \text{and} && D_{GB} = 1.27 \cdot 10^{-2}
\end{aligned}
$$

where D_L denotes the lattice diffusivity in all grains and D_{GB} the diffusivity through grain boundaries. These conditions for the diffusivites are incorporated on the microstructure M1 shown in Figure 6.6 and the loading boundary condition S2 described in Figure 6.12.

The hydrogen lattice distribution over the loading cycles is selectively shown in Figure 6.18 for scenarios GB1-3 where the inner grain diffusivity is kept constant and the grain boundary diffusion coefficient varies.

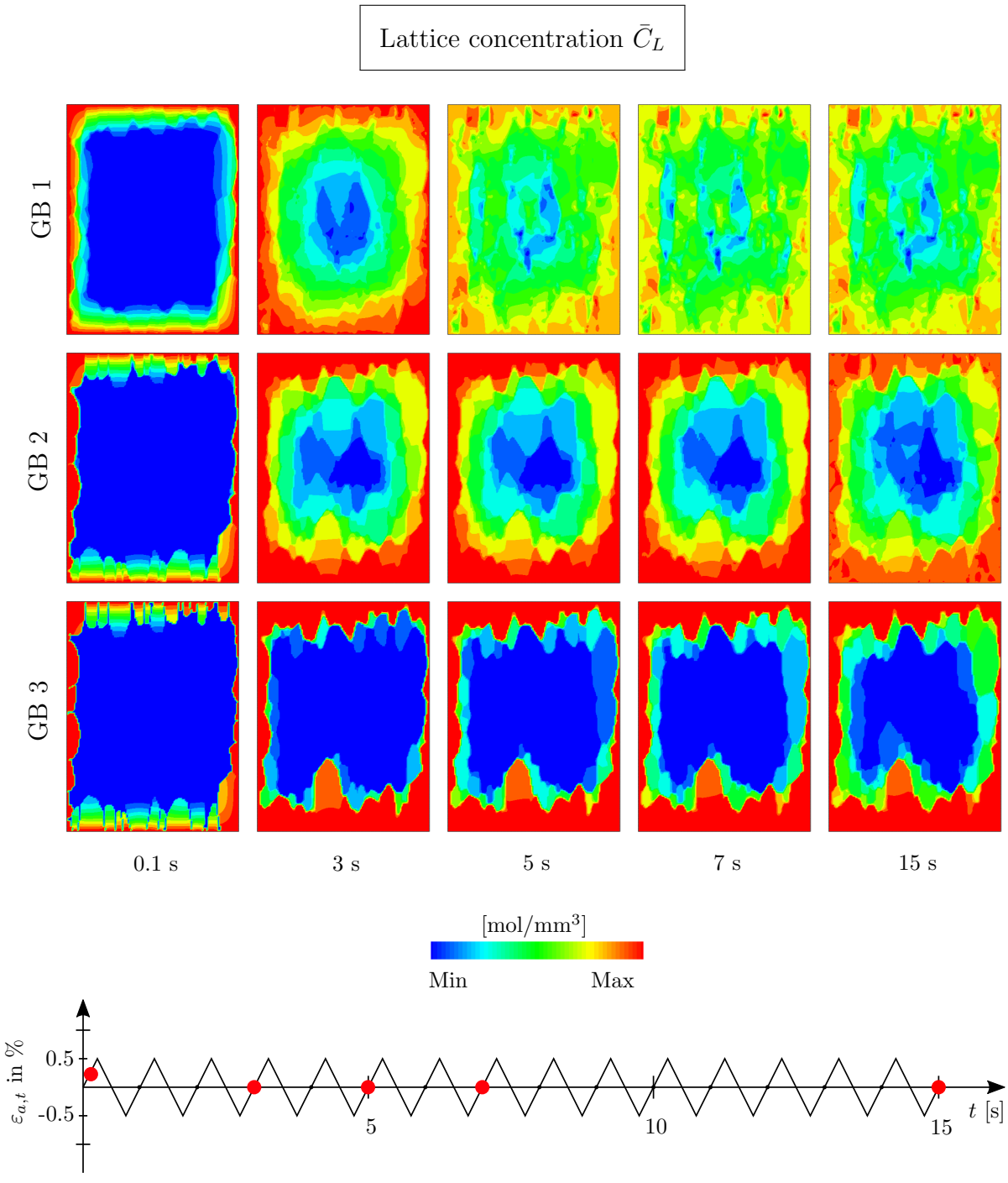

Figure 6.18: Contour plots of hydrogen lattice concentration $\bar{C}_L$ after 0.1, 3, 5, 7 and 15 s of simulated cyclic loading at a total strain amplitude of $\varepsilon_{a,t} = 0.2\%$. From GB1 to GB 3 a decreasing grain boundary diffusivity is imposed on the RVE.

Note, that the contour colors serve a qualitative comparison of diffusion velocities and concentration distributions. To ensure a good understandability, the minimum and maximum

limit of the color bar is individually determined for each snapshot during the simulation. Each scenario is plotted in a separate row while columns indicate different times for the snapshots. These time steps range from 0.1 s to 15 s simulation time and are illustrated with red points at the bottom sketch of the figure. The diffusion behavior can be compared to the plots of S2 in the second column of Figure 6.13, where no grain boundaries are considered. However, here the plots are taken of the simulation with a total strain amplitude of $\varepsilon_{a,t} = 0.2\%$. In GB1 the diffusion starts circularly from the domain boundaries to the inside. A major difference compared to S2 lies in the ragged and frayed edges of the diffusion front. This irregular pattern is provoked by the slightly reduced diffusivity of the grain boundaries. The effect becomes more present with decreasing values for D_{GB} as in GB2 or even more in GB3. Clearly visible is the intensification of the slower diffusion such that the grain boundaries become sharp and apparent due to the much lower concentration compared to the inner grains. With progressing time the diffusion increases the lattice concentration of the entire RVE in GB1. From cycle 5 to 15 an equilibrium state is reached between new hydrogen entering the domain and lattice hydrogen being trapped in the increasing number of trap sites. The effect of decelerated diffusion due to the barrier like grain boundaries can be seen at a progressive rate in GB2 and GB3. Here, the hydrogen diffuses much slower into the center region and in GB3 it barely passes through the first two grain boundary layers. From cycle 1 to 3 the first grain boundaries are overcome filling the grains in the second layer circle subsequently. A hydrogen increase in grains of the third layer cannot be seen until 15 s are over.

In scenarios GB4-6 the inner grain diffusivity varies while the diffusion through the grain boundary is kept at a constant velocity. The contour plots shown in Figure 6.19 follow the same arrangement as in Figure 6.18. A look on the first column with snapshots after 0.1 s of the simulation reveals an increasing retardation of diffusion through the grains from GB4 to GB6, where regions of higher concentrations are blurry and become more sharp. The grain boundaries operate as "diffusion highways" distributing the lattice hydrogen fast through the network of grain boundaries. Similar to GB1 a circular diffusion distribution is developed in GB4 over time. With increasing accumulated plastic strain and newly generated trap sites more hydrogen is bound to traps. In GB5 single grains of larger size in the center region have a reduced lattice concentration due to the retarding effect for diffusion through the grain. This becomes even more pronounce in G 6 where the whole grain morphology can be seen due to the concentration differences in the grain boundaries and the grains, especially the ones with a larger area. Note, that the choice of the diffusion coefficients for D_L and D_{GB} does not raise any claims on physical correctness and simply evaluates the possibility to model grain boundary effects and its consequences on diffusion and fatigue.

Numerically predicted lifetimes to crack initiation are plotted in Figure 6.20. Varying grain boundary diffusivity with constant inner grain diffusion are listed in a) and descending inner grain diffusivities with constant grain boundary diffusion are depicted in b). In general no remarkable changes in the number of fatigue cycles can be observed. The deceleration of hydrogen ingress in the RVE due to barrier like grain boundaries in a) or inner grains in b) is not as severe as reducing the amount of hydrogen in the trap sites. Due to the homogeneously distributed grains and grain boundaries, the supply of lattice hydrogen is still sufficient to fill evolving trap sites in both cases. Only for total strain amplitudes of 0.2% and 0.3% a slightly extended lifetime is noticeable for GB2 and GB3.

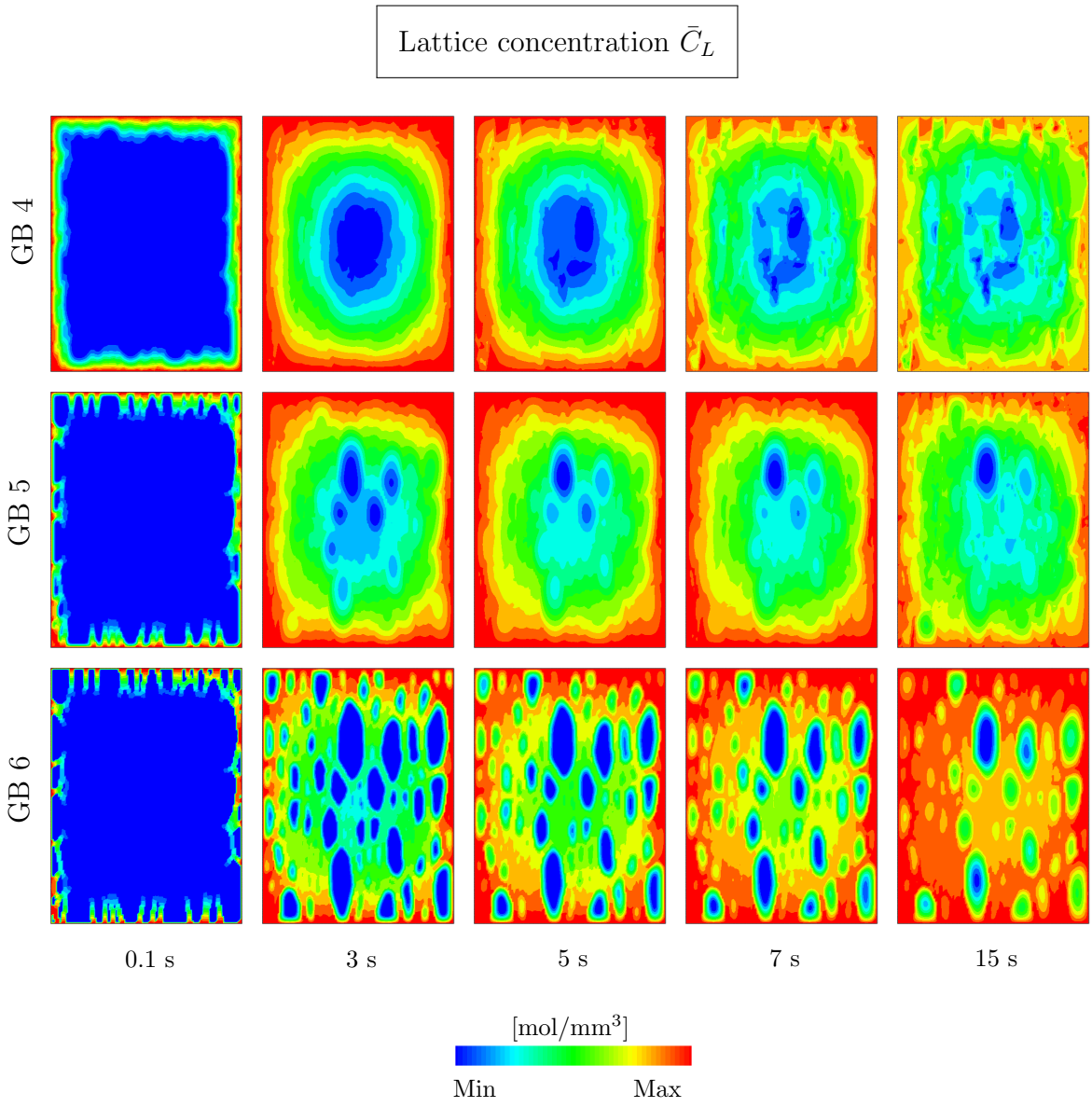

Figure 6.19: A similar visualization of the hydrogen lattice concentration as in 6.18, but with a decreasing inner grain diffusivity and a constant grain boundary diffusion coefficient.

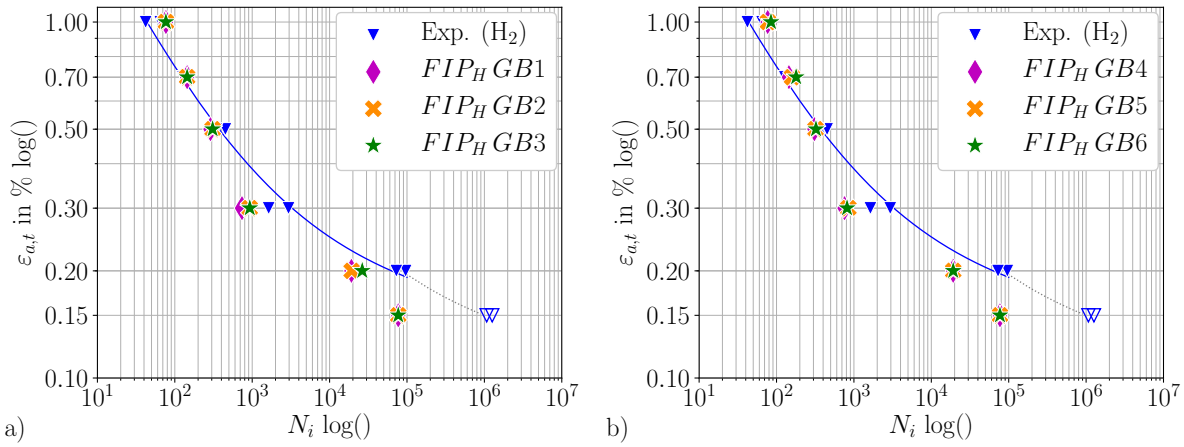

Figure 6.20: Lifetime prediction for different scenarios with varying grain boundary diffusivity in a) and varying inner grain diffusivity in b) with experimental data of Section 4.2.2 as reference.

7. General Discussion

All findings of this work are recapitulated and discussed in the following sections, starting with the experimental observations on the ferritic steel and its material behavior under fatigue in both standard air and hydrogen environments. The numerical model for the description of large strain deformation in polycrystalline materials together with a hydrogen transport model in metals and their ability to predict fatigue behavior is evaluated. Based on the simulation results of different boundary value problems and microstructure variations, the influence of the model setup and microstructural features on fatigue is assessed. Hence, the suitability of the proposed fatigue evaluation framework can be judged.

7.1. Insight on the Material Behavior Based on Experiments

Composition and Microstructure. The investigated material is the ferritic steel 1.4003, with good corrosion-resistant properties due to about 11.9% chromium. This steel is considered to be used for industrial components for the fuel cell mobility. The ductile steel with a rather low yield strength and tensile strength is not preferably used for highly stressed components but for example in applications where its magnetic properties are desired additionally. During operation of the application the material is usually loaded below its yield strength such that the number of cycles to failure due to material fatigue is of interest when evaluating the reliability. There, the microstructure plays a crucial role and is investigated by means of EBSD analysis. The ferrite exhibits large grains from 20 to 80 μm and a slight texture, which are both taken into account in the modeling process.

Experimental Characterization. The quasi-static tensile test reveals a pronounced yield strength and indicates the development of Lüders bands. Reasons for and consequences of this phenomenon are explained in 4.2.2. However, it is important to keep in mind that all subsequent LCF tests are performed on precycled samples to overcome issues in the cyclic testing procedure due to the Lüders bands. A transfer of the presented results towards a component fabricated without any precycling must be conducted with special caution, even when most components are not approximated with unnotched specimen. Following Laue [92] the development of Lüders bands is predominantly observable in unnotched specimens and is unlikely found in notched fatigue samples. The first finding of the LCF testing is derived from the cyclic deformation curve in Figure 4.6. The material exhibits a short hardening or softening phase for both air and hydrogen atmospheres, followed by a cyclic stable stress response over majority of the normalized lifetime in the strain-controlled experiment. The crack initiation at the unnotched axial specimens defined in Figure 4.3 is assumed by a 10% load drop. Differences in the results of both environments are interpreted as variations in the specimens due to the manufacturing or microstructural differences and not as a hydrogen induced cause. This interpretation is supported by the evaluation of the cyclic deformation curve with more samples which are not shown in Figure 4.6 to keep a clear representation of the single curves. Depending on the sample a cyclic deformation curve in hydrogen atmosphere can be found above as well as below the corresponding curve in air atmosphere at the same total strain amplitude. This result is an important key to the modeling approach of the mechanical material response and the subsequent fatigue prediction scheme. First, the hardening behavior seems to be unchanged by hydrogen and a stable cyclic response is

obtained after very few cycles. Hence, isotropic hardening can be neglected as proposed in Boeff [18] or Schäfer [160] and the parameter for kinematic hardening are assumed to be equal for the modeling in air and hydrogen atmosphere. An even stronger argument for the assumption of the same kinematic hardening behavior for both cases is given by comparison of the cyclic stress-strain hystereses. Figure 4.8 reveals an almost identical stress-strain response. The homogenized material behavior allows for the usage of a single mechanical parameter set including the critical resolved shear stress and the parameters adjusting the kinematic hardening. In the macroscopic cyclic stress-strain response no hydrogen induced differences are observable but yet a tremendous hydrogen driven reduction of the fatigue lifetime in the LCF regime can be seen in the strain-based Wöhler curve in Figure 4.10. A reduction of the loading cycles to crack initiation up to one decade is registered at the highest total strain amplitudes. These results are in accordance to experimental findings of Schauer [162] on similar ferritic steels. In his work, LCF tests were also performed for electrochemically precharged samples, which exhibit the same characteristics for the cyclic material and fatigue behavior as the samples tested in hydrogen atmosphere at 10 bar pressure. The significant reduction of the fatigue lifetime under hydrogen and the fact, that no differences in the macroscopic stress-strain response is observable, leads to the following conclusion.

Small Scale Fatigue Set Up. Hydrogen induced degradation takes place locally on a smaller scale, such as in form of slip band localization or accelerated crack propagation. With the available experimental macro fatigue set up introduced in Section 4.2.1 a distinctive identification of a degradation mechanism could not be made, but the necessity of a scale transition from a macro perspective to a smaller scale on microstructure level is reassured. In Honecker [78] first approaches are proposed to investigate fatigue in hydrogen atmosphere on a small scale fatigue set up, where the whole sample gauge can be filmed during cyclic testing in a hydrogen filled chamber. The steady observation of the surface with a microscope should give insights of the interplay of microstructural features, cyclic loading and the resulting degradation. Unfortunately the steel considered in this work exhibits an extremely ductile material behavior, leading to a strong roughening of the micro sample surface. Thus, an identification of crack initiation or propagation location were not possible and the results could not be used to support and validate the numerical model proposed in this work. A repetition of experiments with a material offering more possibilities for new insight in the local degradation mechanisms triggered by hydrogen would be desirable. But with this knowledge on hand, not only sophisticated small scale experiments are relevant but also simulation techniques incorporating information about the material's microstructure.

7.2. Evaluation of the Simulation Model

The continuum mechanical modeling framework introduced in Chapter 5 is divided in three parts, namely the crystal plasticity model, the hydrogen transport model and the generation of a domain representative for the material's microstructure.

Scope of the Crystal Plasticity Model. The large strain elasto-plastic material response for a polycrystal can be numerically described by the CPFEM model under isothermal conditions. The phenomenological approach does not explicitly model dislocation movement but assumes that only dislocation gliding on distinct slip systems is responsible for plastic deformations described in the plastic slip variable. The rate of this

plastic slip can be modified by isotropic and kinematic hardening terms. Critical on this approach is the negligence of pronounced strain gradients. These gradients occur at certain grain boundaries where the misorientation between both grains leads to a mismatch in their deformation behavior and can reproduce grain boundary strengthening known as the Hall-Petch effect, see Section 2.1.2. This effect can be captured by nonlocal models, for instance proposed in Ma & Hartmaier [103], based on the concept of densities of geometrically necessary superdislocations. The complexity and computational intensity of this approach would have shifted the focus of this work. Hence, the simplification of the phenomenological model and the loss of precision were knowingly accepted. Also the Armstrong-Frederick type kinematic hardening model is a simpler choice, with only two material parameter to be determined. Nevertheless, it proves to yield numerical results which fit very well the experimental data. More complex approaches as discussed in Schäfer [160] yield better fits for different materials, such as high-strength martensitic steels, but could not improve the results for the modeling of the ferritic steel investigated in this work.

Coupling Approach with Hydrogen Transport. Hydrogen diffusion through a solid is described by a well-established continuum model, which has mostly been applied in combination with homogeneous elastic or elasto-plastic material models. The possibility to couple the model with crystal plasticity calculations enables the reproduction of microstructure dependent diffusion phenomena, see Miresmaeili et al. [116]. The anisotropy due to varying grain orientation in a polycrystal can be modeled and causes hydrostatic stress peaks. These local peaks result in an accumulation of hydrogen on grain boundaries. Furthermore, the dependency of the evolution of traps sites during plastic straining is a crucial coupling module between the crystal plasticity and diffusion model and has a strong impact on the fatigue behavior. The evolution law (5.21) was originally proposed for pure quasi-static tensile loading, but is adapted in the context of fatigue simulation to cyclic loading and an accumulated plastic strain measure.

Validation Proposals for the Diffusion Model. An experimental determination or ab initio simulation approach of the exact relation between the increase in trap or dislocation density and cyclic loading is inevitable for an enhancement of the proposed diffusion model. In general, the validation of the hydrogen transport model is nontrivial, since hydrogen concentration cannot be measured locally in the bulk. Advanced experimental methods such as atom probe tomography are able to determine small local hydrogen concentrations on the materials surface but are extremely complex and cost intensive. More convenient methods as the thermal desorption spectroscopy can only determine integral hydrogen concentrations and trap binding energies based hydrogen escaping the bulk at different temperatures. Since the focus of this work is on the model setup, material parameter for the diffusion are mainly adapted from literature whereby the ferritic steel is approximated by a pure BCC lattice.

Replication of Microstructures. The simulation domain is generated as close as possible to the real metallic microstructure by means of a RVE. The strategies to generate such a RVE directly from EBSD data or artificially based on statistic information about the microstructure are explained in Section 5.4. A drawback of EBSD based RVEs is the uncertainty about the structure in the third dimension. Only 2D information are obtained and the experimental effort of 3D EBSD imaging is enormous and was not conducted for this work. However, artificial methods allow for the generation of 3D structures but the

underlying tessellation techniques are not able to match the complex grain structures as re-entrant angles which can be seen in EBSD images of the 1.4003 steel. The artificial generation has the advantage of reproducibility and effortless variability to investigate microstructural effects. The impact of a 2D or 3D simulation on the predicted lifetime is negligible small, see Figure 6.9. Hence, in this work performed numerical studies are mostly limited to the 2D case. Only BCC lattices in combination with relatively large ferritic grains are of concern investigating the exemplary material in the present work. An extension to more complex hierarchical structures for martensite modeling can be smoothly incorporated as done by Schäfer [160]. FCC structures are investigated and included in the introduced CPFEM model by Graf [63] for aluminum-copper alloys where different slip systems must be taken into account.

Determination of Material Parameters. The selection strategy for material parameters described in Section 6.1 reduces the set of parameters to be determined to three quantities, the critical resolved shear stress and the kinematic hardening parameters. With the proposed optimization calculations the macroscopic stress-strain response can be matched extremely well and the found parameters are assigned to each grain. In reality, each grain has its unique resistance towards plastic deformation and should have its own set of parameters. The model exhibits a high sensitivity to a varying critical resolved shear stress as shown in Figure 6.5. Especially at lower strain amplitudes these variations influence the predicted lifetime significantly. At the state of current research no better and more practical method to define parameters to match stress-strain response under cyclic loading is known. At least three experiments are necessary for the fitting procedure. A reduction of costs due to sample production and testing time would be an important enhancement, however, no computational models based for instance on molecular dynamics are developed yet able to solve this issue.

Quality of Simulative Fatigue Assessment. The prediction results for fatigue crack initiation under air and hydrogen are shown in Figure 6.11 and proof the ability of the model to deliver an adequate estimation. The predominant conservative forecast could be used to evaluate the suitability of different steels for their usage in hydrogen related applications. A drawback of the model is the increase of deviations between experimental results and simulated lifetimes for lower strain amplitudes. The numerical material response for these low amplitudes contains too much plastic deformation leading to an early predicted failure. As stated above this issue can only be solved with new possibilities to determine the mechanical material parameters, best on the grain level. Furthermore, the crack growth in its early stages should be considered. Since cracks may nucleate also at lower strain amplitudes in the HCF regime, but the crack propagation can be retarded or cracks might stop. The incorporation of the hydrogen concentration in the fatigue damage measure by means of the modified hydrogen dependent FIP introduced in (6.7) must be discussed in detail.

Novel Hydrogen Dependent Damage Term. Vasios [190] proposes an approach to model the hydrogen influence on the mechanical response by including a hydrogen dependency on the critical resolved shear stress. However, this would change the macroscopic stress-strain response where no alteration is observed between air and hydrogen atmosphere. Inspired by the statement of Nanninga [126] who relates an acceleration of crack initiation by an increase in accumulated plastic strain with present local hydrogen, the modification of the FIP based on the accumulated plastic strain was conducted.

With this phenomenological approach convincing results are obtained and the model is able to reproduce the loss of bearable loading cycles under hydrogen atmosphere in the LCF regime. A restriction is given by the required parameter H_T, which regulates the influence of the trapped hydrogen on the evolution of the FIP. The choice of the parameter has a decisive impact on the predicted lifetime, as shown in Figure 6.10. To obtain a realistic numerical prognosis, an experiment under hydrogen at a single strain amplitude must be conducted to fit this sensitivity parameter. With a better understanding of physical degradation mechanisms this phenomenological approach should be revisited and improved. Nevertheless the proposed approach allows for a fast and reliable assessment of the fatigue lifetime to crack initiation under hydrogen with a noteworthy reduced experimental effort.

7.3. Significance of the Microstructure and Loading Conditions

Influence of the Grain Morphology. The sensitivity to changes of the microstructure and boundary conditions of the RVE regarding the fatigue time were investigated by representative numerical examples. The variation of five synthetic microstructures results in a locally different evolution for the FIPs with a consequent change of the critical spot for crack initiation. However the differences are only triggered by alternating constellations of grain orientations, since grain size effects are not considered in the model. This fact is reflected in the lifetime evaluation where no significant variance is observed. To obtain larger variances a change in grain sizes and orientation relations would be required in combination with a model that captures length scale effects.

Consideration of Environmental Loading Scenarios. The application of different charging and loading scenarios proposed in Figure 6.12 shows the ability of the model to handle real life charging situations or various testing conditions. The simulation results confirm experimental observations of Schauer [162] where precharged samples (S1 or S3) and only samples charged during the testing show no significant differences in their lifetime, where both are tested at a frequency of 1 Hz. However, the simulated scenarios on the microstructure level are not one to one comparable with experimental macro samples, since diffusion paths cover different length scales. Moreover, the surface layer was not considered. Most steels exposed to air atmosphere develop an oxide layer which is difficult to characterize due to different chemical components and locally varying thicknesses. However, it is clear that this surface has an effect on the hydrogen uptake. Under cyclical loading the degradation of this layer may also effect the hydrogen uptake. Assuming a passivation effect, a spot with a damaged passivation layer may lead to a facilitated hydrogen uptake and the local concentration may increase in the vicinity of this area. The surrounding hydrogen pressure may also affect the hydrogen uptake but is not considered in this model, whereas Di Leo & Anand [44] propose pressure dependent boundary conditions for the hydrogen diffusion model. Considering the possible industrial applications of the ferritic steel, which are limited to low-pressure conditions, the influence of the pressure is not investigated further in this work. Nevertheless, a possibility to include a surface layer is given in scenario S4 by setting a boundary layer with a lowered diffusion coefficient simulating a passivation surface. Therewith a reduced hydrogen ingress is obtained, resulting in a longer lifetime with decreasing diffusivity of this boundary layer. The physical understanding of the interplay between surface layer and hydrogen uptake is crucial for the design of reliable metal components in hydrogen

applications and should be addressed in future research work. Compared to the diffusion behavior in the material lattice, the uptake over the surface plays a dominant role. As shown in Figure 2.14 the transition from the gas phase over the gas-metal-interface into absorbed hydrogen in the lattice is a multi-stage process which depends strongly on the surface condition of the material.

Interaction with Grain Boundaries. A model approach for the effect of grain boundaries within the microstructure is proposed and investigated. Since various research groups debate controversially about the influence of grain boundaries on hydrogen diffusion through or close to these boundaries, a numerical study considers both, higher and lower grain boundary diffusivity compared to inner grain diffusion. The resulting changes in the hydrogen distribution are visible in the contour plots of Figures 6.18 and 6.19. Again, the influence on the material's lifetime is negligible small. Difficulties arise by the fact, that each type of grain boundaries influence the diffusion behavior differently, see Di Stefano et al. [46]. The types of grain boundaries are divided in high and low angle boundaries with different values Σ describing the degree of fit between the structures of the two adjacent grains. Hence, the model should be able to determine an individual diffusion coefficient for each single grain boundary. Furthermore, the diffusion through and along a grain boundary may also take different diffusion coefficients and the orientation induced anisotropy must also be taken into account.

8. Conclusion

In the present work a computational framework for the prediction of fatigue crack initiation of a ferritic steel under hydrogen atmosphere is presented. The formulation combines hydrogen transport with a phenomenological large strain crystal plasticity model and is implemented by means of the finite element method.

To this end, a review of the material structure of metals is given with a focus on the deformation behavior. Important for the understanding of fatigue mechanisms is the deformation under cyclic loading. With this knowledge the basics of the evaluation of fatigue and crack formation are given. As a second fundamental part of this work, the current state of the art concerning the interaction of hydrogen with metals is presented. This embraces the hydrogen uptake, its distribution in the bulk and the resulting degradation mechanisms. These mechanisms are related to premature failure of metal material under loading with a special focus on fatigue. A last basic module on which this work is build introduces large deformation kinematics in the continuum mechanics context with the notion of point maps, strain and stress measures and finally the classical Newtonian balance laws.

To gain an understanding of the ferritic steel 1.4003 considered for components in the fuel cell system the material is characterized. A microstructure analysis reveals a purely ferritic polycrystalline structure without relevant inclusions. EBSD measurements give an insight in the grain morphology and orientation distribution. These information are used for a realistic representative volume element as simulation domain. Furthermore on the experimental side, LCF fatigue experiments are performed to capture the cyclic material behavior. Strain-controlled test are performed at different total strain amplitudes at $R_\varepsilon = -1$ with unnotched axial specimens, see Figure 4.3, in normal air atmosphere as well as under 10 bar pure hydrogen atmosphere. The material exhibits a cyclic stable material behavior and shows almost no differences in its macroscopic cyclic stress-strain material response in air and hydrogen. However, a tremendous reduction of fatigue lifetime is observed at the hydrogen strain-life curve. These results confirm observations made by Schauer [162] on other ferritic steels with similar compositions.

Motivated by these experimental observations a simulation model is proposed accounting for polycrystalline material deformation coupled with hydrogen diffusion. A phenomenological rate-dependent isothermal crystal plasticity model is introduced in the large strain regime considering the grain orientations of the material's microstructure. A hydrogen transport formulation is implemented which divides the hydrogen concentration in lattice and trap site hydrogen and inherently models the interaction of mechanical quantities, such as the hydrostatic stress and the accumulated plastic strain, on the local diffusion behavior. A suitable simulation environment was identified with the commercial software ABAQUS which framework for user defined materials (UMAT and UMATHT) allow a handy implementation and post processing of the proposed model and the subsequent simulations. The simulation domain in terms of a RVE is created based on measured EBSD data or synthetically based on statistical information about the grain morphology. Both methods are described and applied for the ferritic steel where the first convinces with accuracy and empirical realism while the second has advantages concerning the flexibility and variability.

A calibration procedure for the determination of cyclic material parameter for the simu-

lation is applied which found a suitable set of parameter to mimic the cyclic stress-strain response of the underlying material recorded during the LCF experiments. With these parameters coupled simulation are performed at different strain amplitudes on representative domains. Mechanical quantities obtained from these calculations are then used to determine fatigue indicator parameter as numerical measurements of fatigue at the integration point level during cyclic simulations.

A key contribution of this work is the proposal of a new fatigue assessment procedure considering the local hydrogen concentration in traps as an additional driving quantity for the accumulation of plastic strain leading to premature fatigue failure. A prediction scheme for the fatigue crack initiation location and lifetime is based upon these FIPs. Therewith numerical strain-life curves for scenarios in air and hydrogen atmosphere are determined.

The validation of the simulation model and results with the experimental strain-life curves shows very good agreements in the LCF regime up to 10^5 cycles, especially for the larger total strain amplitudes. Deviations at smaller strain amplitudes are correlated to insufficient accuracy at the simulated stress-strain response of the material and the precision of the conducted experiment concerning the registration of crack growth. Different numerical examples are presented to show the capability of the model to mimic physical phenomena and to investigate the effect of microstructural features. The influence of the orientation distribution and grain morphology is analyzed by means of different microstructures. A comparison between 2D and 3D simulations in air atmosphere is drawn. Furthermore, different hydrogen boundary conditions and charging conditions are investigated as well as the model expansion to consider grain boundaries in the diffusion transport process. The model's sensitivity towards material parameter such as the critical resolved shear stress or the hydrogen influence parameter are evaluated with respect to the stain-life curve.

The potential for a further improvement of this work lies mainly in two aspects. First, the determination of material parameter for the simulation still requires costly experiments. The material and material structure depending set of parameter for the evolution of the shear rate and the kinematic hardening are crucial for the crystal plasticity calculation. A first principle simulation approach for various steels would be desirable. Similarly, a reproducible quantification for hydrogen diffusion constants such as the diffusion velocity for different steel compositions as well as the relation between cyclic plastic deformation and the production of new trap sites are of importance for a simulative approach to predict fatigue.

Second, to improve the model further physical features must be considered. Microstructure features on both the crystal plasticity and the diffusion sides should be taken into account. For example grain boundary interaction or barrier effects to dislocation movements resulting in a grain size dependency (Hall-Petch effect) are not considered yet.

Due to the lack of physical understanding of the role of passivation layers and other surfaces concerning the hydrogen uptake and the influence of the hydrogen pressure applied on the material, an important key for the transferability of the model to component design for reliability is still missing.

The simulation to crack initiation is not satisfying since the crack propagation during cyclic loading might have a considerable portion of the total fatigue lifetime. An exten-

sion considering short crack growth would be the next logical step, but also requires a fundamental understanding of the role of hydrogen on this fatigue stage.

Enriching for a further validation and verification of the proposed model framework would be the application to different steels. From an industrial point of view an application of the concept to a component with real-life requirements and corresponding experiments would be another desirable step for the future. These real-life requirements include hydrogen loading and unloading processes and a combination thereof as well as the assessment of degradation mechanisms under time dependent cyclic mechanical loading. In summary a transition from phenomenological approaches to more physical models should be made but this requires an in-depth understanding of the hydrogen with the microstructure and even smaller scales of polycrystals. New methods combining in situ testing on small samples with atomistic or molecular simulation approaches, see Barrera et al. [9], are promising to elucidate hydrogen effects on deformation of metals.

Despite these shortcomings, the model proposed in this work is a step towards the reliable computational prediction of the fatigue crack initiation of ferritic steels under hydrogen atmosphere. A conservative fatigue estimation can be made with a significant reduction of necessary fatigue experiments and the possibility for an advanced material selection based on microstructure criteria.

Appendix

A. Integration and Implementation for CPFEM

A.1. Integration of Elasto-Plastic Equations

A.1.1. Time Integration Scheme

As stated in Section 5.1.6 the integration of the elasto-plastic equations is required for the numerical implementation and not straight forward. In the UMAT interface of ABAQUS the following quantities $\boldsymbol{\sigma}_n$, $\boldsymbol{F}_n^p$, $\mathbf{SDV_n}$ as well as $\boldsymbol{F}_{n+1}$ are known at the end of time t_n before starting time increment t_{n+1}. The time discretization is performed using an Euler backward scheme and the second Piola-Kirchhoff stress in the intermediate configuration is reformulated as a function of the known total deformation gradient and unknown plastic deformation gradient. Therefore, equation (5.8) is inserted in (5.10) together with the multiplicative split of the deformation gradient (5.1) in the form $\boldsymbol{F}^e = \boldsymbol{F}\boldsymbol{F}^{p^{-1}}$ yielding the stress tensor

$$\tilde{\boldsymbol{S}} = \tfrac{1}{2}\,\mathbb{C}^e : \left((\boldsymbol{F}\boldsymbol{F}^{p^{-1}})^T(\boldsymbol{F}\boldsymbol{F}^{p^{-1}}) - \boldsymbol{1}\right). \tag{A.1}$$

Now recalling the expression for the spatial velocity gradient $\boldsymbol{l}$ (2.28) in terms of $\dot{\boldsymbol{F}}$ as

$$\boldsymbol{l} = \dot{\boldsymbol{F}}\boldsymbol{F}^{-1}, \tag{A.2}$$

and substituting the multiplicative split yields

$$\begin{aligned} \boldsymbol{l} &= \dot{\boldsymbol{F}}\boldsymbol{F}^{-1} = \dot{\overline{\boldsymbol{F}^e\boldsymbol{F}^p}}(\boldsymbol{F}^{p^{-1}}\boldsymbol{F}^{e^{-1}}) \\ &= (\dot{\boldsymbol{F}}^e\boldsymbol{F}^p + \boldsymbol{F}^e\dot{\boldsymbol{F}}^p)(\boldsymbol{F}^{p^{-1}}\boldsymbol{F}^{e^{-1}}) \\ &= \dot{\boldsymbol{F}}^e\boldsymbol{F}^{e^{-1}} + \boldsymbol{F}^e\dot{\boldsymbol{F}}^p\boldsymbol{F}^{p^{-1}}\boldsymbol{F}^{e^{-1}} \\ &= \boldsymbol{l}^e + \boldsymbol{F}^e\tilde{\boldsymbol{L}}^p\boldsymbol{F}^{e^{-1}}. \end{aligned} \tag{A.3}$$

The plastic velocity gradient in the intermediate configuration is identified as

$$\tilde{\boldsymbol{L}}^p = \dot{\boldsymbol{F}}^p\boldsymbol{F}^{p^{-1}}, \tag{A.4}$$

which needs to be pushed forward to the current configuration by $\boldsymbol{F}^e$ and $\boldsymbol{F}^{e^{-1}}$ to contribute to the total spatial velocity gradient. Substituting equation (5.12) into (A.4) and transposing the equation results in

$$\dot{\boldsymbol{F}}^p(\dot{\gamma}^\alpha) = \Big(\sum_{\alpha=1}^{N_{Slip}} \dot{\gamma}^\alpha\tilde{\boldsymbol{M}}^\alpha\Big)\boldsymbol{F}^p(\dot{\gamma}^\alpha). \tag{A.5}$$

This ordinary differential equation (ODE) with the unknown being the time dependent tensor function $\boldsymbol{F}^p(\dot{\gamma}^\alpha)$ is solved following an exponential ansatz as described in Gurtin et al. [65]. A first oder tensor ODE of the form

$$\dot{\boldsymbol{Y}}(t) = \boldsymbol{A}\,\boldsymbol{Y}(t) \qquad t \in [t_1, t_2] \tag{A.6}$$

is solved by

$$\boldsymbol{Y}(t_2) = \exp[(t_2 - t_1)\boldsymbol{A}]\,\boldsymbol{Y}(t_1) \qquad t \in [t_1, t_2]\,. \tag{A.7}$$

Equation (A.5) needs to be integrated over the time interval $[t_n, t_{n+1}]$. Under assumption that $\dot{\gamma}^\alpha$ remains constant during the time interval we obtain (A.5) in its integrated form as

$$\boldsymbol{F}^p_{n+1} = \exp\Big(\sum_{\alpha=1}^{N_{Slip}} \Delta\gamma^\alpha \tilde{\boldsymbol{M}}^\alpha\Big)\boldsymbol{F}^p_n\,. \tag{A.8}$$

The inverse tensor $\boldsymbol{F}^{p^{-1}}_{n+1}$ of the above expression reads

$$\boldsymbol{F}^{p^{-1}}_{n+1} = \boldsymbol{F}^{p^{-1}}_{n} \exp\Big(\sum_{\alpha=1}^{N_{Slip}} -\Delta\gamma^\alpha \tilde{\boldsymbol{M}}^\alpha\Big)\,. \tag{A.9}$$

For more computational efficiency both terms (A.8) and (A.9) can be expanded using Taylor series. This approximation is reasonable for considerable small time increments, see Meissonnier et al. [112]), and results in the following expressions

$$\boldsymbol{F}^p_{n+1} = \Big(\boldsymbol{1} + \sum_{\alpha=1}^{N_{Slip}} \Delta\gamma^\alpha \tilde{\boldsymbol{M}}^\alpha\Big)\boldsymbol{F}^p_n \quad \text{and} \quad \boldsymbol{F}^{p^{-1}}_{n+1} = \boldsymbol{F}^{p^{-1}}_{n}\Big(\boldsymbol{1} - \sum_{\alpha=1}^{N_{Slip}} \Delta\gamma^\alpha \tilde{\boldsymbol{M}}^\alpha\Big)\,. \tag{A.10}$$

By replacing the unknown plastic deformation gradient and its inverse in the expression for the second Piola-Kirchhoff stress in intermediate configuration (A.1) one obtains

$$\tilde{\boldsymbol{S}} = \tfrac{1}{2}\,\mathbb{C}^e : \Big[(\boldsymbol{1} - \sum_{\alpha=1}^{N_{Slip}} \Delta\gamma^\alpha \tilde{\boldsymbol{M}}^{\alpha^T})\boldsymbol{F}^{p^{-T}}_n \boldsymbol{F}^T \boldsymbol{F} \boldsymbol{F}^{p^{-1}}_n (\boldsymbol{1} - \sum_{\alpha=1}^{N_{Slip}} \Delta\gamma^\alpha \tilde{\boldsymbol{M}}^\alpha) - \boldsymbol{1}\Big]\,. \tag{A.11}$$

Now $\tilde{\boldsymbol{S}}$ is formulated in terms of the known total deformation gradient $\boldsymbol{F}_{n+1}$, the known plastic deformation gradient $\boldsymbol{F}^p_n$ and the unknown increment of plastic slips $\Delta\gamma^\alpha$.

A.1.2. Return Mapping Algorithm

The elastic predictor and return-mapping algorithm for integration of the constitutive equations in crystal plasticity formulations is considerable more complex than its isotropic counterpart, as described extensively described in de Souza Neto et al. [42]. Here, the finite strain nonlinearity is not confined to the kinematic level, since the geometric nonlinearity cannot be decoupled from the stress-updating procedure. Assuming that $\Delta\gamma^\alpha$ are known, $\boldsymbol{F}^p_{n+1}$ and also $\boldsymbol{F}^e_{n+1}$ can be updated as

$$\boldsymbol{F}^e_{n+1} = \boldsymbol{F}_{n+1}\boldsymbol{F}^{p^{-1}}_{n+1} = \underbrace{\boldsymbol{F}_{n+1}\boldsymbol{F}^{p^{-1}}_{n}}_{\boldsymbol{F}^e_{trial}}\Big(\boldsymbol{1} - \sum_{\alpha=1}^{N_{Slip}} \Delta\gamma^\alpha \tilde{\boldsymbol{M}}^\alpha\Big)\,. \tag{A.12}$$

The trial elastic deformation gradient is defined as

$$\boldsymbol{F}^e_{trial} = \boldsymbol{F}_{n+1}\boldsymbol{F}^{p^{-1}}_{n}\,, \tag{A.13}$$

and substituted into (A.11) to obtain

$$\tilde{\boldsymbol{S}} = \tfrac{1}{2}\,\mathbb{C}^e : \left[(\boldsymbol{1} - \sum_{\alpha=1}^{N_{Slip}} \Delta\gamma^\alpha \tilde{\boldsymbol{M}}^{\alpha^T})\boldsymbol{F}_{trial}^{e^T}\boldsymbol{F}_{trial}^{e}(\boldsymbol{1} - \sum_{\alpha=1}^{N_{Slip}} \Delta\gamma^\alpha \tilde{\boldsymbol{M}}^{\alpha}) - \boldsymbol{1}\right]. \quad \text{(A.14)}$$

Herby the trial elastic Green strain tensor reads $\boldsymbol{F}_{trial}^{e^T}\boldsymbol{F}_{trial}^{e} = \boldsymbol{C}_{trial}^{e}$. By expanding (A.14) to

$$\begin{aligned}\tilde{\boldsymbol{S}} = \tfrac{1}{2}\,\mathbb{C}^e : \Big[&\boldsymbol{C}_{trial}^{e} - \boldsymbol{C}_{trial}^{e}\sum_{\alpha=1}^{N_{Slip}} \Delta\gamma^\alpha \tilde{\boldsymbol{M}}^{\alpha} - \sum_{\alpha=1}^{N_{Slip}} \Delta\gamma^\alpha \tilde{\boldsymbol{M}}^{\alpha^T}\boldsymbol{C}_{trial}^{e} + \\ &\underbrace{+\sum_{\alpha=1}^{N_{Slip}} \Delta\gamma^\alpha \tilde{\boldsymbol{M}}^{\alpha^T}\boldsymbol{C}_{trial}^{e}\sum_{\alpha=1}^{N_{Slip}} \Delta\gamma^\alpha \tilde{\boldsymbol{M}}^{\alpha}}_{\mathcal{O}(\Delta\gamma^{\alpha^2})} - \boldsymbol{1}\Big],\end{aligned} \quad \text{(A.15)}$$

and neglecting terms of $\mathcal{O}(\Delta\gamma^{\alpha^2})$ an approximation is obtained as

$$\tilde{\boldsymbol{S}} \approx \tfrac{1}{2}\,\mathbb{C}^e : \left[\boldsymbol{C}_{trial}^{e} - \big(\boldsymbol{C}_{trial}^{e}\sum_{\alpha=1}^{N_{Slip}} \Delta\gamma^\alpha \tilde{\boldsymbol{M}}^{\alpha} + \sum_{\alpha=1}^{N_{Slip}} \Delta\gamma^\alpha \tilde{\boldsymbol{M}}^{\alpha^T}\boldsymbol{C}_{trial}^{e}\big) - \boldsymbol{1}\right]. \quad \text{(A.16)}$$

This expression consists of an elastic trial and a plastic corrector part. The current stress state reaches its peak for a purely elastic step and is adjusted by the corrector stress depending on the plastic slip. Both terms are defined as

$$\tilde{\boldsymbol{S}}_{trial} = \tfrac{1}{2}\,\mathbb{C}^e : \left[\boldsymbol{C}_{trial}^{e} - \boldsymbol{1}\right] \quad \text{(A.17)}$$

and

$$\tilde{\boldsymbol{S}}_{cor} = \tfrac{1}{2}\,\mathbb{C}^e : \big(\boldsymbol{C}_{trial}^{e}\sum_{\alpha=1}^{N_{Slip}} \Delta\gamma^\alpha \tilde{\boldsymbol{M}}^{\alpha} + \sum_{\alpha=1}^{N_{Slip}} \Delta\gamma^\alpha \tilde{\boldsymbol{M}}^{\alpha^T}\boldsymbol{C}_{trial}^{e}\big), \quad \text{(A.18)}$$

and provide a short notation for the second Piola-Kirchhoff stress in intermediate configuration in terms of the elastic predictor - plastic corrector scheme

$$\tilde{\boldsymbol{S}}(\Delta\gamma^\alpha) = \tilde{\boldsymbol{S}}_{trial} - \tilde{\boldsymbol{S}}_{cor}(\Delta\gamma^\alpha). \quad \text{(A.19)}$$

Note, that the evolution of the slip depends on the resolved shear stress, which on its part depends on the second Piola-Kirchhoff stress (5.6). Now, stresses are incrementally updated completing the integration of equations, but therefore, all $\Delta\gamma^\alpha$ are required. Hence, stress integration and calculation of $\Delta\gamma^\alpha$ are treated as one problem with its computational implementation commonly being referred to as stress-update algorithm, see Vasios [190], which is in detail explained in the next section.

A.2. Solution of the Local Nonlinear Problem

The above described theory of stress evolution combined with the hardening models of Section 5.1.5 form a local system of nonlinear equations. It contains three unknowns,

namely the second Piola-Kirchhoff stress, the rate of critical resolved shear stress and the rate of resolved backstress

$$\begin{aligned} \boldsymbol{G}_1 &= \tilde{\boldsymbol{S}}_{n+1} - \tilde{\boldsymbol{S}}_{trial} + \tilde{\boldsymbol{S}}_{cor}(\tilde{\boldsymbol{S}}_{n+1}, \tau^{\alpha}_{c,n+1}, \chi^{\alpha}_{n+1}) = 0 && \text{(A.20)} \\ \boldsymbol{G}_2 &= \tau^{\alpha}_{c,n+1} - \tau^{\alpha}_{c,n} - \dot{\tau}^{\alpha}_{c}(\tilde{\boldsymbol{S}}_{n+1}, \tau^{\alpha}_{c,n+1}, \chi^{\alpha}_{n+1})dt = 0 && \text{(A.21)} \\ \boldsymbol{G}_3 &= \chi^{\alpha}_{n+1} - \chi^{\alpha}_{n} - \dot{\chi}^{\alpha}(\tilde{\boldsymbol{S}}_{n+1}, \tau^{\alpha}_{c,n+1}, \chi^{\alpha}_{n+1})dt = 0\,. && \text{(A.22)} \end{aligned}$$

This nonlinear system in the variables $\tilde{\boldsymbol{S}}_{n+1}, \tau^{\alpha}_{c,n+1}, \chi^{\alpha}_{n+1}$ can be solved via a local Newton iteration based on a linearization of (A.20-A.22). The linearization of the system reads

$$\begin{aligned} Lin\{\boldsymbol{G}_1\} &= \boldsymbol{G}_1 + \frac{\partial \mathbf{G}_1}{\partial \tilde{\boldsymbol{S}}}\Delta\tilde{\boldsymbol{S}}_{n+1} + \frac{\partial \mathbf{G}_1}{\partial \tau^{\alpha}_{c,n+1}}\Delta\tau^{\alpha}_{c,n+1} + \frac{\partial \mathbf{G}_1}{\partial \chi^{\alpha}_{n+1}}\Delta\chi^{\alpha}_{n+1} = 0 && \text{(A.23)} \\ Lin\{\boldsymbol{G}_2\} &= \boldsymbol{G}_2 + \frac{\partial \mathbf{G}_2}{\partial \tilde{\boldsymbol{S}}}\Delta\tilde{\boldsymbol{S}}_{n+1} + \frac{\partial \mathbf{G}_2}{\partial \tau^{\alpha}_{c,n+1}}\Delta\tau^{\alpha}_{c,n+1} + \frac{\partial \mathbf{G}_2}{\partial \chi^{\alpha}_{n+1}}\Delta\chi^{\alpha}_{n+1} = 0 && \text{(A.24)} \\ Lin\{\boldsymbol{G}_3\} &= \boldsymbol{G}_3 + \frac{\partial \mathbf{G}_3}{\partial \tilde{\boldsymbol{S}}}\Delta\tilde{\boldsymbol{S}}_{n+1} + \frac{\partial \mathbf{G}_3}{\partial \tau^{\alpha}_{c,n+1}}\Delta\tau^{\alpha}_{c,n+1} + \frac{\partial \mathbf{G}_3}{\partial \chi^{\alpha}_{n+1}}\Delta\chi^{\alpha}_{n+1} = 0\,. && \text{(A.25)} \end{aligned}$$

While Meissonnier et al. [112] solve the nonlinear system fully implicitly but only considering isotropic hardening, Boeff [18] proposes a semi-implicit solution scheme accounting for kinematic hardening. Therein, the evolution of stress and isotropic hardening, represented in the linearized system by (A.23) and (A.24), are solved implicitly, while the evolution of backstress (A.25) is solved explicitly. The semi-implicit scheme reduces implementation effort for the investigation of further kinematic hardening laws, as investigated in Schäfer et al [160]. Hence, the Newton scheme is applied only to (A.23) and (A.24), while (A.25) is coupled explicitly. The incremental form reads

$$\begin{bmatrix} \mathbf{G}_1 \\ \mathbf{G}_2 \end{bmatrix} = -\boldsymbol{J} \begin{bmatrix} \Delta\tilde{\boldsymbol{S}} \\ \Delta\tau^{\alpha}_{c} \end{bmatrix} \qquad \text{with} \qquad \boldsymbol{J} = \begin{bmatrix} \frac{\partial \mathbf{G}_1}{\partial \tilde{\boldsymbol{S}}} & \frac{\partial \mathbf{G}_1}{\partial \tau^{\alpha}_{c}} \\ \frac{\partial \mathbf{G}_2}{\partial \tilde{\boldsymbol{S}}} & \frac{\partial \mathbf{G}_2}{\partial \tau^{\beta}_{c}} \end{bmatrix}, \qquad \text{(A.26)}$$

where $\boldsymbol{J}^{[18\text{x}18]}$ is the Jacobian whose entries are the various partial derivatives of the components of $\boldsymbol{G}_1$ and $\boldsymbol{G}_2$. The Jacobian in the three-dimensional case is a second order tensor and its dimensions are defined by the stress tensor in Voigt notation and twelve slip systems for bbc crystal lattice. This system can be solved for the unknown vector by rearranging (A.26) to

$$\begin{bmatrix} \Delta\tilde{\boldsymbol{S}} \\ \Delta\tau^{\alpha}_{c} \end{bmatrix} = -\boldsymbol{J}^{-1} \begin{bmatrix} \mathbf{G}_1 \\ \mathbf{G}_2 \end{bmatrix}, \qquad \text{(A.27)}$$

provided that the inverse $\boldsymbol{J}^{-1}$ exists. Now, the stress and the critical resolved shear stress can be updated and the next iteration within the newton scheme can be started. The iteration is terminated if the Euclidean norm of the residual vector $\{\boldsymbol{G}_1, \boldsymbol{G}_2\}$ in (A.20-A.21) is less than a certain tolerance. The algorithmic steps outlined before are summarized in Box 1.

A.3. Rate Dependent Tangent Modulus

After the stress update procedure plastic and elastic deformation gradients can be calculated and therewith different stress formulations in reference or current configuration

Box 1: Semi-implicit solution scheme for stress-update algorithm.

1. Set initial values $\tilde{\boldsymbol{S}} = \tilde{\boldsymbol{S}}_n$ and $\tau_c^\alpha = \tau_{c,\,n}^\alpha$.

2. Compute resolved shear stress $\tau^\alpha = \tilde{\boldsymbol{S}} : \tilde{\boldsymbol{M}}^\alpha$ and evolution laws

$$\begin{array}{lrcl} \text{Shear rate evolution:} & \dot{\gamma}^\alpha & = & \dot{\gamma}_0 \left| \frac{\tau^\alpha - \chi_b^\alpha}{\tau_c^\alpha} \right|^m \operatorname{sign}(\tau^\alpha - \chi_b^\alpha) \\ \text{Isotropic hardening:} & \dot{\tau}_c^\alpha & = & \displaystyle\sum_{\beta=1}^{nslip} h_0 M_{\alpha\beta} \Big(1 - \frac{\tau_c^\beta}{\tau_s}\Big)^n |\dot{\gamma}^\beta| \\ \text{Kinematic hardening:} \\ \text{(explicitly)} & \dot{\chi}_b^\alpha & = & A_1 \dot{\gamma}^\alpha - A_2 |\dot{\gamma}^\alpha| \, (\chi_b^\alpha)_n \end{array}$$

3. Compute residuals and check tolerance

$$\boldsymbol{R} := \begin{bmatrix} \boldsymbol{G}_1 \\ \boldsymbol{G}_2 \end{bmatrix} = \begin{bmatrix} \tilde{\boldsymbol{S}} - \tilde{\boldsymbol{S}}_{trial} + \tilde{\boldsymbol{S}}_{cor} \\ \tau^\alpha - \tau_{c,\,n}^\alpha - \dot{\tau}_c^\alpha \, dt \end{bmatrix} \quad . \quad \text{If } [\, \sqrt{\boldsymbol{R}^T \boldsymbol{R}} < tol \,] \text{ go to 5.}$$

4. Set $\boldsymbol{J} := \begin{bmatrix} \frac{\partial \mathbf{G}_1}{\partial \tilde{\boldsymbol{S}}} & \frac{\partial \mathbf{G}_1}{\partial \tau_c^\alpha} \\ \frac{\partial \mathbf{G}_2}{\partial \tilde{\boldsymbol{S}}} & \frac{\partial \mathbf{G}_2}{\partial \tau_c^\beta} \end{bmatrix}$, compute incremental stress and critical resolved shear stress

$$\begin{bmatrix} \Delta \tilde{\boldsymbol{S}} \\ \Delta \tau_c^\alpha \end{bmatrix} = -\boldsymbol{J}^{-1} \begin{bmatrix} \mathbf{G}_1 \\ \mathbf{G}_2 \end{bmatrix} ,$$

perform the updates

$$\tilde{\boldsymbol{S}} = \tilde{\boldsymbol{S}} + \Delta \tilde{\boldsymbol{S}} \,, \quad \tau_c^\alpha = \tau_c^\alpha + \Delta \tau_c^\alpha \,, \quad \chi_{b,\,n+1}^\alpha = \chi_{b,\,n}^\alpha + \dot{\chi}_b^\alpha \, dt$$

and go to 2.

5. Obtain second Piola-Kirchhoff stress and critical resolved shear stress

$$\tilde{\boldsymbol{S}}_{n+1} = \tilde{\boldsymbol{S}}_{trial} - \tilde{\boldsymbol{S}}_{cor}(\Delta \gamma^\alpha) \quad \text{and} \quad \tau_{c,\,n+1}^\alpha = \tau_{c,\,n}^\alpha + \dot{\tau}_c^\alpha \, dt \,.$$

are known. ABAQUS requires the update of the Cauchy stress $\boldsymbol{\sigma}$. The global solution procedure of the set of nonlinear equations within the implicit finite element solver of ABAQUS needs the material tangent modulus to achieve an accurate correction to the incremental kinematics. Note, a quadratic convergence is possible by an accurate determination of the tangent modulus, but the modulus has no influence on the accuracy of the converged solution. The material tangent modulus is the slope of the stress-strain curve at any specified stress or strain. In the purely elastic deformation region the tangent modulus is equivalent to elastic modulus. In a general three-dimensional setting the material tangent is the derivative of the stress tensor with respect to the strain tensor, which yields a fourth-order tensor

$$\mathbb{C} = \frac{\partial \boldsymbol{\sigma}}{\partial \boldsymbol{\varepsilon}} \,. \tag{A.28}$$

While in the small strain setting rigid body motions and large deformations are neglected, in finite deformation theory, with continuously updating current coordinates, the stress rate has to be objective. An objective stress rate ensures that rigid body rotations do not change the invariants of the stress tensor. The constitutive formulation must be invariant to changes of the reference frame. Various objective stress rates exists for large strain formulations. Again ABAQUS dictates the choice of the stress rate and requires besides the Cauchy stress an update of the tangent modulus appropriate to the Jaumann rate of Cauchy stress, see [77, 112, 18], which is a commonly used stress rate in plasticity theory satisfying objectivity.

The material tangent modulus changes according to the used stress rate and stress definition. Detailed derivations of the modulus $\mathbb{C}^{JC}$ appropriate to the Jaumann rate of Cauchy stress is given in Meissonnier et al. [112] and here restated with a slight correction

$$\mathbb{C}^{JC} = J^{-1}\Big[(\boldsymbol{F} \underline{\otimes} \boldsymbol{F}) : \frac{\partial \boldsymbol{S}}{\partial \boldsymbol{E}} : (\boldsymbol{F} \underline{\otimes} \boldsymbol{F})^T\Big] + \boldsymbol{1} \underline{\otimes} \boldsymbol{\sigma}^T + \boldsymbol{\sigma} \bar{\otimes} \boldsymbol{1} - \boldsymbol{\sigma} \otimes \boldsymbol{1} \,, \tag{A.29}$$

where $\underline{\otimes}$ and $\bar{\otimes}$ are the lower and upper tensor products[7]. An explicit relation for the tangent modulus of the second Piola-Kirchhoff stress tensor with respect to the Green strain tensor $\frac{\partial \boldsymbol{S}}{\partial \boldsymbol{E}}$ is required to determine the tangent modulus (A.29). This expression is pushed forward from the reference configuration to the current configuration in the first term of (A.29). Taking the derivative of $\boldsymbol{S}$ with respect to $\boldsymbol{E}$ and using the relation $\boldsymbol{S} = J\boldsymbol{F}^{p^{-1}}\tilde{\boldsymbol{S}}\boldsymbol{F}^{p^{-T}}$ yields

$$\frac{\partial \boldsymbol{S}}{\partial \boldsymbol{E}} = \Big[\boldsymbol{F}^{p^{-1}} \underline{\otimes} \boldsymbol{F}^{p^{-1}}\Big] : \frac{\partial \tilde{\boldsymbol{S}}}{\partial \boldsymbol{E}} + \Big[\boldsymbol{I} \underline{\otimes} \left(\tilde{\boldsymbol{S}}\, \boldsymbol{F}^{p^{-T}}\right)^T + \boldsymbol{F}^{p^{-1}}\, \tilde{\boldsymbol{S}} \bar{\otimes} \boldsymbol{I}\Big] : \frac{\partial \boldsymbol{F}^{p^{-1}}}{\partial \boldsymbol{E}} \,. \tag{A.30}$$

Considering the hyper-elastic approach for the material description (5.7), $\frac{\partial \tilde{\boldsymbol{S}}}{\partial \boldsymbol{E}}$ can be determined and pulled back to the reference configuration by (A.30). The constitutive coupling between the stress and slip resistance described in Sections A.1 and A.2 and its influence on the material tangent is considered in the following procedure, where the solution strategy proposed by Boeff [18] is adopted. At the locally converged material point the equations (A.20-A.22) are fulfilled in the range of a given tolerance and approximately

[7] $\boldsymbol{A} \underline{\otimes} \boldsymbol{B} = (\boldsymbol{A} \underline{\otimes} \boldsymbol{B})_{ijkl} = A_{ik}B_{jl}$ and $\boldsymbol{A} \bar{\otimes} \boldsymbol{B} = (\boldsymbol{A} \bar{\otimes} \boldsymbol{B})_{ijkl} = A_{il}B_{jk}$

zero. We introduce a strain perturbation $\Delta \boldsymbol{E}$ only to residuum equation (A.23) yielding the following system

$$\frac{\partial \mathbf{G}_1}{\partial \tilde{\boldsymbol{S}}} \Delta \tilde{\boldsymbol{S}}_{n+1} + \frac{\partial \mathbf{G}_1}{\partial \tau^{\alpha}_{c,\,n+1}} \Delta \tau^{\alpha}_{c,\,n+1} + \frac{\partial \mathbf{G}_1}{\partial \chi^{\alpha}_{n+1}} \Delta \chi^{\alpha}_{n+1} + \frac{\partial \mathbf{G}_1}{\partial \boldsymbol{E}} \Delta \boldsymbol{E} = 0 \tag{A.31}$$

$$\frac{\partial \mathbf{G}_2}{\partial \tilde{\boldsymbol{S}}} \Delta \tilde{\boldsymbol{S}}_{n+1} + \frac{\partial \mathbf{G}_2}{\partial \tau^{\alpha}_{c,\,n+1}} \Delta \tau^{\alpha}_{c,\,n+1} + \frac{\partial \mathbf{G}_2}{\partial \chi^{\alpha}_{n+1}} \Delta \chi^{\alpha}_{n+1} = 0 \tag{A.32}$$

$$\frac{\partial \mathbf{G}_3}{\partial \tilde{\boldsymbol{S}}} \Delta \tilde{\boldsymbol{S}}_{n+1} + \frac{\partial \mathbf{G}_3}{\partial \tau^{\alpha}_{c,\,n+1}} \Delta \tau^{\alpha}_{c,\,n+1} + \frac{\partial \mathbf{G}_3}{\partial \chi^{\alpha}_{n+1}} \Delta \chi^{\alpha}_{n+1} = 0\,. \tag{A.33}$$

As described in Section A.2 the system is again solved semi-explicitly by considering the influence of isotropic hardening on the material tangent modulus only and derive a simplified solution procedure. In the following the indicator for the current time $n+1$ is omitted in the notation. By multiplying (A.31) with $\frac{1}{\Delta \boldsymbol{E}}$ and expanding the terms in the middle by $\frac{\partial \tilde{\boldsymbol{S}}}{\partial \tilde{\boldsymbol{S}}}$ one obtains

$$\frac{\partial \mathbf{G}_1}{\partial \tilde{\boldsymbol{S}}} \frac{\partial \tilde{\boldsymbol{S}}}{\partial \boldsymbol{E}} + \frac{\partial \mathbf{G}_1}{\partial \tau^{\alpha}_{c}} \frac{\partial \tau^{\alpha}_{c}}{\partial \tilde{\boldsymbol{S}}} \frac{\partial \tilde{\boldsymbol{S}}}{\partial \boldsymbol{E}} + \frac{\partial \mathbf{G}_1}{\partial \boldsymbol{E}} = 0\,. \tag{A.34}$$

The material tangent in intermediate configuration can be found by rearranging this term as

$$\frac{\partial \tilde{\boldsymbol{S}}}{\partial \boldsymbol{E}} = -\Big[\, \frac{\partial \mathbf{G}_1}{\partial \tilde{\boldsymbol{S}}} + \frac{\partial \mathbf{G}_1}{\partial \tau^{\alpha}_{c}} \frac{\partial \tau^{\alpha}_{c}}{\partial \tilde{\boldsymbol{S}}} \,\Big]^{-1} \frac{\partial \mathbf{G}_1}{\partial \boldsymbol{E}} = 0\,. \tag{A.35}$$

The change of the critical resolved shear stress with respect to the small perturbation leading to an increment in the stress can be derived from (A.32) by multiplication with $\frac{1}{\Delta \tilde{\boldsymbol{S}}}$ and rearranging to

$$\frac{\partial \tau^{\alpha}_{c}}{\partial \tilde{\boldsymbol{S}}} = -\Big(\frac{\partial \mathbf{G}_2}{\partial \tau^{\alpha}_{c}}\Big)^{-1} \frac{\partial \mathbf{G}_2}{\partial \tilde{\boldsymbol{S}}}\,, \tag{A.36}$$

which can be inserted in A.35 and yield the final expression

$$\frac{\partial \tilde{\boldsymbol{S}}}{\partial \boldsymbol{E}} = -\Big[\, \frac{\partial \mathbf{G}_1}{\partial \tilde{\boldsymbol{S}}} - \frac{\partial \mathbf{G}_1}{\partial \tau^{\alpha}_{c}} \Big(\frac{\partial \mathbf{G}_2}{\partial \tau^{\alpha}_{c}}\Big)^{-1} \frac{\partial \mathbf{G}_2}{\partial \tilde{\boldsymbol{S}}} \,\Big]^{-1} \frac{\partial \mathbf{G}_1}{\partial \boldsymbol{E}} = 0\,. \tag{A.37}$$

The tangent moduli in intermediate configuration $\frac{\partial \tilde{\boldsymbol{S}}}{\partial \boldsymbol{E}}$ is pulled back to the reference configuration $\frac{\partial \boldsymbol{S}}{\partial \boldsymbol{E}}$ by (A.30) and then inserted into (A.29).

References

[1] Abdolvand, H. [2018]: *Progressive modelling and experimentation of hydrogen diffusion and precipitation in anisotropic polycrystals.* International Journal of Plasticity.

[2] Altenbach, J.; Altenbach, H. [1994]: *Einführung in die Kontinuums-Mechanik.* Teubner.

[3] Alvaro, A.; Olden, V.; Akselsen, O. M. [2013]: *3D cohesive modelling of hydrogen embrittlement in the heat affected zone of an X70 pipeline steel.* International Journal of Hydrogen Energy, 38(18): 7539–7549.

[4] Ananthan, V. S.; Hall, E. O. [1991]: *Macroscopic aspects of Lüders band deformation in mild steel.* Acta Metallurgica et Materialia, 39(12): 3153–3160.

[5] Arnaudov, N.; Kolyshkin, A.; Bacher-Höchst, M.; Weihe, S. [2018]: *Mikrostruktursimulation der Ermüdungsrissinitiierung unter Wasserstoffatmosphäre.* In *45. Tagung des DVM-Arbeitskreises Betriebsfestigkeit, Renningen*, Vol. 45, pp. 293–308, ISSN 0944–5242.

[6] Asaro, R. J.; Needleman, A. [1985]: *Texture development and strain hardening in rate dependent polycrystals.* Acta Metallurgica, 33(6): 923–953.

[7] Asaro, R. J.; Rice, J. R. [1977]: *Strain localization in ductile single crystals.* Journal of the Mechanics and Physics of Solids, 25(5): 309–338.

[8] Bachmann, F.; Hielscher, R.; Schaeben, H. [2010]: *Texture analysis with MTEX–free and open source software toolbox.* In *Solid State Phenomena*, Vol. 160, pp. 63–68. Trans Tech Publ.

[9] Barrera, O.; Bombac, D.; Chen, Y.; et al. [2018]: *Understanding and mitigating hydrogen embrittlement of steels: a review of experimental, modelling and design progress from atomistic to continuum.* Journal of Materials Science, 53: 6251–6290.

[10] Barrera, O.; Cocks, A. C. F. [2013]: *Computational modelling of hydrogen embrittlement in welded structures.* Philosophical Magazine, 93(20): 2680–2700.

[11] Barrera, O.; Tarleton, E.; Cocks, A. C. F. [2015]: *Hydrogen embrittlement mechanisms in metals: a modelling approach.* In *SIMULIA Community Conference.*

[12] Barrera, O.; Tarleton, E.; Tang, H. W.; Cocks, A. C. F. [2016]: *Modelling the coupling between hydrogen diffusion and the mechanical behaviour of metals.* Computational Materials Science, 122: 219–228.

[13] Basquin, O. H. [1910]: *The Exponential Law of Endurance Tests.* In *Proc Am Soc Test Mater*, Vol. 10, pp. 625–630.

[14] Bathe, K.-J. [2002]: *Finite-Elemente-Methoden*, Vol. 2. Springer Berlin.

[15] Bauschinger, J. [1886]: *Über die Veränderung der Elastizitätsgrenze und Festigkeit des Eisens und Stahls durch Strecken und Quetschen, durch Erwärmen und Abkühlen und durch oftmals wiederholte Beanspruchung.* Mitteilungen aus dem mechanisch-technischen Laboratorium der technischen Hochschule in München, 13.

[16] Bennett, V. P.; McDowell, D. L. [2003]: *Polycrystal orientation distribution effects on microslip in high cycle fatigue.* International Journal of Fatigue, 25(1): 27–39.

[17] Birnbaum, H. K.; Sofronis, P. [1994]: *Hydrogen-enhanced localized plasticity - a mechanism for hydrogen-related fracture.* Materials Science and Engineering: A, 176(1-2): 191–202.

[18] Boeff, M. [2016]: *Micromechanical modelling of fatigue crack initiation and growth.* Ph.D. Thesis, Ruhr-Universität Bochum.

[19] Boeff, M.; Ul Hassan, H.; Hartmaier, A. [2017]: *Micromechanical modeling of fatigue crack initiation in polycrystals.* Journal of Materials Research, 32(23): 4375–4386.

[20] Böhlke, T.; Jöchen, K.; Kraft, O.; Löhe, D.; Schulze, V. [2010]: *Elastic properties of polycrystalline microcomponents.* Mechanics of Materials, 42(1): 11–23.

[21] Böllinghaus, T.; Hoffmeister, H.; Middel, C. [1996]: *Scatterbands for hydrogen diffusion coefficients in steels having a ferritic or martensitic microstructure and steels having an austenitic microstructure at room temperature.* Welding in the World/Le Soudage dans le Monde, 1(37): 16–23.

[22] Bonet, J.; Wood, R. D. [1997]: *Nonlinear continuum mechanics for finite element analysis.* Cambridge University Press.

[23] Braithwaite, F. [1854]: *On the Fatigue and Consequent Fracture of Metals.* In *Minutes of the Proceedings of the Institution of Civil Engineers*, Vol. 13, pp. 463–467. ICE Virtual Library.

[24] Bravais, A. [1859]: *Mémoire sur les systèmes des points distribuées régulièrement sur un plan ou dans l'espace.* Journal de l'Ecole Polytechnique, 19: 1–128.

[25] Brocks, W.; Falkenberg, R.; Scheider, I. [2012]: *Coupling aspects in the simulation of hydrogen-induced stress-corrosion cracking.* Procedia IUTAM, 3: 11–24.

[26] Bugaev, V. N.; Gavriljuk, V. G.; Petrov, Y. N.; Tarasenko, A. V. [1997]: *Mechanism of hydrogen-induced phase transformations in metals and alloys.* International Journal of Hydrogen Energy, 22(2-3): 213–218.

[27] Bunge, H. J. [1985]: *Representation of preferred orientations.* In *Preferred Orientation in Deformed Metal and Rocks*, pp. 73–108. Elsevier.

[28] Cailletaud, G. [1992]: *A micromechanical approach to inelastic behaviour of metals.* International Journal of Plasticity, 8(1): 55–73.

[29] Castelluccio, G. M. [2012]: *A study on the influence of microstructure on small fatigue cracks.* Ph.D. Thesis, Georgia Institute of Technology.

[30] Castelluccio, G.M.; McDowell, D. L. [2014]: *Mesoscale modeling of microstructurally small fatigue cracks in metallic polycrystals.* Materials Science and Engineering: A, 598: 34–55.

[31] Castelluccio, G. M.; McDowell, D. L. [2016]: *Microstructure-sensitive small fatigue crack growth assessment: Effect of strain ratio, multiaxial strain state, and geometric discontinuities.* International Journal of Fatigue, 82: 521–529.

[32] Chaboche, J.-L. [1986]: *Time-independent constitutive theories for cyclic plasticity.* International Journal of Plasticity, 2(2): 149–188.

[33] Chaboche, J.-L. [2008]: *A review of some plasticity and viscoplasticity constitutive theories.* International Journal of Plasticity, 24(10): 1642–1693.

[34] Charles, Y.; Nguyen, H. T.; Gaspérini, M. [2017]: *Comparison of hydrogen transport through pre-deformed synthetic polycrystals and homogeneous samples by finite element analysis.* International Journal of Hydrogen Energy, 42(31): 20336–20350.

[35] Cherepanov, G. P. [1967]: *The propagation of cracks in a continuous medium.* Journal of Applied Mathematics and Mechanics, 31(3): 503–512.

[36] CHMC, ANSI/CSA [2014]: *Test methods for evaluating material compatibility in compressed hydrogen applications - Metals. 1-2014.*

[37] Christ, H.-J. [2009]: *Ermüdungsverhalten metallischer Werkstoffe.* Wiley-VCH, 2 Edition.

[38] Christ, H.-J. [2013]: *Wechselverformung von Metallen: zyklisches Spannungs-Dehnungs-Verhalten und Mikrostruktur*, Vol. 9. Springer-Verlag.

[39] Coffin, L. [1954]: *The problem of thermal stress fatigue in austenitic steels at elevated temperatures.* In *Symposium on Effect of Cyclic Heating and Stressing on Metals at Elevated Temperatures.* ASTM International.

[40] Counts, W. A.; Wolverton, C.; Gibala, R. [2010]: *First-principles energetics of hydrogen traps in α-Fe: Point defects.* Acta Materialia, 58(14): 4730–4741.

[41] Courtney, T. H. [2005]: *Mechanical behavior of materials.* Waveland Press, 2 Edition.

[42] De Souza Neto, E. A.; Peric, D.; Owen, D. R. J. [2008]: *Computational methods for plasticity: theory and applications.* John Wiley & Sons.

[43] Díaz, A.; Alegre, J. M.; Cuesta, I. I. [2016]: *Coupled hydrogen diffusion simulation using a heat transfer analogy.* International Journal of Mechanical Sciences, 115: 360–369.

[44] Di Leo, C. V.; Anand, L. [2013]: *Hydrogen in metals: A coupled theory for species diffusion and large elastic–plastic deformations.* International Journal of Plasticity, 43: 42–69.

[45] DIN EN ISO, 17081 [2008]: *Elektrochemisches Verfahren zur Messung der Wasserstoffpermeation und zur Bestimmung von Wasserstoffaufnahme und -transport in Metallen. 2008-07.*

[46] Di Stefano, D.; Mrovec, M.; Elsässer, C. [2015]: *First-principles investigation of hydrogen trapping and diffusion at grain boundaries in nickel.* Acta Materialia, 98: 306–312.

[47] Dönges, B. [2017]: *Ermüdungsmechanismen eines Duplexstahls bei niedrigen Spannungsamplituden: experimentelle Charakterisierung und modellmäßige Beschreibung des Einflusses der Mikrostruktur auf die Lebensdauer.* Ph.D. Thesis, University of Siegen.

[48] Du, Y. A.; Ismer, L.; Rogal, J.; Hickel, T.; Neugebauer, J.; Drautz, R. [2011]: *First-principles study on the interaction of H interstitials with grain boundaries in α-and γ-Fe.* Physical Review B, 84(14): 144121.

[49] Ellyin, Fe. [2012]: *Fatigue damage, crack growth and life prediction.* Springer Science & Business Media.

[50] Essmann, U.; Gösele, U.; Mughrabi, H. [1981]: *A model of extrusions and intrusions in fatigued metals I. Point-defect production and the growth of extrusions.* Philosophical Magazine A, 44(2): 405–426.

[51] Farukh, F.; Zhao, L. G.; Barnard, N. C.; Whittaker, M. T.; McColvin, G. [2018]: *Computational modelling of full interaction between crystal plasticity and oxygen diffusion at a crack tip.* Theoretical and Applied Fracture Mechanics, 96: 707–719.

[52] Fatemi, A.; Socie, D. F. [1988]: *A critical plane approach to multiaxial fatigue damage including out-of-phase loading.* Fatigue & Fracture of Engineering Materials & Structures, 11(3): 149–165.

[53] Ferreira, P. J.; Robertson, I. M.; Birnbaum, H. K. [1998]: *Hydrogen effects on the interaction between dislocations.* Acta Materialia, 46(5): 1749–1757.

[54] Fick, A. [1855]: *Über Diffusion.* Annalen der Physik, 170(1): 59–86.

[55] Flanagan, T. B.; Mason, N. B.; Birnbaum, H. K. [1981]: *The effect of stress on hydride precipitation.* Scripta Metallurgica, 15(1): 109–112.

[56] Frappart, S.; Feaugas, X.; Creus, J.; Thebault, F.; Delattre, L.; Marchebois, H. [2010]: *Study of the hydrogen diffusion and segregation into Fe–C–Mo martensitic HSLA steel using electrochemical permeation test.* Journal of Physics and Chemistry of Solids, 71(10): 1467–1479.

[57] Frederick, C. O.; Armstrong, P. J. [1966]: *A mathematical representation of the multiaxial Bauschinger effect.* CEBG Report RD/B/N, 731.

[58] Frederick, C. O.; Armstrong, P. J. [2007]: *A mathematical representation of the multiaxial Bauschinger effect.* Materials at High Temperatures, 24(1): 1–26.

[59] Gangloff, R. P.; Somerday, B. P. [2012]: *Gaseous hydrogen embrittlement of materials in energy technologies: the problem, its characterisation and effects on particular alloy classes.* Woodhead Publishing.

[60] Gerberich, W. W; Oriani, R. A.; Lji, M.-J.; Chen, X.; Foecke, T. [1991]: *The necessity of both plasticity and brittleness in the fracture thresholds of iron.* Philosophical Magazine A, 63(2): 363–376.

[61] Ghosh, S.; Nowak, Z.; Lee, K. [1997]: *Tessellation-based computational methods for the characterization and analysis of heterogeneous microstructures.* Composites Science and Technology, 57(9-10): 1187–1210.

[62] Gottstein, G. [2001]: *Physikalische Grundlagen der Materialkunde.* Springer Heidelberg, 2 Edition.

[63] Graf, M. [2018]: *Mikromechanische Fatigue-Simulation zur Analyse der Rissinitiierung in metallischen Werkstoffen.* Master Thesis, University of Stuttgart.

[64] Gross, D.; Seelig, T. [1996]: *Bruchmechanik*, Vol. 2. Springer.

[65] Gurtin, E.; Fried, M. E.; Anand, L. [2009]: *Continuum Mechanics and Thermodynamics.*

[66] Haibach, E. [2002]: *Betriebsfestigkeit, Verfahren und Daten zur Bauteilberechnung*, Vol. 2. Springer-Verlag Berlin Heidelberg.

[67] Hall, E. O. [1951]: *The deformation and ageing of mild steel: II characteristics of the Lüders deformation.* Proceedings of the Physical Society. Section B, 64(9): 742.

[68] Hao, Y. [2018]: *Simulation of Hydrogen Diffusion in Metallic Materials.* Master Thesis, Institute for Applied Materials, Karlsruhe Institute of Technology (KIT).

[69] Haupt, P. [2002]: *Continuum mechanics and theory of materials.* Springer.

[70] Hennessey, C.; Castelluccio, G. M.; McDowell, D. L. [2017]: *Sensitivity of polycrystal plasticity to slip system kinematic hardening laws for Al 7075-T6.* Materials Science and Engineering: A, 687: 241–248.

[71] Herring, D. H. [2010]: *Hydrogen Embrittlement.* Wire Forming Technology International, 13(4): 24–27.

[72] Hickel, T.; Nazarov, R.; McEniry, E. J.; Leyson, G.; Grabowski, B.; Neugebauer, J. [2014]: *Ab initio based understanding of the segregation and diffusion mechanisms of hydrogen in steels.* JOM, 66(8): 1399–1405.

[73] Hill, R. [1965]: *A self-consistent mechanics of composite materials.* Journal of the Mechanics and Physics of Solids, 13(4): 213–222.

[74] Hirth, J. P. [1980]: *Effects of hydrogen on the properties of iron and steel.* Metallurgical Transactions A, 11(6): 861–890.

[75] Hoch, B. O. [2015]: *Modelling of hydrogen diffusion in heterogeneous materials: implications of the grain boundary connectivity.* Ph.D. Thesis, Université de La Rochelle.

[76] Hochhalter, J. D.; Littlewood, D. J.; Christ Jr, R. J.; Veilleux, M. G.; Bozek, J. E.; Ingraffea, A. R.; Maniatty, A. M. [2010]: *A geometric approach to modeling microstructurally small fatigue crack formation: II. Physically based modeling of microstructure-dependent slip localization and actuation of the crack nucleation mechanism in AA 7075-T651.* Modelling and Simulation in Materials Science and Engineering, 18(4): 045004.

[77] Holzapfel, G. A. [2000]: *Nonlinear Solid Mechanics: A Continuum Approach for Engineering.* John Wiley & Sons.

[78] Honecker, F. [2018]: *Experimentelle Ermittlung mechanischer Werkstoffeigenschaften auf der Mikroskala an Stählen zum Einsatz in Wasserstoffumgebung.* Master Thesis, University of Applied Sciences Osnabrück.

[79] Huang, Y. [1991]: *A user-material subroutine incroporating single crystal plasticity in the ABAQUS finite element program.* Harvard University.

[80] Hutchinson, J. W. [1976]: *Bounds and self-consistent estimates for creep of polycrystalline materials.* In *Proceedings of the Royal Society of London A*, Vol. 348, pp. 101–127. The Royal Society.

[81] Ilin, D. N.; Saintier, N.; Olive, J.-M.; Abgrall, R.; Aubert, I. [2014]: *Simulation of hydrogen diffusion affected by stress-strain heterogeneity in polycrystalline stainless steel.* International Journal of Hydrogen Energy, 39(5): 2418–2422.

[82] Jacobson, M. Z.; Colella, W. G.; Golden, D. M. [2005]: *Cleaning the air and improving health with hydrogen fuel-cell vehicles.* Science, 308(5730): 1901–1905.

[83] Jemblie, L.; Olden, V.; Akselsen, O. M. [2017]: *A review of cohesive zone modelling as an approach for numerically assessing hydrogen embrittlement of steel structures.* Philosophical Transactions of the Royal Society A: Mathematical, Physical and Engineering Sciences, 375(2098): 20160411.

[84] Jiang, D. E.; Carter, E. A. [2004]: *Diffusion of interstitial hydrogen into and through bcc Fe from first principles.* Physical Review B, 70(6): 064102.

[85] Kanezaki, T.; Narazaki, C.; Mine, Y.; Matsuoka, S.; Murakami, Y. [2008]: *Effects of hydrogen on fatigue crack growth behavior of austenitic stainless steels.* International Journal of Hydrogen Energy, 33(10): 2604–2619.

[86] Kim, N.-H.; Oh, C.-S.; Kim, Y.-J.; Yoon, K.-B.; Ma, Y.-W. [2012]: *Hydrogen-assisted stress corrosion cracking simulation using the stress-modified fracture strain model.* Journal of Mechanical Science and Technology, 26(8): 2631–2638.

[87] Korsunsky, A. M.; Dini, D.; Dunne, F. P. E.; Walsh, M. J. [2007]: *Comparative assessment of dissipated energy and other fatigue criteria.* International Journal of Fatigue, 29(9-11): 1990–1995.

[88] Krom, A. H. M.; Koers, R. W. J.; Bakker, A. [1999]: *Hydrogen transport near a blunting crack tip.* Journal of the Mechanics and Physics of Solids, 47(4): 971–992.

[89] Kröner, E. [1958]: *Kontinuumstheorie der Versetzungen und Eigenspannungen.* Ergebnisse der Angewandten Mathematik, 5: 7–5.

[90] Krupp, U. [2005]: *Mikrostrukturelle Aspekte der Rissinitiierung und -ausbreitung in metallischen Werkstoffen.* Universität Siegen.

[91] Kumnick, A. J.; Johnson, H. H. [1980]: *Deep trapping states for hydrogen in deformed iron.* Acta Metallurgica, 28(1): 33–39.

[92] Laue, S. [2004]: *Experimentelle und theoretische Untersuchungen zur Ausbreitung kurzer Ermüdungsrisse in gekerbten Proben des Stahls Cm15.* Ph.D. Thesis, Universität Bremen.

[93] Lee, E. H. [1969]: *Elastic-plastic deformation at finite strains.* Journal of Applied Mechanics, 36(1): 1–6.

[94] Legrand, E.; Bouhattate, J.; Feaugas, X.; Touzain, S.; Garmestani, H.; Khaleel, M.; Li, D. S. [2013]: *Numerical analysis of the influence of scale effects and microstructure on hydrogen diffusion in polycrystalline aggregates.* Computational Materials Science, 71: 1–9.

[95] Lehmann, E. [2013]: *Computational homogenisation of polycrystalline elastoplastic microstructures at finite deformation.* Ph.D. Thesis, Leibniz Universität Hannover.

[96] Liang, Y; Sofronis, P.; Aravas, N. [2003]: *On the effect of hydrogen on plastic instabilities in metals.* Acta Materialia, 51(9): 2717–2730.

[97] Li, J. C. M.; Oriani, R. A.; Darken, L. S. [1966]: *The thermodynamics of stressed solids.* Zeitschrift für Physikalische Chemie, 49: 271–290.

[98] Lufrano, J.; Sofronis, P.; Birnbaum, H. K. [1998]: *Elastoplastically accommodated hydride formation and embrittlement.* Journal of the Mechanics and Physics of Solids, 46(9): 1497–1520.

[99] Lynch, S. P. [1986]: *A fractographic study of hydrogen-assisted cracking and liquid-metal embrittlement in nickel.* Journal of Materials Science, 21(2): 692–704.

[100] Lynch, S. P. [1988]: *Environmentally assisted cracking: overview of evidence for an adsorption-induced localised-slip process.* Acta Metallurgica, 36(10): 2639–2661.

[101] Lynch, S. P. [2011]: *Hydrogen embrittlement (HE) phenomena and mechanisms.* In *Stress Corrosion Cracking*, pp. 90–130. Elsevier.

[102] Lynch, S. P. [2012]: *Metallographic and fractographic techniques for characterising and understanding hydrogen-assisted cracking of metals.* In Gangloff, R. P.; Somerday, B. P. (Editors): *Gaseous Hydrogen Embrittlement of Materials in Energy Technologies: The Problem, its Characterisation and Effects on Particular Alloy Classes*, pp. 274–346. Woodhead Publishing.

[103] Ma, A.; Hartmaier, A. [2014]: *On the influence of isotropic and kinematic hardening caused by strain gradients on the deformation behaviour of polycrystals.* Philosophical Magazine, 94(2): 125–140.

[104] Mandel, J. [1971]: *Plasticité classique et viscoplasticité: course held at the Department of Mechanics and Solids.*

[105] Man, J.; Klapetek, P.; Man, O.; Weidner, A.; Obrtlík, K.; Polák, J. [2009]: *Extrusions and intrusions in fatigued metals. Part 2. AFM and EBSD study of the early growth of extrusions and intrusions in 316L steel fatigued at room temperature.* Philosophical Magazine, 89(16): 1337–1372.

[106] Man, J.; Obrtlík, K.; Polák, J. [2009]: *Extrusions and intrusions in fatigued metals. Part 1. State of the art and history.* Philosophical Magazine, 89(16): 1295–1336.

[107] Manonukul, A.; Dunne, F. P. E. [2004]: *High- and low-cycle fatigue crack initiation using polycrystal plasticity.* In *Proceedings of the Royal Society of London A: Mathematical, Physical and Engineering Sciences*, Vol. 460, pp. 1881–1903. The Royal Society.

[108] Manson, S. S. [1954]: *Behavior of materials under conditions of thermal stress.* In *NACA Technical Report 1170.*

[109] Marsh, P. G.; Gerberich, W. W. [1992]: *Influence of microstructure and texture on fatigue crack initiation in HSLA steel in hydrogen and nitrogen atmospheres.* In *First International Conference on Microstructures and Mechanical Properties of Aging Materials*, pp. 287–292.

[110] McDowell, D. L.; Dunne, F. P. E. [2010]: *Microstructure-sensitive computational modeling of fatigue crack formation.* International Journal of Fatigue, 32(9): 1521–1542.

[111] McNabb, A.; Foster, P. K. [1963]: *A new analysis of the diffusion of hydrogen in iron and ferritic steels.* Trans. Metall. Soc. AIME, 227(3): 618–627.

[112] Meissonnier, F. T.; Busso, E. P.; O'Dowd, N. P. [2001]: *Finite element implementation of a generalised non-local rate-dependent crystallographic formulation for finite strains.* International Journal of Plasticity, 17(4): 601–640.

[113] Miehe, C. [2015]: *Geometrical Methods for Nonlinear Continuum Mechanics and Continuum Thermodynamics.* Lecture notes.

[114] Miehe, C. [2016]: *Theoretical and Computer-Oriented Material Theory.* Lecture notes.

[115] Miller, W. H. [1839]: *A treatise on crystallography.* Cambridge, For J. & J. J. Deighton.

[116] Miresmaeili, R.; Saintier, N.; Notsu, H.; Olive, J.-M.; Kanayama, H. [2010]: *One-way coupled crystal plasticity-hydrogen diffusion simulation on artificial microstructure.* Journal of Computational Science and Technology, 4(2): 105–120.

[117] Moody, N. R.; Robinson, S. L.; Garrison Jr, W. M. [1990]: *Hydrogen effects on the properties and fracture modes of iron-based alloys.* Res Mech., 30(2): 143–206.

[118] Moriconi, C; Hénaff, G.; Halm, D. [2014]: *Cohesive zone modeling of fatigue crack propagation assisted by gaseous hydrogen in metals.* International Journal of Fatigue, 68: 56–66.

[119] Morris, M. A.; Bowker, M.; King, D. A. [1984]: *Kinetics of adsorption, desorption and diffusion at metal surfaces.* In *Comprehensive Chemical Kinetics*, Vol. 19, pp. 1–179. Elsevier.

[120] Morrow, J. D. [1965]: *Cyclic Plastic Strain Energy and Fatigue of Metals.* ASTM STP 378, 45.

[121] Murakami, Y. [2007]: *Effects of hydrogen on metal fatigue.* In *Proceedings of International Hydrogen Energy Development Forum, Fukuoka*, pp. 96–105.

[122] Murakami, Y.; Matsunaga, H. [2006]: *The effect of hydrogen on fatigue properties of steels used for fuel cell system.* International Journal of Fatigue, 28(11): 1509–1520.

[123] Murakami, Y.; Ritchie, R. O. [2012]: *Effects of hydrogen on fatigue-crack propagation in steels.* In Gangloff, R. P.; Somerday, B. P. (Editors): *Gaseous Hydrogen Embrittlement of Materials in Energy Technologies: The Problem, its Characterisation and Effects on Particular Alloy Classes*, pp. 379–417. Woodhead Publishing.

[124] Nagumo, M. [2004]: *Hydrogen related failure of steels–a new aspect.* Materials Science and Technology, 20(8): 940–950.

[125] Nagumo, M. [2012]: *Conformity between mechanics and microscopic functions of hydrogen in failure.* ISIJ international, 52(2): 168–173.

[126] Nanninga, N. E. [2012]: *Fatigue crack initiation and fatigue life of metals exposed to hydrogen.* In Gangloff, R. P.; Somerday, B. P. (Editors): *Gaseous Hydrogen Embrittlement of Materials in Energy Technologies: The Problem, its Characterisation and Effects on Particular Alloy Classes*, pp. 347–378. Woodhead Publishing.

[127] Neeraj, T.; Srinivasan, R.; Li, J. [2012]: *Hydrogen embrittlement of ferritic steels: observations on deformation microstructure, nanoscale dimples and failure by nanovoiding.* Acta Materialia, 60(13-14): 5160–5171.

[128] Nemat-Nasser, S.; Hori, M. [2013]: *Micromechanics: overall properties of heterogeneous materials*, Vol. 37. Elsevier.

[129] Nishikawa, S.; Kikuchi, S. [1928]: *Diffraction of Cathode Rays by Calcite.* Nature.

[130] Oh, C.-S.; Kim, Y.-J.; Yoon, K.-B. [2010]: *Coupled analysis of hydrogen transport using ABAQUS.* Journal of Solid Mechanics and Materials Engineering, 4(7): 908–917.

[131] Ohno, N.; Wang, J.-D. [1993]: *Kinematic hardening rules with critical state of dynamic recovery, part I: formulation and basic features for ratchetting behavior.* International Journal of Plasticity, 9(3): 375–390.

[132] optiSLang [2014]: *Methods for multi-disciplinary optimization and robustness analysis.* Technical report, Dynardo, Weimar.

[133] Oriani, R. A. [1970]: *The diffusion and trapping of hydrogen in steel.* Acta Metallurgica, 18(1): 147–157.

[134] Orowan, E. [1934]: *Zur Kristallplastizität.* Zeitschrift für Physik, 98(5-6): 382–387.

[135] Osipov, N.; Gourgues-Lorenzon, A.-F.; Marini, B.; Mounoury, V.; Nguyen, F.; Cailletaud, G. [2008]: *FE modelling of bainitic steels using crystal plasticity.* Philosophical Magazine, 88(30-32): 3757–3777.

[136] Paris, P.; Erdogan, F. [1963]: *A critical analysis of crack propagation laws.* Journal of Basic Engineering, 85(4): 528–533.

[137] Pedersen, A.; Jonsson, H. [2009]: *Simulations of hydrogen diffusion at grain boundaries in aluminum.* Acta Materialia, 57(14): 4036–4045.

[138] Peirce, D.; Asaro, R. J.; Needleman, A. [1983]: *Material rate dependence and localized deformation in crystalline solids.* Acta Metallurgica, 31(12): 1951–1976.

[139] Petch, N. J. [1953]: *The cleavage strength of polycrystals.* Journal of the Iron and Steel Institute, 174: 25–28.

[140] Pfeil, L. B. [1926]: *The effect of occluded hydrogen on the tensile strength of iron.* Proceedings of the Royal Society of London A, 112(760): 182–195.

[141] Pisarev, A. A. [2012]: *Hydrogen adsorption on the surface of metals.* In Gangloff, R. P.; Somerday, B. P. (Editors): *Gaseous Hydrogen Embrittlement of Materials in Energy Technologies: Mechanisms, Modelling and Future Developments*, pp. 3–26. Woodhead Publishing.

[142] Pisarev, A. A.; Ogorodnikova, O. V. [1997]: *Elementary processes near the interface between hydrogen gas and solid.* Journal of Nuclear Materials, 248: 52–59.

[143] Pohl, M. [2014]: *Hydrogen in metals: a systematic overview.* Practical Metallography, 51(4): 291–305.

[144] Polák, J. [1987]: *On the role of point defects in fatigue crack initiation.* Materials Science and Engineering, 92: 71–80.

[145] Polanyi, M. [1934]: *Über eine Art Gitterstörung, die einen Kristall plastisch machen könnte.* Zeitschrift für Physik, 89(9-10): 660–664.

[146] Protopopoff, E.; Marcus, P. [2002]: *Surface Effects on Hydrogen Entry into Metals.* In *Corrosion Mechanisms in Theory and Practice*, pp. 62–105. CRC Press.

[147] Przybyla, C. P.; McDowell, D. L. [2010]: *Microstructure-sensitive extreme value probabilities for high cycle fatigue of Ni-base superalloy IN100.* International Journal of Plasticity, 26(3): 372–394.

[148] Pundt, A. [2004]: *Hydrogen in nano-sized metals.* Advanced Engineering Materials, 6(1-2): 11–21.

[149] Quey, R.; Dawson, P. R.; Barbe, F. [2011]: *Large-scale 3D random polycrystals for the finite element method: Generation, meshing and remeshing.* Computer Methods in Applied Mechanics and Engineering, 200(17-20): 1729–1745.

[150] Quey, R.; Renversade, L. [2018]: *Optimal polyhedral description of 3D polycrystals: method and application to statistical and synchrotron X-ray diffraction data.* Computer Methods in Applied Mechanics and Engineering, 330: 308–333.

[151] Quey, R.; Villani, A.; Maurice, C. [2018]: *Nearly uniform sampling of crystal orientations.* Journal of Applied Crystallography, 51(4).

[152] Radaj, D.; Vormwald, M. [2007]: *Ermüdungsfestigkeit.* Springer, 3 Edition.

[153] Repetto, E. A.; Ortiz, M. [1997]: *A micromechanical model of cyclic deformation and fatigue-crack nucleation in fcc single crystals.* Acta Materialia, 45(6): 2577–2595.

[154] Rice, J. R. [1968]: *A path independent integral and the approximate analysis of strain concentration by notches and cracks.* Journal of Applied Mechanics, 35(2): 379–386.

[155] Rice, J. R. [1971]: *Inelastic constitutive relations for solids: an internal-variable theory and its application to metal plasticity.* Journal of the Mechanics and Physics of Solids, 19(6): 433–455.

[156] Robertson, I. M.; Martin, M. L.; Fenske, J. A. [2012]: *Influence of hydrogen on the behavior of dislocations.* In Gangloff, R. P.; Somerday, B. P. (Editors): *Gaseous Hydrogen Embrittlement of Materials in Energy Technologies: Mechanisms, Modelling and Future Developments*, pp. 166–206. Woodhead Publishing.

[157] Robertson, I. M.; Sofronis, P.; Nagao, A.; Martin, M. L.; Wang, S.; Gross, D. W.; Nygren, K. E. [2015]: *Hydrogen embrittlement understood.* Metallurgical and Materials Transactions A, 46(6): 2323–2341.

[158] Roters, F. [2011]: *Advanced material models for the crystal plasticity finite element method: development of a general CPFEM framework.* Technical report, Fachgruppe für Materialwissenschaft und Werkstofftechnik.

[159] Sangid, M. D.; Maier, H. J.; Sehitoglu, H. [2011]: *The role of grain boundaries on fatigue crack initiation–an energy approach.* International Journal of Plasticity, 27(5): 801–821.

[160] Schäfer, B.; Song, X.; Sonnweber-Ribic, P.; Ul Hassan, H.; Hartmaier, A. [2019]: *Micromechanical Modelling of the Cyclic Deformation Behav-*

ior of Martensitic SAE 4150 – A Comparison of Different Kinematic Hardening Models. Metals, 9(3): 368.

[161] Schäfer, B.; Sonnweber-Ribic, P.; Ul Hassan, H.; Hartmaier, A. [2019]: *Micromechanical Modelling of the Influence of Strain Ratio on Fatigue Crack Initiation in a Martensitic Steel – A Comparison of Different Fatigue Indicator Parameters.* Materials, 12(18): 2852.

[162] Schauer, G. [2018]: *Auslegungsansatz für Stahlbauteile bei Ermüdungsbeanspruchung in Druckwasserstoffatmosphäre.* Ph.D. Thesis, University of Stuttgart.

[163] Schauer, G.; Roetting, J.; Hahn, M.; Schreijaeg, S.; Bacher-Höchst, M.; Weihe, S. [2015]: *Influence of Gaseous Hydrogen on Fatigue Behavior of Ferritic Stainless Steel–A Fatigue-life Estimation.* Procedia Engineering, 133: 362–378.

[164] Schijve, J. [2008]: *Fatigue of Structures and Materials.* Springer Science & Business Media, 2 Edition.

[165] Schneider, K.; Klusemann, B.; Bargmann, S. [2017]: *Fully periodic RVEs for technological relevant composites: not worth the effort!* Journal of Mechanics of Materials and Structures, 12(4): 471–484.

[166] Schröder, J.; Hackl, K. [2013]: *Plasticity and beyond: microstructures, crystal-plasticity and phase transitions*, Vol. 550. Springer.

[167] Schwartz, A. J.; Kumar, M.; Adams, B. L.; Field, D. P. [2010]: *Electron Backscatter Diffraction in Materials Science.* Springer-Verlag US.

[168] Schwarz, H.-R [2013]: *Methode der finiten Elemente: eine Einführung unter besonderer Berücksichtigung der Rechenpraxis*, Vol. 47. Springer-Verlag.

[169] Schwittek, P. [2015]: *Micromechanical and Continuum Modeling of Hydrogen Assisted Steel Degradation.* Ph.D. Thesis, Ruhr-Universität Bochum.

[170] Shan, D. B.; Zong, Y. Y.; Lv, Y.; Guo, B. [2008]: *The effect of hydrogen on the strengthening and softening of Ti–6Al–4V alloy.* Scripta Materialia, 58(6): 449–452.

[171] Shenoy, M.; Zhang, J.; McDowell, D. L. [2007]: *Estimating fatigue sensitivity to polycrystalline Ni-base superalloy microstructures using a computational approach.* Fatigue & Fracture of Engineering Materials & Structures, 30(10): 889–904.

[172] Smit, R. J. M.; Brekelmans, W. A. M.; Meijer, H. E. H. [1998]: *Prediction of the mechanical behavior of nonlinear heterogeneous systems by multi-level finite element modeling.* Computer Methods in Applied Mechanics and Engineering, 155(1-2): 181–192.

[173] Sofronis, P.; McMeeking, R. M. [1989]: *Numerical analysis of hydrogen transport near a blunting crack tip.* Journal of the Mechanics and Physics of Solids, 37(3): 317–350.

[174] Sorić, J.; Wriggers, P.; Allix, O. [2018]: *Multiscale Modeling of Heterogeneous Structures.* Springer.

[175] Stroeven, M.; Askes, H.; Sluys, L. J. [2002]: *A numerical approach to determine representative volumes for granular materials.* In *Fifth World Congress on Computational Mechanics*, pp. 1–15.

[176] Suresh, S. [1998]: *Fatigue of materials.* Cambridge University Press.

[177] Suzuki, A.; Mishin, Y. M. [2004]: *Diffusion mechanisms in grain boundaries.* In *Journal of Metastable and Nanocrystalline Materials*, Vol. 19, pp. 1–24. Trans Tech Publ.

[178] Sweeney, C. A.; Dunne, F. P. E.; McHugh, P. E.; Leen, S. B. [2015]: *Micro-scale testing and micromechanical modelling for high cycle fatigue of CoCr stent material.* Journal of the Mechanical Behavior of Biomedical Materials, 46: 244–260.

[179] Sylwestrowicz, W.; Hall, E. O. [1951]: *The deformation and ageing of mild steel.* Proceedings of the Physical Society. Section B, 64(6): 495.

[180] Taha, A.; Sofronis, P. [2001]: *A micromechanics approach to the study of hydrogen transport and embrittlement.* Engineering Fracture Mechanics, 68(6): 803–837.

[181] Takai, K.; Homma, Y.; Izutsu, K.; Nagumo, M. [1996]: *Identification of trapping sites in high-strength steels by secondary ion mass spectrometry for thermally desorbed hydrogen.* Journal of the Japan Institute of Metals, 60(12): 1155–1162.

[182] Taylor, G. I. [1934]: *The mechanism of plastic deformation of crystals. Part I. -Theoretical.* Proceedings of the Royal Society of London A, 145(855): 362–387.

[183] Toribio, J.; Kharin, V. [2015]: *A generalised model of hydrogen diffusion in metals with multiple trap types.* Philosophical Magazine, 95(31): 3429–3451.

[184] Toribio, J.; Kharin, V. [2017]: *Hydrogen Transport to Fracture Sites in Metals and Alloys: Multiphysics Modelling.* Procedia Structural Integrity, 5: 1291–1298.

[185] Truesdell, C.; Noll, W. [1965]: *The Non-Linear Field Theories of Mechanics*, Vol. 3, pp. 1–602. Springer.

[186] Turnbull, A. [1993]: *Modelling of environment assisted cracking.* Corrosion science, 34(6): 921–960.

[187] Turnbull, A. [2012]: *Hydrogen diffusion and trapping in metals.* In Gangloff, R. P.; Somerday, B. P. (Editors): *Gaseous Hydrogen Embrittlement of Materials in Energy Technologies: Mechanisms, Modelling and Future Developments*, pp. 89–128. Woodhead Publishing.

[188] Ul Hassan, H.; Govind, K.; Hartmaier, A. [2019]: *Micromechanical modelling of coupled crystal plasticity and hydrogen diffusion.* Philosophical Magazine, 99(1): 92–115.

[189] Uyama, H.; Mine, Y.; Murakami, Y.; Nakashima, M.; Morishige, K. [2005]: *Effects of hydrogen charge on cyclic stress-strain properties and fatigue behavior of carbon steels.* Journal of the Society of Materials Science Japan, 54(12): 1225–1230.

[190] Vasios, N. [2015]: *Crystal plasticity: A rate-independent constitutive model. The effect of hydrogen concentration.* Diploma Thesis, University of Thessaly.

[191] Wang, J.; Wang, H.; Fan, Y. [2018]: *Techno-economic challenges of fuel cell commercialization.* Engineering, 4(3): 352–360.

[192] Wendler-Kalsch, E. [2000]: *Grundlagen und Mechanismen der Wasserstoff-induzierten Korrosion metallischer Werkstoffe.* Wasserstoff und Korrosion, 2: 7–53.

[193] Wöhler, A [1860]: *Versuche über die Festigkeit der Eisenbahnwagenachsen.* Zeitschrift für Bauwesen, 10: 160–161.

[194] Wood, W. A. [1958]: *Formation of fatigue cracks.* Philosophical Magazine, 3(31): 692–699.

[195] Wu, B.; Vajragupta, N.; Lian, J.; Hangen, U.; Wechsuwanmanee, P.; Münstermann, S. [2017]: *Prediction of plasticity and damage initiation behaviour of C45E+ N steel by micromechanical modelling.* Materials & Design, 121: 154–166.

[196] Xing, X.; Chen, W.; Zhang, H. [2015]: *Prediction of crack propagation under cyclic loading based on hydrogen diffusion.* Materials Letters, 152: 86–89.

[197] Yao, J.; Cahoon, J. R. [1991]: *Experimental studies of grain boundary diffusion of hydrogen in metals.* Acta Mtallurgica et Materialia, 39(1): 119–126.

[198] Yeratapally, S. R.; Glavicic, M. G.; Hardy, M.; Sangid, M. D. [2016]: *Microstructure based fatigue life prediction framework for polycrystalline nickel-base superalloys with emphasis on the role played by twin boundaries in crack initiation.* Acta Materialia, 107(C): 152–167.

[199] Zapffe, C. A.; Worden, C. O. [1951]: *Fractographic registrations of fatigue.* Transactions of the American Society for Metals, 43: 958–969.

[200] Zeman, J. [2003]: *Analysis of composite materials with random microstructure.* Ph.D. Thesis, Czech Technical University.

[201] Zhang, K.-S.; Ju, J. W.; Li, Z.; Bai., Y.-L.; Brocks, W. [2015]: *Micromechanics based fatigue life prediction of a polycrystalline metal applying crystal plasticity.* Mechanics of Materials, 85: 16–37.

[202] Zienkiewicz, O. C. [1975]: *Methode der finiten Elemente.* München: Hanser, 1975.

[203] Zimmermann, I. A. [2013]: *Hybrid Micro-Macro Modeling of Texture Evolution in Polycrystal Plasticity Based on Microstructural Reorientation Continua.* Ph.D. Thesis, University of Stuttgart.

Curriculum Vitae

Personal Data

Name	Nikolai Arnaudov
Date of Birth	September 17th, 1992
Place of Birth	Wertheim, Germany
Parents	Claudia und Dr.-Ing. Konstantin Arnaudov
Siblings	Dr. med. Theresa Arnaudov

School Education

1998–2002	Elementary school "Grundschule Dertingen", Wertheim
2002–2011	High school "Dietrich-Bonhoeffer-Gymnasium", Wertheim

University Education

2011–2014	Bachelor of Science in Simulation Technology, University of Stuttgart
2014–2016	Master of Science in Simulation Technology, University of Stuttgart
04–08/2015	Visiting Researcher, Computational Micromechanics of Materials Lab, Stanford University, USA

Professional Occupation

2016–2019	Ph.D. candidate Robert Bosch GmbH, Reliability for Metallic Components and Materials, Center for Research and Advanced Engineering, Renningen and Material Testing Institute, University of Stuttgart
2019–present	Reliability Engineer Robert Bosch GmbH, Chassis Systems Control, Leonberg

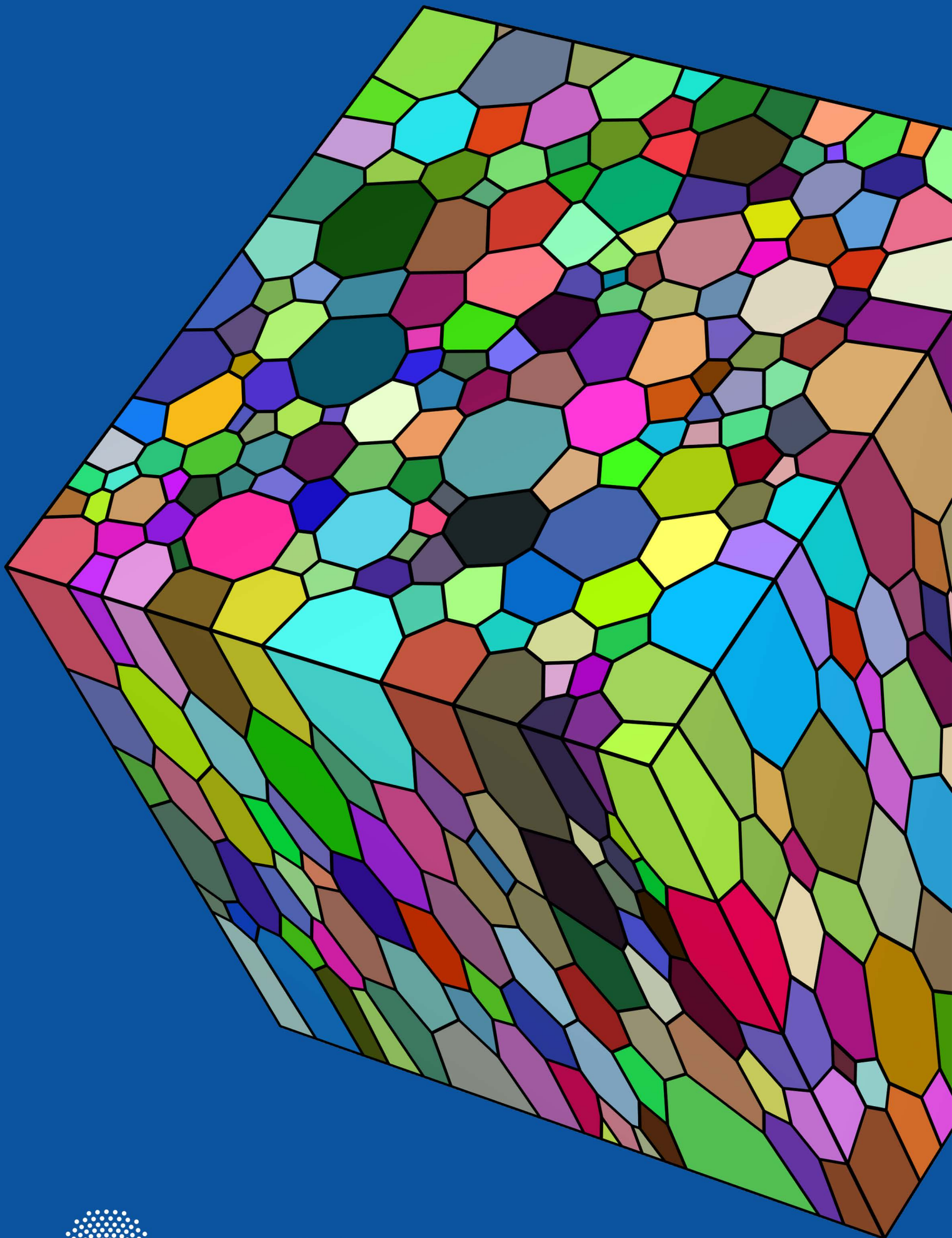

Universität Stuttgart

ISBN: 978-3-946789-10-9